
REVIEWS

Electrical and Optical Properties of Pristine and Polymerized Fullerenes

T. L. Makarova

Ioffe Physicotechnical Institute, Russian Academy of Sciences, Politekhnicheskaya ul. 26, St. Petersburg, 194021 Russia

Submitted June 22, 2000; accepted for publication June 26, 2000

Abstract—The band structure, optical, photoelectric and transport properties of solids composed of fullerene molecules linked by van der Waals bonds or forming polymers are considered. Particular attention is concentrated on different polymerization mechanisms. © 2001 MAIK “Nauka/Interperiodica”.

INTRODUCTION

The fullerenes discovered in 1985 [1] have been widely investigated after a simple method of fabrication was devised [2] and after the superconductivity of their compounds with alkali elements was discovered [3]. Tens of thousands of scientific works have been published as a result of the recent decade’s studies of fullerenes. Diverse fullerene derivatives can be conventionally divided into the following groups: van der Waals crystals, polymerized fullerenes, intercalated compounds, and exohedral, endohedral, and substituted fullerenes. In the present review we consider the problems that were not sufficiently discussed in the monographs [4–7], i.e., the properties of fullerenes as materials with semiconductor band structure and possible effects on these properties by the appearance of bonds stronger than the van der Waals bond. The necessity for such an approach to analysis of the existing works can be illustrated by the fact that the experimental and theoretical energy gaps of the C_{60} fullerene vary widely within a range of 1.43–2.35 eV. The paper does not concern fullerene superconductivity, since comprehensive information on this problem can be found in other reviews [8, 9].

STRUCTURAL FEATURES OF FULLERENES

Nonplanarity, Different Bond Lengths

The fullerene electronic structure is determined, as in all carbon compounds, by the π -electron system. Chemically, fullerenes can be considered three-dimensional (3D) analogues of planar aromatic compounds, with the essential difference that their π -electron system is continuously conjugated. The nonplanarity of the molecules leads to strong strains, resulting in a lower thermodynamic stability of fullerenes in comparison with graphite [6]. It is commonly accepted (for the sake of simplicity) that carbon atoms of the fullerene cell have the sp^2 hybridization. However, such a statement is not quite correct, this being possible only for

planar structures: the nonplanarity leads to partial rehybridization. For C_{60} , admixture of σ -bonds yields the $sp^{2.278}$ state [10].

An essential characteristic of fullerenes is the bond alternation determining both their electronic properties and their ability to form intermolecular bonds. Bonds linking two hexagons ([6, 6]-bond, 1.39 Å) are double bonds shorter than single bonds at the interface between a pentagon and a hexagon ([5, 6]-bond, 1.45 Å). Bond alternation can not be accounted for by nonplanarity and a strained skeleton: the strain is a consequence of the pyramidal structure of the σ -bonds and has nothing to do with their length. Moreover, the difference in the bond length decreases for C_{60}^{6-} and disappears for C_{60}^{12-} [11]. Therefore, the cause is the occupancy of molecular orbitals. Sixty π -electrons of the buckminster fullerene are distributed in the following way. The completely filled s , p , d , f , and g shells contain, respectively, 2, 6, 10, 14, and 18 electrons: in total 50. The complete filling leads to a homogeneous distribution of angular momenta; the hypothetical C_{60}^{10+} molecule shows no departures from the icosahedral symmetry and has no differences in bond lengths. The remaining ten electrons occupy the fifth h -level, which can accommodate twenty-two electrons. Under the icosahedral symmetry, the state $l = 5$ splits into irreducible representations $H_u + T_{1u} + T_{2u}$. The lower level in the neutral molecule H_u is completely filled with ten electrons forming a configuration that is entirely similar to that of localized σ -orbitals directed along the [6, 6] bonds. This leads to a weak localization of the π -electrons along the edge between the hexagons. Addition of twelve electrons to the empty t_{1u} and t_{2u} levels restores the symmetry and equalizes the bond lengths [6].

The calculated bond lengths and eigenfrequencies of the molecule [12] are in good agreement with exper-

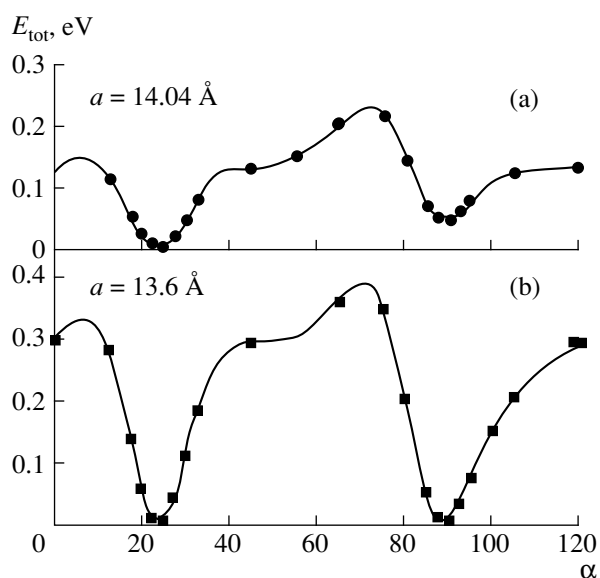


Fig. 1. Total energy per C_{60} molecule as a function of the rotation angle in the structure $Pa3$ for two different lattice constants; the value $a = 13.6 \text{ \AA}$ is related to an external pressure of 1.5 GPa [19].

iments on Raman scattering, IR absorption, and inelastic neutron scattering [13, 14].

Orientational Structure of C_{60}

The molecule orientation influences such features of the electronic structure as degeneracy, dispersion, bandwidth, and the position of valence and conduction band extrema [15]. At least four different states of solid C_{60} can be singled out: glass phase, simple cubic (SC) lattice, quasi-free rotation phase [most frequently face-centered cubic (fcc), but reports on of a close-packed hexagonal (CPH) lattice can be found in the literature], and polymerized phase.

It is commonly believed that molecules are rotating freely, have a spheroidal shape, and form a fcc lattice at temperatures above 249–260 K. However, even in this phase the rotation is not completely free, since there is a strong intermolecular orientational correlation. The correlated clusters are as large as 40 Å in size near the orientational transition temperature [16]. At low temperatures, the crystal undergoes a transition to an SC lattice with four molecules in the elementary cell. The transition does not involve any displacement of molecules, being due only to mutual ordering. The rotational motion gives way to hopping and libration about the equilibrium orientation [17, 18]. At a temperature of 90 K, jumps are frozen out, and a transition to the glass phase occurs.

Ordering in the SC phase is not complete, since two orientations of molecules are possible. Electron-saturated interpentagon bonds may be directed toward the electron-depleted pentagon faces (P -orientation) or

hexagon faces (H -orientation). The energy related to the P -orientation is 40 meV smaller than that for H -orientation; the barrier between the two minima is 130 meV per molecule. The calculated orientational dependence of the total energy of the fullerite is presented in Fig. 1 [19]. The lower minimum is related to the P -orientation.

The orientational states undergo dramatic changes upon applying pressure, which is considered in detail in the review [9]. Raising the external pressure makes the molecule rotation slower and enhances the rotational anisotropy. Therefore, the pressure induces a transition into the SC phase. In addition, the H - and P -orientations have different lattice constants. This accounts for the rather small thermal expansion coefficient of fullerite: the expansion is accompanied by reorientation. It follows from Fig. 1 that both orientations are equiprobable for the lattice constant $a = 13.6 \text{ \AA}$, corresponding to a pressure of 1.5 GPa.

At 260 K, the pentagon orientation amounts to 60%. By applying pressure, the equilibrium can be shifted toward the H -orientation, and a completely oriented phase of C_{60} can be produced [20] despite the fact that the exponential character of the P - and H -orientations distribution, in principle, forbids the existence of any completely oriented phase. An abrupt change of the phase would be expected if the coherent collective movement of all molecules is taken into account along with the rotation of a single molecule. It seems reasonable to assume that the crystal consists of a large number of P - and H -oriented microdomains, rather than of a mixture of irregularly oriented molecules. Switching into a completely oriented phase will occur when 11 out of 12 molecules are oriented. Once formed, the H -phase can be supposed to preserve stability to the point of the phase transition.

Electronic Structure of C_{60}

Since the electronic structure of fullerenes is considered in practically all monographs [4–7], we present only basic data. Data on the energy range close to the Fermi level remain contradictory up to now. The band structure of the fcc C_{60} is like the energy level distribution in an isolated C_{60} cluster. Fullerite C_{60} is a semiconductor with a minimum of the energy gap at the X point of the Brillouin zone. Calculations in the quasi-particle approximation predict a value of 2.15 eV [21] for the HOMO–LUMO gap¹ and the local density technique gives an obviously underestimated value of 1.5 eV [22] (Fig. 2). The gap values given by various methods are presented in Fig. 3.

It can be assumed that the most reliable value for the energy distance between HOMO and LUMO midbands is 3.36 eV [32] at a theoretical value of 3 eV [21]. The

¹ HOMO stands for the highest occupied molecular orbital, and LUMO, for the lowest unoccupied molecular orbital.

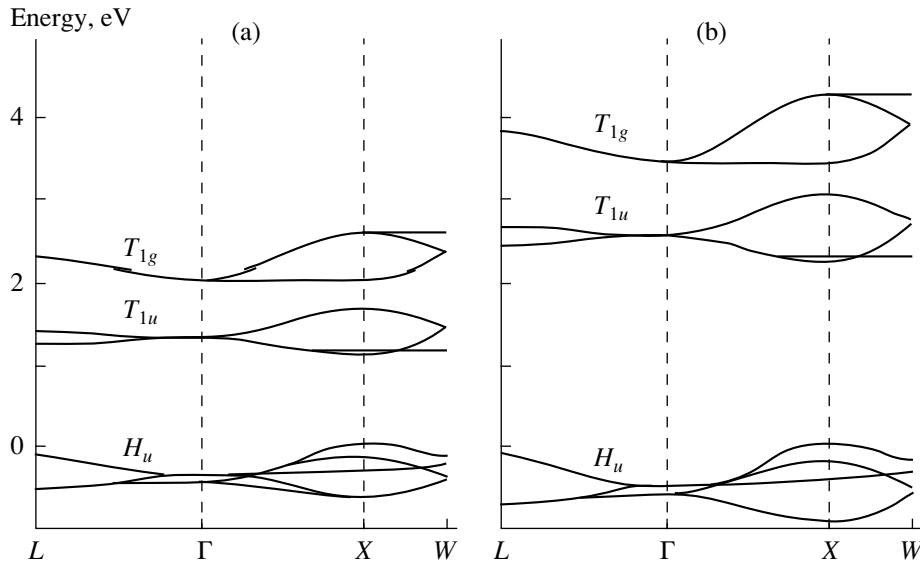


Fig. 2. Calculation of energies of the higher occupied molecular orbitals (H_u), lower unoccupied molecular orbitals (T_{1u}) and the next-higher orbitals (T_{1g}) for undoped solid C_{60} with $Fm3$ symmetry: (a) local density technique and (b) quasiparticle method [21].

ionization potential is 7.58 [33] or 7.62 eV [34], the electron affinity equals 2.65 eV [35, 36], and the lower triplet state energy is 1.7 eV [37]. The work function is found to be 4.53 eV for C_{60} amorphous films [38].

Comparison of absorption spectra for the electronic s -shell of C_{1s} atom indicates an essential similarity of the electronic structure and the electron–electron interaction in C_{60} clusters in the gas and solid states. Interactions characteristic of solids are not important in this new material, and the electron correlation effects are mainly intramolecular [39].

The intermolecular Coulomb interaction energy $U = 1.6$ eV [24]. Such a U value must lead to appearance of Frenkel excitons with energy of about 1.5–2 eV. Calculated (1.58 and 1.30 eV) and measured (1.83 and 1.55 eV) exciton energies were reported in [40]. The formation of Frenkel excitons and charge-transfer (CT) excitons with an excited electron and hole on different molecules was considered in detail in [41, 42].

The band structure of fullerene films was thoroughly studied by surface photovoltage spectroscopy [23, 43–45]. This method consists in measuring changes in the surface potential, caused by illumination. The potential changes through photostimulated emission of carriers from surface states into the bulk. The formation of the surface signal requires both photogeneration and separation of charge carriers. Thus, the measured response contains information concerning both the band gap width and characteristics of band states. The following parameters were determined: mobility edge 2.25 eV and optical gap 1.65 eV. In addition, there exist density-of-state tails extending into the optical gap of C_{60} films and other deep states. The acceptor level lies 0.8 eV below the conduction band

tail, and the donor level, 1.25 eV higher than the valence band tail (Fig. 4).

Annealing at moderate temperatures reduces the density of states in the bands. Upon annealing, the photovoltage at 2.25 eV increases, and that at 1.65 eV decreases. Improving the crystallinity decreases the density of states outside the band, making the carrier lifetime longer. The signal at 1.65 eV is the same in oxygen-free and oxygenated films; therefore, oxygen is not a reason for band tail formation. States in the gap are more likely to be due to dynamic disorder associated with molecular rotation rather than with static disorder of structural, compositional, or topological nature.

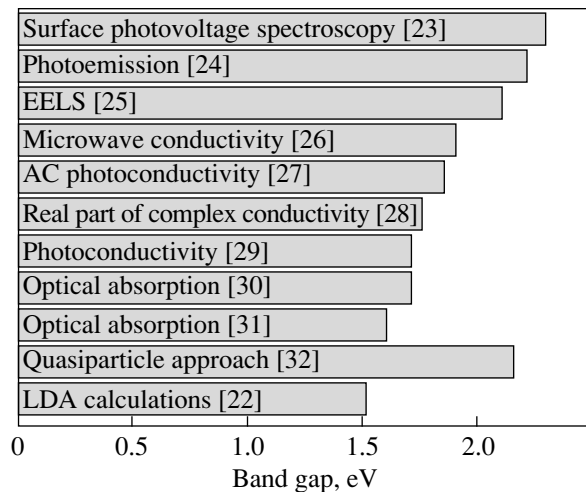


Fig. 3. Energy gaps of C_{60} fullerene, obtained in various studies.

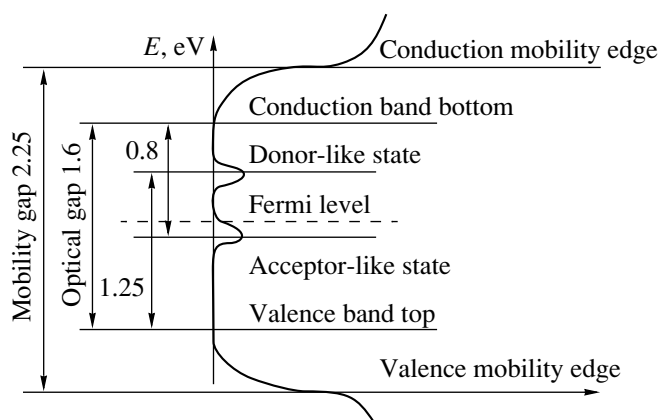


Fig. 4. Electronic structure of C_{60} thin films [43].

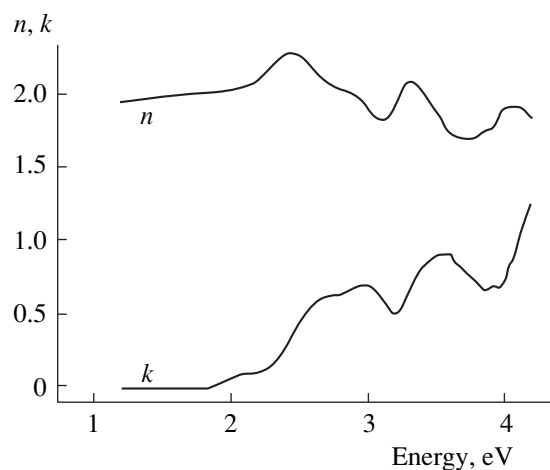


Fig. 5. Spectral dependence of the refractive index and extinction coefficient of the C_{60} film grown on a silicon substrate, measured by spectroscopic ellipsometry.

Daylight illumination of a sample in air reduces the surface photovoltage signal from donor states and enhances that from acceptor states. An electron spin resonance (ESR) study indicated that the concentration of C_{60}^+ paramagnetic defects increases. It is assumed that the donor level is related to the unbound intercalated oxygen and that the acceptor level is created in chemical reaction of oxygen with fullerene. The increase in both the intensity of the peak at $E_v + 1.25$ eV and the number of the paramagnetic centers is likely to be a consequence of the increasing number of dangling carbon bonds.

OPTICAL PROPERTIES OF FULLERENES

Optical properties of C_{60} fullerenes are generally the following. The infrared (IR) absorption spectrum contains four lines at 527, 576, 1183, and 1429 cm^{-1} . The absorption spectrum in the visible and ultraviolet (UV)

ranges contains peaks related to allowed optical transitions at 3.5–5.6 eV and to excitons at energies below 3 eV. Collective excitations give rise to two kinds of plasmons, π and $\pi + \sigma$, related to excitation of π -electrons or the electronic system as a whole. Raman scattering spectra (RS) contain two “breathing” A_g -modes related to symmetric oscillations of the entire molecule (497 cm^{-1}) and of pentagons (1469 cm^{-1}), and eight H_g -modes: 270, 433, 709, 773, 1103, 1253, 1424, and 1576 cm^{-1} . IR and Raman spectroscopies of fullerenes were described in [4, 5, 7]. Electron transition energies were calculated in [46–49]. Optical transitions between the HOMO and LUMO bands are forbidden by symmetry, and attention is mostly given in this section to the fundamental absorption edge, which is studied using optical absorption spectra in the visible and UV ranges [30, 31, 50–52] and ellipsometric spectra of films [53, 54] (Fig. 5) and single crystals [55].

The optical absorption of fullerene films can on the whole be described in terms conventional for amorphous semiconductors. The optical band gap is 1.8–1.9 eV for C_{60} and 1.66 eV for C_{70} [56], an Urbach tail and subband absorption by defects are observed. Measurement of the absorption in the visible region as a function of temperature, hydrostatic pressure, and magnetic field has shown that the spectral features near the absorption edge are due to excitons [57].

The energy region near the absorption edge was divided in [58] into three ranges, marked by letters A, B, and C in Fig. 6. The optical band within the A-range is described by the equation

$$\alpha(E)h\nu \propto (E - E_0)^2. \quad (1)$$

The absorption edge in the B-range has the characteristic Urbach shape:

$$\alpha(E) = \alpha_0 \exp(E - E_1)/E_u. \quad (2)$$

The values $E_0 = 1.7$ and 1.65 eV, Urbach parameter $E_u = 30$ and 37 meV were obtained at, respectively, 77 and 293 K. In the range C, a subbandgap absorption on impurities was observed at both temperatures. The absorption edge and the Urbach tail parameter are independent of temperature at $T < 150$ K and vary gradually at $150 \text{ K} < T < 260$ K and steeply at $T > 260$ K. Prolonged exposure of a film to air makes the subbandgap absorption higher, but does not affect the Urbach tail slope. Therefore, the Urbach tail is not a result of the oxygen intercalation, being an inherent property of the C_{60} material. The temperature dependence can be explained in terms of a correlation between the density of electronic states, orientational disordering of molecules, and the structural phase transition. At high temperatures, when C_{60} molecules can freely rotate, rotational, librational, and intermolecular vibrational degrees of freedom become important. Moreover, additional phonon modes related to fluctuations of intermolecular states come into action. Electron-phonon inter-

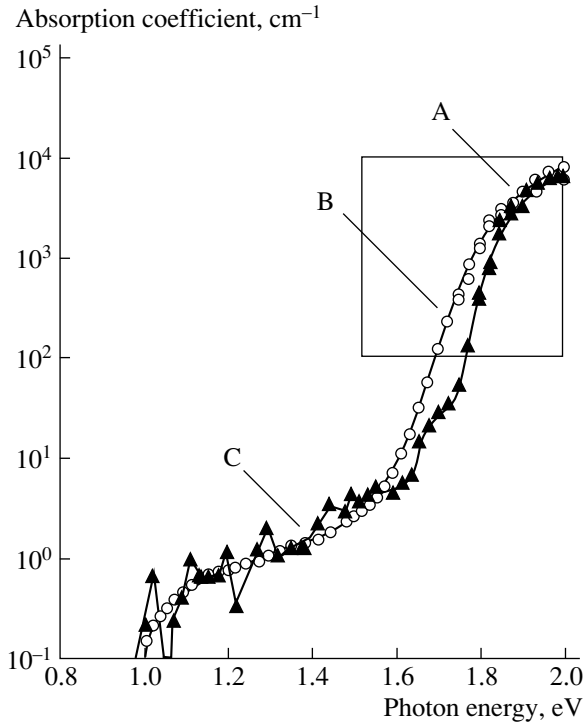


Fig. 6. Optical absorption of a 5- μm -thick C_{60} film, measured by photothermal deflection spectroscopy. Measurement temperatures: (triangles) 77 and (circles) 293 K [58].

action is enhanced in the free rotation phase. The contribution of thermal and structural disorder to the Urbach tail leads to its fast enhancement at temperatures above 260 K.

An accurate study of optical transitions in C_{60} was done in [30] by comparing the optical spectra of C_{60} films on mica with the transmission of toluene, hexane, and heptane solutions. Experimental spectra were decomposed into the Gaussian–Lorentzian components, and tables of electronic transitions, reproduced in part in Table 1, were composed on their basis.

A schematic diagram of the electronic levels in C_{60} in solid and molecular states is presented in Fig. 7. The strongest transitions in the optical spectrum correspond to the D , $E + F$, and G bands related, respectively, to the dipole-allowed optical transitions $h_g, g_g \rightarrow t_{1u}$, $h_u \rightarrow h_g$, $h_g, g_g \rightarrow t_{2u}$. The intensity of the D -band related to the second and third allowed transitions is essentially lower in doped fullerenes, owing to the filling of the lower state in the conduction band formed by molecular states t_{1u} . The molecular band F in the solid phase splits into $F1$ and $F2$ because of the splitting of the five-fold degenerate levels ($h_u(h_g)$) into the three- and twofold degenerate levels ($t_u(t_g)$, $e_u(e_g)$) [59].

Identification of the two lower transitions, $h_u \rightarrow t_{1u}$ and $h_u \rightarrow t_{1g}$, is more complicated. The molecular state $t_{1g}h_u^{-1}$ is a set of electron-hole excited states with

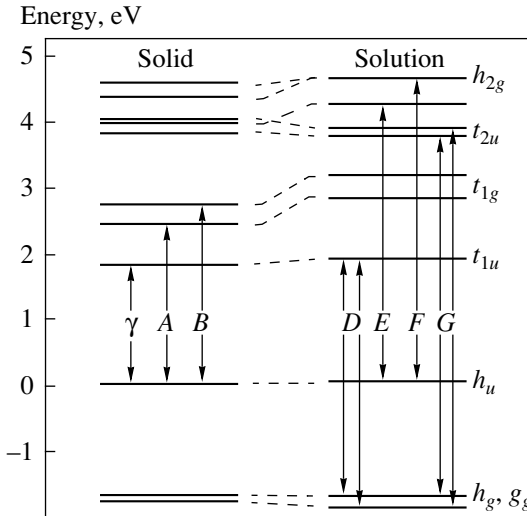


Fig. 7. Electronic energy levels in solid C_{60} and in C_{60} solution in n -hexane [30].

symmetry T_{1u} , T_{2u} , H_u , and G_u [60]. The lower allowed transition $h_u \rightarrow t_{1g}$ into the excited state T_{1u} must occur at an energy of about 3 eV. This transition is difficult to identify experimentally for two reasons: firstly, the oscillator strength is rather small and must be about 3% of that for the transition at 3.5 eV [61]; secondly, phonon-induced transitions of comparable intensity into the excited T_{2u} , H_u , and G_u states forming the B group must be observed within the same energy range.

Table 1. Spectral features for C_{60} films and solutions. All energies given in eV

Band	C_{60} film	C_{60} solution	Transition
γ_0	1.918	1.995	$h_u \rightarrow t_{1u} + T_u$, $H_u, G_z(+H_g, A_g)$
γ_1		2.035	
γ_2	1.992	2.070	
γ_3	2.028	2.105	
γ_3	2.097	2.180	
A	2.41		
B	2.70		$h_z \rightarrow t_{1g}$
C	3.2		
$D1$	3.489	3.58	$h_g, g_g \rightarrow t_{1u}$
$D2$	3.541	3.732	
E	3.99	4.21	$h_z \rightarrow h_g$
$F1$	4.36		
$F2$	4.546	4.6	
$G1$	5.500	5.437	$h_g, g_g \rightarrow t_{2u}$
$G2$	5.77	5.73	

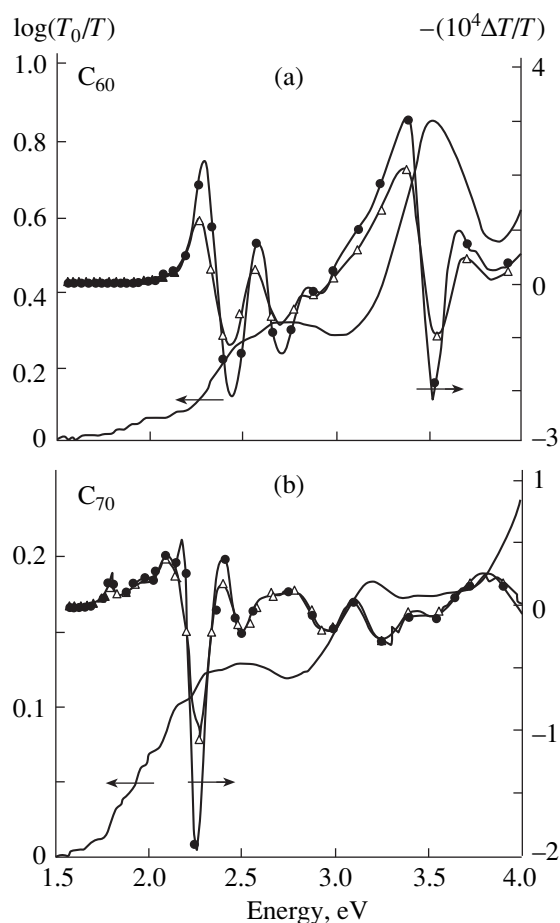


Fig. 8. Absorption (solid lines) and electroreflection (dash dot) spectra of (a) C_{60} and (b) C_{70} films [62]; circles 77 and triangles 293 K.

The A-group is attributed by the authors to the $t_{1g}h_u^{-1}$ electron-hole state parity forbidden in an isolated molecule, but becoming partially allowed because of level splitting.

Table 2. Main spectral features for C_{60} and C_{70} films. Electroabsorption (i), $i = 1, 2, 3$ stands for the position of the strongest modulations in an electroabsorption spectrum. All energies measured in eV

	C_{60}	C_{70}
Absorption edge	1.85	1.80
0-0 singlet electronic transition (fluorescence)	1.84	1.79
0-0 triplet electronic transition (phosphorescence)	1.50	1.59
Allowed optical transition 1	3.60	2.45
Onset of the luminescence quenching	2.35	1.85
Onset of carrier photogeneration	2.35	1.85
Electroabsorption 1	2.4	1.85
Electroabsorption 2	2.7	2.26
Electroabsorption 3	3.5	3.60

The γ -group arises from the forbidden molecular transition $h_u \rightarrow t_{1u}$. These transitions reveal themselves because of the excitation of the odd vibrational mode, and higher electronic states of this group must depend on the Jahn-Teller distortion [50].

A more refined consideration of the optical absorption edge requires taking into account the excitonic effects [41, 62, 63]. Both the electron-hole excitations without spin flip (singlet excitons) and triplet excitons, having somewhat lower energies because of the absence of the exchange interaction, should be taken into consideration [42].

Roughly speaking, the UV and visible absorption spectra retain characteristic features of molecules in the gas phase or in solution. In this regard, fullerenes are typical molecular crystals. However, the lowering of the symmetry and the presence of a crystal field in fullerenes affect the selection rules and the energies of the intermolecular excitations (shift and splitting of degenerate electronic levels). The optical properties of fullerenes depend equally on intra- and intermolecular processes. The former lead to the formation of Frenkel excitons, and the latter give rise to CT-excitons in which the two charges are localized on different molecules. Excitons of these two kinds were considered in detail in [62]. Forbidden Frenkel excitons with energies of 1.55, 1.87, and 2.2 eV exist inside the C_{60} HOMO-LUMO band. The first allowed exciton is at 3.6 eV.

The CT-exciton energy is estimated as follows

$$E_{ct} = I - A - 2P + C(r), \quad (3)$$

$$C(r) = -e^2/r - \Delta P_{eh}(r), \quad (4)$$

where $I = 7.62$ eV is the ionization potential [34]; $A = 2.65$ eV is the electron affinity [36]; P is the polarization energy, i.e., $2P$ is the energy of polarization induced by a pair of infinitely remote charges imbedded in the crystal; $C(r)$ is the Coulomb interaction energy; and $\Delta P_{eh}(r)$ is a change in the polarization energy as a result of charge approaching to a finite distance r . Two CT states are essential for the fullerene C_{60} ; $(1/2, 1/2, 0)$ and $(1, 0, 0)$, with electron-hole distances of, respectively, 10.01 and 14.15 Å. There are six such states in the C_{70} fullerene.

The specific features observed in spectral studies are most likely due to mixing of exciton states of two kinds. The band at 2.43 eV is a consequence of the excitation series due to electron transfer from the HOMO state of one molecule at the position $(1, 0, 0)$ to the LUMO state of the nearest neighbor situated at the position $(1/2, 1/2, 0)$. The next series appears at 3.5 eV. Commonly, it is not observed experimentally because of its closeness to the first allowed transition at 3.6 eV (T_{1u}). The charge-transfer states are associated with the allowed intramolecular excitations and form the band at 2.7 eV.

The authors of [62] compiled a table of the optical properties of C_{60} and C_{70} films (Table 2), based on a

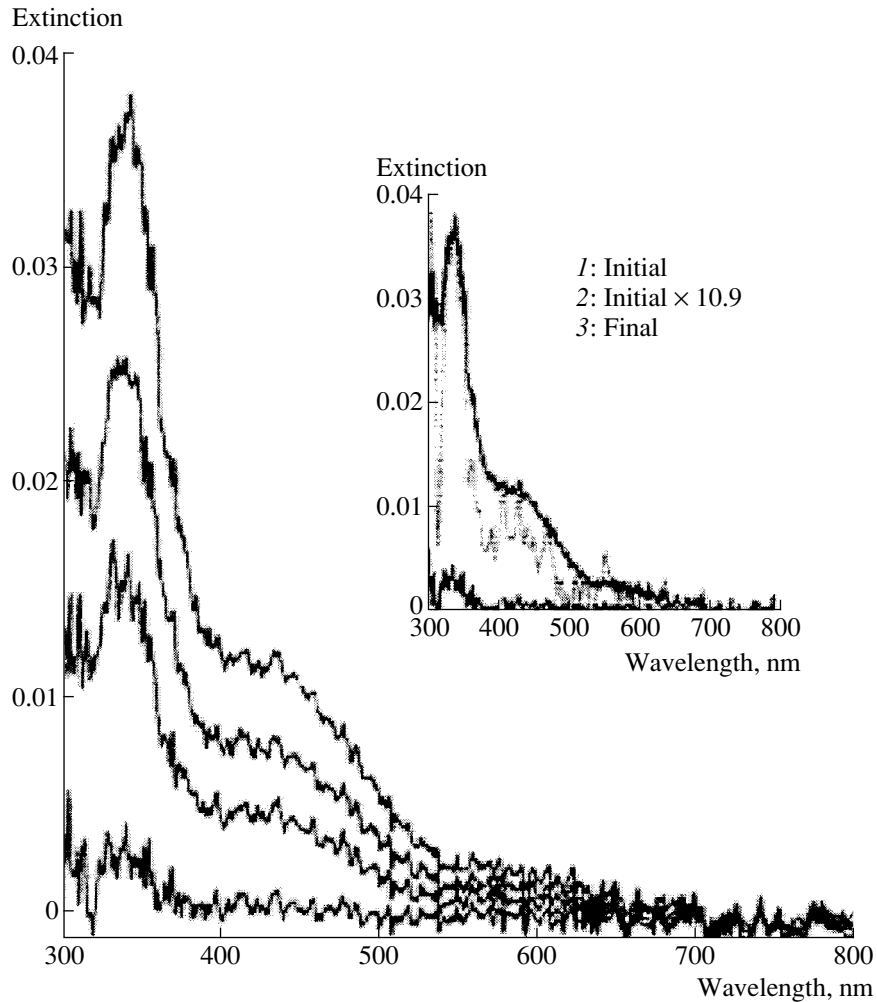


Fig. 9. Evolution of the absorption spectra of a beam of isolated C_{60} microcrystals evaporated in an atmosphere of argon. The curves are arranged so that the time increases from bottom to top. The initial spectrum is compared with the final one in the insert. Spectra are normalized to intensity of the peak related to the transition h_g-t_{1u} [63].

study of the absorption spectra, fluorescence, and electroabsorption modulation (Fig. 8).

The evolution of the C_{60} absorption spectra in going from a molecular to the solid state was considered in [63]. Only a single absorption peak at 3.76 eV (h_g-t_{1u}) is observed in the gas phase. With increasing molecule concentration, a shoulder appears at 3.54 eV, which may result from a small distance between the h_u and h_g levels or from splitting of the h_g and t_{1u} levels, and a wide band emerges at energies below 3 eV at high concentrations. In experiments on a beam of free microcrystals, absorption at 4 and 3.64 eV was observed and identified as the tail of the h_u-h_g transition and the transition h_g-t_{1u} (Fig. 9). Then a 2.91 eV band appeared and rapidly increased in intensity, and also a weak band below 2.25 eV. The band at 2.91 eV was attributed to the CT exciton for the following reasons: it is not observed on isolated molecules; its energy is higher than the lowest Frenkel exciton energy; the band width

exceeds 0.5 eV, i.e., the band width in solid C_{60} . The absorption spectra of quasi-isolated single crystals, i.e. microcrystals deposited onto a substrate, are similar, but the CT-exciton energy is red-shifted (2.75 eV) and has a more complicated structure. The CT-exciton band in the C_{60} film is also shifted relative to the isolated microcrystals (2.78 eV). With increasing film thickness, the band related to the transition h_g-t_{1u} is slightly shifted to lower energies. Absorption appears at energies below 2.25 eV, with a bend at 1.98 eV. The long-wavelength absorption by C_{60} films essentially varies from sample to sample, this being presumably due to defects [64].

Time-resolved differential absorption spectra show that the decay dynamics can be described in terms of the model of localized excitations. Self-trapped electrons are generated by excitations and then transform into polarons; the latter recombine in collisions occurring as a result of intersite jumps [65].

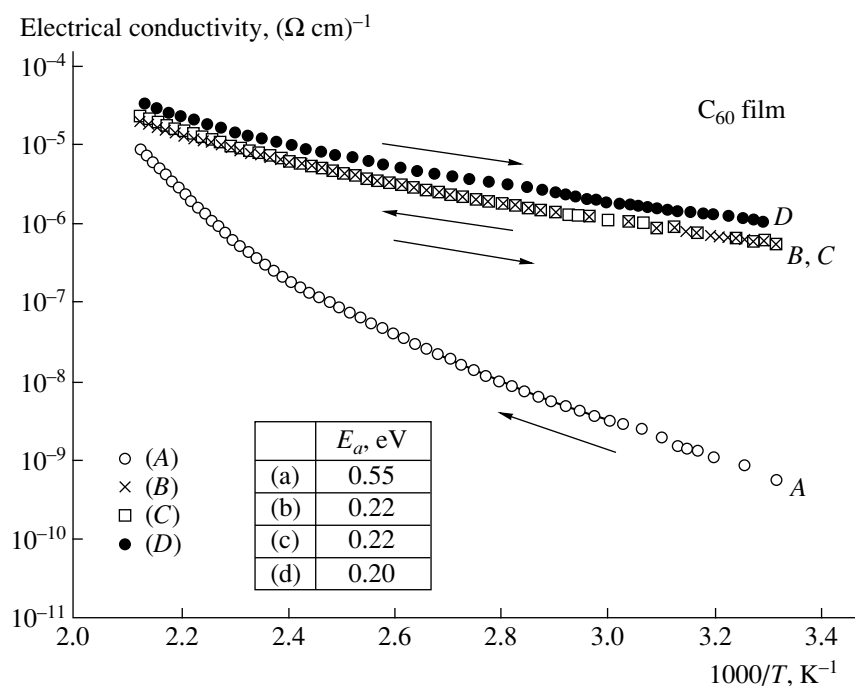


Fig. 10. Temperature dependence of the C_{60} film conductivity. Curves A and C are related to the first and third measurements. Curves B and D are related to the second and fourth measurements and are taken with temperature lowered after annealing at 200°C in the course of, respectively, two and six hours [75].

Photoinjection of electron-hole pairs, leading to an increase in the absorption by the films in the region of optical transitions at 1.6 and 2.3 eV and to a long-wavelength shift of the transition at 3.5 eV [66], was observed in C_{60} films. Photoinduced absorption in C_{60} films is due not only to optical transitions but also to singlet and triplet excitons and polarons. The local-field

effects should be taken into account since intermolecular interactions partly allow optical excitation of the singlet excitons [67].

Delocalization of electrons within a single molecule and the isolated state of the molecules lead to the nonlinear optical properties considered in [4, 6, 68]. A third-order optical nonlinearity was observed [69–71], and it was shown that two-phonon absorption is the main nonlinear process at the 3.76 eV absorption peak. Accurate measurements demonstrated that the third-order nonlinear susceptibility is rather small, which may be a result of screening [72]. Notwithstanding the lattice inversion symmetry, a second harmonic generation occurs in thin C_{60} films at a wavelength of $1.064\ \mu\text{m}$ [73]. Such a phenomenon may be due not only to the influence of the surface, but also to a contribution from magnetic dipole transitions [74].

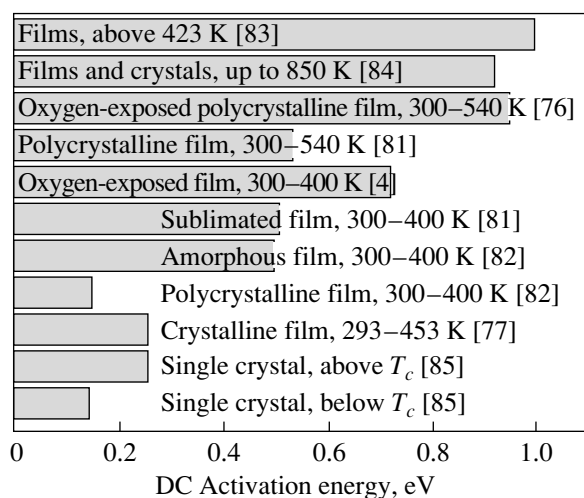


Fig. 11. Activation energy of conductivity, obtained in measurements on fullerene crystals and films in the presence and absence of oxygen.

ELECTRICAL PROPERTIES OF FULLERENES

Analysis of published data on the conductivity of fullerenes reveals the following features: n -type semiconductor conduction is observed; activation energies are essentially lower than half the energy gap, reaching this value only at high temperatures; upon interaction with oxygen, the conductivity falls by several orders of magnitude. The conductivity of the crystalline material exceeds that of the amorphous fullerene.

Results of measurement at room temperature and higher are mostly reported because of the high resistivity of fullerenes (Fig. 10). The activation energy and the dark conductivity of polycrystalline films at room temperature are, respectively, 0.3–0.6 eV and 10^{-6} – 10^{-8} ($\Omega \text{ cm}$)⁻¹ [75–78]. For amorphous films, these values fall within the intervals 0.5–1.1 eV and 10^{-7} – 10^{-14} ($\Omega \text{ cm}$)⁻¹ [29, 79–82]. The activation energies of conductivity obtained in different works are presented in Fig. 11.

Transport Parameters

Data on the transport parameters of fullerenes are rather scanty. The hole conductivity above and below the phase transition was measured by the transit-time technique, and the obtained values for, respectively, holes and electrons were 0.5 and 1.65 $\text{cm}^2/(\text{V s})$ [86]. At the point of the orientational phase transition, the mobility changes abruptly by a factor of 1.5, but within the ranges of 50–250 and 250–350 K the mobility is independent of temperature, which necessitates caution in using the band conduction model. The drift mobilities for electrons [$1.3 \text{ cm}^2/(\text{V s})$] and holes [$2 \times 10^{-4} \text{ cm}^2/(\text{V s})$] and the recombination time of $1.7 \times 10^{-6} \text{ s}$ [87] were obtained from the photocurrent measurement on films.

The transport mechanisms in C_{60} films were studied using the field effect technique [88, 89]. A conventional MOSFET structure was used: a C_{60} film on heavily oxidized silicon. The results indicate that C_{60} is an *n*-type semiconductor. The mobility and carrier density at room temperature are, respectively, $4.8 \times 10^{-5} \text{ cm}^2/(\text{V s})$ and $5.6 \times 10^{14} \text{ cm}^{-3}$ [89]; a larger mobility of $8 \times 10^{-2} \text{ cm}^2/(\text{V s})$ was obtained in [90]. The mobility of charges at the fullerene–insulator interface is estimated at $2 \times 10^{-3} \text{ cm}^2/(\text{V s})$, with the values obtained varying widely between samples [88].

The complex conductivity of C_{60} and C_{70} films was measured in the frequency range 10 – 10^6 Hz at 10 – 750 K [28]. The high-frequency dielectric constant ϵ_∞ is 2.6 for C_{60} and 4.6 for C_{70} . In the case of C_{70} , tunneling of small polarons was observed.

Conductivity and Structure

There is a strong correlation between the crystal structure of C_{60} films and their electrical and optical properties. However, this is not easy to explain. Since the molecules are linked by van der Waals bonds, the defect structure itself does not give rise to dangling bonds. A disruption of the molecule integrity is necessary. With improving crystallinity of films, their conductivity increases, and the activation energy of conductivity falls [38]. It has been repeatedly mentioned that the higher the temperature of a substrate on which the film is deposited (which favors higher structural perfection [91]), the higher the conductivity [92, 93].

The effect of annealing on the conductivity of C_{60} films with a chaotic domain structure was studied [83]. The room-temperature conductivity was 6.3×10^{-10} ($\Omega \text{ cm}$)⁻¹. At temperatures above 423 K, an activation behavior was observed, with the activation energy increasing with growing film thickness (0.8 and 1.0 eV), but remaining in strict accordance with the energy gap obtained from absorption spectra (1.63 and 2.08 eV). At lower temperatures, non-activated behavior dominates, with its contribution decreasing upon annealing.

The effect of annealing temperature on the structure and conductivity was studied in [94]. The conductivity of films annealed at temperatures above 473 K was one order of magnitude lower than that for lower annealing temperatures. An X-ray phase analysis has shown that at room temperature the fcc phase coexists in films with the CPH phase and with a new phase with planes parallel to the substrate surface and spaced by 0.95 nm. This new phase could appear as a result of packing of C_{60} molecules between the fcc crystallites. The decrease in the conductivity can be accounted for by the disappearance of this new phase through annealing and the resulting increase in the intercrystallite potential barriers. In measuring the time dependence of the conductivity of films maintained at constant temperature, a rise in conductivity and a decreasing amount of the CPH phase are found. Annealing of films at high temperature leads to their ordering, eliminates defect-related states in the gap, and leads to higher activation energy.

The orientational state of crystalline fullerenes strongly affects their transport properties. In the phase transition region, changes in the activation energy are observed [75, 85]. However, nothing definite can be told about changes in the energy gap because of the activation energies, attributed to the presence of an impurity level. Measurements of the C_{60} film resistance in the range 12–300 K indicated that both phase transition points $T_0 = 260$ K and $T_g = 90$ K are depressed by the action of oxygen [95].

The ac conductivity is proportional to temperature and frequency below 150 K [96], which is characteristic of hopping via localized states at the Fermi level. Above 200 K, a fast rise in conductivity and transition to thermally activated behavior are observed, with two activation energies of 0.389 and 0.104 eV above and below some temperature point, which can be accounted for by the coexistence of the crystalline and amorphous phases. The frequency dependence of conductivity obeys the power law ω^s ($s = 0.8$). Similar results were obtained on C_{60} and C_{70} films [97]: at high temperatures the conductivity was frequency-independent, with a power law dependence observed at low temperatures. A conclusion was made that with increasing temperature the dominating mechanism changes from hopping conduction to thermal activation.

At high temperature, both films and single crystals have $2E_a = 1.85$ eV [84]. Similar data were obtained in a study of the ac conductivity and contactless micro-

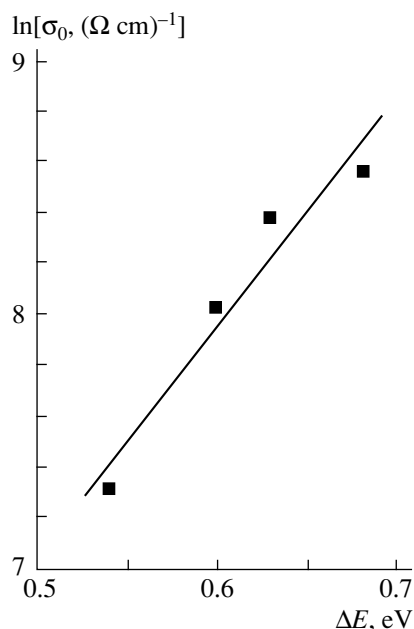


Fig. 12. Relation between the pre-exponential factor and the activation energy of conductivity of C_{60} thin films exposed to different doses of oxygen [102].

wave conductivity of C_{60} single crystals [98]. An activation behavior with a frequency-independent activation energy $E_a = 0.9$ eV is observed at high temperatures. At low temperatures, the conductivity is frequency-dependent and weakly depends on temperature, which can be accounted for by the influence of impurities. At 425 K, the conductivity of the C_{60} single crystal decreases [78], which can be attributed to a redistribution of molecules, leading to localization of electronic states.

The conductivity of single crystals was measured under pressures of up to 1 GPa [99]. The activation energy decreases in the PCC phase, but is constant in the SC phase.

Nonlinear transport properties of C_{60} cluster films were observed and accounted for by a large difference between the activation energies for the bulk and the surface transport in clusters [100].

Conduction Models

Several models have been proposed for explaining the fullerene conductivity. In the simplest model, the mechanism of conduction in graphite along the c -axis direction is extended to fullerene crystals [101], so that the conductivity is estimated to be 1/60 of the graphite conductivity in the c -axis direction, multiplied by the fullerene to graphite density ratio ($\rho_{C_{60}}/\rho_{gr} = 0.74$).

The available experimental results [96, 97] suggest that the fullerene conductivity can be described in terms of the conduction mechanism of disordered semi-

conductors. The dominating mechanism is determined by the temperature: at low temperatures, we have variable-range-hopping (VRH) conduction transforming into hopping between nearest neighbors. At higher temperatures, activated hopping via band tail states (a sort of VRH) dominates, and only at very high temperatures approaching the sublimation temperature can band conduction via delocalized states be observed.

The gross statistical scatter of experimental activation energies leads to a conclusion that the Meyer–Neldel rule must be fulfilled in fullerene materials [102]. This rule is as follows. If a material shows the semiconductor conduction,

$$\sigma = \sigma_0 \exp(-E_a/kT), \quad (5)$$

then, in disordered materials, the activation energy and the pre-exponential factor of the conductivity are related by

$$\sigma_0 = \sigma_{00} \exp(-E_a/kT_0), \quad (6)$$

where σ_{00} and T_0 are the Meyer–Neldel parameters (Fig. 12).

This relation is observed, e.g., for chemically close semiconductors or different samples of the same semiconductor, fabricated by different techniques, i.e., having different impurity concentrations; at different substrate temperatures; under different oxygen pressures in annealing; etc. [103]. The relation is valid for amorphous and polycrystalline semiconductors, and materials with electronic, ionic, and polaronic types of conduction. This universal rule requires that only a single condition should be met: there must exist inhomogeneity of some kind. The transport in inhomogeneous systems can be described as multiple trapping of carriers on localized states with their subsequent thermal release. The carrier mobility is not constant, but shows dispersion: $\mu(T) = \mu_{00}(\omega t)$, with μ_{00} being a microscopic mobility normalized to the density of states. Thus, the pre-exponential factor of conductivity contains the time of carrier release from the deepest trap, which is inversely proportional to the number of traps within the given energy range. The experimentally measured activation energy is the depth of the deepest trap that captures a carrier at a distance equal to the mean free path. The Meyer–Neldel rule is fulfilled if the trap depths are distributed exponentially. This supposition has been confirmed experimentally by measurements of the surface photovoltage [44] and non-stationary photoconductivity. The following values were obtained for, respectively, C_{60} and C_{70} : $\sigma_{00} = 1.5 \times 10^{-3}$ ($\Omega \text{ cm}$) $^{-1}$, $T_0 = 0.044$ eV, $\sigma_{00} = 1.25 \times 10^{-5}$ ($\Omega \text{ cm}$) $^{-1}$, and $T_0 = 0.027$ eV [104].

Effect of Oxygen on Conductivity

It has been repeatedly noted that the conductivity of single crystals [85] and films HAMED93 LEE94 C_{60} [76, 105] is 3–6 orders of magnitude lower under the

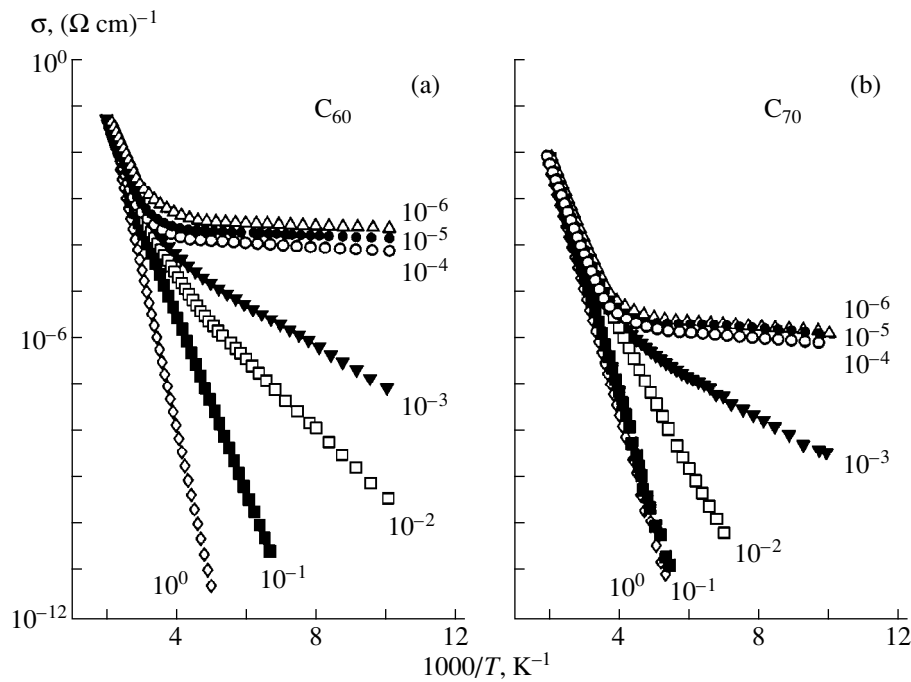


Fig. 13. Temperature dependence of (a) C_{60} and (b) C_{70} films at different oxygen pressures. The figures at curves give the oxygen pressures, Torr.

action of oxygen. The spectral dependence of the photoconductivity of films in an atmosphere of oxygen atmosphere coincides qualitatively with that in oxygen-free films, but its absolute values are much lower [105]. The effect of oxygen on the conductivity and photoconductivity of fullerenes C_{60} [106–108] and C_{70} [109] is most often accounted for by assuming that the intercalated oxygen creates trap levels for carriers and neutralizes defects forming localized electronic states.

Keeping C_{60} films in an atmosphere of argon, nitrogen, or helium has no effect on the conductivity, while exposure to oxygen induces an abrupt fall of the conductivity by several orders of magnitude [76]. The properties of films are practically restored on heating in a vacuum to 160–180°C. However, interaction with oxygen under illumination leads to irreversible changes in conductivity: its room temperature value falls to 10^{-14} $(\Omega \text{ cm})^{-1}$, with the activation energy increasing to 0.95 eV. The effect of oxygen on the conductivity can be understood in terms of the creation of a random potential that localizes electronic states at the HOMO–LUMO band edges and the role of oxygen as a trap for electrons. Under illumination, oxygen enters into a chemical reaction to form C–O bonds.

The conductivity of C_{70} films exposed to oxygen decreases with time by the power law, with three different time intervals observed, each characterized by its own exponent. Evidently, this is associated with different mechanisms of oxygen interaction with fullerene [110].

The temperature dependence of the C_{60} and C_{70} film conductivity was measured in [111] at 77–500 K under

oxygen pressures in the range 10^{-1} – 10^{-6} Torr (Fig. 13). At high temperatures, band conduction is observed in both materials, with hopping via localized states at the Fermi level dominating at low temperatures. In addition, the contribution of a third mechanism, associated with hopping via localized states at the conduction and valence band edges, should be taken into account in the whole temperature interval. This mechanism is characterized by activation energies increasing from 0.2 to 0.4 eV, with growing oxygen pressure in the measuring chamber. It was shown that oxygen negligibly affects the band conduction mechanism, but effectively quenches the hopping mechanisms.

Penetration of oxygen into fullerene films was studied by dielectric spectroscopy [112]. Changes in the frequency and temperature dependences of the low-frequency complex dielectric function $\epsilon(\omega)$ under the action of oxygen were interpreted in the following way. Rather weak charge transport occurs between C_{60} and O_2 molecules occupying interstices. Owing to the large size of the C_{60} molecule, a large dipole moment is formed, related to the applied ac field via the diffusion-controlled relaxation mechanism. This leads to an essential increase in the dielectric constant, giving rise to a wide peak of dielectric losses. With increasing oxygen content, the interstices become completely filled, intersite hopping is suppressed, and the dielectric loss peaks disappear along with the increased polarization.

The oxygen penetration into the C_{60} films was studied by the optical absorption methods [58]. The sub-bandgap absorption strongly increases under the action

of oxygen, and an absorption peak noticeable at 77 K appears. The subbandgap absorption is closely related to the electron spin density. The spin-related signal may come from unpaired electrons of $C_{60}O$, being induced by charge transfer between the C_{60} molecule and oxygen.

Conductivity of Doped Fullerenes

Doping with alkali metals is not considered in the present review, with the exception of the cases when doped fullerenes form polymers. Transport properties of A_xC_{60} compounds (with A standing for an alkali or alkaline-earth metal) have been described in numerous reviews [8, 113–119] and in original papers [25, 26, 120–129].

Doping of C_{60} films with metal impurities (In, Sb) markedly increases the conductivity, with the semiconducting character of conduction retained; the activation energy is within 0.1–0.17 eV. The change in the conductivity can be accounted for by an increase in both the carrier density and the mobility [79, 82]. Exposure to oxygen leads to similar changes in the conductivity of doped and undoped films, which can be accounted for by the formation of a trap level lying 0.7 eV below the conduction band bottom.

In Sn-doped C_{60} films, a new ESR signal appears, increasing with the Sn concentration. The conductivity increases, and the activation energy decreases. Hall effect measurements indicate an *n*-type conduction [130, 131].

C_{60} films prepared by deposition from an ionized cluster beam were implanted with phosphorus, argon, and helium ions. Collisions with ions lead to amorphization of the film and disintegration of molecules. The resistivity of the film decreases with increasing irradiation intensity. Phosphorus-doped films feature *n*-type conduction. Films fabricated by simultaneous sputtering of fullerene and aluminum had *p*-type conductivity; the addition of aluminum improved their photoelectric properties [132].

Al–oxide– C_{60} –Pb and Pb–oxide– C_{60} –Pb structures are studied by tunneling spectroscopy. A narrow 6–7-meV-wide semiconductor band is observed at low temperatures. The band corresponds to a semiconductor created by Pb-doping of the fullerene [133].

Sm_6C_{60} fulleride was synthesized with a use of a high-temperature solid-state reaction. Its transport properties at temperatures below 180 K are described in terms of the theory of metal granules; a weak temperature dependence of the resistivity is observed at high temperatures [134].

The $Sr_{0.56}C_{60}O_{1.5}$ compound has ionic conductivity with extremely low absolute value [135], which clearly distinguishes it from Sr-doped C_{60} exhibiting metallic properties [136].

PHOTOCONDUCTIVITY

Photoconductivity spectra of fullerenes are, on the whole, similar to the absorption spectra. The main spectral features are related to excitons, rather than to interband transitions; carrier generation mechanisms under consideration include charge separation in the bulk and at the surface, exciton–exciton interactions, exciton photoionization, and release of charges from traps. The similarity of the absorption and photoconductivity spectra indicates that the Frenkel and CT excitons may relax into the same lower state of the Frenkel exciton. Excitons dissociate and create charge carriers scattering on surfaces, lattice oscillations, impurities, and defects. Since the Frenkel exciton has energy less than the energy gap, the conduction is phonon-assisted [63]. The photocurrent in C_{60} films is proportional to light intensity and applied voltage and increases with decreasing modulation frequency, which may be due to the effect of deep traps.

C_{70} shows higher quantum yield than C_{60} . The C_{60} energy gap was found from Fowler plots to be 1.7 [29, 137] and 1.6 eV [138]; the value for C_{70} is 1.5 eV [29]. Arrhenius behavior is observed above room temperature, with activation energy of 0.50 eV for dark conductivity and 0.20 eV for photoconductivity. At lower temperatures, the conductivity is almost temperature independent [137]. The photoconductivity of fullerenes essentially depends on the degree of crystallinity [138]. Similar to the case of dark conductivity, a strong effect of oxygen on the photoconductivity is observed (Fig. 14). Formation of deep traps due to the interaction of fullerenes with oxygen is assumed to reduce the carrier lifetime, which leads to a photoconductivity drop by 3–6 orders of magnitude [106, 108].

A strong peak at 1.65 eV, related to a weak absorption band, is observed in the photoconductivity spectrum of a C_{60} single-crystal [139]. The peak differs from the wide photoconductivity band near 1.8 eV in its dependence on temperature and on illumination intensity: the photoconductivity shows a superlinear character in contrast to the sublinear dependence for the wide band. Within the energy range centered at 1.65 eV, a negative photoconductivity is found with photoreponse time of 0.01 s, transforming into positive photoconductivity at longer pulses [140]. The positive photoconductivity decreases, and the negative increases as temperature is lowered. This is interpreted as resulting from coexistence of traps with small thermal emission rate and Stockman's fast recombination centers.

A bandgap of 1.85 eV at 300 K was obtained from AC photoconductivity measurements on C_{60} films with gold electrode, with the band gap increasing with decreasing temperature to become 1.91 eV at 250 K, in correspondence with a change in the crystal structure [27]. The strong temperature dependence of the optically allowed direct band $E_g(T)$ was described in terms of the electron-phonon interaction via localized C_{60} phonon modes [141].

Remanent internal photopolarization was observed in thin C_{60} films [142]. The effect differs from the photoelectret state observed in other materials in the absence of fast photodepolarization. The model of photogenerated carrier trapping by deep centers was considered together with the suppression of their recombination by a distortion of the C_{60} molecule, caused by the presence of a localized charge. Defect states in C_{60} single crystals were determined using the persistent photoconductivity spectra [143]. It was assumed that the energy level of the defect lies 0.48 eV below the conduction band bottom. The conclusion that states are present in the gap was also based on a study of the IR photoconductivity of C_{60} single crystals [144]. Calculations based on a supposition that there is a peak of the density of localized states, originating from the Frenkel exciton band, inside the gap [145] were carried out in order to explain the obtained temperature dependence of the exponent γ for the C_{60} film photoconductivity.

The photoconductivity was studied as a function of the applied field, wavelength, and illumination intensity [146]. The photocurrent depends on the polarity of the illuminated electrode, with the asymmetry depending both on the applied voltage and on the light penetration depth. The effect can be accounted for by the difference in electron injection from the Al-cathode and by different electron and hole mobilities. The dependence of the photoconductivity of C_{60} films on the illumination intensity was found to obey the power law [147]. The model of a continuous distribution of states in the gap was applied to describe this dependence.

The increase in photoconductivity in a dc magnetic field was explained by the effect of the field on the multiplicity of the electron-hole pair states [148]. Light generates pairs in short-lived singlet states, which can transit under the action of, e.g., spin-orbit interaction, into a significantly longer-lived triplet state, which reduces the recombination probability and increases the dissociation efficiency. The role of the magnetic field can be reduced to raising the triplet state filling.

The dynamics of photoexcited carriers was studied by the methods of nonstationary photoconductivity and nonstationary photoinduced absorption [149, 150]. The transport is described in terms of the model of multiple trapping; the creation of deep traps quenching the conductivity is accounted for by the action of oxygen. The thermally activated long-lived component of the photoconductivity is frozen out at low temperatures. The time-resolved nonstationary photoconductivity has a local maximum at $T = 240$ K, i.e. at the phase transition point. The presence of disorder is indicated by the existence of long-lived thermally activated photoconductivity component.

Time-resolved photoconductivity shows that the photogeneration process in C_{60} films can be described by the Onsager pair generation model. The quantum yield depends on the photon energy, electric current, temperature. The product of the mobility by the life-

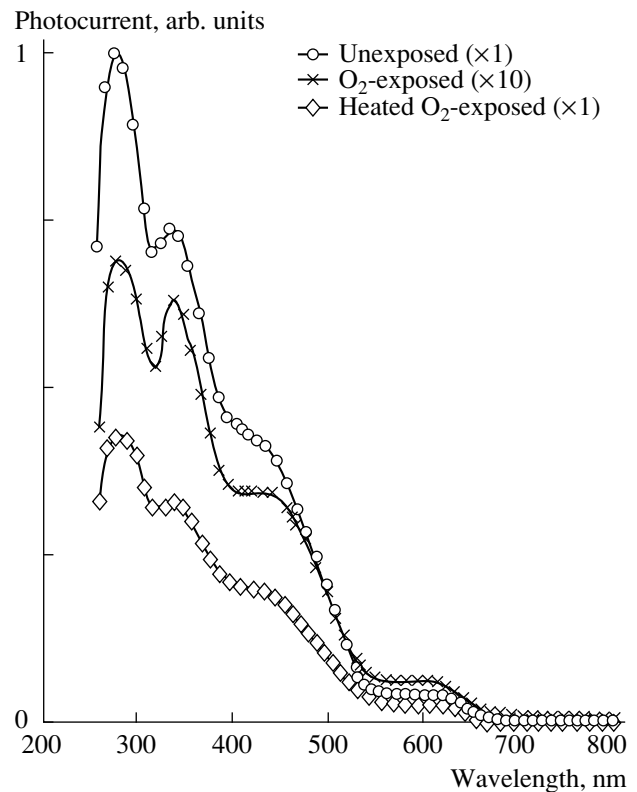


Fig. 14. Spectral dependence of photoconductivity ($T = 260$ K) of 13-nm-thick C_{60} films oxygen-free, oxygen-saturated, and heated in an atmosphere of oxygen [135].

time with respect to electron trapping was determined: $\mu\tau = 4 \times 10^{-10} \text{ cm}^2 \text{ V}^{-1}$ [151].

PHOTOLUMINESCENCE

The peak at 1.69 (1.68) eV, related to emission from the C_{60} bulk, and a few weak features identified as emission by Frenkel excitons residing on the X-center [152] were found. The peak at 1.76 eV is related to the surface exciton X-centers. The luminescence peak at 1.68 eV decreases due to a laser illumination. Evidently, a lowering of symmetry due to distortion of molecules is observed. However, this peak increases due to illumination in a presence of oxygen [153].

Absorption spectra of the C_{60} films taken at 7 K meet the photoluminescence spectra at the point 1.8 eV taken to be the optical gap. Peaks at 1.69 and 1.52 eV and weak features in the range 1.76–1.42 eV [63] were observed in the photoluminescence spectra (Fig. 15).

Photoluminescence depends on the morphology of fullerene films. The photoemission peak is shifted to lower energies for films of high crystallinity [93]. The luminescence, electroluminescence, and photoconductivity spectra are influenced by the intermolecular excitation with charge transport [62, 154, 155]. The singlet and triplet excitons trapped by crystal defects are assumed to give the main contribution to C_{60} single-

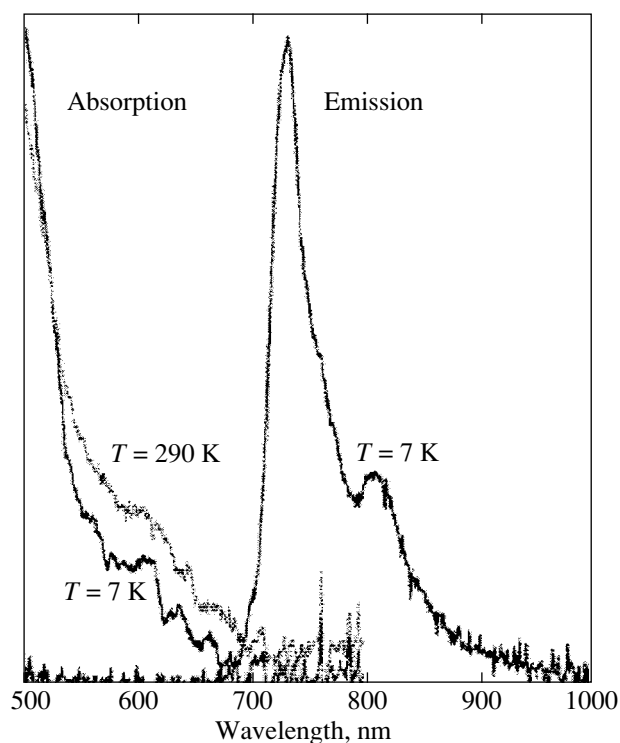


Fig. 15. Absorption and emission spectra of a C_{60} film [63].

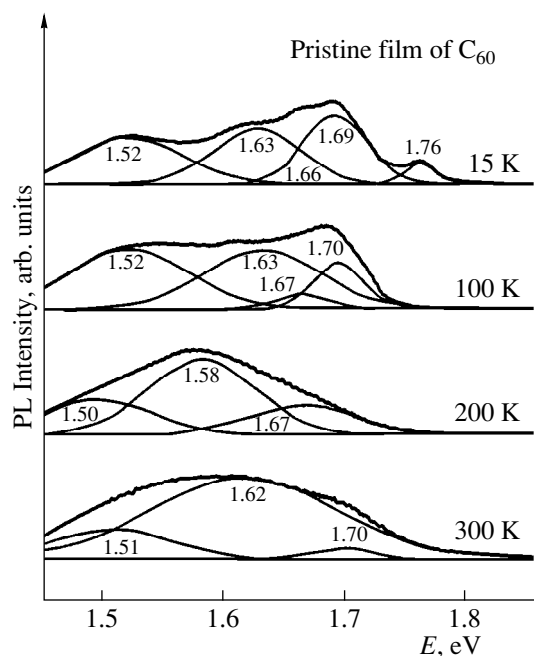


Fig. 16. Luminescence spectra of C_{60} films, taken at small illumination intensity [158].

crystal photoluminescence [156]. The symmetry violation is so strong for C_{60} molecules on defects that it makes the oscillator strength of phonon-free optical transitions comparable with the strongest optical transitions assisted by intramolecular vibrations.

Strong distinctions are observed between C_{60} crystal luminescence spectra, depending on the presence of physical or chemical defects, strains in the crystal, and other specific features related to the process of fabrication. Under laser irradiation, peaks at 1.73 and 1.76 eV appear in the visible range, interpreted as emission from metastable defects [157]. The temperature dependence of the photoluminescence spectra is given in [158] (Fig. 16).

The complex structure of the absorption and luminescence spectra in the long-wavelength region may be a consequence of a combination of the intra- and intermolecular vibrations. The broad shifted band is accounted for by the model of a self-trapped exciton. If the photogenerated Frenkel exciton stays on the molecule longer than the molecular vibration period, it can be trapped by the lattice. The exciton recombines emitting light and exciting intra- and intermolecular vibrations. That is why the emission is observed at lower energies than the absorption, and the spectrum has a complex structure with a great number of phonon peaks [63]. An alternative explanation of the spectrum is also possible [159]: some defects, such as oxygen, higher fullerenes, and structural disorder, can make the transition $t_{1u}-h_u$ allowed.

POLYMERIZATION OF FULLERENES

Enhancement of Intermolecular Interaction

Intermolecular interactions must essentially influence electrical and optical properties of solids composed of the fullerene molecules. This may occur in two ways. The enhancement of the interaction may lead to a metallic, or even superconducting state, as in the case of silicon. However, one has to take into account the ability of carbon to form various hybridized states. If, for some reason, the sp^2 hybridization is changed to sp^3 , this will lead to the formation of a diamond-like solid. Measurements on granulated C_{60} [160] have shown that the sample volume decreases with increasing pressure, which is accompanied by a decrease in the resistivity and the gap. Nevertheless, the transition to the metallic state was not observed, since an abrupt transition to a more insulating phase took place instead, most likely induced by the formation of covalent intermolecular bonds. A similar result was obtained in [161], where dependence of the absorption edge on the applied pressure was measured. Extrapolation of the absorption edge shift under pressure predicted a transition to the metallic state at 33 GPa. However, an irreversible transition into a transparent phase occurred in the range of 17–25 GPa (it should be noted that this experiment has never been reproduced, notwithstanding numerous attempts). Raman spectra indicated a transition into a new carbon phase having nothing in common with C_{60} , graphite, or diamond. A linear shift of the optical absorption edge under pressure with a slope of 0.14 eV/GPa was observed [162]. A transition

to the amorphous carbon phase occurred at 20 GPa, with this phase being no more transparent than the amorphous carbon obtained using other methods.

Theoretical calculations of the C_{60} behavior with decreasing intermolecular distances were carried out [163]. The band structure was calculated as a function of the C_{60} lattice constant and was expressed in terms of pressure, using the compression modulus. It follows from the calculations that pressure induces a decrease in the energy gap at the X and Γ points and an increase in the static dielectric constant. The gap decreases almost linearly under pressure with a slope $\partial E_g / \partial \ln a = 9.2$ eV, where a is the lattice constant. The charge-density map evidences that covalent bonds can be formed at a pressure of 13 GPa. The calculated energy gap at this point is 0.69 eV and, therefore, metallization under pressure is unachievable.

More recently, studies were reported, confirming experimentally the appearance of the covalent bonds between fullerene molecules. Under the action of visible or UV radiation C_{60} transits into the photopolymerized phase [164], which is insoluble in toluene or other C_{60} solvents. Doping with alkali metals was found to lead, under certain conditions, to the formation of linear chains [165]. The structure of the linear polymer RbC_{60} was determined by X-ray diffraction analysis to be orthorhombic below 350 K. The orthorhombic phase $o\text{-}AC_{60}$ was studied with other alkali metals ($A = K, Rb, Cs$) [166]. A single crystal of $(KC_{60})_N$ [167] a few millimeters long was grown; the degree of polymerization exceeded 100000. It was shown that C_{60} can be transformed into another structure under high pressure and temperature [168]. The structure of this material was determined as rhombohedral, with lattice parameters $a = 9.22$ Å and $c = 24.6$ Å. The intermolecular distance in such a phase was about the carbon bond length, which implied that covalent bonds can be formed between molecules.

Dimerization of substituted [169] and endohedral [170] fullerenes was observed. The presence of an unpaired electron was the driving force in these cases.

Thus, there are three ways for fullerene polymerization: photo-excitation, charge transfer, and the action of pressure.

What Occurs in Photoexcitation?

Oxygen-free C_{60} films were transformed into a photopolymerized state [164] under the action of UV and visible light. The process occurred only in the fcc phase, i.e., at temperatures above 260 K. The authors assumed that the phototransformation goes by the cycloaddition mechanism $[2 + 2]$, with the double intramolecular bonds broken and a four-atom carbon ring formed (Fig. 17). The following requirement to the topology of reacting molecules must be fulfilled for the reaction to proceed: the molecules must be close enough to each other, and their double bonds must be

parallel. This requirement can be only met in the phase of free molecular rotation.

The configuration depicted in Fig. 17 can also be denoted by 66/66. This means that every molecule has double bonds between two hexagons. If, e.g., a molecule has one bond along the mutual edge of the pentagon and hexagon broken, such a configuration will be denoted by 56/66. In principle, such a configuration is possible like many others, but all of them are less thermodynamically stable than the monomer [170, 171].

A conclusion was made, based on a study of the photo-polymerization reaction kinetics, that the reaction occurs between the monomer C_{60} in an excited (triplet) state and another monomer in the ground state [172].

Since oxygen quenches the triplet state [173], the reaction does not occur in its presence. The C_{70} fullerene is significantly less liable to polymerization than C_{60} for geometrical reasons, and a radiation dose inducing a complete transformation of C_{60} created only disordered dimers in C_{70} . Both materials return to the initial state under heating.

Illumination in the presence of oxygen leads to another process, photo-assisted diffusion [173]. The oxygen diffusion rate increases about tenfold. Prolonged illumination leads to the stoichiometric $C_{60}O_2$. This phase is also insoluble in toluene. The efficiency of photopolymerization and photoassisted diffusion is essentially lowered if femtosecond pulses are used instead of the continuous illumination [174].

The polymerization reaction takes place within the temperature range 260–400 K, and the type of polymerization, identified using the Raman spectra, is determined by temperature [175, 176]. It was shown by atomic-force microscopy of C_{60} films deposited on mica that films illuminated at temperatures above 350 K form dimers and trimers with an unusually short intermolecular distance of 8.8 ± 0.1 Å (Fig. 18a). At temperatures below 320 K, polymer chains appear on the illuminated surface. They include mostly six molecules with an intermolecular distance of 9.2 Å. Strains in the film lead to the formation of undulate patterns on the surface, looking like a herring bone (Fig. 18b) [177].

The photo-polymerized phase is difficult to obtain in large volume because of the strong absorption and small penetration depth of light. C_{60} polymerization methods yielding colloid solutions [178] and water suspensions were proposed [179, 180]. The phototransformed C_{60} , obtained in the form of powder, had an fcc lattice with a parameter 0.25 Å smaller than that in the monomer [181]. This material is assumed to consist of trimers and tetramers.

Polymerization of fullerenes can also be accomplished by plasma treatment [182] and the action of an ion [183] or electron [184] beam, which is promising for its use as a resist [185]. The idea of such treatment is as before: to create an excited state of the fullerene molecule. This can be done in another way: by adding

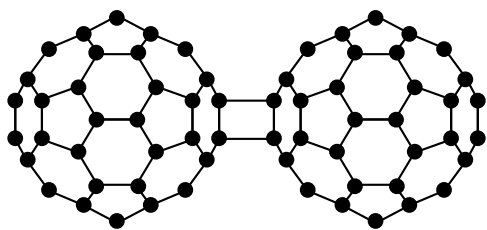


Fig. 17. Schematic representation of a fullerene dimer.

a chemical element that readily donates its electron to unoccupied molecular orbitals, i.e., using intercalation.

What Occurs in Intercalation?

An intercalation compound is a material in which atoms, ions, or molecules are captured in between the crystal lattice layers [186]. Formally, there is no chemical bonding between the intercalants and the host lattice [187]. Fullerenes belong to a 3D variety of the intercalation compounds. Voids in the lattice are large enough to accommodate any chemical element. However, not all elements can form 3D intercalation compounds [188]. They are mainly alkali, alkaline-earth, and rare-earth metals. It is believed that the key factor regarding the possibility of formation of 3D intercalation compounds is the sum of the metal work function e_ϕ and the cohesion energy E_{coh} . If this sum is less than the energy of the lower unfilled molecular orbital, $e_\phi + E_{\text{coh}} < E_{\text{lumo}}$, then the intercalation energy $E_{\text{intc}} = E_{\text{lumo}} - e_\phi - E_{\text{coh}}$ is positive, and 3D intercalation compounds can be formed [189].

The interest in intercalation of fullerenes appeared just after Krachmer's discovery of the possibility of obtaining fullerenes in macroscopic amounts. The intercalation of alkali metals was found to lead to metallic properties [190] and superconductivity [3]. The best account, in our opinion, of the fullerene superconductivity was given in a review [8].

In the initial state, C_{60} has an upper filled band h_u and a lower unfilled band t_{1u} ; the latter can take up no more than six electrons. Based on a simplest band-model consideration, one would assume that the compound A_6C_{60} must be an insulator, while any lower stoichiometry must lead to metallic properties. This is not quite correct. Adding one [191–193] or three [190] atoms leads to metallic properties, while A_4C_{60} is a band insulator [194].

The compounds AC_{60} were extensively studied because of their interesting phase diagram [195, 196] and quasi-1D behavior [197]. The possibility of their polymerization placed them in a new class of superconductors: linear polymers [198]. Under fast cooling of AC_{60} ($A = \text{Cs}$ or Rb), a new conducting phase appears [195]. The following transformations are observed upon heating from 4 to 473 K. A 3D conducting ori-

ented phase with an SC lattice exists at low temperatures. At temperatures below 150–125 K, a transition into a dimerized insulating phase takes place; then it transforms into a 1D conducting phase and then into the fcc lattice. Phase diagrams of RbC_{60} and KC_{60} were studied by ESR spectroscopy [196, 199, 200]. A schematic of a 1D polymer KC_{60} is presented in Fig. 19 [201].

As in the case of photopolymerization, the initial state for a transition into the polymer phase is always the fcc lattice, and molecular disordering of C_{60} is a good starting point for polymerization.

What Occurs under Pressure?

The first polymer obtained under pressure had a rhombohedral structure [168]. In later experiments, C_{60} was found to transform upon heating under pressure into three different phases: orthorhombic, tetragonal, and rhombohedral [202]. The phases were identified using their X-ray spectra. A more precise identification of these structures was done later [203].

The pressure–temperature phase diagram was studied systematically by several groups [9, 204–206]. Successive transitions from the fcc to a polymerized orthorhombic and then to a 2D polymerized phase occur with increasing temperature. At 800–900 K, the C_{60} cage disintegrates to form an amorphous sp^2 -coordinated phase. A mixture of R and T phases is formed at 2–4 GPa and 673–1073 K, and a pure R -phase, at 4–8 GPa and the same temperatures [207]. Partial coalescence of molecules may occur in polymerization [208].

Changes in the structure and electronic states on applying a pressure of up to 50–55 GPa to the C_{60} fullerene at room temperature were considered in [209]. The fcc structure is nearly unchanged at the beginning, but the π -plasmon becomes forbidden because of a decrease in the intercluster distance; then the basic structure stays unchanged and intercluster bonds are created. In the third stage, the fullerene structure disintegrates to become amorphous, and sp^3 bonds are created. In the fourth stage, a diamond-like phase without long-range order is created.

The C_{60} and C_{70} polymerization and amorphization under pressure [210] were studied by X-ray diffraction analysis and scanning tunneling microscopy (STM). The previously studied photopolymerization of these substances aided in understanding the difference in their behavior. Polymerization is accompanied by a shrinkage of the C_{60} molecule, but expansion of the C_{70} molecule. This determines their dissimilar behavior in amorphization. The amorphization of C_{60} under pressure is irreversible since it is accompanied by polymerization distorting the molecule shape. The C_{70} molecules have smaller compressibility and are less liable to polymerization. That is why the amorphization of C_{70} is reversible.

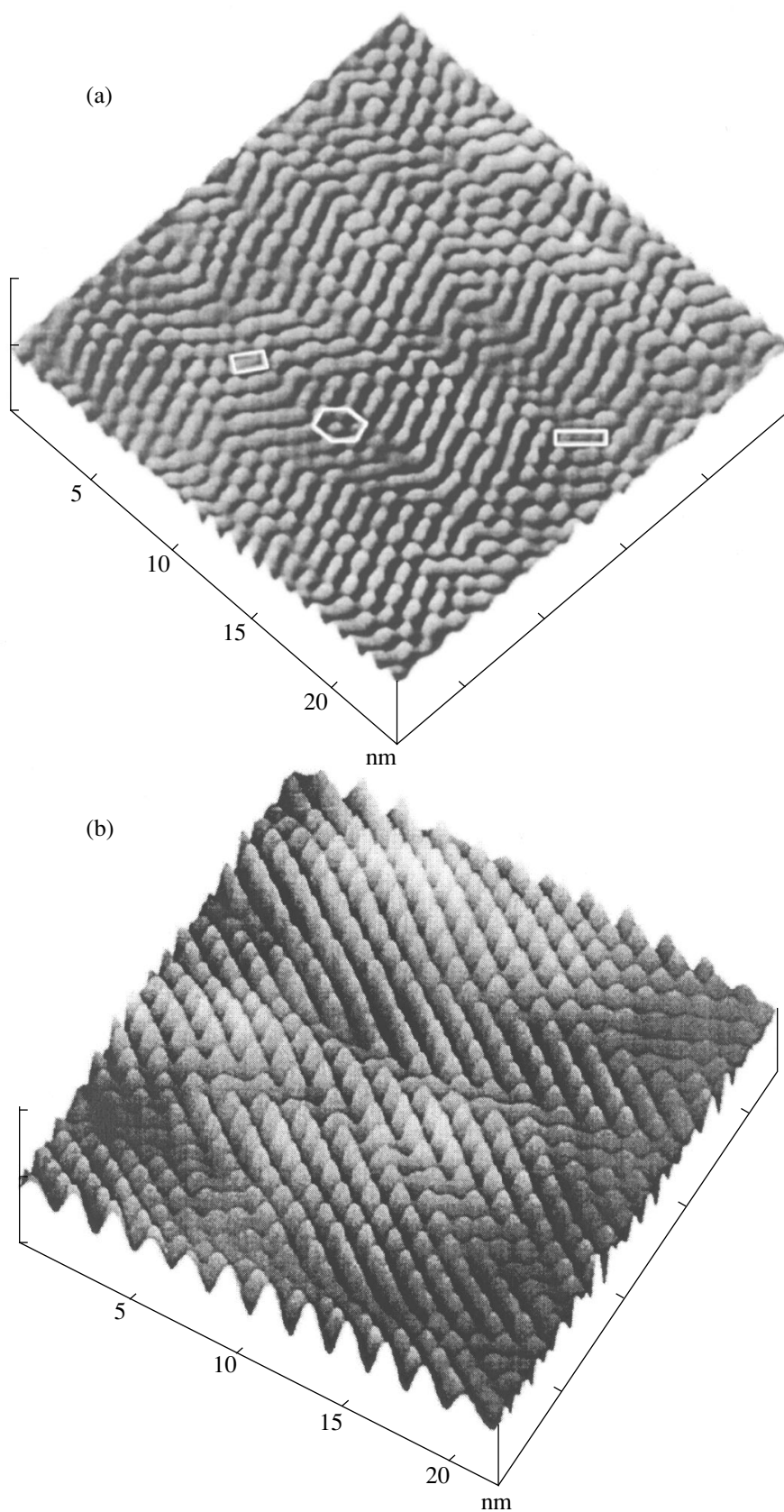


Fig. 18. Atomic force microscopy with molecular resolution for C₆₀ fullerene films photopolymerized at different temperatures: (a) $T = 360$ K, no long-range order, only dimers and trimers can be seen; intermolecular distances 8.8 Å. (b) $T = 300$ K, linear chain up to six molecules long; surface having a herring backbone structure; intermolecular distances 9.2 Å [177].

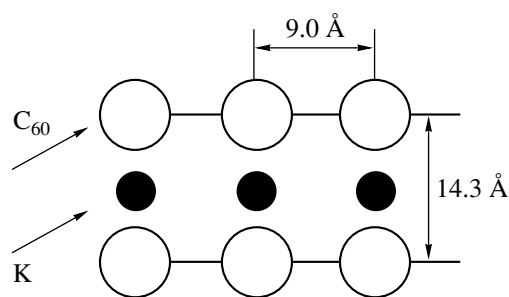


Fig. 19. Schematic of the KC_{60} linear polymer [201].

At certain combinations of pressure and temperature a 3D polymerization is observed. At a non-hydrostatic pressure $P = 6.5\text{--}13$ GPa, $T = 300\text{--}2100$ K, superhard and ultrahard forms of carbon were obtained [211]. The crystal structure was identified as distorted volume-centered cubic lattice. A transition to the diamond structure can be traced. The 3D nature of polymerization was revealed in experiments with the synchrotron radiation [212]. The super- and ultrahard 3D-polymerized fullerenes differ in their properties, such as the mass density, specific heat, velocity of sound, elasticity modulus, and electrical properties both from diamond and from other modifications of carbon. Ultrahard fullerite exceeds diamond in hardness [213].

INTERMOLECULAR BONDS

Some of the basic questions in studying fullerene polymers is the following: Are intermolecular bonds really covalent, and how do they appear?

Evidence in favor of the appearance of covalent bonds in AC_{60} compounds, with A standing for K, Rb, or Cs, was obtained from X-ray spectra. The calculated atomic positions in [2 + 2]-cycloaddition agree with experimental data [197].

The orthorhombic phase $o-A_1C_{60}$ (A = K, Rb, or Cs) was studied and a mechanism of ion-induced [2 + 2]-cycloaddition suggested in [166]. The [2 + 2]-cycloaddition of two neutral fullerene molecules is thermally forbidden by the Woodward–Hoffmann rules.² A reaction of this kind is allowed between an excited molecule and a molecule in the ground state. Interaction of a singly occupied π^* -orbital of the photo-excited molecule with an unoccupied π^* -orbital of the molecule in the ground state leads to a symmetrically allowed and energetically favorable transition (Fig. 20). The interaction of two C–C double bonds can be described as follows. When a negative ion reacts with a molecule in neutral ground state, the interaction of the singly occupied and the vacant π^* -orbitals results in a lower energy

² Woodward–Hoffmann rules: the rules regulating the product formation in organic chemical reactions. They are derived from a consideration of ways by which reagent's orbitals transform into the those of the reaction product and also from the conservation of the orbital symmetry during the process [187].

transition state. In the case of C_{60} ions, π^* -orbitals are replaced by triply degenerate t_{1u} orbitals; therefore, the stabilizing interactions of singly occupied and vacant orbitals may also be effective between two ions. That is why the [2 + 2]-cycloaddition reactions of two ions are thermally allowed as well.

The fullerene structure polymerized under pressure was later described using the same kind of bonds as in the case of A_1C_{60} polymer chains. The obtained results [168] were interpreted as a rhombohedral polymer; a calculation of the X-ray spectra was done taking into account the creation of bonds and the distortion of the molecule [214]. The [2 + 2]-cycloaddition mechanism is also characteristic of polymerization under pressure: such a result was obtained by comparing experimental and model NMR spectra, with account taken of the polymer configuration and the appearance of nonequivalent carbon atoms because of the molecule distortion [215–217].

X-ray photoelectron spectroscopy (XPS) confirm the hypothesis that the sp^2 hybridization changes to sp^3 upon polymerization. A decrease in the density of π^* -states is clearly seen in the C_{1s} excitation spectrum of the Rb_1C_{60} compound [218]. This cannot be explained only in terms of the carbon cage distortion and the electronic charge transfer from Rb^{5s} to the carbon molecular orbital. The charge density additionally decreases, owing to four sp^3 -hybridized carbon atoms localized at the connection point of the molecules. A decrease in the C_{1s} peak intensity is also observed for photopolymerized C_{60} films [219, 220]. The mechanism of the [2 + 2]-cycloaddition reaction was studied theoretically [221]. The spatial arrangements of the neutral and anionic dimers were calculated; barriers for reactions were found on this basis. The barriers were found to disappear for the anionic dimer, first singlet, and first triplet excited states of the neutral dimer, which clears the way for a spontaneous polymerization. A critical distance of 2.12 \AA was found to exist, at which the [2 + 2] cycloaddition occurs as a mutual exchange of positions in the energy spectrum between HOMO and LUMO.

The polymerization is a result of the mutual exchange between HOMO and LUMO of two molecules. The lower unoccupied orbitals (LUMO), i.e., bonds between the C_{60} molecules, are stabilized when the molecules approach each other, and they become occupied at the critical intermolecular distance via energy level exchange between molecular orbitals and the HOMO. In the case of photopolymerization, the system is stimulated to transition because the bonding molecular orbital between molecules is occupied by a photo-excited electron. In the case of an alkali metal, its electronic charge is transferred to the bonding intermolecular orbital, which leads to spontaneous polymerization.

The photopolymerized phase and the polyanionic reaction have one feature in common: the electrons

occupy levels that were not occupied before. In the case of laser irradiation, the electrons are transferred from the occupied part of the molecular orbital spectrum. In intercalation, electrons are transferred from alkali metals. The explanation of the intermolecular reaction mechanism relies on the fact that the electronic charge redistribution stimulates reactions of this type.

However, later experimental results have shown that the above-described mechanism of [2 + 2]-cycloaddition is not unique. A single, rather than double, C–C bond was found in RbC_{60} and KC_{60} dimers [222].

Calculations of the optimal geometry and total energy of the neutral and charged C_{60} dimers indicate that the 66/66 cycloaddition is stable in the former case, and the single intermolecular bond, in the latter [223]. In the neutral case, no minimum energy was found for the isomer with a single bond [224].

The theoretical supposition that the fullerene chains are connected by the [2 + 2] cycloaddition is based on the extrapolation of calculations for the neutral dimer $(\text{C}_{60})_2$. A report of a single bond in RbC_{60} and KC_{60} [229] demonstrated that the picture is not so simple. A system with a single bond has an advantage over the bound [2 + 2] isomer only if doubly charged $(\text{C}_{60}^{2-})_2$ are considered instead of the neutral dimers. This puts serious restrictions on various extrapolations both from neutral to charged systems and from dimers to polymers. A study of the $(\text{C}_{60}^{n-})_p$ polyanion stability [225] indicated that polymers bound by a single bond are becoming more stable with charge increasing up to $n = 3$. The theoretical consideration was confirmed by X-ray analysis of the $\text{Na}_2\text{RbC}_{60}$ and Na_4C_{60} compounds.

The whole body of experimental data and theoretical concepts gives good reason to state that the charge state determines the arrangement of polymer bonds [226]. An answer to the question as to why one fullerene is bound by double, and another by single bonds will be the first step on the way to understanding the polymerization mechanisms.

The binding mechanism is controlled by the charge state. The covalent interfullerene double bonds require two electrons per bond. The [2 + 2]-cycloaddition reaction does not require any additional electrons. Therefore, the neutral fullerene photopolymerizes, is compressed, or chemically dimerized only in accordance with the [2 + 2] mechanism, irrespective of how many neighbors are linked.

The class $(\text{C}_{60}^{1-})_n$ is characterized by the presence of a single unpaired electron. Therefore, after one interfullerene C–C bond is formed, the reaction halts, and polymerization in this way is impossible. However, if there are electrons in the (C_{60}^{j-}) state with $j > 1$, polymerization becomes possible. That is why the single

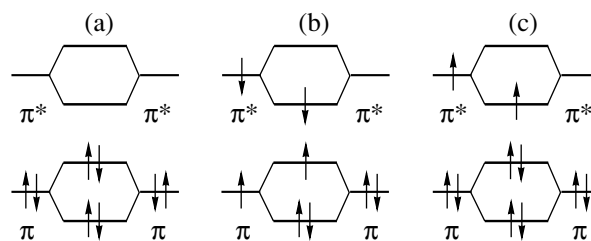


Fig. 20. Diagrams of interaction of molecular orbitals in [2 + 2]-cycloaddition. (a) Thermally forbidden reaction between two molecules in the ground state, (b) photo-chemically allowed reaction between molecules in the ground and excited states, and (c) assumed thermally allowed ionic reaction [166].

bond is possible in the dimer, but not in the polymer phase RbC_{60} .

The system Na_4C_{60} with single bonds is unique: every C_{60}^{4-} anion is involved in four interfullerene single bonds in it [227]. The 2D polymer phase with single bonds is stable only when the C_{60} molecule is doped with four electrons [228]. The polymer Na_4C_{60} transforms into the monomer phase at 500 K [229]. The transition is reversible; the high-temperature phase is similar to other compounds but has shorter interfullerene distances.

The following remark is appropriate in conclusion. The evidence for the complete transition of sp^2 - into sp^3 -hybridization and, therefore, for the blocking of the π -conjugation of the electronic system at the joining point of molecules does not seem convincing to the author. First, one can estimate from Fig. 17 that covalent angles of the four-fold coordinated carbon atoms are not equal to 109.47° , as is the case in diamond (their values are close to 90° and 118°). Second, the formation energy of this bond is estimated at 1.6 eV, which is much less than in diamond [230]. Similar to the fullerene molecule having $sp^{2.278}$ rather than sp^2 hybridization, the intermolecular bonds can have hybridization other than sp^3 , and, therefore, the change in the fullerite properties can be not so dramatic as that predicted by theories. The orbital hybridization at the joining point of molecules plays a decisive role in considering the transport properties of fullerites.

POLYMERIZATION MECHANISMS

A wide variety of structures appear upon polymerization. Examples of doped polymers bound by single bonds, both 1D [228, 231] and 2D [227], indicated that the valence of molecule plays a decisive role in determining the nature of intermolecular bonds and type of polymerization. In the case of undoped polymers, intermolecular bonds are always [2 + 2]-cycloadditions, with various polymer structures obtained by varying the synthesis conditions. The type of polymerization can be changed by a slight variation of the synthesis

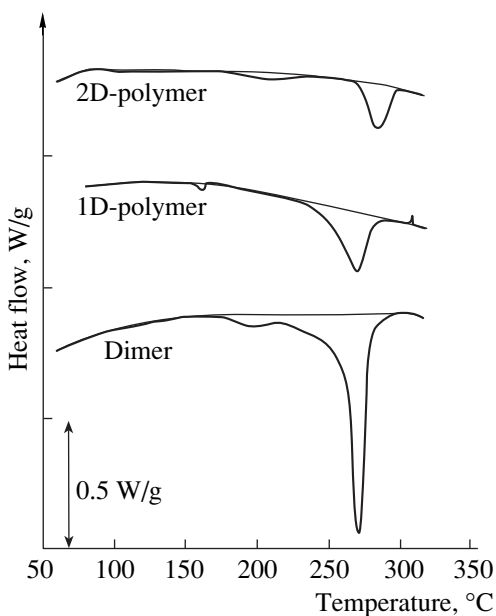


Fig. 21. Differential scanning calorimetry (DSC) of the dimer and 2D rhombohedral polymer in heating at a rate of $10^{\circ}\text{C}/\text{min}$. All materials have transformed into the monomer phase after completion of the DSC experiment [235].

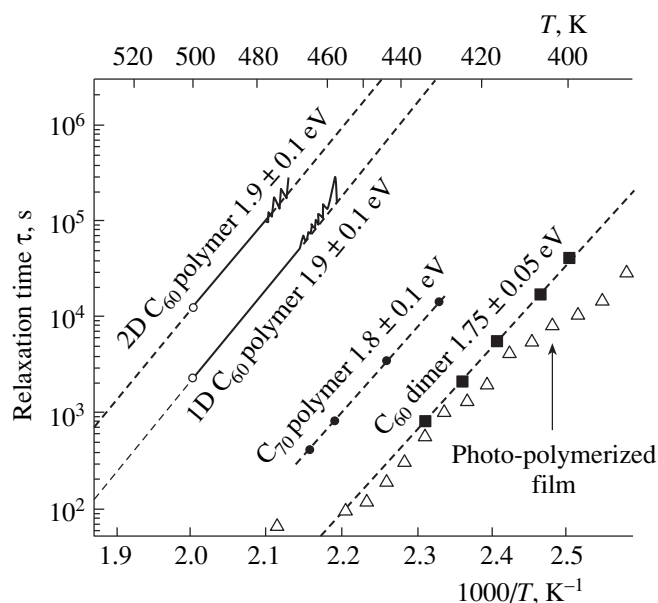


Fig. 22. Comparison of the depolymerization rates for 1D and 2D C_{60} polymers, C_{60} dimers, C_{70} polymers, and photopolymerized C_{60} films [237].

temperature; i.e., all polymer structures exist in a narrow temperature range. What is the driving force of polymerization?

It is natural to assume that the formation of interfullerene bonds stabilizes the fullerite. Calculations [232] predicted an increase in the stability of *O*, *T*, and *R* phases with a growing number of bonds. This result

took no account of distortions or interchain and intersheet interactions. To estimate the energy gain per intercluster bond, the total energy of the system was considered, having four components [233, 234]: (i) energy of a distorted C_{60} molecule, (ii) van der Waals energy of intersheet interaction, (iii) van der Waals intrasheet interaction energy, and (iv) energy of formation of C–C intercluster bonds. Both for the tetragonal and for the rhombohedral phases, the calculation yields 1.6 eV per bond.

The following experimental facts are to be taken into consideration when analyzing the polymerization mechanisms.

1. Polymerization of the neutral C_{60} is thermally forbidden by the Woodward–Hoffmann rule. However, it proceeds under a pressure of several GPa.

2. Depolymerization occurs under rather mild conditions, such as heating to 200°C and normal pressure, while polymerization requires high pressure and temperature.

3. Measurements by differential scanning calorimetry (DSC) indicated that depolymerization is an endothermic reaction. This means that the polymer phase is more stable than the monomer phase, in complete accordance with the theoretical concepts.

4. The most energetically unfavorable is the rhombohedral phase and, at the same time, it most frequently occurs in polymerization under pressure.

In other words, the transformation into a more stable polymer phase requires more severe conditions, while that into an unstable phase is easier.

A calorimetric study [235] has shown that polymers are more stable than monomers. It may be assumed that formation of polymer bonds lowers the total energy. All polymer forms transform into monomers on heating to 200°C . The depolymerization reaction is endothermic, which the higher stability of polymers in comparison with monomers (Fig. 21).

The bond dissociation of the photopolymer obeys the Arrhenius law with an activation energy of 1.25 eV [236]; the activation energy is 1.75 ± 0.05 eV for a dimer obtained under pressure and 1.9 ± 0.1 eV for 1D and 2D piesopolymers [237]. Despite the activation energies being very close, the rate of dimer depolymerization is four orders of magnitude faster than that for the 1D and 2D polymers (Fig. 22). It has been reported that the thermal stabilities of the heavily and weakly polymerized fullerenes are fundamentally different [238].

Calculations show that the optimal dimer energy is lower than the total energy of two separate molecules by 0.47 eV, the infinite polymer chain has energy gain per molecule of 0.44 eV [170].

However, according to the DSC data, the stabilization energy decreases with increasing number of intermolecular bonds per molecule (Fig. 21). All polymer phases are more stable than monomers, and they exist in the temperature range one order of magnitude nar-

lower than the energy difference between the fullerene and graphite. The energy diagram of several crystalline phases of pure carbon is presented in Fig. 23. The most stable phase is graphite. The energies of diamond and fullerene, reckoned from the graphite level, are, respectively, 0.020 and 0.42 eV per carbon atom. The difference between the polymer and monomer forms of C_{60} is much smaller. The existence of distinct phases within the narrow energy range is a very interesting feature of fullerenes as an allotropic form of carbon.

In addition, it is seen from Figs. 21 and 23 that the polymer phase energy grows with increasing number of $[2 + 2]$ bonds. Experimental data indicate that not only the gain in energy through bonding, but also the energy loss caused by distortions of molecules should be taken into account when analyzing the energy balance of the polymer forms. If the first component dominates, the energy of the polymer form is lower. However, the intermolecular bonding leads to a significant deformation of the molecular cage. In the case of a dimer, the distortion energy is compensated for by intramolecular relaxation. With an increasing number of intermolecular bonds, the distortion becomes much more pronounced, the stabilization is less effective, and the total energy of the polymer grows with the increasing number of bonds.

The next surprising fact is that polymers, rather than dimers, are commonly formed in C_{60} compression, despite the fact that the dimer is the most stable fullerite. At the same time, the most common phase is the energetically unfavorable rhombohedral form [202]. This result indicates that polymerization under pressure is not controlled only energetically.

The dynamic aspect of polymerization was considered in [239]. The polymerization of crystalline C_{60} was studied theoretically, and a conclusion was made that the distortion of molecules plays a key role in the polymerization under pressure [239]. The molecular dynamics of C_{60} collisions and disintegration were calculated, with particular attention paid to the symmetry of molecular orbitals, an indicator of the creation of intermolecular bonds in collisions.

The barrier height for the interfullerene bond creation is twice the destruction barrier: 4.15 eV vs. 2.83 eV. The local density approximation calculations give a slightly smaller value of 2.4 eV. Qualitatively, this can be attributed to the significant difference of the molecular distortions in collisions and disintegration. The contraction and extension along the intermolecular bond are critical for the explanation of the difference in the polymerization and depolymerization conditions. When a dimer is forming, the double bonds on the molecule equator are extended. External pressure cannot extend the molecule. It slightly draws them together without essential distortion. Molecules are distorted by the arising internal stresses. When the internal stress equilibrates the external force, a dimer is formed.

Model calculations show that the stability of a molecule against distortions leads to high activation ener-

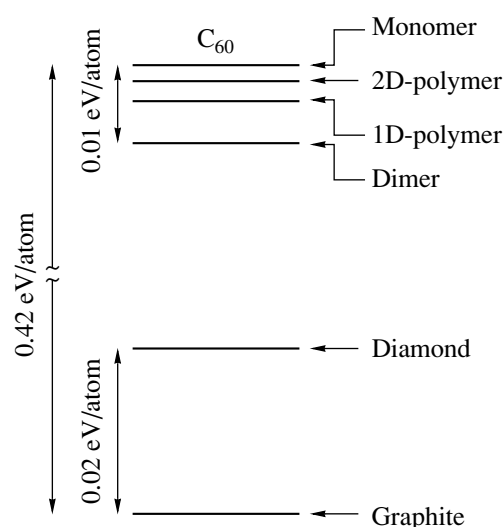


Fig. 23. Energy levels for various solid states of carbon [235].

gies for polymerization under pressure. The return of the molecule into its initial state and relaxation of bonds require less energy and, therefore, the activation energy for bond rupture is lower than that for bond creation.

The unique properties of the fullerene polymerization reaction stem from the large number of molecular degrees of freedom, leading to existence of various polymeric forms within a narrow energy range. Oriented molecular packing with reactive double bonds being in close contact with one another plays an essential role in the creation of a certain polymerized phase. In the ideal form, such contacts are possible neither in the fcc nor in any of the oriented phases P or H . However, theoretical calculations [203, 204] indicate that any polymerized phase is preceded by the corresponding molecular precursor state. While this state is achieved by polymerization in the oriented H -phase [9] for the rhombohedral phase, a two-stage process is required for the tetragonal phase [241].

The mechanism of the photopolymerization reaction, stages of photopolymerization stages, and the role of excitons in the process were studied in [242]. For the dimerization process to begin, two fullerene molecules (denoted by digits 1 and 2 in Fig. 24a) must come close enough one to another, to a distance ΔR_r . This shifts other molecules, particularly the nearest neighbors, denoted by digits 3–6, to a distance $\Delta R'_r$. Fourteen more molecules, surrounding the above-mentioned six, will suffer a pronounced shift.

In addition, there will be changes in the relative arrangement of molecules. Two positions are the most energetically favorable: the double bonds of the fullerene molecule may be directed toward the hexagon or pentagon of the neighboring molecules (as shown in the inset in Fig. 24b; see also Fig. 1). However, dimer-

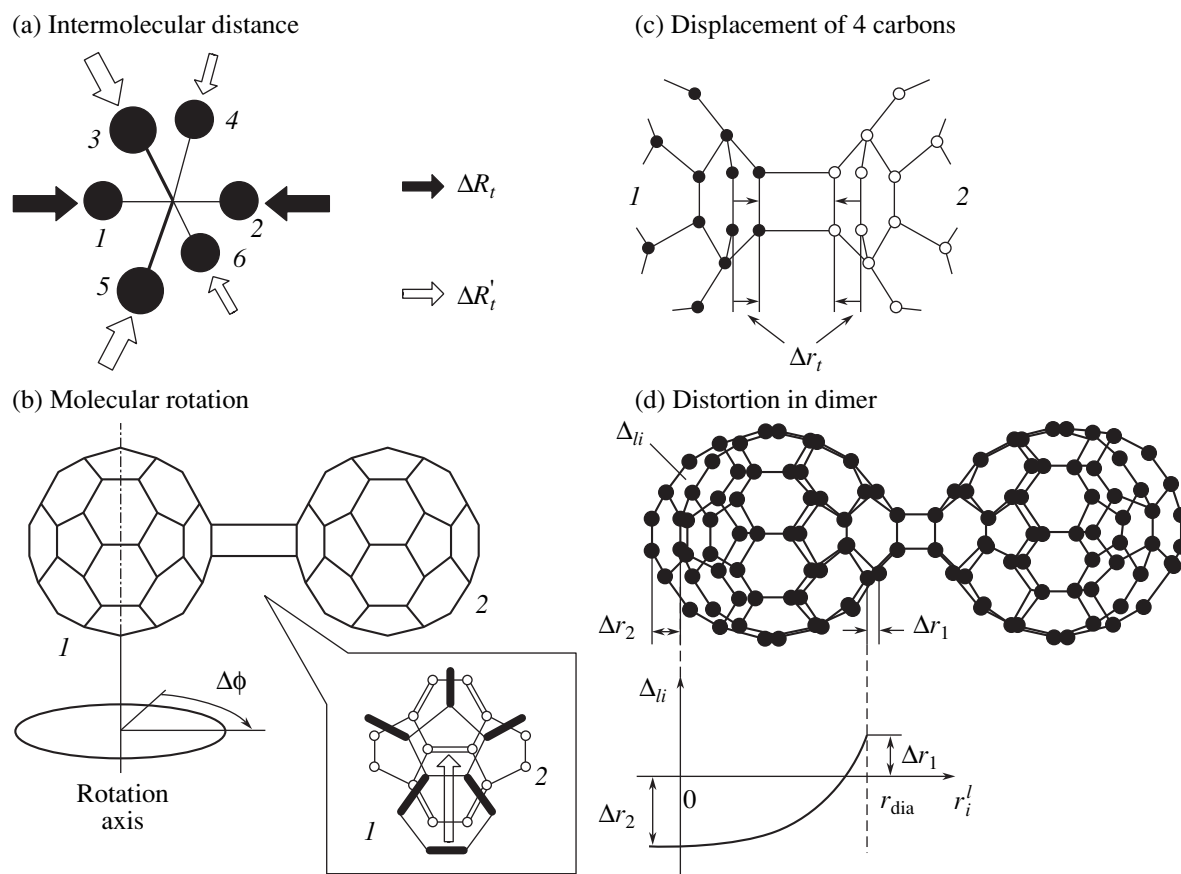


Fig. 24. Different distortions of the cage after photoinduced dimerization of crystalline C_{60} . (a) Center of mass shifts for every molecule shown by black circles; (b) rotation of molecules until double bonds become parallel, thick and thin lines represent, respectively, molecules nos. 1 and 2; (c) shift of carbon atoms in the direction normal to the molecule surface; and (d) cage distortion along the dimer axis after completion of the cycloaddition reaction [242].

ization can not occur in such a configuration, since one of the molecules must be rotated by an angle $\Delta\phi$ to make the double bonds parallel.

After rotation into a proper position for dimerization, the molecule changes its shape (Fig. 24c). The double bonds involved in the reaction shift in the direction normal to the molecule surface. The carbon atoms shift accordingly to a distance Δr_t .

Finally, dimerization essentially distorts the molecules. The dimer is stretched along its axis, owing to release of the stress energy. The elliptic distortion of the cage is designated in Fig. 24d as a shift Δl_i of each l_i carbon atom along the dimer axis. A calculation of the most stable dimerized structure gave the following parameters: $\Delta R_t = 0.65 \text{ \AA}$; $\Delta R'_t = -0.20 \text{ \AA}$; $\Delta\phi = 0.375\pi$; $\Delta r_t = 0.195 \text{ \AA}$. A simple expression for calculating the shift of each atom along the dimer axis is presented.

It is believed [242] that an essential condition for the onset of the dimerization process is the formation of the CT exciton. Calculations imply that the CT exciton has

a significantly stronger interaction with the lattice phonons than does the Frenkel exciton.

Illumination of the fullerene crystal induces photo-generation of free excitons producing some deformation of the lattice. During the relaxation process, the CT exciton is forming, located on neighboring molecules and inducing their attraction. Previously, the fast decaying component of the luminescence spectrum was shown [243] to be due to the CT-exciton self-trapping. The energy released in the self-trapping is transferred to the lattice. Certainly, the capture of an exciton is not enough to overcome the energy barrier between the monomer and dimer phases, and a multiphoton excitation is required. It was shown that 10^5 photons are necessary to create a single bond, [244]. The exciton created by the first photon relaxes mainly on the structural defects creating the precursor stage of the dimerization process. This state is long-lived and can be excited by the next photons. Successive multiphoton excitations lead to essential structural changes, and dimerization occurs when the energy of the metastable state exceeds the potential barrier.

BAND STRUCTURE OF POLYMERIZED FULLERENES

Changes in the fullerene band structure are the most interesting aspect of the polymerization. There exists a vast body of sometimes contradictory theoretical and, to a lesser extent, experimental data on this problem.

Band Structure of Photopolymers

Dimers or short chains comprising up to six [177] or seven molecules [245] appear in photopolymerization. It was shown in [220] that when analyzing the C_{1s} line satellite intensity photopolymerization saturates at six bonds per molecule, but characteristics of the obtained polymer were not given. The Raman spectra of films taken in polymerization saturation under similar conditions indicate unambiguously a linear polymerization [244]. 2D polymerization is unlikely, since it is accompanied by a strong distortion of molecules and an increase in the total energy of the system, which is only possible under a strong external action.

If the C_{60} molecules had true graphite-like sp^2 -bonds, the polymerization would be energetically unfavorable. The “superfluous” electrons leading to alternation of double and single bonds ensure the stability of the dimer, a nucleus of the polymerized phase.

Symmetry lowering leads to splitting of the strongly degenerated spectrum of the C_{60} molecule into eight different representations transformed as $s, x, y, z, xy, yz, zx, xyz$. However, in the case of dimers and linear chains, the perturbations directed along the x and y axes are rather weak, which gives rise to quasi-degenerate states [246]. The density of electronic states of the C_{60} dimer is presented in Fig. 25. The lower unoccupied molecular orbital T_{1u} splits into two degenerate (x, y)-states and a z -state, which manifests itself in the spectrum as a double peak. Similar to the case of an isolated molecule, the upper occupied orbital is H_u , and the distance between the HOMO and LUMO is smaller than that in the monomer C_{60} .

Band Structure of Piezopolymers

The band structure of 2D (rhombohedral and tetragonal) fullerenes was calculated [233, 234] using the local density approximation technique. It was emphasized that the electronic structure of these phases retains its 3D nature because of the small interlayer spacing and strong interaction between the layers.

The following processes occur in fullerene polymerization in the rhombohedral phase.

1. Twelve sp^3 -like carbon atoms involved in intermolecular bonding appear at each molecule.
2. Molecules are distorted, their diameter in the direction normal to the polymerization plane decreases.

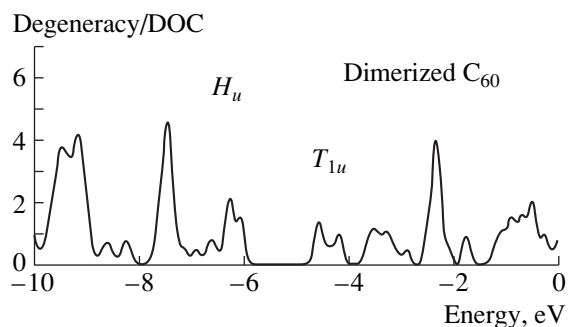


Fig. 25. Density of electronic states of C_{60} dimer. States of the lower unoccupied molecular orbital T_{1u} split into a quasi-doublet and singlet states, while the upper occupied molecular orbital H_u mixes with the lower G_g and H_g levels, which leads to a general broadening of the spectrum [246].

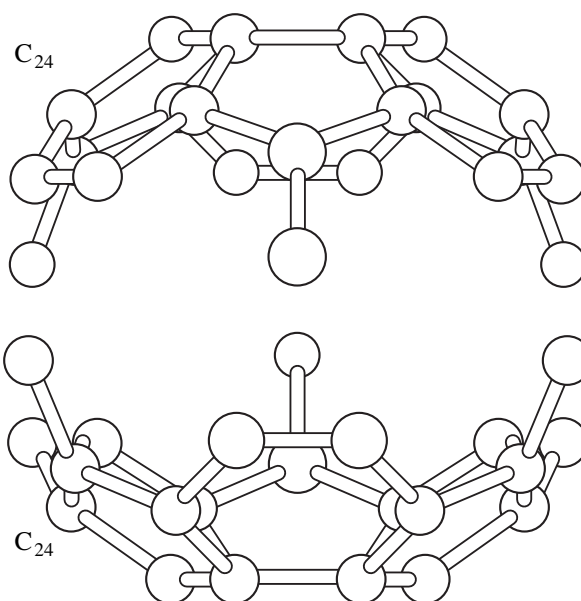


Fig. 26. Schematic of the geometric structure of the π -electron system in the rhombohedral phase of the C_{60} fullerene. Hemispherical C_{24} clusters form a triangular lattice above and below the polymerization planes [234].

3. The intermolecular distances become shorter not only within the polymerization plane, but between the planes as well.

4. Atoms retaining π state are separated into two groups: those lying above and below the polymerization plane (Fig. 26).

As a result, the electronic structure has nothing in common with the initial one. The basic features are as follows (Fig. 27).

1. The valence band top is at the Z point, and the conduction band bottom, at the F point. The energy gap is 0.35 eV. Despite that the polymerization transforms sp^2 into sp^3 , the energy gap does not approach that of diamond; by contrast, it becomes 0.7 eV narrower.

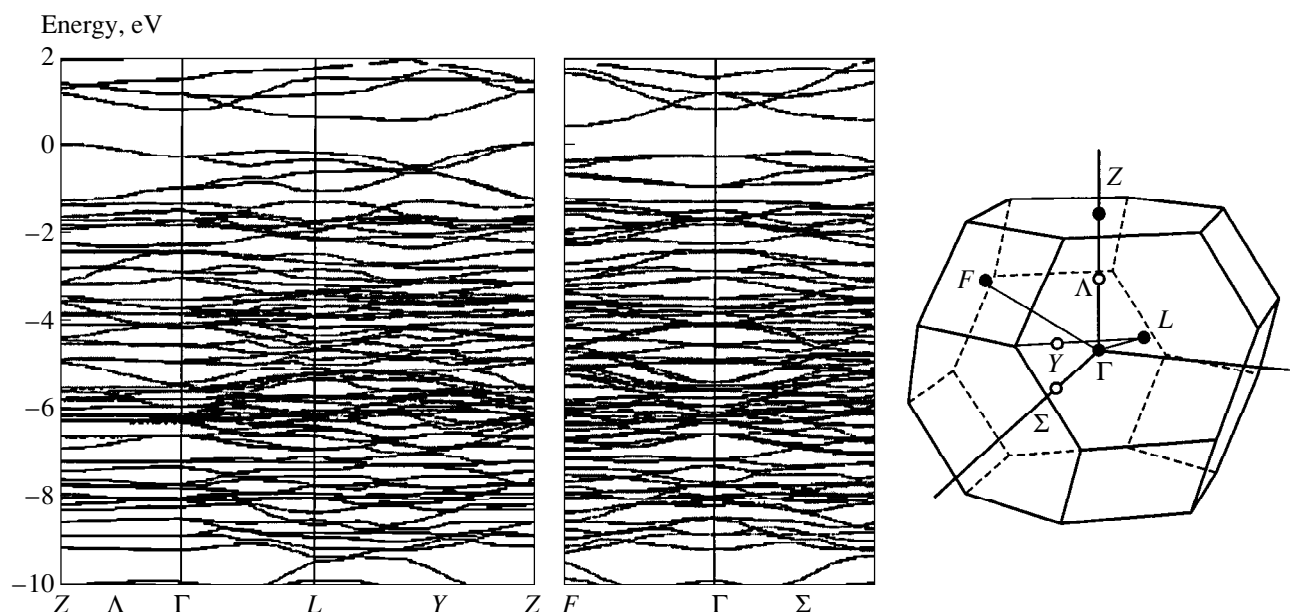


Fig. 27. Band structure of the C_{60} rhombohedral phase. Energy is measured from the valence band center at the Z point. The symmetry points and lines of the first Brillouin zone are shown [233].

2. In the case of molecular C_{60} , the triply degenerate states form an isolated conduction band, while in the rhombohedral case the lower branch of the conduction band is separated from all higher states.

3. The dispersion of bands is significantly stronger than in the fcc C_{60} case.

4. All unoccupied states form a single conduction band.

5. Although the system has a 2D packing, large dispersion along the Λ line indicates that electronically this is a 3D system. The effective mass (m^*/m_0) components in the three directions are on the same order of magnitude: 0.2, 0.7, and 0.9 for electrons; 0.5, 0.6, and 1.8 for holes.

6. A strong dispersion is observed deep inside the valence band related to the σ states, which is due to the formation of the intercluster bonds.

The strong distinctions in the electronic structure are due to the fact that characteristics of the lower conduction and higher valence bands are determined by the topology of the π -electron system. Only forty-eight atoms out of sixty are in the π -state in the rhombohedral structure. Moreover, these atoms are divided into two equivalent groups, each comprising twenty-four atoms, lying above and below the polymerization plane. Therefore, when considering the π -band, twenty-four-atomic clusters, and not the molecule, play the role of the structural element. Since the most important states around the gap are π -states, it is quite natural that the band structure drastically differs from the initial one.

Fifty-two atoms are in the π -state in the tetrahedral phase. The electronic structure is basically similar to

the rhombohedral case. The distance between the valence band top at the Z point and the conduction band bottom lying on the Σ -line is 0.72 eV. This phase is also characterized by a separated branch of the conduction band. All unoccupied states strongly overlap, constituting a continuous conduction band. A strong dispersion along the Σ and Δ lines, i.e. along the polymerization directions, is clearly seen for the lower, i.e., σ -states. A pronounced dispersion along the Λ line indicates that the tetragonal system also has a 3D nature. The effective mass components at the conduction band bottom are: (m^*/m_0) = 1.2, 0.4, and 1.1; those at the valence band top: 0.5, 0.5, and 0.8.

The charge density in the intercluster C–C bond is the same as in the intraccluster bond. The atoms linking polymerized molecules do have a quadruple coordination, as in the case of diamond. However, the angles significantly differ from the classical values of $109^\circ 47'$ (90° and 118°). The interfullerene chemical bond energy in the polymerized material is less than 2 eV, which is significantly smaller than the value for the ideal bond between sp^3 -hybridized carbon atoms [230].

The charge density distribution in the perpendicular direction drastically differs from that within the plane: no noticeable charge density is present in the interplanar space. Thus, the interlayer interaction in 2D C_{60} polymers is considered as being of the van der Waals type, similar to graphite.

Calculations indicate that in contrast to 2D-polymerized polymers, the electronic structure of the 3D polymer is metal-like [247]. The metal–insulator structural transition is predicted at a pressure of about 20 GPa. The metallic state is created through a com-

plete change of the π -electronic system, resulting from the distortion of molecules and overlapping of the π -like states of the triply coordinated atoms with the hybridization essentially different from sp^2 . The 3D polymer has a large density of states at the Fermi level, estimated to be 7.7 states per C_{60} molecule for each spin. On this basis, one would expect superconducting properties of the material.

Calculations based on the extent of π -conjugation between isolated molecules were carried out [248, 249]. It was assumed that the conjugation parameter is zero for isolated molecules and unity for those covalently bound. The HOMO and LUMO bands are shown to move toward each other with increasing conjugation parameter. The increase in the conjugation parameter leads to a semiconductor-metal transition. Formation of both T - and H -polymers was considered. The expected metallic state is a result of band crossover, related to the wave function symmetry [250]. Calculations based on the π electron conjugation predict that the 1D polymer C_{60}^{-1} is always a metal, while the C_{60}^{-2} polymer transits from the nondirect-gap to direct-gap semiconductor with increasing conjugation parameter. Doping must reduce the HOMO-LUMO bandwidth because of the polaronic effects. In the author's opinion, these calculations are valid only for small conjugation parameters, since at the instant of covalent bond formation the π -electronic system changes, and the conjugation parameter is bound to abruptly fall. On the other hand, the author considers as another extreme case calculations based on the complete localization of the electrons in polymerization. An adequate calculation is bound to take into account the presence of the π -conjugated regions in the polymerized fullerene.

The geometric structure and the energy spectrum of the rhombohedral phase, calculated using the tight-binding approximation method [232], also indicate that the new phase must be a semiconductor. However, the presence in a solid of defective intermolecular bonds (e.g., those linked in a different way) can affect this conclusion. Examples of molecule linking to dimers are given in [171]. The 66/66 bond (Fig. 17) joins in the standard way, but the 56/56, 56/65, 56/66 bonds (where 56 and 65 stand for bonds between the neighboring pentagons and hexagons) may appear as well. The density of states for the 66/66 dimer and hexagonal C_{60} are similar (bands at 1.3 and 1.0 eV, the same energy positions). However, the density of states of dimers linked via pentagons is essentially different, and tails of HOMO and LUMO extend into the gap (Fig. 28). Surely, the 66/66 dimer is more stable. Nevertheless, the 56-bond inevitably appears if an improperly oriented molecule appears in the polymer.

Defects of this kind may lead to the synthesis of a material with semi-metallic properties. The presence of a single 56-bond in [2 + 2]-cycloaddition strongly

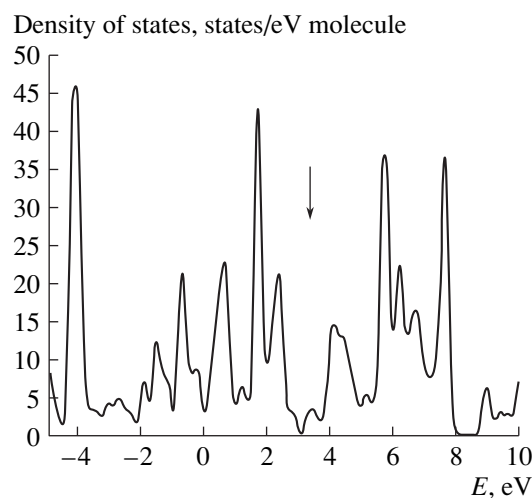


Fig. 28. Density of states for a dimer linked according to the 56/66 scheme [233].

affects the electronic properties, smearing the HOMO-LUMO gap.

Band Structure of Intercalated Polymers

For a charged linear polymer, theories predict both quasi-1D [165] and 3D nature [166, 251], both metallic [252, 253] and insulating properties resulting from a Peierls transition [254], or Fermi surface nesting [255, 256] or reduction of the transfer integral along the polymer chains [257].

The energy gap of the linear polymer obtained in [166] must be, according to calculations, 0.3 eV for the neutral polymer and 0.13 eV for the charged one [258]. On the other hand, it was assumed [165] that the linear polymer RbC_{60} can be considered a quasi-1D metal. This conclusion was based on analysis of an exceptionally narrow ESR line, which is a measure of the rate of the spin-lattice relaxation rate, combined with wide X-ray lines indicating a strong disorder. Disorder is bound to increase the relaxation rate, the same is caused by the presence of heavy rubidium ions. The narrowing of the ESR line indicates quasi-one-dimensionality, since in this case the spin relaxation remains weak even if the disorder is strong.

At temperatures below 50 K, the elementary cell of the linear polymers is distorted. A quasi-1D metal is unstable with respect to formation of a spin- or charge density wave. The charge density wave appears in the following way. In the initial state, the lower unoccupied fullerene molecular orbital is six-fold degenerate. The orthorhombic ligand field splits them into three doubly degenerate states. The lower level is half-occupied, and the charge density wave is related to the elementary cell doubling through alternation of longer and shorter bonds. Thus, addition of an electron from an alkali

metal atom to C_{60} leads to the formation of a half-filled conduction band.

If the spin density wave is formed, the magnetic interaction doubles the elementary cell along the a direction. In both cases, a gap opens at the Fermi level, and the density of states obtained by measuring the spin susceptibility decreases at low temperatures.

Experimental data indicate that the spin density rather than charge density wave appears in doped fullerenes. Temperature dependences of the ESR line width and g -factor are characteristic of antiferromagnetic (AFM) correlations and confirm the hypothesis of the spin density wave. This idea is supported by the observation of an increase in spin-lattice relaxation rate in the metal phase, which may result from AFM fluctuations. In quasi-1D systems, fluctuations may persist up to temperatures significantly above that of the Peierls transition.

The phase diagram of charge and spin density waves in the C_{60} polymers was calculated in [254]. The model calculations predict a spin density wave at a distance between the molecular surfaces exceeding 1.5 Å and a charge density wave, which is the C_{60} -sphere polarization wave, at shorter distances. Coexistence of both the waves is predicted for the experimentally found distances.

However, the opposite arguments have been put forward as well. It has been noticed [166] that the quasi-1D nature of the polymer system is not obvious, since the π -electron conjugation is interrupted in the four-member ring linking the molecules. The maximal π -electron overlapping occurs not between the nearest neighbors but between the next sp^2 -coordinated carbon atoms that are not bound directly and lie significantly farther than the sp^3 -atoms of the σ -conjugated pair. However, the molecules are so closely located along the polymer chains that the intrachain overlap of the π -electrons may exceed that for electrons of the carbon atoms belonging to different chains. The distance between the nearest sp^2 -coordinated atoms is estimated to be 3.05 Å, while the smallest possible distance between atoms of neighboring chains is 3.25 Å.

It was stated [251] that the electronic structure of linear polymers remains essentially three-dimensional, and magnetic fluctuations favor creation of an uncommon AFM-ordered structure with a semi-metallic electronic spectrum.

Band structure calculations indicated that the dispersion along the chains is comparable in magnitude to that across the chains. Electron hops in the structure are practically isotropic; the Fermi surface is three-dimensional. The band t_{1u} splits into three conduction subbands as a result of symmetry lowering. The degree of symmetry violation is significant in comparison with the conduction band width of 0.5 eV. The lower band is almost half-occupied because of the charge transfer, but stays essentially three-dimensional.

Qualitatively similar dispersions along and across the chains follow from the two structural features.

1. Valent orbitals of the nearest intermolecular carbon atoms are rehybridized from 3-coordinated into 4-coordinated in order to join two neighboring C_{60} molecules. Therefore, the conduction π -band in this polymerized phase contains only a minor contribution from the nearest neighbors on adjacent molecules, and the dispersion in this direction depends on the interaction of next-nearest neighbors.

2. Even at relatively weak interchain hops, the dispersion across the chains is ensured by the high coordination of molecules in the transverse direction. At a larger interchain distance this feature will be lost, and hopping along the chains will dominate.

It seems likely that the quasi-1D character of the linear polymers is possible if the interchain distance will be increased by intercalation with large-size atoms. Such a transition from the 3D to 1D behavior would be extremely interesting.

The calculation of the electronic structure of a linear fullerene polymer based on the optimized fullerene trimer geometry [252] indicates the presence of both dispersion and non-dispersion bands, which indicates the existence of localized and delocalized (extended) states. The states at the Fermi level are localized. However, there exists a very narrow gap of 0.2–0.3 eV, separating these states from the unoccupied dispersion band. This gap may become a pseudogap or even disappear under the influence of neighboring ions or chains, which will manifest itself in the appearance of metallic conduction via lower localized states.

There exist other approaches to the assessment of the electronic structure. The electronic structure of the C_{60}^{-1} linear polymer was calculated using the tight-binding approximation method taking into account both σ and π electrons [257]. The linear polymer remains a semiconductor with an energy gap of 1.1 eV, with the degeneracy of the lower unoccupied band lifted. The unoccupied band is an order of magnitude narrower than that in the A_3C_{60} compounds, indicating that the C_{60}^{-1} polymer (orthorhombic RbC_{60}) is a strongly correlated system. However, the lower unoccupied band is very narrow (0.01 eV), which indicates that the transfer integral t is small along the chain. A strong decrease in the transfer integral between the molecules leads to the insulating A_1C_{60} phase.

It was shown in [255, 256] that the dimensionality of a system strongly affects its properties. In the case of AC_{60} ($A = K, Rb, Cs$) the instability with respect to the spin density wave formation is due to the nearly ideal nesting of the 3D Fermi surface. The RbC_{60} and CsC_{60} compounds are unique systems, since the instability of the metallic phase in them results from the half-filling of the conduction band, rather than from their lowered dimensionality. The disappearance of the instability in the potassium compound is related to a strong deviation from half-filling of the band.

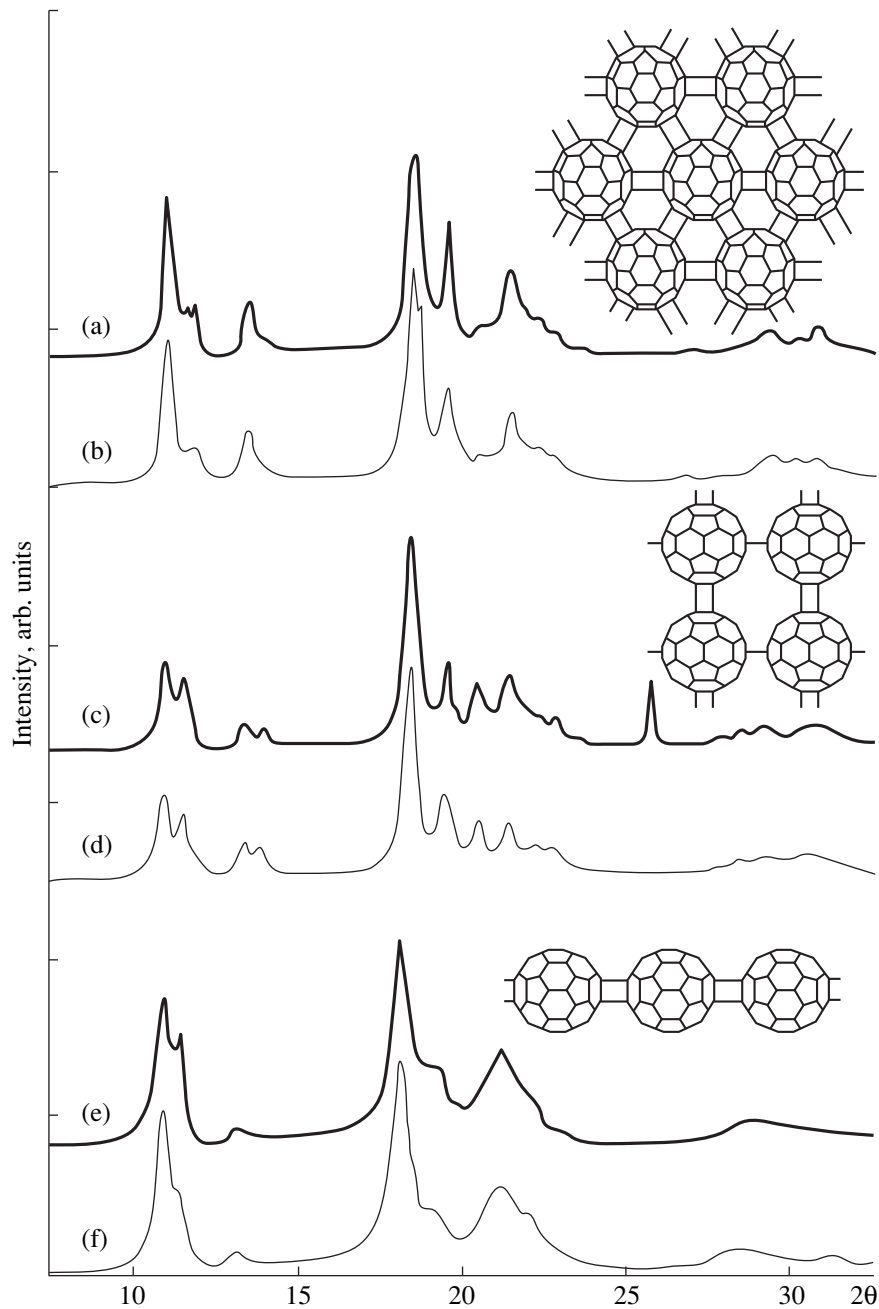


Fig. 29. Experimental (thick lines) and calculated (thin lines) X-ray diffraction patterns for the rhombohedral phase (a, b), a mixture of rhombohedral and tetragonal phases (c, d), and purely orthorhombic phases (e, f) [202].

Not only the intermolecular bond formation, but also changes inside the molecule itself are to be taken into account in band structure calculations. With a semi-empirical model applied to the π electrons and lattice relaxation taken into account, properties of the neutral and charged linear polymers have been studied [259]. In both cases the intermolecular bonds are stretched. The appearance of polaron-like objects or charge density waves, which can play the role of charge carriers, is assumed in the charged polymer case. The

linking bonds are stretched by 0.03 \AA , and the internal bonds contract. In total, the majority of double bonds are stretched, thereby losing to some extent their double character. The cage distortion is located near the equator. The superfluous electron is localized at the joint region. It occupies an orbital that has bonding intramolecular and antibonding intermolecular components. It is this fact that accounts for changes in bond lengths.

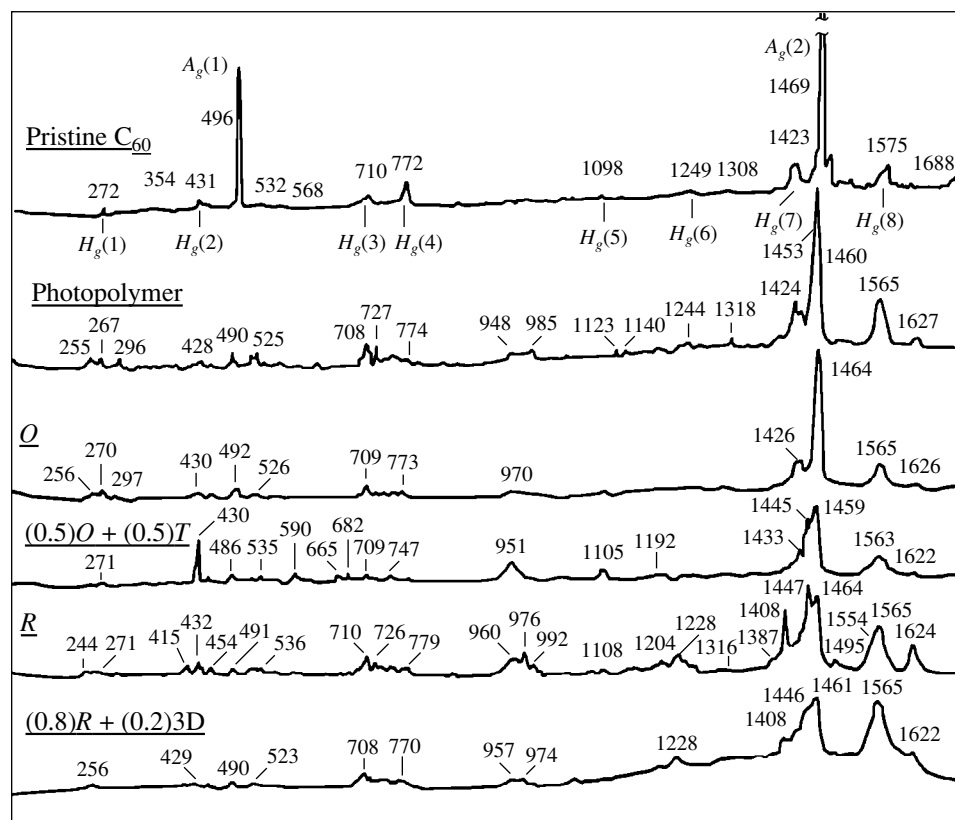


Fig. 30. Raman spectra of C_{60} film, photopolymerized C_{60} film, and various piezopolymer phases: $O + T$ = orthorhombic + tetragonal, R = rhombohedral, $R + 3D$ = rhombohedral + 3D [274].

PROPERTIES OF POLYMERIZED FULLERENES

Structure of Polymers

The structure of the obtained polymers was studied by X-ray methods used to reveal the arrangement of atoms and determine distances between them (Fig. 29) [202]. Further studies demonstrated that various kinds of packing of the ABC planes are possible in the rhombohedral phase, that tetragonal packing is distinguished by 90° rotation of each layer relative to the preceding one [203, 240], and that there are two orthorhombic phases differing in structure [260]. The linear polymers KC_{60} and RbC_{60} have different chain orientations [261].

An X-ray analysis of a polymerized C_{60} single crystal indicated that in the case of an orthorhombic polymerization, not only do the distances along the chain decrease, but also the (111) planes are shifted, with the (111) distance becoming shorter [262].

An X-ray analysis of the 3D C_{60} polymer indicated that the molecules are linked, in addition to the conventional bond, by a new type of bond: [3 + 3]-cycloaddition, oriented along the body diagonal and the shape of the molecule is strongly distorted [263, 264].

Mechanical Properties

Under certain conditions of fullerene polymerization, an unusually hard phase may appear [265, 266]. A study by acoustic spectroscopy of the ultrahard fullerenes fabricated at 13 GPa indicated that the longitudinal velocity of sound (17–26 km/s) in them exceeds that in any other solid [267]. The transverse velocity of sound is about 7.2–9.6 km/s. The compression modulus of 1 TPa is higher than that in diamond. An uncommon combination of the high strength and high plasticity of the C_{60} polymers was found [268].

Under a pressure of 3.5–8 GPa, the mechanical properties of the material are mostly determined by the synthesis temperature, rather than by pressure [269]. The formation of superhard phases at high pressure is due to the 3D ordering of the sp^2 -hybridized structure. High synthesis temperature leads to 3D polymerization and formation of a disordered network with high density of sp^3 -states and further to formation of a diamond-like structure.

An increase in hardness was also observed for photopolymers [270]. The maximal effect was achieved at a wavelength of 700 nm; the occurrence of the maximum is accounted for by the rise in the photopolymerization efficiency with increasing wavelength, with simultaneously decreasing light penetration depth [271].

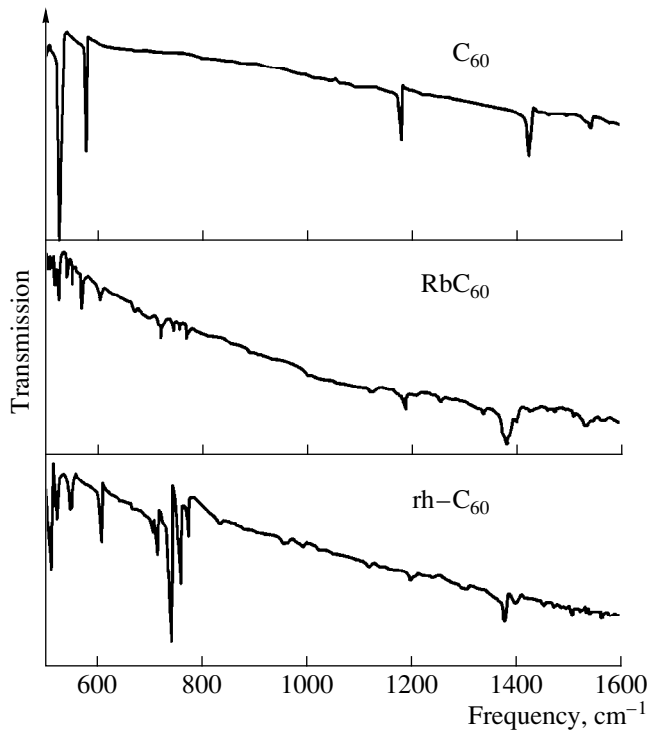


Fig. 31. IR absorption spectra of C_{60} , RbC_{60} , and rhombohedral phase of C_{60} [275].

Spectroscopy of Polymers

The symmetry lowering in polymerization influences the IR absorption and Raman scattering spectra. Vibrations of the $[C_{60}]_N$ oligomer with $N = 2, 3,$ and 4 were calculated together with the intensities of Raman lines [272]. Calculations of the intramolecular modes and IR absorption spectra of C_{60} dimers were carried out [246]. The Raman spectra of the C_{60} dimers and dimer-like $C_{60}O$, $C_{60}O_2$ oxides were studied experimentally [273].

Raman spectra were studied for photopolymers and the rhombohedral, tetragonal, and orthorhombic piezopolymer phases [274] (Fig. 30). The H_{1g} and F_{1u} modes are split in polymerization, and the intramolecular mode is softened, which is due to a decrease in the number of the C–C bonds in the cage. The pentagonal pinch-mode splits into six lines whose relative intensity is sensitive to the type of polymerization. The frequencies of the $A_g(2)$ and $F_{1u}(4)$ modes depend linearly on the molecule coordinates: softening is observed with slopes of about 19 and $58 \text{ cm}^{-1}/\text{\AA}$, respectively. The difference between the symmetries of linear chains and 2D polymers clearly manifests itself in the IR absorption spectra (Fig. 31) of the linear polymer RbC_{60} and rhombohedral C_{60} [275].

The Raman spectra of photopolymerized C_{60} films and those polymerized under low pressure are very similar, but the photopolymer spectra contain a greater

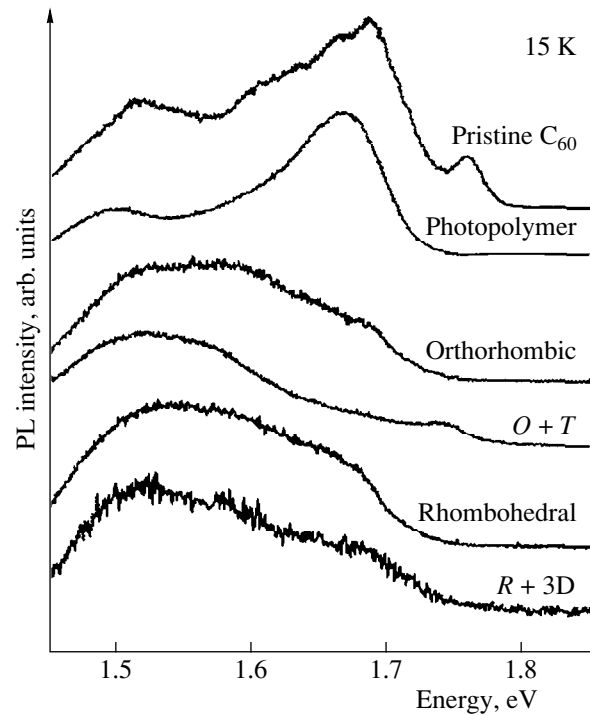


Fig. 32. Comparison of PL spectra taken at 15 K for various kinds of polymerized C_{60} [158].

number of features. In particular, the 1454 cm^{-1} line can be interpreted as one due to a branched polymer chain [276, 277].

The EELS spectrum shows an extension of intra-band transitions in laser phototransformation of C_{60} , with the energy gap remaining unchanged [278]. At the same time, exposure to an electron beam leads to a decrease in the gap and in the π -plasmon energy in the C_{60} fullerite [279].

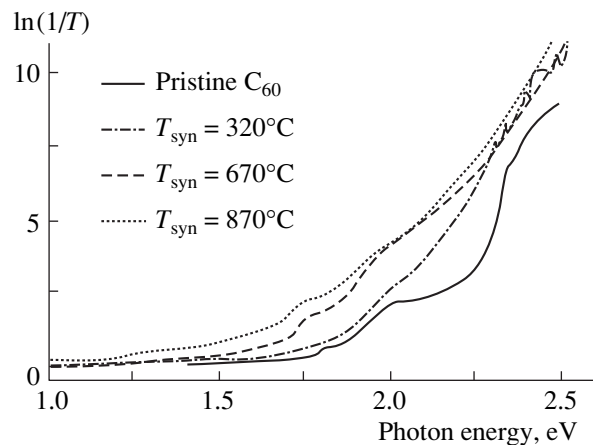


Fig. 33. Transmission spectra for the 1D and 3D fullerenes obtained at 6 GPa [282].

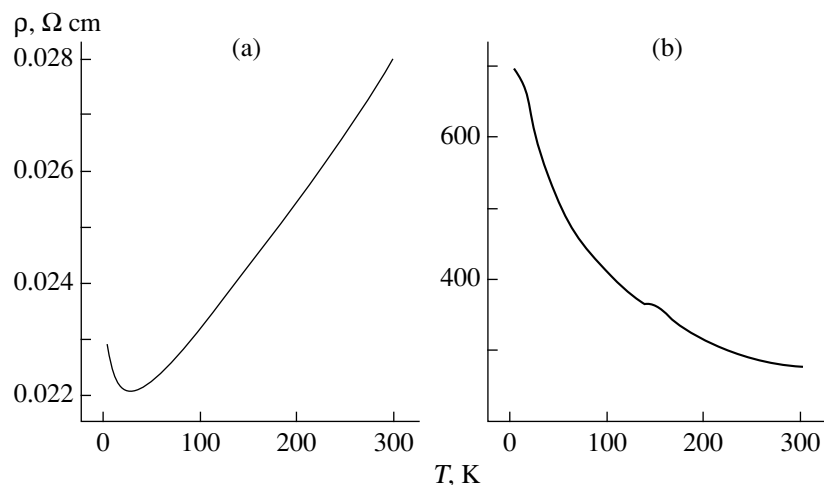


Fig. 34. Temperature dependence of the conductivity in the polymerization plane (a) and across polymerized planes (b) for highly oriented rhombohedral polymerized C_{60} phase [285].

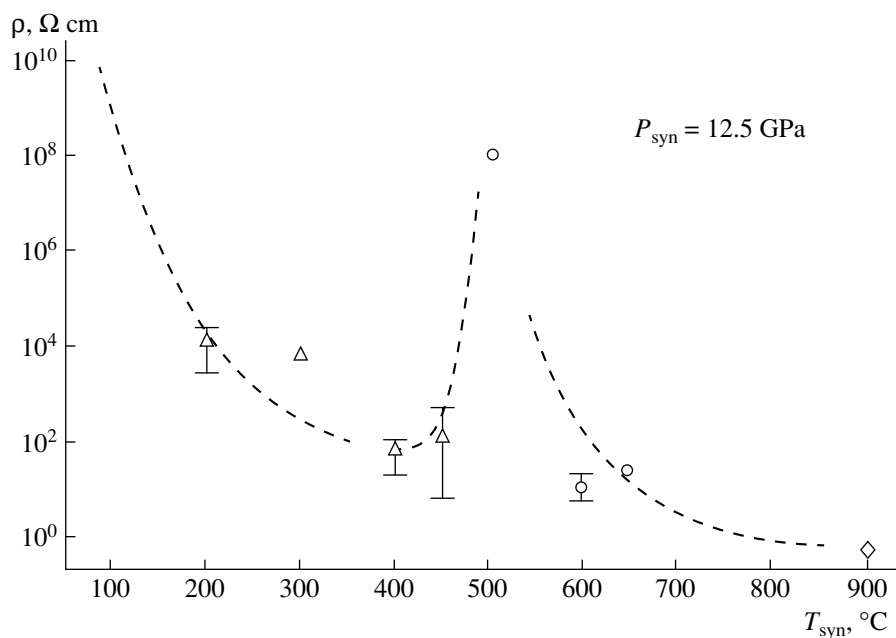


Fig. 35. Resistivity under standard conditions for phases obtained from the C_{60} fullerene: 3D polymer (triangles), amorphous carbon (circles), diamond-like nanocrystal phase (rhombs). Abscissa: synthesis temperature T_{syn} [282].

Optical Absorption and Luminescence

Optical absorption and photoluminescence (PL) spectra of polymerized fullerenes have essentially broader bands compared with those in monomeric samples [280]. In addition, the optical absorption ranges and PL peaks are shifted to the lower energies. The results are interpreted in terms of symmetry lowering. PL spectra of various phases of the polymerized C_{60} were compared in [158] (Fig. 32). Oxygen-containing polymeric fullerene films demonstrate strong lumines-

cence in the near-IR and visible ranges (1.50–2.36 eV) [281]. Annealing reduces the PL intensity.

The transmission spectra of 1D and 2D polymers indicate that they retain their semiconductor properties with energy gaps of, respectively, 1.1 and 1.4 eV; raising the polymerization temperature shifts the absorption edge to longer wavelengths (Fig. 33) [282].

Electrical Properties

The transport properties of polymers have been studied inadequately, except for intercalation polymers.

(KC₆₀)_n has metallic conductivity, whereas (RbC₆₀)_n, and (CsC₆₀)_n are conductors at high temperatures, but exhibit a metal–insulator transition at 50 and 40 K [198]. The properties of Rb_xC₆₀ films (mainly at $x = 1$) strongly depend on the kind of thermal treatment. Fast cooling leads to a metastable metallic phase, while slow cooling results in a phase transition between two conducting phases [283].

Polymerization at low pressures (up to 2.5 GPa) leads to a rise in conductivity and makes lower the slope of the semiconductor-like temperature dependence [284]. However, the domain nature of structures obtained upon polymerization leads to a competition of the intra- and interdomain conduction mechanisms. Thus, the experimentally measured activation energy is not a parameter related to the band gap. The activation energy and the pre-exponential factor are related by the Meyer–Neldel formula, which points to a trap-controlled conduction mechanism [285]. Polymerization under pressures of 6–8 GPa leads, as mentioned above, to the formation of an oriented rhombohedral phase, and this phase shows a gigantic conductivity anisotropy (Fig. 34). If a 2D polymer is formed at a temperature above the limiting skeleton disintegration temperature (about 800°C), the conductivity abruptly increases by four orders of magnitude [286].

The superhard phases formed under pressure from C₆₀ molecules possess high conductivity coinciding at room temperature with that of vitreous carbon, but the temperature dependence is very weak and has a metallic character [287]. However, a tendency for the resistivity to decrease is replaced under more severe structure formation conditions by an abrupt rise in resistivity at the instant of the amorphous diamond phase formation (Fig. 35) [282].

CONCLUSION

In this review, an attempt was made to consider solids based on fullerenes as semiconductor materials and to collect all physical properties characterizing them in this regard. Evidently, notwithstanding the vast body of data on this problem, there still exist large unstudied fields; in particular, this concerns the experimental data on the properties of fullerenes in the polymerized state.

ACKNOWLEDGMENTS

I thank the colleagues who allowed me to reproduce the graphical data chosen to illustrate the key points of the text and the publishing houses that gave permission to publish the figures.

This study was supported by the Russian Foundation for Basic Research (project no. 99-02-18170) and by the Alexander von Humboldt Foundation.

REFERENCES

1. H. W. Kroto, J. R. Heath, S. C. O'Brien, *et al.*, *Nature* **318**, 162 (1985).
2. W. Kraetschmer, L. D. Lamb, K. Fostiropoulos, and D. R. Huffman, *Nature* **347**, 354 (1990).
3. A. F. Hebard, M. J. Rosseinsky, R. C. Haddon, *et al.*, *Nature* **350**, 600 (1991).
4. M. S. Dresselhaus, G. Dresselhaus, and P. C. Eklund, *Science of Fullerenes and Carbon Nanotubes* (Academic, San Diego, 1995).
5. *Optical and Electronic Properties of Fullerenes and Fullerene-Based Materials*, Ed. by J. Shinar (Marcel Dekker, New York, 1999).
6. *Fullerenes and Related Structures*, Ed. by A. Hirsch (Springer-Verlag, Berlin, 1999).
7. *Fullerene Polymers and Fullerene Polymer Composites*, Ed. by P. C. Eklund (Springer-Verlag, Berlin, 2000).
8. O. Gunnarson, *Rev. Mod. Phys.* **69**, 575 (1997).
9. B. Sundqvist, *Adv. Phys.* **48**, 1 (1999).
10. R. C. Haddon, *Science* **261**, 1545 (1993).
11. W. Andreoni, F. Gygi, and M. Parinellö, *Phys. Rev. Lett.* **68**, 823 (1992).
12. B. Bürgi, E. Blanc, D. Schwarzenbach, *et al.*, *Angew. Chem. Int. Ed. Engl.* **31**, 640 (1992).
13. X. Q. Wang, C. Z. Wang, and K. M. Ho, *Phys. Rev. B* **48**, 1884 (1993).
14. S. Baroni, *J. Chem. Phys.* **100**, 8537 (1994).
15. B.-L. Gu, Y. Maruyama, J.-Z. Yu, *et al.*, *Phys. Rev. B* **49**, 16 202 (1994).
16. L. Pintschovius, S. L. Chaplot, G. Roth, and G. Heger, *Phys. Rev. Lett.* **75**, 2843 (1995).
17. P. A. Heiney, J. E. Fischer, A. R. McGhie, *et al.*, *Phys. Rev. Lett.* **66**, 2911 (1991).
18. W. I. F. David, R. M. Ibberson, J. C. Matthewman, *et al.*, *Nature* **353**, 147 (1991).
19. K.-P. Bohnen and R. Heid, *Phys. Rev. Lett.* **83**, 1167 (1999).
20. B. Sundqvist, O. Andersson, A. Lundin, and A. Soldatov, *Solid State Commun.* **93**, 109 (1995).
21. E. L. Shirley and S. G. Louie, *Phys. Rev. Lett.* **71**, 133 (1993).
22. S. Saito and A. Oshiyama, *Phys. Rev. Lett.* **66**, 2637 (1991).
23. B. Mishori, E. A. Katz, D. Faiman, and Y. Shapira, *Solid State Commun.* **102**, 489 (1997).
24. R. W. Lof, M. A. van Veenendaal, B. Koopmans, *et al.*, *Phys. Rev. Lett.* **68**, 3924 (1992).
25. E. Sohmen, J. Fink, and W. Kraetschmer, *Z. Phys. B* **86**, 87 (1992).
26. T. Rabenau, A. Simon, R. K. Kremer, and E. Sohmen, *Z. Phys. B* **90**, 69 (1993).

27. T. Ohgami, Y. Shimada, H. Kubota, *et al.*, *Physica B* (Amsterdam) **239**, 32 (1997).
28. P. Mondal, P. Lunkenheimer, and A. Loidl, *Z. Phys. B* **99**, 527 (1996).
29. M. Hosoya, K. Ichimura, Z. H. Wang, *et al.*, *Phys. Rev. B* **49**, 4981 (1994).
30. J. Hora, P. Pánek, K. Navrátil, *et al.*, *Phys. Rev. B* **54**, 5106 (1996).
31. A. Skumanich, *Chem. Phys. Lett.* **182**, 486 (1991).
32. R. Schwedhelm, L. Kipp, A. Dallmeyer, and M. Skibowski, *Phys. Rev. B* **58**, 13 176 (1998).
33. J. de Vries, H. Steger, B. Kamke, *et al.*, *Chem. Phys. Lett.* **188**, 159 (1992).
34. R. D. Beck, R. Weis, R. Rockenberebr, and M. M. Kappes, *Surf. Rev. Lett.* **3**, 771 (1996).
35. Lai-Sheng Wang, J. Conceicao, Jin Changming, and R. E. Smalley, *Chem. Phys. Lett.* **182**, 5 (1991).
36. O. V. Boltalina, L. N. Sidorov, A. Y. Borschevsky, *et al.*, *Rapid Commun. Mass Spectrom.* **7** (11), 1009 (1993).
37. R. E. Haufler, Lai-Sheng Wang, L. P. F. Chibante, *et al.*, *Chem. Phys. Lett.* **179**, 449 (1991).
38. S. Gonda, M. Kawasaki, T. Arakane, and H. Koinuma, *Mater. Res. Soc. Symp. Proc.* **349**, 25 (1994).
39. S. Krummacher, M. Biermann, M. Neeb, *et al.*, *Phys. Rev. B* **48**, 8424 (1993).
40. E. L. Shirley, L. X. Benedict, and S. G. Louie, *Phys. Rev. B* **54**, 10 970 (1996).
41. M. Knupfer and J. Fink, *Phys. Rev. B* **60**, 10 731 (1999).
42. F. Bechstedt, M. Fiedler, and L. J. Sham, *Phys. Rev. B* **59**, 1857 (1999).
43. B. Mishori, Y. Shapira, A. Belu-Matian, *et al.*, *Chem. Phys. Lett.* **264**, 163 (1997).
44. B. Mishori, E. A. Katz, D. Faiman, *et al.*, *Fullerene Sci. Technol.* **6**, 113 (1998).
45. E. A. Katz, D. Faiman, B. Mishori, *et al.*, *J. Appl. Phys.* **84**, 3333 (1998).
46. G. F. Bertsch, A. Bulgac, D. Tomanek, and Y. Wang, *Phys. Rev. Lett.* **67**, 2690 (1991).
47. B. Friedman and J. Kim, *Phys. Rev. B* **46**, 8638 (1992).
48. K. Harigaya and S. Abe, *Phys. Rev. B* **49**, 16746 (1994).
49. D. Li, S. Velasquez, and S. E. Schnatterly, *Phys. Rev. B* **49**, 2969 (1994).
50. S. Leach, M. Vervloet, A. Despres, *et al.*, *Chem. Phys.* **160**, 451 (1992).
51. Y. Wang, J. M. Holden, A. M. Rao, *et al.*, *Phys. Rev. B* **45**, 14 396 (1992).
52. T. Gotoh, S. Nonomura, S. Hirata, and S. Nitta, *Appl. Surf. Sci.* **114**, 278 (1997).
53. M. K. Kelly, P. Etchegoin, D. Fuchs, *et al.*, *Phys. Rev. B* **46**, 4963 (1992).
54. T. L. Makarova, *Mol. Cryst. Liq. Cryst. Sci. Technol., Sect. C* **7**, 199 (1996).
55. P. Milani, M. Manfredini, G. Guizzetti, *et al.*, *Solid State Commun.* **90**, 639 (1994).
56. W. Zhou, S. Xie, S. Qian, *et al.*, *J. Appl. Phys.* **80**, 459 (1996).
57. C. Hartmann, M. Zigone, G. Martinez, *et al.*, *Phys. Rev. B* **52**, R5550 (1995).
58. T. Gotoh, S. Nonomura, H. Watanabe, *et al.*, *Phys. Rev. B* **58**, 10 060 (1998).
59. N. Troullier and J. L. Martins, *Phys. Rev. B* **46**, 1754 (1992).
60. K. Yabana and G. F. Bertsch, *Chem. Phys. Lett.* **197**, 32 (1992).
61. M. I. Salkola, *Phys. Rev. B* **49**, 4407 (1994).
62. S. Kazaoui, N. Minami, Y. Tanabe, *et al.*, *Phys. Rev. B* **58**, 7689 (1998).
63. S. Mochizuki, M. Sasaki, and R. Ruppin, *J. Phys.: Condens. Matter* **10**, 2347 (1998).
64. V. Capozzi, G. Gasamassima, G. F. Lorusso, *et al.*, *Solid State Commun.* **9**, 853 (1996).
65. S. Ishihara, I. Ikemoto, S. Suzuki, *et al.*, *Chem. Phys. Lett.* **295**, 475 (1998).
66. A. V. Bazhenov, A. V. Gorbunov, and K. G. Volkodav, *Pis'ma Zh. Éksp. Teor. Fiz.* **60** (5), 326 (1994) [*JETP Lett.* **60**, 331 (1994)].
67. A. V. Bazhenov, A. V. Gorbunov, M. Yu. Maksimyyuk, and T. N. Fursova, *Zh. Éksp. Teor. Fiz.* **112** (1), 246 (1997) [*JETP* **85**, 135 (1997)].
68. L. W. Tutt and T. F. Boggess, *Prog. Quantum Electron.* **17**, 299 (1993).
69. F. Z. Henari, D. N. Weldon, and W. J. Blau, *Adv. Mater. Opt. Electron.* **4**, 413 (1994).
70. F. Kajzar, C. Taliani, R. Zamboni, *et al.*, *Synth. Met.* **77**, 257 (1996).
71. S. Couris, E. Koudoumas, A. A. Ruth, and S. Leach, *J. Phys. B* **28**, 4537 (1995).
72. L. Geng and J. C. Wright, *Chem. Phys. Lett.* **249**, 105 (1996).
73. D. Wilk, D. Johannsmann, C. Stanners, and Y. R. Shen, *Phys. Rev. B* **51**, 10 057 (1995).
74. Z. Shuai and J. L. Bredas, *Mol. Cryst. Liq. Cryst.* **256**, 801 (1994).
75. H. Habuchi, S. Nitta, D. Han, and S. Nonomura, *J. Appl. Phys.* **87**, 8580 (2000).
76. A. Hamed, Y. Y. Sun, Y. K. Tao, *et al.*, *Phys. Rev. B* **47**, 10873 (1993).
77. A. Zahab and L. Firlej, *Solid State Commun.* **87**, 893 (1993).
78. He Peimo, Xu Yabo, Z. Xuanjia, and Li Wenzhou, *Solid State Commun.* **89**, 373 (1994).
79. K. Hoshimono, S. Fujimori, and S. Fujita, *Jpn. J. Appl. Phys., Part 2* **32**, L1070 (1993).
80. T. Takahashi, S. Suzuki, T. Morikawa, *et al.*, *Phys. Rev. Lett.* **68**, 1232 (1992).

81. S. Fujimori, K. Hoshimono, and S. Fujita, *Solid State Commun.* **89**, 437 (1994).
82. T. Asakawa, M. Sasaki, M. Yoshimoto, *et al.*, *Mater. Res. Soc. Symp. Proc.* **349**, 185 (1994).
83. A. Belumarian, R. Manailia, T. Stoica, *et al.*, *Fullerene Sci. Technol.* **3**, 495 (1995).
84. T. Rabenau, S. Roth, and R. K. Kremer, *Acta Phys. Pol. A* **87**, 881 (1995).
85. T. Arai, Y. Murakami, H. Suematsu, *et al.*, *Solid State Commun.* **84**, 827 (1992).
86. E. L. Frankenivch, Y. Maruyama, and H. Ogata, *Chem. Phys. Lett.* **214**, 39 (1993).
87. G. Priede, B. Pietzak, and R. Konenkamp, *Appl. Phys. Lett.* **71**, 2160 (1997).
88. C. P. Jarrett, K. Pichler, R. Newbould, and R. H. Friend, *Synth. Met.* **77**, 35 (1996).
89. K. Kaneto, K. Yamanaka, K. Rikitake, *et al.*, *Jpn. J. Appl. Phys.*, Part 1 **35**, 1802 (1996).
90. R. C. Haddon, A. S. Perel, R. C. Morris, *et al.*, *Appl. Phys. Lett.* **67**, 121 (1995).
91. T. L. Makarova, I. B. Zakharova, T. I. Zubkova, and A. Ya. Vul', *Fiz. Tverd. Tela (St. Petersburg)* **41** (2), 354 (1999) [*Phys. Solid State* **41**, 319 (1999)].
92. K. Rikitake, T. Akiyama, W. Takashima, and K. Kaneto, *Synth. Met.* **86**, 2357 (1997).
93. K. Kaneto, K. Rikitake, T. Akiyama, and H. Hasegawa, *Jpn. J. Appl. Phys.*, Part 1 **36**, 910 (1997).
94. J. L. Gong, G. B. Ma, and G. H. Chen, *J. Mater. Res.* **11**, 2071 (1996).
95. M. Jaime and M. Nunez-Requeiro, *Appl. Phys. A: Mater. Sci. Process* **A60**, 289 (1995).
96. F. Yan, Y. N. Wang, Y. N. Huang, *et al.*, *Phys. Lett. A* **201**, 443 (1995).
97. N. I. Nemchuk, T. L. Makarova, O. I. Konkov, *et al.*, *Mol. Cryst. Liq. Cryst. Sci. Technol.*, Sect. C **7**, 183 (1996).
98. R. K. Kremer, T. Rabenau, W. K. Maser, *et al.*, *Appl. Phys. A: Solids Surf.* **A56**, 211 (1993).
99. S. Matsuura, T. Ishiguro, K. Kikuchi, *et al.*, *Fullerene Sci. Technol.* **3**, 437 (1995).
100. Y. Xu, J. Y. Kondo, Y. Shionoiri, and Y. Ochiai, *Jpn. J. Appl. Phys.*, Part 1 **38**, 347 (1999).
101. J. Stankowski and J. Martinek, *Solid State Commun.* **100**, 717 (1996).
102. J. C. Wang and Y. F. Chen, *Appl. Phys. Lett.* **73**, 948 (1998).
103. J. C. Dyre, *J. Phys. C* **19**, 5655 (1986).
104. T. L. Makarova, T. Wegberg, B. Sundqvist, V. Agafonov, V. A. Davydov, A. V. Rakhmanina, and L. S. Kashevarova, in *Recent Advances in the Chemistry and Physics of Fullerenes and Related Materials VII*, Ed. by K. M. Kadish, D. M. Guldi, and P. V. Kamat (Electrochemical Society, Pennington, 1999), *Proc. Electrochem. Soc.* **99-12**, 628 (1999).
105. M. Kaiser, W. K. Maser, H. J. Byrne, *et al.*, *Solid State Commun.* **87**, 281 (1993).
106. C. H. Lee, G. Yu, K. Pakbaz, *et al.*, *Mol. Cryst. Liq. Cryst. Sci. Technol.*, Sect. A **256**, 769 (1994).
107. V. I. Srdanov, C. H. Lee, and N. S. V. Sariciftci, *Thin Solid Films* **257**, 233 (1995).
108. C. H. Lee, G. Yu, B. Kraabel, *et al.*, *Phys. Rev. B* **49**, 10572 (1994).
109. H. Habuchi, S. Nitta, S. Nonomura, and D. Han, *Mol. Cryst. Liq. Cryst. Sci. Technol.*, Sect. C **10**, 93 (1998).
110. D. X. Han, H. Habuchi, and S. Nitta, *Phys. Rev. B* **57**, 3773 (1998).
111. N. I. Nemchuk, T. L. Makarova, and A. Ya. Vul', in *Recent Advances in the Chemistry and Physics of Fullerenes and Related Materials III*, Ed. by R. S. Ruoff and K. M. Kadish (Electrochemical Society, Pennington, 1996), *Proc. Electrochem. Soc.* **96-10**, 464 (1996).
112. B. Pevzner, A. F. Hebard, and M. S. Dresselhaus, *Phys. Rev. B* **55**, 16439 (1997).
113. *High T_c Superconductivity and the C₆₀ Family: Proceedings of the CCAST Symposium/Workshop, Beijing, 1994*, Ed. by Sunqi Feng (Gordon & Breach, Luxembourg, 1995).
114. J. E. Fisher and P. A. Heiney, *J. Phys. Chem. Solids* **54**, 1725 (1993).
115. K. Prassides, H. W. Kroto, R. Taylor, *et al.*, *Carbon* **30**, 1277 (1992).
116. K. Holczer and R. L. Whetten, *Carbon* **30**, 1261 (1992).
117. K. Tanigaki, *Mater. Sci. Eng. B* **19**, 135 (1993).
118. V. Buntar and H. W. Weber, *Supercond. Sci. Technol.* **9**, 599 (1996).
119. J. S. Schilling, J. Diederichs, and A. Gandyopadhyay, in *Recent Advances in the Chemistry and Physics of Fullerenes and Related Materials IV*, Ed. by R. S. Ruoff and K. M. Kadish (Electrochemical Society, Pennington, 1997), *Proc. Electrochem. Soc.* **97-14**, 980 (1997).
120. K. S. Kim, J. M. Park, J. Kim, *et al.*, *Phys. Rev. Lett.* **84**, 2425 (2000).
121. X.-D. Xiang, J. G. Hou, G. Briceno, *et al.*, *Science* **256**, 1190 (1992).
122. O. Klein, G. Gruner, S.-M. Huang, *et al.*, *Phys. Rev. B* **46**, 11 247 (1992).
123. C. Christides, D. A. Neumann, K. Prassides, *et al.*, *Phys. Rev. B* **46**, 12 088 (1992).
124. X.-D. Xiang, J. G. Hou, V. H. Crespi, and A. Zettl, *Nature* **361**, 54 (1993).
125. A. F. Hebard, T. T. M. Palstra, R. C. Haddon, and R. M. Fleming, *Phys. Rev. B* **48**, 9945 (1993).
126. W. A. Vareka and A. Zettl, *Phys. Rev. Lett.* **72**, 4121 (1994).
127. V. H. Crespi, J. G. Hou, X.-D. Xiang, *et al.*, *Phys. Rev. B* **46**, 12064 (1992).
128. V. P. Antropov, O. Gunnarsson, and A. I. Liechtenstein, *Phys. Rev. B* **48**, 7651 (1993).

129. J. S. Lannin and M. Mitch, *Phys. Rev. B* **50**, 6497 (1994).
130. N. Ke, W. Y. Cheung, S. P. Wong, and S. Q. Peng, *Carbon* **35**, 759 (1997).
131. J. H. Yao, Y. J. Zou, D. Y. He, and G. H. Chen, *Mater. Lett.* **33**, 27 (1997).
132. D. J. Fu, Y. Y. Lei, J. C. Li, *et al.*, *Appl. Phys. A: Mater. Sci. Process.* **A67**, 441 (1998).
133. D. Mendoza, F. Morales, and R. Escudero, *Fullerene Sci. Technol.* **6**, 801 (1998).
134. H. Chen, Z. S. Liu, S. Y. Li, *et al.*, *Phys. Rev. B* **60**, 6183 (1999).
135. Q. M. Zhang, Y. N. Huang, H. M. Shen, *et al.*, *Appl. Phys. Lett.* **67**, 3417 (1995).
136. G. P. Kochanski, A. F. Hebard, R. C. Haddon, and A. T. Fiory, *Science* **255**, 184 (1992).
137. S. Kazaoui, R. Ross, and N. Minami, *Solid State Commun.* **90**, 623 (1994).
138. T. Asakawa, M. Sasaki, T. Shirashi, and K. Koinuma, *Jpn. J. Appl. Phys., Part 1* **34**, 1958 (1995).
139. S. Matsuura, T. Ishiguro, K. Kikuchi, and Y. Achiba, *Phys. Rev. B* **51**, 10 217 (1995).
140. Y. Ishijima and T. Ishiguro, *J. Phys. Soc. Jpn.* **65**, 1574 (1996).
141. K. C. Chiu, J. S. Wang, and C. Y. Lin, *J. Appl. Phys.* **79**, 1784 (1996).
142. E. A. Katz, V. Lyubin, D. Faiman, *et al.*, *Solid State Commun.* **100**, 781 (1996).
143. K. C. Chiu, J. S. Wang, Y. T. Dai, and Y. F. Chen, *Appl. Phys. Lett.* **69**, 2665 (1996).
144. E. V. Korovkin and R. K. Nikolaev, *Fiz. Tverd. Tela (St. Petersburg)* **41**, 1113 (1999) [*Phys. Solid State* **41**, 1015 (1999)].
145. D. Mendoza and R. Escudero, *Solid State Commun.* **100**, 507 (1996).
146. J. Kalinowski, G. Giro, N. Camaioni, *et al.*, *Synth. Met.* **77**, 181 (1996).
147. V. Augelli, L. Schiavulli, T. Ligonzo, and A. Valentini, *Nuovo Cimento D* **20**, 1377 (1998).
148. Yu. A. Osip'yan, R. K. Nikolaev, S. Z. Shmurak, *et al.*, *Fiz. Tverd. Tela (St. Petersburg)* **41**, 2097 (1999) [*Phys. Solid State* **41**, 1926 (1999)].
149. D. Moses, C. H. Lee, B. Kraabel, *et al.*, *Synth. Met.* **70**, 1419 (1995).
150. C. H. Lee, G. Yu, D. Moses, and V. I. Srdanov, *Synth. Met.* **70**, 1413 (1995).
151. R. Konenkamp, R. Engelhardt, and R. Henninger, *Solid State Commun.* **97**, 285 (1996).
152. W. Guss, J. Feldmann, E. O. Gubel, *et al.*, *Phys. Rev. Lett.* **72**, 2644 (1994).
153. T. Ohno, K. Matsuishi, and S. Onari, *Solid State Commun.* **101**, 785 (1997).
154. S. Kazaoui, R. Ross, and N. Minami, *Phys. Rev. B* **52**, R11 665 (1995).
155. M. Knupfer and J. Fink, *Phys. Rev. B* **60**, 10 731 (1999).
156. V. V. Kveder, V. D. Negrii, É. A. Shteinman, *et al.*, *Zh. Éksp. Teor. Fiz.* **113** (2), 734 (1998) [*JETP* **86**, 405 (1998)].
157. U. D. Venkateswaran, M. G. Schall, Y. Wang, *et al.*, *Solid State Commun.* **96**, 951 (1995).
158. U. D. Venkateswaran, D. Sanzi, A. M. Rao, *et al.*, *Phys. Rev. B* **57**, R3193 (1998).
159. B. Friedman and K. Harigaya, *Phys. Rev. B* **47**, 3975 (1993).
160. M. Nunez-Requeiro, P. Monceau, A. Rassat, *et al.*, *Nature* **354**, 289 (1991).
161. F. Moshary, N. H. Chen, I. F. Silvera, *et al.*, *Phys. Rev. Lett.* **69**, 466 (1992).
162. D. W. Snoko, K. Syassen, and A. Mittelbach, *Phys. Rev. B* **47**, 4146 (1993).
163. Y. N. Xu, M. Z. Huang, and W. Y. Ching, *Phys. Rev. B* **46**, 4241 (1992).
164. A. M. Rao, P. Zhou, K. A. Wang, *et al.*, *Science* **259**, 955 (1993).
165. O. Chauvet, G. Oszlanyi, L. Forro, *et al.*, *Phys. Rev. Lett.* **72**, 2721 (1994).
166. S. Pekker, L. Forro, L. Mihaly, and A. Janossy, *Solid State Commun.* **90**, 349 (1994).
167. S. Pekker, A. Janossy, L. Mihaly, *et al.*, *Science* **265**, 1077 (1994).
168. Y. Iwasa, T. Arima, R. M. Fleming, *et al.*, *Science* **264**, 1570 (1994).
169. T. Pichler, M. Knupfer, M. S. Golden, *et al.*, *Phys. Rev. Lett.* **78**, 4249 (1997).
170. G. B. Adams, J. B. Page, O. F. Sankey, and M. O'Keeffe, *Phys. Rev. B* **50**, 17 471 (1994).
171. D. L. Strout, R. L. Murry, C. H. Xu, *et al.*, *Chem. Phys. Lett.* **214**, 576 (1993).
172. Y. Wang, J. M. Holden, Z. Dong, *et al.*, *Chem. Phys. Lett.* **211**, 341 (1993).
173. P. C. Eklund, A. M. Rao, P. Zhou, *et al.*, *Thin Solid Films* **257**, 185 (1995).
174. V. O. Kompanets, N. N. Mel'nik, B. C. Hess, and S. V. Chekalin, *Pis'ma Zh. Éksp. Teor. Fiz.* **68** (4), 200 (1998) [*JETP Lett.* **68**, 344 (1998)].
175. B. Burger, J. Winter, and H. Kuzmany, *Z. Phys. B* **101**, 227 (1996).
176. S. Park, H. Han, R. Kaiser, *et al.*, *J. Appl. Phys.* **84**, 1340 (1998).
177. A. Hassanien, J. Gasperi, J. Demsar, *et al.*, *Appl. Phys. Lett.* **70**, 417 (1997).
178. Y.-P. Sun, B. Ma, C. E. Bunker, and B. Liu, *J. Am. Chem. Soc.* **117**, 12 705 (1995).
179. V. V. Lavrov, I. V. Arkhangel'skii, E. V. Skokan, *et al.*, *Mol. Mater.* **10**, 283 (1998).
180. V. V. Lavrov, E. V. Skokan, I. V. Arkhangel'skii, *et al.*, *Func. Mat.* **5** (3), 376 (1998).

181. T. Pusztai, G. Oszlányi, G. Faigel, *et al.*, AIP Conf. Proc. **486**, 20 (1999).
182. N. Takahashi, H. Dock, N. Matsuzawa, and M. Ata, J. Appl. Phys. **74**, 5790 (1993).
183. J. Kastner, H. Kuzmany, and L. Palmetshofer, Appl. Phys. Lett. **65**, 543 (1994).
184. Y. B. Zhao, D. M. Poirier, R. J. Pechman, and J. H. Weaver, Appl. Phys. Lett. **64**, 577 (1994).
185. A. Matsutani, F. Koyama, and K. Iga, Jpn. J. Appl. Phys., Part 1 **37**, 4211 (1998).
186. M. S. Dresselhaus, *Intercalation in Layered Materials* (Plenum, New York, 1987).
187. *Concise Science Dictionary* (Oxford Univ. Press, Oxford, 1991).
188. W. B. Zhao, J. Chen, K. Wu, *et al.*, J. Phys.: Condens. Matter **6**, L631 (1994).
189. G. K. Werthem, Solid State Commun. **88**, 97 (1993).
190. R. C. Haddon, A. F. Hebard, M. J. Rossensky, *et al.*, Nature **350**, 320 (1991).
191. S. C. Erwin and M. R. Pederson, Phys. Rev. Lett. **67**, 1610 (1991).
192. S. Saito and A. Oshiyama, Phys. Rev. B **44**, 11536 (1991).
193. K. Khazeni, V. H. Crespi, J. Hone, *et al.*, Phys. Rev. B **56**, 6627 (1997).
194. R. F. Kiefl, T. L. Duty, J. W. Schneider, *et al.*, Phys. Rev. Lett. **69**, 2005 (1992).
195. M. Kosaka, K. Tanigaki, T. Tanaka, *et al.*, Phys. Rev. B **51**, 12 018 (1995).
196. P. Petit and J. E. Fisher, Appl. Phys. A: Mater. Sci. Process. **A64**, 283 (1997).
197. P. W. Stephens, G. Bortel, G. Falgel, *et al.*, Nature **370**, 636 (1994).
198. F. Bommeli, L. Degiorgi, P. Wachter, *et al.*, Phys. Rev. B **51**, 14 794 (1995).
199. V. A. Atsarkin, V. V. Demidov, and G. A. Vasneva, Phys. Rev. B **56**, 9448 (1997).
200. V. A. Atsarkin and V. V. Demidov, Zh. Éksp. Teor. Fiz. **113** (3), 1048 (1998) [JETP **86**, 572 (1998)].
201. K. Khazeni, J. Hone, N. G. Chopra, *et al.*, Appl. Phys. A: Mater. Sci. Process. **A64**, 263 (1997).
202. M. Nunez-Requeiro, L. Marques, J. L. Hodeau, *et al.*, Phys. Rev. Lett. **74**, 278 (1995).
203. A. V. Dzyabchenko, V. N. Agafonov, and V. A. Davydov, Crystallogr. Rep. **44**, 13 (1999).
204. L. Marques, J. L. Hodeau, M. Nunez-Requeiro, and M. Perroux, Phys. Rev. B **54**, R12633 (1996).
205. L. Marques, J. L. Hodeau, and M. Hunez-Regueiro, Mol. Cryst. Liq. Cryst. Sci. Technol., Sect. C **8**, 49 (1996).
206. V. A. Davydov, L. S. Kashevarova, A. V. Rakhmanina, *et al.*, Pis'ma Zh. Éksp. Teor. Fiz. **63** (10), 778 (1996) [JETP Lett. **63**, 818 (1996)].
207. V. A. Davydov, L. S. Kashevarova, A. V. Rakhmanina, *et al.*, Carbon **35**, 735 (1997).
208. B. Keita, L. Nadjjo, V. A. Davydov, *et al.*, New J. Chem. **19**, 769 (1995).
209. H. Hirai and K. Kondo, Phys. Rev. B **51**, 15 555 (1995).
210. C. N. R. Rao, A. Govindaraj, H. N. Aiyer, and R. Seshadri, J. Phys. Chem. **99**, 16814 (1995).
211. V. D. Blank, S. G. Buga, N. R. Serebryanaya, *et al.*, Phys. Lett. A **220**, 149 (1996).
212. L. Marques, M. Mezouar, J. L. Hodeau, *et al.*, Science **283**, 1720 (1999).
213. V. D. Blank, S. G. Buga, N. R. Serebryanaya, *et al.*, Carbon **36**, 665 (1998).
214. G. Oszlányi and L. Forro, Solid State Commun. **93**, 265 (1995).
215. C. Goze, F. Rachdi, L. Hajji, *et al.*, Phys. Rev. B **54**, R3676 (1996).
216. F. Rachdi, C. Goze, L. Hajji, *et al.*, J. Phys. Chem. Solids **58**, 1645 (1997).
217. P.-A. Persson, U. Edlund, P. Jacobsson, *et al.*, Chem. Phys. Lett. **258**, 540 (1996).
218. T. Pichler, M. Knupfer, M. S. Golden, *et al.*, Appl. Phys. A: Mater. Sci. Process. **A64**, 301 (1997).
219. A. Nakao, J. Onoe, and K. Takeuchi, Surf. Sci. Spectra **5**, 313 (1998).
220. J. Onoe and K. Takeuchi, Phys. Rev. Lett. **79**, 2987 (1997).
221. S. Stafstrom and J. Fagerstrom, Appl. Phys. A: Mater. Sci. Process. **A64**, 307 (1997).
222. G. Oszlányi, G. Bortel, G. Faigel, *et al.*, Phys. Rev. B **54**, 11 849 (1996).
223. J. Kurti and K. Nemeth, Chem. Phys. Lett. **256**, 119 (1996).
224. G. E. Scuseria, Chem. Phys. Lett. **257**, 583 (1996).
225. S. Pekker, G. Oszlányi, and G. Faigel, Chem. Phys. Lett. **282**, 435 (1998).
226. G. M. Bendele, P. W. Stephens, K. Prassides, *et al.*, Phys. Rev. Lett. **80**, 736 (1998).
227. G. Oszlányi, G. Baumgartner, G. Faigel, and L. Forro, Phys. Rev. Lett. **78**, 4438 (1997).
228. M. Hjort and S. Stafstrom, Synth. Met. **103**, 2422 (1999).
229. G. Oszlányi, G. Baumgartner, G. Faigel, *et al.*, Phys. Rev. B **58**, 5 (1998).
230. S. Saito and S. Okada, AIP Conf. Proc. **442**, 198 (1998).
231. K. Prassides, K. Vavakis, K. Kordatos, *et al.*, J. Am. Chem. Soc. **119**, 834 (1997).
232. C. H. Xu and G. E. Scuseria, Phys. Rev. Lett. **74**, 274 (1995).
233. S. Okada and S. Saito, Phys. Rev. B **55**, 4039 (1997).
234. S. Okada and S. Saito, Phys. Rev. B **59**, 1930 (1999).
235. Y. Iwasa, K. Tanoue, T. Mitani, and T. Yagi, Phys. Rev. B **58**, 16 374 (1998).
236. Y. Wang, J. M. Holden, X. Bi, and P. C. Eklund, Chem. Phys. Lett. **217**, 413 (1994).

237. P. Nagel, V. Pasler, S. Lebedkin, *et al.*, Phys. Rev. B **60**, 16920 (1999).
238. V. V. Brazhkin, A. G. Lyapin, and S. V. Popova, Pis'ma Zh. Éksp. Teor. Fiz. **64** (11), 755 (1996) [JETP Lett. **64**, 802 (1996)].
239. T. Ozaki, Y. Iwasa, and T. Mitani, Chem. Phys. Lett. **285**, 289 (1998).
240. A. V. Dzyabchenko, V. N. Agafonov, and V. A. Davydov, Crystallogr. Rep. **44**, 18 (1999).
241. V. A. Davydov, L. S. Kashevarova, A. V. Rakhmanina, *et al.*, Phys. Rev. B **58**, 14786 (1998).
242. M. Suzuki, T. Iida, and K. Nasu, Phys. Rev. B **61**, 2188 (2000).
243. A. Nakamura, M. Ichida, T. Yajima, *et al.*, J. Lumin. **66-67**, 383 (1995).
244. T. L. Makarova, V. I. Sakharov, I. T. Serenkov, and A. Ya. Vul', Fiz. Tverd. Tela (St. Petersburg) **41** (3), 554 (1999) [Phys. Solid State **41**, 497 (1999)].
245. K. Esfarjani, Y. Hashi, J. Onoe, *et al.*, Phys. Rev. B **57**, 223 (1998).
246. M. R. Pederson and A. A. Quong, Phys. Rev. Lett. **74**, 2319 (1995).
247. S. Okada, S. Saito, and A. Oshiyama, Phys. Rev. Lett. **83**, 1986 (1999).
248. K. Harigaya, Phys. Rev. B **52**, 7968 (1995).
249. K. Harigaya, Chem. Phys. Lett. **242**, 585 (1995).
250. K. Harigaya, Chem. Phys. Lett. **253**, 420 (1996).
251. S. C. Erwin, G. V. Krishna, and E. J. Mele, Phys. Rev. B **51**, 7345 (1995).
252. S. Stafstrom, M. Boman, and J. Fagersrom, Europhys. Lett. **30**, 295 (1995).
253. Y. Cao, W. P. Shi, W. Q. Zhou, *et al.*, Chem. Phys. Lett. **308**, 445 (1999).
254. P. R. Surján, Appl. Phys. A: Mater. Sci. Process. **A64**, 315 (1997).
255. M. Fally and H. Kuzmany, Phys. Rev. B **56**, 13861 (1997).
256. H. Kuzmany, B. Burger, M. Fally, *et al.*, Physica B (Amsterdam) **244**, 186 (1998).
257. K. Tanaka, Y. Matsuura, Y. Oshima, *et al.*, Chem. Phys. Lett. **241**, 149 (1995).
258. P. R. Surjan and K. Nemeth, Solid State Commun. **92**, 407 (1994).
259. M. Springborg, Phys. Rev. B **52**, 2935 (1995).
260. V. Agafonov, V. A. Davydov, L. S. Kashevarova, *et al.*, Chem. Phys. Lett. **267**, 193 (1997).
261. P. Launois, R. Moret, J. Hone, and A. Zettl, Phys. Rev. Lett. **81**, 4420 (1998).
262. R. Moret, P. Launois, P.-A. Persson, and B. Sundqvist, Europhys. Lett. **40**, 55 (1997).
263. L. A. Chernozatonskii, N. R. Serebryanaya, and B. N. Mavrin, Chem. Phys. Lett. **316**, 199 (2000).
264. N. R. Serebryanaya, Solid State Commun. **114**, 537 (2000).
265. V. D. Blank, S. G. Buga, M. Yu. Popov, *et al.*, Zh. Tekh. Fiz. **39** (8), 153 (1994) [Tech. Phys. **39**, 828 (1994)].
266. H. Szwarc, V. A. Davydov, S. A. Plotianskaya, *et al.*, Synth. Met. **77**, 265 (1996).
267. V. D. Blank, V. M. Levin, V. M. Prokhorov, *et al.*, Zh. Éksp. Teor. Fiz. **114** (4), 741 (1998) [JETP **87**, 741 (1998)].
268. V. V. Brazhkin, A. G. Lyapin, S. V. Popova, *et al.*, J. Appl. Phys. **84**, 219 (1998).
269. A. G. Lyapin, V. V. Brazhkin, E. L. Gromnitskaya, *et al.*, Appl. Phys. Lett. **76**, 712 (2000).
270. M. Tachibana, H. Sakuma, and K. Kojima, J. Appl. Phys. **82**, 4253 (1997).
271. M. Tachibana, K. Kojima, H. Sakuma, *et al.*, J. Appl. Phys. **84**, 1944 (1998).
272. D. Porezag, M. R. Pederson, Th. Frauenheim, and Th. Köhler, Phys. Rev. B **52**, 14963 (1995).
273. S. Lebedkin, A. Gromov, S. Giesa, *et al.*, Chem. Phys. Lett. **285**, 210 (1998).
274. A. M. Rao, P. C. Eklund, J.-L. Hodeau, *et al.*, Phys. Rev. B **55**, 4766 (1997).
275. K. Kamarás, Y. Iwasa, and L. Forry, Phys. Rev. B **55**, 10999 (1997).
276. T. Wågberg, P.-A. Persson, B. Sundqvist, and P. Jacobsson, Appl. Phys. A: Mater. Sci. Process. **A64**, 223 (1997).
277. T. Wågberg, P. Jacobsson, and B. Sundqvist, Phys. Rev. B **60**, 4535 (1999).
278. G. P. Lopinski, J. R. Fox, and J. S. Lannin, Chem. Phys. Lett. **239**, 107 (1995).
279. Yu. S. Gordeev, V. M. Mikushkin, and V. V. Shnitov, Fiz. Tverd. Tela (St. Petersburg) **42**, 371 (2000) [Phys. Solid State **42**, 381 (2000)].
280. Y. Wang, J. M. Holden, A. M. Rao, *et al.*, Phys. Rev. B **51**, 4547 (1995).
281. C. Xu, G. Chen, E. Xie, and J. Gong, Appl. Phys. Lett. **70**, 2641 (1997).
282. G. Lyapin, V. V. Brazhkin, S. V. Popova, *et al.*, Phys. Status Solidi B **211**, 401 (1999).
283. M. C. Martin, D. Koller, X. Du, *et al.*, Phys. Rev. B **49**, 10 818 (1994).
284. T. L. Makarova, A. Ya. Vul', V. A. Davydov, L. S. Kashevarova, A. V. Rakhmanina, and P. Scharff, in *Recent Advances in the Chemistry and Physics of Fullerenes and Related Materials IV*, Ed. by R. S. Ruoff and K. M. Kadish (Electrochemical Society, Pennington, 1997), Proc. Electrochem. Soc. **97-14**, 1157 (1997).
285. M. Tokumoto, B. Narymbetov, H. Kobayashi, *et al.*, in *Proceedings of the IWEP-2000*, Ed. by H. Kuzmany (in press).
286. T. L. Makarova, T. Wågberg, B. Sundqvist, *et al.*, Mol. Cryst. Liq. Cryst. Sci. Technol., Sect. C **13**, 151 (2000).
287. M. E. Kozlov, M. Hirabayashi, K. Nozaki, *et al.*, Appl. Phys. Lett. **66**, 1199 (1995).

Translated by S. Ktitorov

Edited by M. Tagirdzhanov

ATOMIC STRUCTURE AND NONELECTRONIC PROPERTIES OF SEMICONDUCTORS

Heteroepitaxy of II–VI Compound Semiconductors on Cooled Substrates

A. P. Belyaev* and V. P. Rubets

St. Petersburg Technological Institute, Moskovskii pr. 26, St. Petersburg, 198013 Russia

*e-mail: Belyaev@tu.spb.ru

Submitted June 16, 2000; accepted for publication July 26, 2000

Abstract—Epitaxial CdTe and CdS films were grown by condensation in vacuum on substrates cooled to subzero temperatures on the Celsius scale. The films were examined by X-ray and electron diffraction. Temperature dependences of the growth rate were measured at various incident fluxes. Conditions under which the films grew with anomalously low rates were identified. These conditions were found to correlate with the structural perfection of the films. The obtained results were compared with the experimental data for epitaxial Au films grown under highly nonequilibrium conditions. The experimental results are consistent with the soliton-based model for heteroepitaxy. © 2001 MAIK “Nauka/Interperiodica”.

INTRODUCTION

It is commonly accepted that heteroepitaxy is possible only at high temperatures. However, a surprising result has been recently obtained. Belyaev *et al.* [1, 2] reported that vapor-phase heteroepitaxial growth of CdTe films can be accomplished on substrates cooled to subzero Celsius temperatures (highly nonequilibrium conditions). A model was proposed explaining this phenomenon by the initiation of nonlinear waves of the soliton type, which are induced by misfit dislocations at the interface between the growing film and the substrate. Belyaev *et al.* [3] reported also that some samples prepared under highly nonequilibrium conditions exhibit unusual properties. In this paper, we report new experimental data that support the soliton-based model and improve our understanding of processes of condensation under highly nonequilibrium conditions.

EXPERIMENTAL

Films were synthesized on muscovite-mica substrates cooled by liquid nitrogen in a quasi-closed system [2]. The film thickness varied from 1 to 2 μm . The incident flux was adjusted by changing the sublimation temperature. The growth rate was calculated from the film thickness and the growth time.

Film thicknesses were measured using an MII-4 microinterferometer. Electron diffraction patterns were taken with an ÉMR-100 electron diffractometer. Phase composition was determined by X-ray diffraction using a DRON-2 diffractometer. The X-ray diffraction patterns were interpreted using the ASTM database.

RESULTS

We studied the formation of CdTe, CdS, and Au films under highly nonequilibrium conditions. The main experimental results are summarized in Figs. 1–4.

Figure 1 shows a semilogarithmic plot of the growth rate versus inverse substrate temperature for the CdTe films prepared under highly nonequilibrium conditions. This plot is characterized by two temperature ranges in which the films grow with anomalously low rates (regions I and II in Fig. 1). The layers grown in these temperature ranges have perfect structures, which is illustrated by the typical electron diffraction patterns of the CdTe films synthesized at substrate temperatures $T_s = 220$ and 180 K (Figs. 2a and 2b, respectively). For comparison, Fig. 2c presents the electron diffraction pattern of the film prepared under different highly nonequilibrium conditions ($T_s = 260$ K).

The films grown in temperature ranges I and II differ in phase composition. The layers grown in temperature range I have a cubic structure, whereas the films prepared in range II contain cubic and hexagonal phases. This is confirmed by X-ray diffraction patterns shown in Fig. 3.

Figure 1 also illustrates the effect of the incident flux on the process of the film formation under highly nonequilibrium conditions. Curves 1, 2, and 3 were measured at fluxes $R = 1.8 \times 10^{17}$, 8.0×10^{17} , and $8.5 \times 10^{18} \text{ cm}^{-2} \text{ s}^{-1}$, respectively. Comparing these curves, we can see that, as the incident flux increases, the curves become smoother, and the temperature ranges of low-rate oriented growth shift to higher temperatures. The structural perfection of the films deteriorates with increasing R .

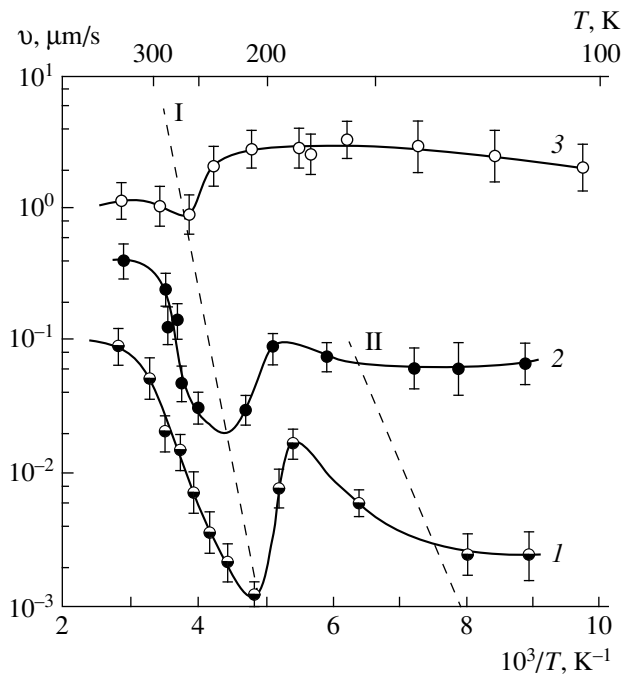


Fig. 1. Growth rate versus inverse substrate temperature for the CdTe films prepared under highly nonequilibrium conditions at incident fluxes $R = (1) 1.8 \times 10^{17}$, $(2) 8.0 \times 10^{17}$, and $(3) 8.5 \times 10^{18} \text{ cm}^{-2} \text{ s}^{-1}$.

Similar experimental results were obtained for CdS films. The plot of the growth rate versus inverse substrate temperature also shows two temperature ranges of low-rate oriented growth: from 230 to 240 K and from 140 to 150 K. Single- and two-phase epitaxial films were grown in the first and the second temperature ranges, respectively (see Figs. 4a, 4b). The structural perfection of the layers prepared under other conditions was considerably worse. The increase in the incident flux also impairs the crystal perfection of the films. The only difference between the experimental results for CdTe and CdS is that the CdS films grown in the first temperature range have a hexagonal structure instead of cubic one.

For comparison, we studied the formation of Au films under highly nonequilibrium conditions. The plot of the growth rate versus inverse temperature shows that there is only one temperature range in which oriented films grow with an anomalously low rate (from 150 to 160 K). The films have a cubic structure.

DISCUSSION

As shown previously [1, 2, 4], the film formation under highly nonequilibrium conditions involves several steps: nucleation (formation of disperse particles in the vapor phase), condensation of the disperse particles on the substrate surface, incorporation (orientation of the disperse particles in a potential field of the substrate), coalescence of the disperse particles, and the

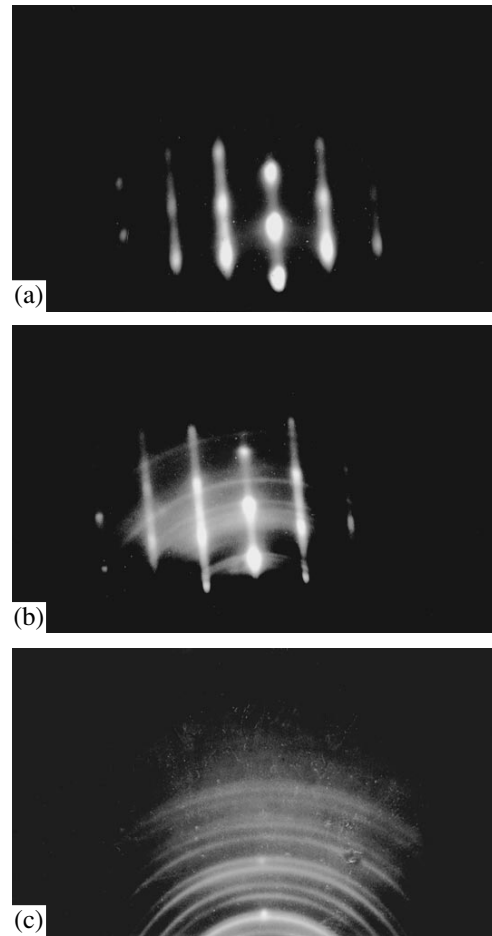


Fig. 2. Representative electron diffraction patterns of the CdTe films synthesized under highly nonequilibrium conditions at an incident flux $R = 1.8 \times 10^{17} \text{ cm}^{-2} \text{ s}^{-1}$ and substrate temperatures $T_r = (a) 220$, $(b) 180$, and $(c) 260 \text{ K}$.

formation of a continuous film. From the standpoint of crystal perfection, the crucial stage is the incorporation. Incorporation on a cooled substrate results in the epitaxial alignment of the disperse particles only under certain conditions and needs virtually no activation.

In connection with this, Belyaev *et al.* [1] proposed a fundamentally new hypothesis for the incorporation mechanism (soliton-based model). This model implies that the disperse particles are oriented in the substrate field due to nonlinear soliton-type waves initiated by misfit dislocations and able to accomplish mass transfer virtually without dissipation of energy. For the solitons to arise, lattice parameters of the disperse particles, $b(T_f)$, and the substrate, $a(T_r)$, should satisfy the following inequality:

$$\frac{a(T_r) - b(T_f)}{b(T_f)} > (2/\pi)^{3/2} \sqrt{f/\lambda a(T_r)}. \quad (1)$$

Here, f and λ are the parameters accounting for the forces acting between atoms of the disperse particles

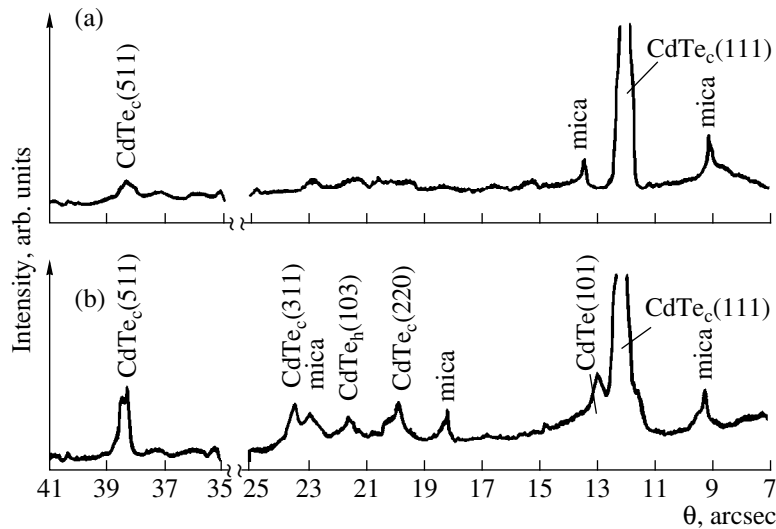


Fig. 3. Representative X-ray diffraction patterns of the CdTe films synthesized under highly nonequilibrium conditions at an incident flux $R = 1.8 \times 10^{17} \text{ cm}^{-2} \text{ s}^{-1}$ and substrate temperatures $T_r =$ (a) 220 and (b) 180 K.

and atoms of the substrate and between atoms of the substrate, respectively. If $b(T_f)$ is close to $a(T_r)$, this condition can be met by varying the temperature of the substrate, T_r , or the disperse particles, T_f .

Let us consider the experimental results in terms of the soliton-based model. Figure 1 presents the plot of the growth rate versus inverse temperature. This plot shows the ranges of low-rate growth in which the films with the best structural quality are obtained. However, it is the soliton-based model that suggests the presence of such ranges. In this model, the temperature of the disperse particles remains high for a finite time after their condensation on a substrate [1]. Apart from other factors, this time depends on whether nonlinear oscillations are initiated in the system. If solitons do not arise, energy is dissipated fast, reevaporation of atoms and molecules from the disperse particles is virtually absent, and the growth rate is high; however, the structural perfection of the prepared films is poor. To the contrary, if solitons are initiated in the system, kinetic energy of the disperse particles remains high for long periods, atoms and molecules reevaporate intensely from the disperse particles, the growth rate is low, and the film structure is perfect due to the high mobility of the disperse particles.

A necessary condition for the initiation of solitons is inequality (1), which seemingly does not suggest the presence of several temperature ranges of epitaxial growth. However, inequality (1) does not take into account that II-VI compounds can crystallize in both cubic and hexagonal structures with essentially different lattice parameters [5]. With allowance made for this fact, the presence of two temperature ranges of epitaxial growth is evident from inequality (1). One range corresponds to the cubic structure; another, to the hexagonal structure.

The experimental results are in agreement with the above reasoning. Two ranges of heteroepitaxial growth are revealed for the CdTe and CdS films. In the first temperature range, single-phase (cubic CdTe and hexagonal CdS) films are grown. In the second temperature range, two-phase films (containing cubic and hexagonal phases) are obtained (see Figs. 2–4). At the same time, only one range of oriented growth is found for gold, which crystallizes only in a cubic structure.

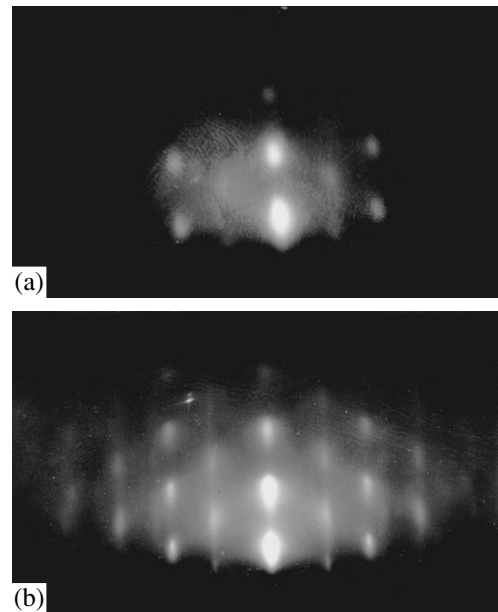


Fig. 4. Representative electron diffraction patterns of the CdS films synthesized under highly nonequilibrium conditions at an incident flux $R = 1.2 \times 10^{18} \text{ cm}^{-2} \text{ s}^{-1}$ and substrate temperatures $T_r =$ (a) 235 and (b) 145 K.

Let us consider now the effect of the incident flux on the temperature dependence of the growth rate in terms of the soliton-based model. First of all, let us recall that we increased the incident flux by raising the sublimation temperature. This means that, as the incident flux increases, its average temperature rises, which, in turn, increases the temperature of the disperse particles. As a result, the lattice parameter of the disperse particles changes, which, according to the soliton-based model [inequality (1)], should shift the range of oriented growth. The experimental data (Fig. 1) confirm this conclusion.

Moreover, the fact that the range of oriented growth shifts to higher temperatures also agrees with the soliton-based model. In terms of this model, the low-temperature boundary of the range of oriented growth corresponds to a certain ratio between lattice parameters of the disperse particles and the substrate, which is achieved at a certain ratio between their temperatures. Consequently, if the temperature of the disperse particles increases (as the incident flux rises), the substrate temperature at which the oriented growth becomes possible should also increase.

The effect of the incident flux on the temperature dependence of the growth rate manifests itself in smoothing of the curves and in the corresponding change in the crystal perfection of the films.

In fact, according to the soliton-based model, the formation of nonlinear waves orienting the disperse particles on the substrate takes a finite time. As the incident flux increases, the rate of condensation of the disperse particles on the substrate also increases, and the nonlinear waves have no time to form. The disperse particles can coalesce before they become best oriented in the potential field of the substrate.

CONCLUSION

Based on the above, we made the following conclusions.

1. The growth of II–VI films under highly nonequilibrium conditions involves processes that allow for the formation of epitaxial structure.
2. The conditions for the epitaxial growth correlate with the conditions for initiation of nonlinear waves predicted by the soliton-based model for heteroepitaxy.
3. The temperature dependences of the growth rate for II–VI films prepared under highly nonequilibrium conditions can be understood in terms of the soliton-based model.

ACKNOWLEDGMENTS

This study was supported by the Russian Foundation for Basic Research, project no. 99-03-32676.

REFERENCES

1. A. P. Belyaev, V. P. Rubets, and I. P. Kalinkin, *Fiz. Tverd. Tela (St. Petersburg)* **39** (2), 382 (1997) [*Phys. Solid State* **39**, 333 (1997)].
2. A. P. Belyaev, V. P. Rubets, and I. P. Kalinkin, *Neorg. Mater.* **34** (3), 281 (1998).
3. A. P. Belyaev, V. P. Rubets, and I. P. Kalinkin, *Fiz. Tekh. Poluprovodn. (St. Petersburg)* **31** (8), 966 (1997) [*Semiconductors* **31**, 823 (1997)].
4. S. A. Kukushkin and A. V. Osipov, *Usp. Fiz. Nauk* **168** (10), 1083 (1998) [*Phys. Usp.* **41**, 983 (1998)].
5. I. P. Kalinkin, V. B. Aleskovskii, and A. V. Simashkevich, *Epitaxial Films of II–VI Compounds* (Leningrad, 1978).

Translated by N. Izyumskaya

ATOMIC STRUCTURE AND NONELECTRONIC PROPERTIES OF SEMICONDUCTORS

Molecular-Dynamics Simulation of Structural Properties of $\text{Ge}_{1-x}\text{Sn}_x$ Substitutional Solid Solutions

V. G. Deibuk* and Yu. G. Korolyuk

Fed'kovich State University, ul. Kotsyubinskogo 2, Chernovtsy, 58012 Ukraine

* e-mail: vdei@chdu.cv.ua

Submitted July 18, 2000; accepted for publication July 26, 2000

Abstract—Structural properties of $\text{Ge}_{1-x}\text{Sn}_x$ substitutional solid solutions were investigated using a molecular-dynamics simulation with the Tersoff three-particle potential. Composition dependences were calculated for pair distribution functions, the total energy of the system, and bond lengths in compositional-disordered alloys. A satisfactory agreement was obtained between the calculated and experimental values of lattice constants. The Vegard law was shown to be obeyed for $x < 0.7$. © 2001 MAIK “Nauka/Interperiodica”.

1. INTRODUCTION

In recent years, many experimental and theoretical studies have been devoted to investigating the physical properties of semiconductors and semimetals with tetrahedral bonds. A search for optoelectronic direct-gap materials on the basis of Group IV semiconductors stimulated the development of new crystal-growing technologies such as molecular-beam epitaxy and laser crystallization. The research efforts follow several basic lines. One of them includes the artificial destruction of the cubic symmetry and combination of states of the lower conduction band at the point Γ (for example, Si–Ge superlattices [1]); the second method consists in growing metastable alloys with a diamond structure and fundamental energy gap at the point Γ (for example, Ge–Sn alloys [2]). Furthermore, the strained $\text{Si}_{1-x}\text{Ge}_x$ and $\text{Si}_{1-x-y}\text{Ge}_x\text{C}_y$ nanostructures on Si [3] have been studied intensively. Nevertheless, many theoretical and experimental investigations of strained layers in the superlattices have shown that they had either an indirect gap or a very weak optical strength oscillator. At the same time, calculations [4] show that, in the range of $0.26 \leq x \leq 0.74$, $\text{Ge}_{1-x}\text{Sn}_x$ becomes the direct-gap alloy, and the laser crystallization made it possible to obtain $\text{Ge}_{0.7}\text{Sn}_{0.3}$ microcrystalline films [2]. Furthermore, the phase diagrams were constructed theoretically and the conditions for obtaining the extended solubility limits for the given system under an external pressure were predicted [5].

The numerical simulation is one way of investigating alloy properties at finite temperatures. In this paper, we report the results of numerical experiments that involve the simulation of the structural properties of the Ge–Sn compositional-disordered substitutional solid solutions with a diamond structure. In these experiments, we used the Tersoff three-particle potential [6],

which is successfully used in studying the structural, dynamic, and thermodynamic properties of many crystals and alloys [7]. The main purpose of this study is to test the chosen model for predicting the structural properties of Ge–Sn solid solutions.

2. DETAILS OF SIMULATION

As the technique for direct simulation at the atomic level, the classical molecular dynamics (MD) requires that the interatomic interaction potentials be known. Among many empirical model potentials, which have been suggested for tetrahedral semiconductors, the Tersoff three-particle potential turned out to be the most successful for investigating many properties of semiconductor compounds [8]. The interatomic potential energy of interaction between two neighboring atoms i and j has the following form [6]:

$$V_{ij} = f_C(r_{ij})[a_{ij}f_R(r_{ij}) + b_{ij}f_A(r_{ij})], \quad (1)$$

where the repulsive and attractive terms are given by

$$f_R(r) = A \exp(-\lambda r), \quad (2)$$

$$f_A(r) = -B \exp(-\mu r), \quad (3)$$

$$f_C(r) = \begin{cases} 1, & r < R, \\ \frac{1}{2} + \frac{1}{2} \cos \left[\frac{\pi(r-R)}{2(S-R)} \right], & R < r < S, \\ 0, & r > S, \end{cases} \quad (4)$$

and b_{ij} is the many-body order parameter describing how the local atomic ordering associated with the presence of other neighboring (k th) atoms influences the

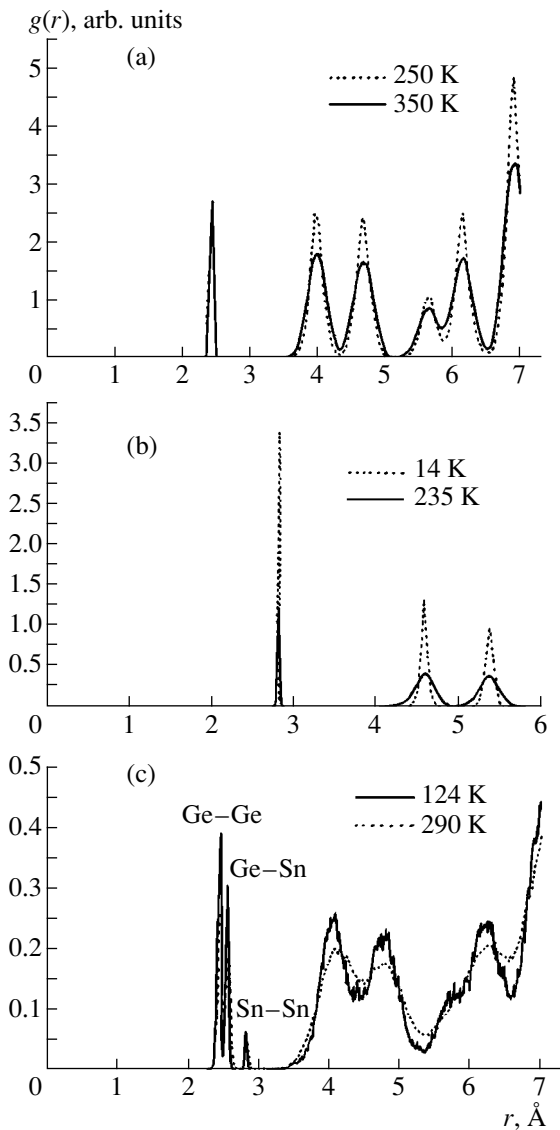


Fig. 1. Binary distribution function $g(r)$ for (a) Ge, (b) Sn, and (c) $\text{Ge}_{0.74}\text{Sn}_{0.26}$.

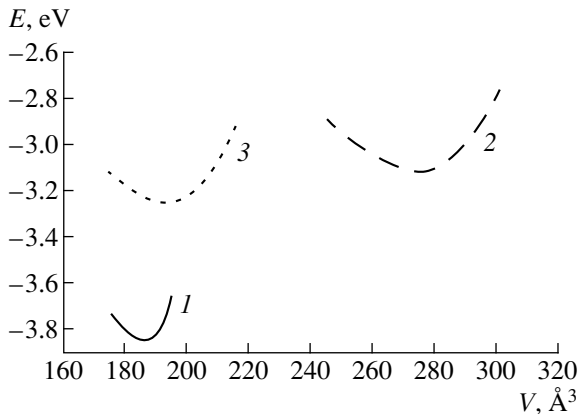


Fig. 2. Total energy E as a function of a volume V for (1) Ge, (2) Sn, and (3) $\text{Ge}_{0.74}\text{Sn}_{0.26}$.

bond-formation energy. This is the multiparticle function of the positions of atoms i, j , and k and has the form

$$b_{ij} = (1 + \beta^n \zeta_{ij}^n)^{-1/2n}, \quad (5)$$

where

$$\zeta_{ij} = \sum_{k(\neq i, j)} f_C(r_{ik}) g(\theta_{ijk}) \exp[\lambda_3^3 (r_{ij} - r_{ik})^3], \quad (6)$$

$$g(\theta) = 1 + \frac{c^2}{d^2} - \frac{c^2}{d^2 + (h - \cos \theta)^2}, \quad (7)$$

$$a_{ij} = (1 + \alpha^n \eta_{ij}^n)^{-1/2n}, \quad (8)$$

$$\eta_{ij} = \sum_{k(\neq i, j)} f_C(r_{ik}) \exp[\lambda_3^3 (r_{ij} - r_{ik})^3], \quad (9)$$

ζ is the effective coordination number; and $g(\theta)$ is a function of the angle between \mathbf{r}_{ij} and \mathbf{r}_{ik} , which is adjusted to stabilize the tetrahedral structure. We note that, for the purpose of simplifying the form of the potential, λ_3 and α were taken to be equal to zero [6] in the calculations. The constants $A, B, n, c, d, h, \lambda, R, S, \beta$, and μ for Ge were taken from [6], and those for Sn were determined for the first time by setting the graytin cohesion energy equal to 3.12 eV per atom [9] (see table).

Our model involves $N = 216$ particles, whose initial positions are specified in the tetrahedral sites of a cell formed by $3 \times 3 \times 3$ unit cells of the diamond type. We used the periodic boundary conditions. The chosen procedure is based on solving the Newton equation set using the fast form of the Verlet algorithm [10], which does not lead to the accumulation of roundoff errors as it is self-starting.

After the system passed to an equilibrium state with a time step $\Delta t = 0.15 \times 10^{-15}$ s, we calculated the pair distribution function $g(r)$ [11] for Ge, Sn, and $\text{Ge}_{0.74}\text{Sn}_{0.26}$ (Fig. 1) at various temperatures. The position of the $g(r)$ first peak determines the distance from the selected lattice site to the first neighboring tetrahedral site, which agrees with experimental data [9]. At the same time, with increasing temperature, the peaks of the pair distribution function broaden somewhat and become slightly displaced, which is indicative of the conservation of the tetrahedral crystalline structure. When the $\text{Ge}_{1-x}\text{Sn}_x$ substitutional solid solutions are formed, the first peak of the pair distribution function splits into three peaks corresponding to the Ge-Ge, Ge-Sn, and Sn-Sn bonds (Fig. 1c), with their intensity being determined by the number of the corresponding bonds in the alloy. Moreover, in the process of simula-

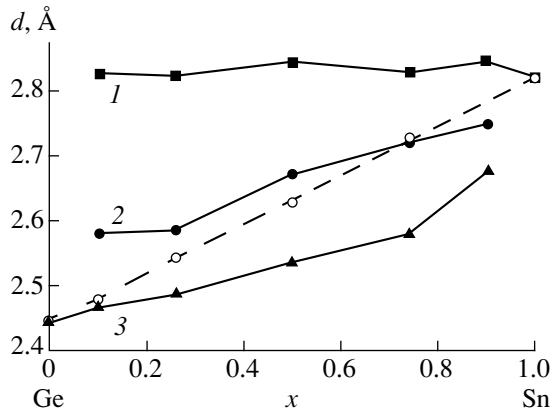


Fig. 3. Bond-length (d) distribution for (1) Sn-Sn; (2) Sn-Ge, and (3) Ge-Ge in the $\text{Ge}_{1-x}\text{Sn}_x$ alloy at 290 K. The dashed line corresponds to the Vegard law.

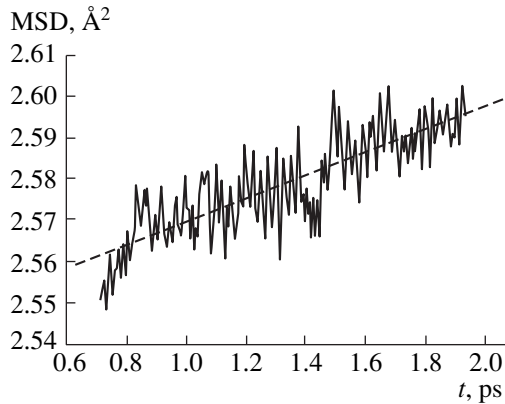


Fig. 4. Mean-square displacements of atoms in the $\text{Ge}_{0.74}\text{Sn}_{0.26}$ solid solution at 290 K.

tion, we controlled the coordination number, which corresponded to the number of the nearest neighbors in this structure. This system behavior is confirmed by the

Parameters of the Tersoff potential for α -Sn and Ge

Parameter	α -Sn	Ge [6]
A , eV	2848	17.69
B , eV	658.62	419.23
λ , Å ⁻¹	2.25	2.4451
μ , Å ⁻¹	1.62	1.7047
β	6.01×10^{-7}	9.01×10^{-7}
n	0.74	0.75627
c	1.4×10^5	1.0643×10^5
d	14.5	15.65
h	-0.502	-0.43884
R , Å	2.8	2.8
S , Å	3.2	3.1

behavior of the system total energy as a function of temperature.

In the course of simulation, the lattice constant a of the solid solution under investigation was determined from the condition for the minimum of total energy E as a function of volume V (Fig. 2). In particular, according to our calculations at temperature $T = 300$ K, $a = 5.659$ Å (the experimental value is 5.657 Å [9]) for Ge and $a = 6.490$ Å (the experimental value is 6.489 Å [9]) for Sn. The molecular-dynamic simulation enabled us to investigate the bond-length distribution in the alloy for the case of varying molar composition. According to the virtual-crystal approximation, the Ge-Sn periodic virtual crystal is described by a mean potential

$$V_{\langle \text{Ge-Sn} \rangle}(\mathbf{r}) = \sum_i v(\mathbf{r} - \mathbf{R}_i), \quad (10)$$

where $v(\mathbf{r}) = [(1-x)v_{\text{Ge}}(\mathbf{r}) + xv_{\text{Sn}}(\mathbf{r})]$, $v_{\text{Ge}}(\mathbf{r})$ and $v_{\text{Sn}}(\mathbf{r})$ are the corresponding atomic potentials; and \mathbf{R}_i is the radius vector of the i th lattice site. In Fig. 3, we show the results of calculations of the distribution of bond lengths d in the alloy at $T = 290$ K. The dashed line represents the virtual-crystal approximation, and the dots correspond to the simulation results. The data obtained show that the Vegard law is reasonably well obeyed in the region of concentrations $x < 0.7$; at the same time, the deviations from this law take place for $0.7 < x < 1.0$.

The mean-square displacements of atoms can be readily calculated from the relationship

$$\langle r^2(t) \rangle = \frac{1}{N} \sum_{i=1}^N \langle |\mathbf{r}_i(t) - \mathbf{r}_i(0)|^2 \rangle. \quad (11)$$

The results of simulation of the time variation in the mean-square displacements are shown in Fig. 4, which indicates that the motion of solid-solution atoms is diffusive. However, the migration of atoms increases in the melting region, which is related to the diffusion effects.

Thus, a simple empirical three-particle potential in combination with the molecular-dynamics method makes it possible to correctly simulate the structural properties of a Ge-Sn compositional-disordered substitutional solid solution. It also makes it possible to gain a better insight into the basic physical properties of new promising semiconductor systems.

REFERENCES

1. F. F. Sizov, Yu. N. Kozyrev, V. P. Klad'ko, *et al.*, *Fiz. Tekh. Poluprovodn.* (St. Petersburg) **31**, 922 (1997) [*Semiconductors* **31**, 786 (1997)].
2. S. Oguz, W. Paul, T. F. Deutsh, *et al.*, *Appl. Phys. Lett.* **43**, 848 (1983).

3. F. Krasil'nik and A. V. Novikov, *Usp. Fiz. Nauk* **170**, 338 (2000).
4. K. A. Mäder, A. Baldereschi, and H. von Känel, *Solid State Commun.* **69**, 1123 (1989).
5. T. Soma and H. Matsuo Kagaya, *Phys. Status Solidi B* **147**, 109 (1988).
6. J. Tersoff, *Phys. Rev. B* **39**, 5566 (1989).
7. D. W. Brenner, *Phys. Status Solidi B* **217**, 23 (2000).
8. F. Benkabou, P. Becker, M. Certier, and H. Aourag, *Phys. Status Solidi B* **209**, 223 (1998).
9. A. Chen and A. Sher, *Semiconductor Alloys: Physics and Material Engineering* (Plenum, New York, 1995).
10. H. Gould and J. Tobochnik, in *An Introduction to Computer Simulation Methods: Applications to Physical Systems* (Addison-Wesley, Reading, 1988; Mir, Moscow, 1990), Part 1.
11. J. M. Ziman, *Models of Disorder: The Theoretical Physics of Homogeneously Disordered Systems* (Cambridge Univ. Press, Cambridge, 1979; Mir, Moscow, 1982).

Translated by V. Bukhanov

ATOMIC STRUCTURE AND NONELECTRONIC PROPERTIES OF SEMICONDUCTORS

Low-Temperature Diffusion of Indium into Germanium Assisted by Atomic Hydrogen

V. M. Matyushin

Zaporozh'e State Technical University, Zaporozh'e, 69063 Ukraine

Submitted June 16, 2000; accepted for publication August 2, 2000

Abstract—Indium diffusion stimulated by an energy release due to molecule formation from atomic hydrogen is studied. Germanium *n*-type crystals with a deposited indium film 0.2–0.3 μm thick were exposed to atomic hydrogen over different periods of time (up to 2×10^4 s) at approximately room temperature. Indium diffusion into germanium was studied using laser mass spectrometry and X-ray structural analysis, and also by measuring the transmission spectra in infrared region of the spectrum. Based on the data obtained experimentally, mechanisms of stimulated heterodiffusion and accompanying processes are proposed. © 2001 MAIK "Nauka/Interperiodica".

INTRODUCTION

Diffusion is considered as one of the most widely used present-day methods of semiconductor technology. However, the reduction of diffusion time to a practically acceptable value implies the use of high temperatures (especially, when electrically active dopants are introduced). This can entail a number of negative consequences, such as the considerable redistribution of previously introduced impurities, parasitic film growth, deep background impurity diffusion, and so on. Moreover, at high temperatures, the control of local introduction of impurities into the crystal becomes considerably more complicated. All these circumstances increase the spread of the electrical parameters of the semiconductor crystal and structures based on it, decrease their stability, and reduce the device yield. Therefore, a decrease in the temperature of heterodiffusion is of considerable scientific and practical interest.

An effective reduction of the overall temperature of a processed structure can be attained by the local stimulation of diffusion in the relevant areas of a semiconductor crystal. For this purpose, the energy of an exothermic reaction on the surface of the crystal, which acts as a catalyst, can be used. The most adequate reaction here seems to be molecule formation from atomic hydrogen, since this yields a comparatively large amount of energy (4.5 eV per single recombination event [1]). For a sufficient concentration of atomic hydrogen in the gas phase, the diffusion can be effectively stimulated on the surface and at the surface layer of a semiconductor crystal.

The low-temperature diffusion of Cu, Ni, and Au into Ge stimulated by atomic hydrogen was studied in [2–4]. However, the diffusion of In into Ge is of primary practical interest, since In is an electrically active impurity that produces a very shallow acceptor level in

Ge band gap, which is convenient for *p*-region formation [5].

EXPERIMENTAL

In order to obtain atomic hydrogen, the molecules of hydrogen were dissociated in high-frequency discharge plasma. The molecular hydrogen was extracted by electrolysis from KOH solution (20%) in distilled water. After that, the hydrogen passed through a fore chamber for intercepting the KOH drops, a desiccating column (filled with granulated KOH alkali) and entered the working chamber. Calorimetric measurements of atomic hydrogen concentration in the reaction volume [6] yielded $5 \times 10^{20} \text{ m}^{-3}$ of hydrogen at a pressure of 15–20 Pa.

The samples were placed in the working chamber at a distance of 0.25 m from the discharge area, thus keeping out hydroxyl and hydrogen ions [7]. Temperature measurements were performed using a Chromel–CopeI thermocouple fixed at the sample surface. Upon being exposed to H atoms, the samples were heated due to the energy of recombination only, and their temperature did not exceed $T = 330 \text{ K}$.

The substrates were *n*-Ge crystals with (111) surface orientation, resistivity $\rho = 1.5 \times 10^5 \Omega \text{ m}$, and a dislocation density of 10^6 m^{-2} . Indium films were deposited by thermal evaporation in vacuum in a VUP-4 system. The total film thickness amounted to 0.2–0.3 μm . During deposition of In, the sample temperature did not exceed 400 K. At higher temperatures ($T > 400 \text{ K}$), a continuous indium film was not obtained; instead, indium gathered in drops because of its low melting temperature (429 K). The film thickness was measured using a MAR-2 X-ray microanalyzer. The surface condition was examined using a MIM-7 500-power microscope.

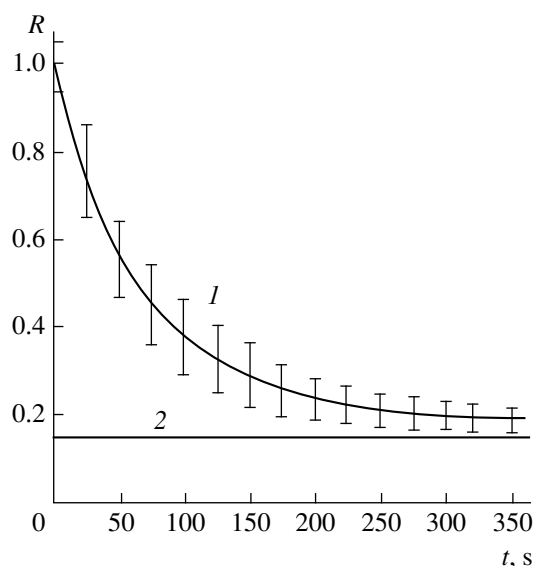


Fig. 1. The diffuse reflectivity R of the germanium crystal surface (1) with the indium film and (2) without indium film versus the time of its exposure to atomic hydrogen t .

To test the uniformity of the indium film on the germanium crystal surface, a diffuse reflection of the laser beam from the surface was monitored. A helium–neon (He–Ne) laser beam with a wavelength of $\lambda = 0.63 \mu\text{m}$ was focused onto the surface at an angle of 30° to the normal. The intensity of the diffuse scattered light depended on the surface relief. The reflected light was focused with a lens onto the detecting area of a FÉU-79 photomultiplier. A useful signal from FÉU-79 was fed to a digital current-measuring device. Since the indium film surface was considerably rougher than that of the polished germanium crystals, the method described above made it possible to monitor the surface condition of samples subjected to atomic hydrogen over different periods of time.

Current–voltage (I – V) characteristics of the samples were measured using an L2-56 unit.

The impurity distribution in the germanium crystal was studied by laser mass spectrometry. We used an ÉMAL-2 system for laser sputtering and the subsequent electrical and magnetic separation of ions. Indium concentration was determined from the intensity of the corresponding line in the mass spectrum. An X-ray structural analysis of the germanium crystal structure was performed using a Dron system with the monochromatic radiation of copper. The concentration of electrically active indium atoms (atoms residing at the lattice sites) was evaluated from measuring the resistivity ρ by a single-probe method [8] and comparing ρ in the indium-doped surface layers with that in bulk germanium (with the surface layer removed in a mixture of $\text{HNO}_3 : \text{HF} : \text{CH}_3\text{COOH} = 2 : 3 : 6$). The concentration was derived from the resistivity ρ according to the nomogram reported in [9]. The con-

ductivity type of the doped layer was determined from the Hall effect measurements performed with a compensating circuit using a stationary current and a constant magnetic field [8].

The transmission spectra of samples in the infrared (IR) region of the spectrum were measured using an IKS-21 spectrometer.

RESULTS AND DISCUSSION

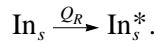
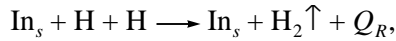
Under the effect of the energy generated during the adsorption of H atoms and molecule formation, indium films were sputtered. Indium films were removed faster (within 100–300 s) compared to copper, nickel or gold film sputtering [2–4]. This is due to the formation of volatile compounds of indium with hydrogen [10]. The remaining indium collected on the germanium surface and formed drops 100–200 μm in diameter. Figure 1 shows the diffuse reflectivity R of the samples exposed to atomic hydrogen for different periods of time t . It is evident that, as t grows, R rapidly decreases and approaches that of the germanium surface without deposited indium.

Along with the film sputtering, indium was observed to penetrate from the surface into the surface and bulk layers of germanium crystals. Profiles of indium concentration C in germanium crystals after their exposure to atomic hydrogen for different periods of time are shown in Fig. 2. Curve 1 corresponds to a Ge sample with the In film subsequently etched off in HNO_3 . It is clearly seen that, during film deposition, indium diffusion into germanium is not observed. As a result of the exposure of samples for 1800 s to atomic hydrogen, In atoms penetrate into Ge (Fig. 2, curve 2). After further exposure, simultaneously with indium penetration into germanium, there also occurs sputtering of the indium-doped germanium layer, which leads to a decrease in indium concentration in the surface layer. However, in the deeper layers, In concentration increases due to the drive-in of In in bulk Ge (Fig. 2, curve 3). The prolonged exposure to atomic H (at $t > 2 \times 10^4$ s) leads to the complete sputtering of the In-doped Ge layer, with no In atoms being detected in Ge.

The Hall effect measurement of the treated samples indicated that In-doped layers changed the conduction from n - to p -type. From the resistivity measurements, the concentration of active In (In atoms residing at Ge lattice sites) in the surface region is found to be approximately 10^{23}m^{-3} .

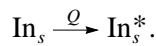
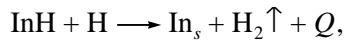
Based on the experimental results presented above, it seems reasonable that In introduction in Ge under the action of atomic H can be treated as a two-stage process: the penetration of In into the surface layer and its subsequent diffusion in the Ge bulk. The penetration of indium atoms is directly assisted by the energy released in the proceeding chemical reactions. Since the In film is sputtered at an early stage of exposure to atomic H (100–300 s), the main sources of In drops remain on the

surface. Indium atoms sputtered on the Ge surface act as recombination centers for H atoms and acquire a part of the released recombination energy Q_R :



Here, In_s and In_s^* correspond to the unexcited and excited states of In atoms located on the Ge surface, respectively.

Another source of indium is presented by InH molecules. When adsorbed on a germanium surface, they can react to produce atomic indium:



The energy released Q is expressed as

$$Q = Q_R - Q_1,$$

where Q_1 is the bonding energy of In–H (~1 eV [10]).

During the chemical reaction of hydrogen atoms, the energy release takes approximately 10^{-10} s (time of exchange interaction). Therefore, the release and dissipation of the released energy are consistent with the θ -flare concept [11]. In view of the fact that, in the vicinity of the θ -flare, the temperature is very high (about the fusion temperature), the generation of defects and multiphonon scattering increase in importance. The formation of defects, specifically vacancies, and phonon effects facilitate the penetration of surface In atoms into the surface layer. Estimations of mean free paths of the longitudinal (L_{\parallel}) and transverse (L_{\perp}) phonons showed that [12] $L_{\parallel} \gg L_{\perp}$ and $L_{\parallel} \sim 10$ nm, indicating that the most effective H-stimulated phonon interaction takes place at a depth comparable with that of the maximum concentration at the midstage of H diffusion stimulation (Fig. 1, curve 2).

It is known [5, 13] that, in the course of thermomodification, In atoms occupy the Ge lattice sites and diffuse mostly via the vacancy mechanism. An effective vacancy generation in the active zone is assisted by atomic H, which leads to an enhanced In diffusion via vacancies. In our case, however, indium atoms resided not only in vacancies, but in interstices as well. This is in line with the results of X-ray structural analysis, which has revealed the presence of deformation in the surface layer of Ge doped by In under the action of atomic H. The maximum strain of the crystal lattice corresponds to curve 2 (Fig. 2), i.e., to the conditions of atomic H treatment when the In concentration in the Ge surface layer is maximum. This situation most closely corresponds to the assumption that diffusion occurs through the surface into a semi-infinite crystal with zero initial concentration and a constant diffusant concentration on the surface. The coefficient of indium dif-

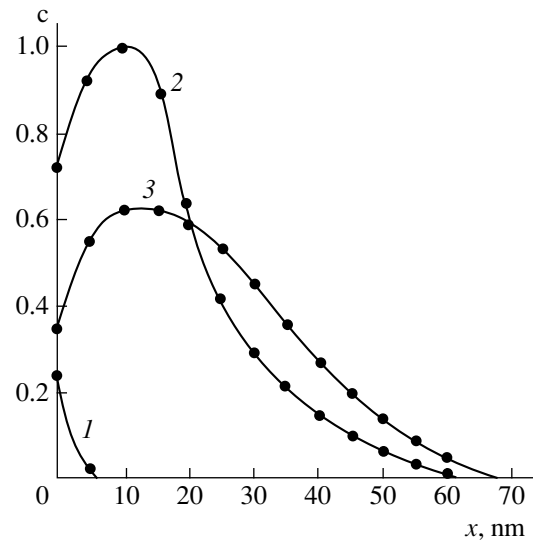


Fig. 2. Depth profile (along x-axis) of indium concentration in germanium (1) untreated samples and after the exposure to hydrogen for (2) $t = 1800$ and (3) 3600 s.

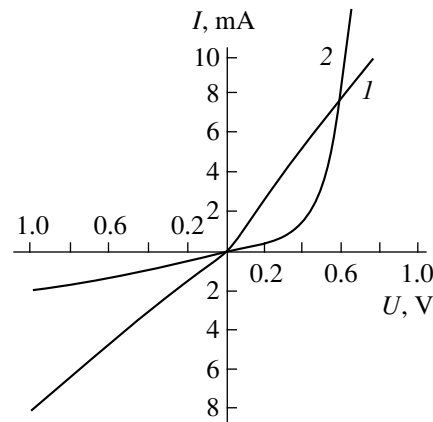


Fig. 3. The I - V characteristic of (1) untreated sample and (2) after the exposure to hydrogen for 1800 s.

fusion into germanium calculated for this case is approximately 1.4×10^{-19} m²/s, which corresponds to the thermal diffusion of In into Ge at $T = 910$ K, although the temperature of samples in our experiment did not exceed 330 K.

If indium is localized at the lattice sites of germanium, it acts as an acceptor impurity; i.e., it forms p -type regions [5, 11]. It is evident, therefore, that, in our case, in the initial n -type Ge crystals, In deposition and H treatment lead to the formation of p - n junctions. Figure 3 shows the I - V characteristic of In-doped Ge sample exposed to atomic H for $t = 1800$ s. The “Softness” of this characteristic is related to the considerable leakage current through the unprotected ends of the crystal.

The transmission spectra measured in the wavelength range $\lambda = 5\text{--}10\ \mu\text{m}$ indicate that In-doped Ge samples exposed to atomic H are noticeably absorptive, whereas the initial Ge, as well as Ge samples after the In film etching in HNO_3 , are transparent in this spectral range. Maximum absorption is observed at 0.2 eV, which corresponds to the energy level of $E_v + 0.2\ \text{eV}$ introduced by a self-interstitial atom into the band gap of a heavily doped germanium crystal [14]. This means that, as In atoms penetrate into the surface Ge layer during surface treatment with H, they can displace the Ge atoms from the lattice sites into the interstices.

CONCLUSION

The effect of atomic hydrogen causes rapid removal of the indium film from the germanium surface as a result of the formation of volatile compounds of indium with hydrogen. This effectively stimulates In diffusion into the surface Ge layer at a temperature close to 295 K. Indium penetrates into the Ge "active" region ($\sim 10\ \text{nm}$), where the generation of defects occurs and multiphonon scattering of energy released during the H to H_2 recombination takes place. Furthermore, indium atoms can reside both at the sites and in interstices of the germanium crystal lattice.

Low-temperature chemistimulated diffusion of indium into germanium results in $p\text{--}n$ junction formation, which is testified by Hall-effect study of the surface region.

Thus, the low-temperature H-assisted heterodiffusion can be used with good results in electronic technology for introducing a specified amount of acceptor impurity into germanium without additional heating.

REFERENCES

1. V. A. Lavrenko, *Recombination of Hydrogen Atoms on Solid Surfaces* (Naukova Dumka, Kiev, 1973).
2. V. M. Matyushin, V. P. Shapovalov, and A. R. Koshman, *Int. J. Hydrogen Energy* **22** (2/3), 259 (1997).
3. V. M. Matyushin, V. I. Lishchenko, and A. N. Gorban', *Ukr. Fiz. Zh.* **32** (9), 1407 (1997).
4. V. M. Matyushin, *Zh. Tekh. Fiz.* **69** (7), 73 (1999) [*Tech. Phys.* **44**, 804 (1999)].
5. B. I. Boltaks, *Diffusion in Semiconductors* (Fizmatgiz, Moscow, 1961; Academic, New York, 1963).
6. V. A. Sokolov and A. N. Gorban', *Luminescence and Adsorption* (Nauka, Moscow, 1969).
7. F. F. Vol'kenshtein, A. N. Gorban', and V. A. Sokolov, *Radical-Recombination Luminescence of Semiconductors* (Nauka, Moscow, 1976).
8. L. P. Pavlov, *Methods for Determining Key Parameters of Semiconducting Materials* (Vyssh. Shkola, Moscow, 1975).
9. A. I. Kurnosov and V. V. Yudin, *Production Technology of Semiconductor Devices* (Vyssh. Shkola, Moscow, 1974).
10. *Interaction of Hydrogen with Metals: A Handbook*, Ed. by A. P. Zakharov (Nauka, Moscow, 1987).
11. B. I. Mogilevskii and A. F. Chudnovskii, *Thermal Conductivity of Semiconductors* (Nauka, Moscow, 1972).
12. C. T. Glassbrenner and G. A. Sluck, *Phys. Rev.* **134** (4), 1058 (1964).
13. W. C. Dunlap, *Phys. Rev.* **94** (8), 1931 (1954).
14. M. W. Valenta and C. Ramasastry, *Phys. Rev.* **106** (1), 73 (1957).

Translated by A. Sidorova-Biryukova

ATOMIC STRUCTURE AND NONELECTRONIC PROPERTIES OF SEMICONDUCTORS

A New Magnetic Semiconductor $\text{Cd}_{1-x}\text{Mn}_x\text{GeP}_2$

G. A. Medvedkin^{1,2}, T. Ishibashi², T. Nishi², and K. Sato²

¹ *Ioffe Physicotechnical Institute, Russian Academy of Sciences, Politekhnicheskaya ul. 26,
St. Petersburg, 194021 Russia*

² *Faculty of Technology, Tokyo University of Agriculture and Technology, 2-24-16 Nakacho, Koganei,
Tokyo 184-8588, Japan*

Submitted August 8, 2000; accepted for publication August 16, 2000

Abstract—A new semiconductor material, which comprises a solid solution of a ternary diamond-like semiconductor and transition element Mn, was grown and investigated. According to X-ray diffraction data, the crystal structure of the material is similar to that of the CdGeP_2 host substance with a chalcopyrite-type crystal structure. The interplanar distances and the unit cell parameter decrease with an increase in Mn content: $a = 5.741 \text{ \AA} \rightarrow 5.710 \text{ \AA} \rightarrow 5.695 \text{ \AA}$ in the series of $\text{CdGeP}_2 \rightarrow \text{Cd}_{1-x}\text{Mn}_x\text{GeP}_2 \rightarrow \text{Cd}_{1-y}\text{Mn}_y\text{GeP}_2$ compounds ($x < y$). The surface composition and in-depth concentration profiles for elements of a Cd–Mn–Ge–P quaternary system were investigated using electron microscopy and energy dispersive X-ray spectroscopy. The molecular concentration ratio for Mn and Cd at a depth of $0.4 \mu\text{m}$ is $\text{Mn}/\text{Cd} = 0.2$. © 2001 MAIK “Nauka/Interperiodica”.

1. INTRODUCTION

A ternary semiconductor family with a general formula II-IV-V_2 was obtained in the form of single crystals and has been investigated rather intensively for the last 40 years. This family was predicted in the earlier papers of Folberth and Goryunova [1, 2] as a group of crystal-chemistry analogs to the III–V binary compounds. Some compounds of this family (ZnGeP_2 , CdGeAs_2) are promising due to good nonlinear optic characteristics, others (CdSnP_2 , CdGeP_2 , CdSiAs_2) due to their polarization-optics and emission properties as well as high photosensitivity and a wide range of possibilities in heteroepitaxy of solid solutions with binary compounds (GaAs , InP) [3–5].

A Group II element, for instance, Cd or Zn (metals of the IIB Subgroup), exhibits its usual valence 2+ in the II-IV-V_2 semiconductors. It is known that a series of elements of the periodic table can exhibit a valence differing from the number of the group. For example, the transition *d*-metal Mn exhibits a valence of 2+ and 3+ in solid solutions with II–VI binary compounds and III–V binary compounds, respectively. In addition, Mn can exhibit a higher valence (up to 7+) in non-diamond-like oxides, which possess no semiconductor properties. In recent years, considerable attention was paid to dilute magnetic semiconductors based on traditional binary semiconductors II–VI and III–V. As of now, the CdMnTe and GaMnAs ternary solid solutions with magnetic properties are being extensively investigated. However, up to now, Mn has not been considered as a promising constituent of solid solutions with II-IV-V_2 ternary compounds. Material with a low content of Mn dopant exhibited no magnetic or other properties of any value [3]. Mn-containing compounds with a similar

chemical formula II-IV-V_2 were not predicted in early papers. For this reason, no adequate efforts were undertaken in order to obtain these materials. However, according to recent theoretical investigations, a dilute magnetic semiconductor can exhibit ferromagnetic properties due to the double exchange mechanism [6]. For example, the Mn-containing ZnO binary compound exhibits ferromagnetic or antiferromagnetic ordering due to the effect of codoping, i.e., combined doping with the acceptors/donors and a magnetic element. As for II-IV-V_2 ternary semiconductor compounds, the effect of codoping with intrinsic point defects is determined by the existence of two types of cations. Because of this, we focused our efforts on the Mn-substituted CdGeP_2 compound in search of an earlier unknown dilute magnetic semiconductor.

This study is devoted to preparation and investigation of the microstructure properties and unit cell parameters of a new semiconductor material found in a Cd–Mn–Ge–P system.

2. EXPERIMENTAL

In order to obtain the CdMnGeP_2 solid solution, we used a solid-state chemical reaction technique. The single-crystal CdGeP_2 was used as a host material. The vacuum deposition of the Mn layer and the subsequent reaction accompanied by Mn diffusion into the substrate were carried out in a vacuum chamber with a molecular-beam epitaxy setup (Eiko Engineering, Japan). The residual pressure in the chamber was about 1.4×10^{-8} Torr. Specific technological parameters of the process (time, rate, and temperature) will be described elsewhere. The surface quality of the initial substrate and modified sur-

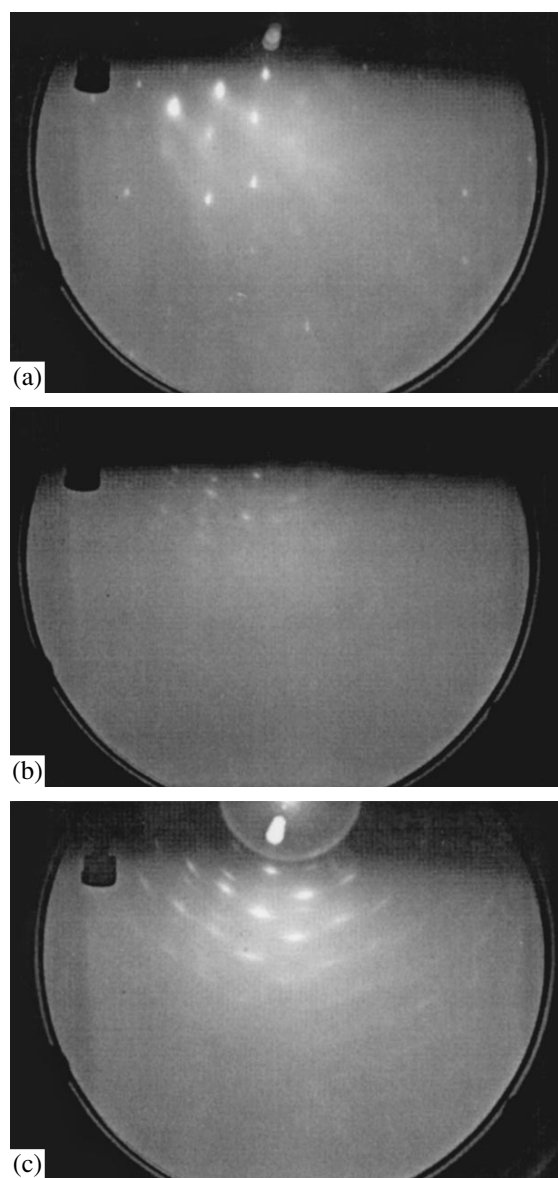


Fig. 1. RHEED patterns for different stages in preparing the $\text{Cd}_{1-x}\text{Mn}_x\text{GeP}_2$ layer on the CdGeP_2 crystal, with a [111] direction. (a) Initial surface, (b) the surface after molecular-beam deposition of the Mn layer, and (c) the surface after completing the solid-state chemical reaction.

face for each stage of the technological process was monitored by a reflection high-energy electron diffraction (RHEED) technique. Microstructural investigations of the surface and cleaved surface of the structure were investigated using an energy dispersive X-ray analysis (EDX) and field-emission scanning electron microscopy (FE-SEM). The investigations were carried out using a Hitachi S-4500 electron microscope with an EMAX-577OW accessory and an S782XI Si detecting crystal (Horiba Ltd.) with a spectral resolution of 144 eV. X-ray diffraction measurements were carried out using Rigaku RAD-IIC and Rigaku RAD-B (InP

crystal-monochromator) setups. The orientation of the crystal was also confirmed by the measurements of the Laue X-ray diffraction patterns on a Rigaku R-AXIS X-ray diffraction setup. Diffraction investigations were carried out at various X-ray radiation intensities (CuK_α , Ni filter) in order to vary the absorption depth in the layer and substrate.

3. RESULTS AND DISCUSSION

The RHEED patterns of the initial CdGeP_2 surface oriented close to (112) and the same surface subsequent to the Mn layer deposition before and after the solid-state reaction are shown in Fig. 1. The high quality of the substrate-crystal surface is evident from Fig. 1a. Deposition of the Mn layer leads to the disappearance of single-crystal type atomic ordering (Fig. 1b). On completing the reaction, the layer obtained has a uniform surface microstructure with a specific texture (Fig. 1c).

The thickness and chemical composition of the layers obtained for the CdMnGeP_2 solid solution were monitored using the EDX and FE-SEM methods. The typical EDX surface spectrum is shown in Fig. 2. The component ratio was calculated automatically with regard to the background noise (shown by the dashed line in Fig. 2) and using standard samples. Investigation of a cleaved cross section of the sample yielded information about the component distribution over the sample depth. The concentration profiles for elements involved in the reaction are shown in Fig. 3. It can be seen that the total concentration of $\text{Cd} + \text{Ge} + \text{P}$ decays near the surface, while the Mn concentration increases. Assuming that Mn primarily replaces Cd, we found that the concentration ratio Mn/Cd at the surface reached 53.4%. The possibility of Mn substitution for other atomic sites (Ge and P) is much lower, and the low content of the GeP phase on the surface also confirms our assumption that $\text{Mn} \rightarrow \text{Mn}_{\text{Cd}}$ is a major substitution process. The Mn concentration decays rather rapidly, and even at a depth of $0.6 \mu\text{m}$ the Mn/Cd ratio is 12.7%, and at a depth of $2.5 \mu\text{m}$ this ratio is 0.9%. The Mn concentration profile can be described by an exponential decay

$$C = C_0 + A \exp(-x/t),$$

where C_0 is the Mn background concentration, which was taken to be equal to zero (see experimental data in Fig. 3 for $d > 10 \mu\text{m}$); A is a constant, which has the meaning of the limiting concentration on the surface; and t is the effective thickness, over which the limiting concentration decays by a factor of e .

The X-ray diffraction measurements of the crystals demonstrated that the $\text{Cd}_{1-x}\text{Mn}_x\text{GeP}_2$ layer grown had a crystal structure similar to that of CdGeP_2 . No other phases were found except for the GeP phase that apparently existed in the sample. However, its concentration was much lower than that of the two major phases. The

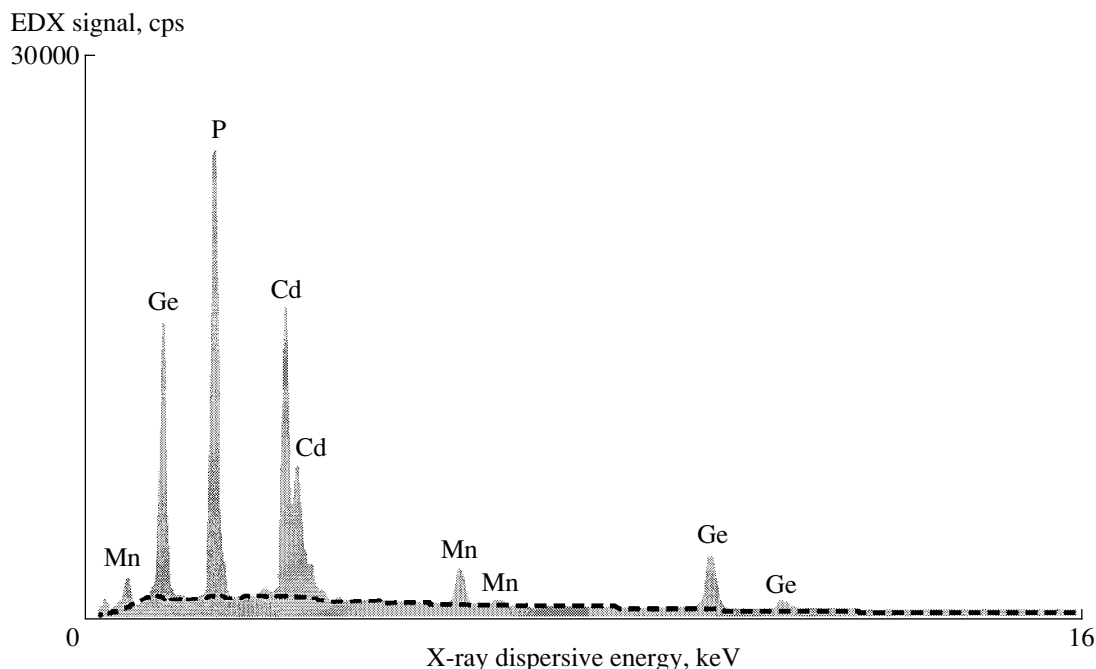


Fig. 2. X-ray energy dispersion spectrum for the $\text{Cd}_{1-x}\text{Mn}_x\text{GeP}_2$ sample. The chemical elements analyzed are indicated at the corresponding peaks. No other elements were observed.

$2\theta/\theta$ spectrum for the experimental conditions of the X-ray dominant absorption in the layer is shown in Fig. 4. The existence of diffraction reflections of four orders is indicative of the high quality of the crystal and the layer. The ratio of corresponding interplanar spacings is $d_1 : d_2 : d_3 : d_4 = 1 : 2 : 3 : 4$ and the ratio of peak (integrated) intensities for these four reflections is $16 : 7 : 3 : 1$ ($7.4 : 3.9 : 1.4 : 1$).

The major peak for the (112) reflection as well as for reflections of higher orders (244), (366), and (488) is shifted to larger 2θ angles compared to the CdGeP_2 substrate. This shift is indicative of a smaller unit-cell parameter for the layers obtained. Actually, from the estimation of the covalent radii for Cd and Mn (1.405 and 1.17 Å), we could expect a decrease in interplanar spacings for the solid solution with an increase in the Mn concentration. The unit-cell parameters were calculated assuming that the crystal structures are similar for CdGeP_2 and CdMnGeP_2 . The following expression was used: $a = d\sqrt{2}/\cos\vartheta_{112}$, where $d = n\lambda/2\sin\theta$ is the interplanar spacing, and $\vartheta_{112} = 37.0^\circ$ is the angle between the tetragonal axis and the (112) plane in the CdGeP_2 crystal. The results obtained for two samples with different compositions are indicative of a decrease in the unit cell parameter with an increase in the Mn concentration, namely, $a = 5.741 \text{ \AA} \rightarrow 5.710 \text{ \AA} \rightarrow 5.695 \text{ \AA}$ for the series $\text{CdGeP}_2 \rightarrow \text{Cd}_{1-x}\text{Mn}_x\text{GeP}_2 \rightarrow \text{Cd}_{1-y}\text{Mn}_y\text{GeP}_2$ ($x < y$). Thus, the $\text{Cd}_{1-x}\text{Mn}_x\text{GeP}_2$ layer comprises a single crystal phase (excluding a thin tex-

ured surface layer) with a crystal structure similar to that of chalcopyrite. We note that the thin textured layer ($t < 0.1 \mu\text{m}$) can be removed easily in an adequate chemical etchant, for example, in Br_2/MeOH . The single-crystal layer with a high Mn content is thereupon conserved.

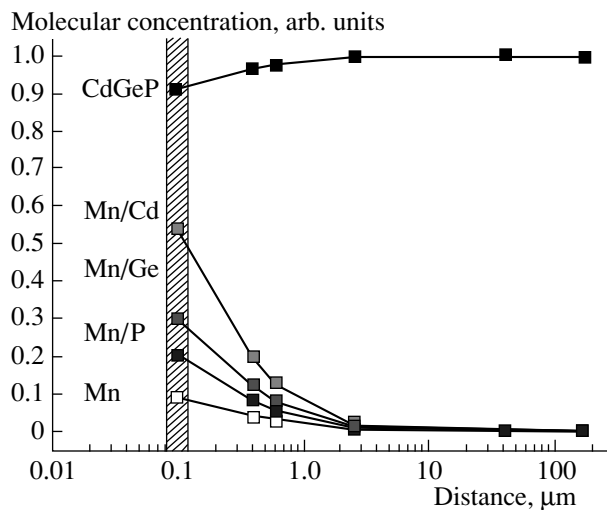


Fig. 3. Concentration profiles for chemical elements in the $\text{CdGeP}_2/\text{CdMnGeP}_2$. The CdGeP notation corresponds to the total concentration of three elements. The sample surface is arbitrarily shown by a hatched band.

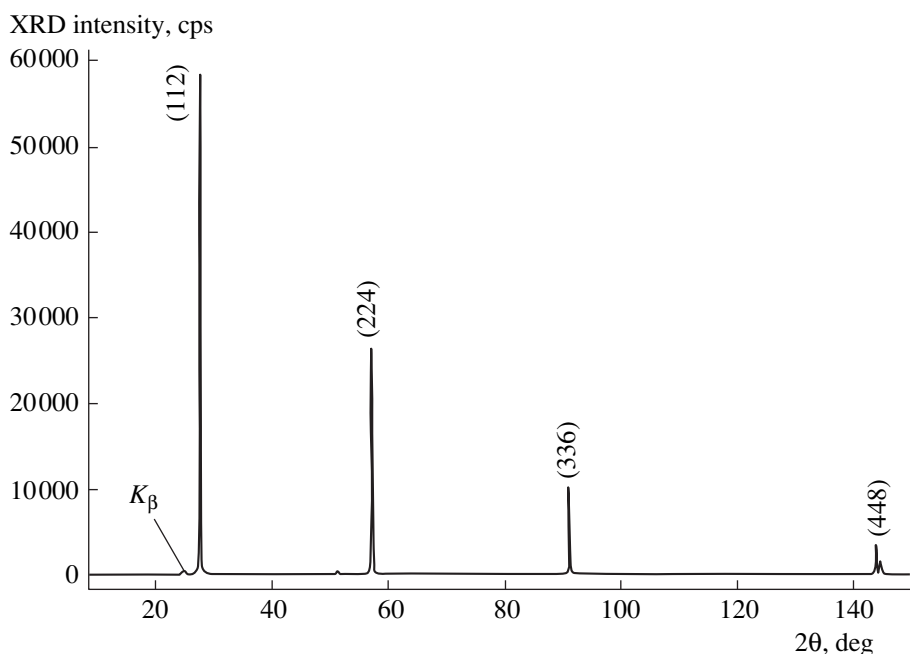


Fig. 4. X-ray diffraction spectrum for 2θ - $2\theta/\theta$ scanning. Crystal orientation (112), temperature $T = 300$ K. Reflection peaks of all four orders for $\text{Cd}_{1-x}\text{Mn}_x\text{GeP}_2$ are shifted in relation to CdGeP_2 substrate to larger angles.

The measurement of the photoluminescence spectra demonstrates that the major spectral peak is shifted to the near-ultraviolet range. This result indicates that the new $\text{Cd}_{1-x}\text{Mn}_x\text{GeP}_2$ material on the surface of the crystal has a band gap more than two times larger ($E_g > 3.5$ eV) than that for CdGeP_2 ($E_g = 1.7$ eV). Magnetization of the samples investigated was also detected, with the shape of the hysteresis loop being characteristic of ferromagnets. The saturation magnetic field was $H_S = 2$ kOe, and the coercivity H_C was about 0.5 kOe at room temperature. The measurement of the temperature dependence of magnetization yielded a Curie temperature of $T_C = 320$ K, which is a record value for diamond-like semiconductors [7, 8]. These and other properties of the new magnetic semiconductor will be described in detail elsewhere.

4. CONCLUSION

The chemical composition, microstructure, and crystal-chemistry properties of the new $\text{Cd}_{1-x}\text{Mn}_x\text{GeP}_2$ magnetic semiconductor were investigated. It was demonstrated that the formation of new semiconductor phases with a crystalline structure similar to that of chalcopyrite is possible in the II-IV-V₂ ternary semiconductor family. The layer of the $\text{Cd}_{1-x}\text{Mn}_x\text{GeP}_2$ solid solution comprises a single crystal with a unit-cell parameter smaller than that of CdGeP_2 .

ACKNOWLEDGMENTS

This study was supported by the Japanese Foundation for the Promotion of Science (JSPS, Tokyo). We thank M.E. Boiko for his productive participation in the discussion of the X-ray diffraction measurements.

REFERENCES

1. O. G. Folberth, BRG Patent No. 1.044.980, kl. 21g 11/02 (November 14, 1955).
2. N. A. Goryunova, *Compound Diamond-Like Semiconductors* (Sov. Radio, Moscow, 1968).
3. Landolt-Börnstein: *Semiconductors: Physics of Ternary Compounds*, Ed. by O. Madelung (Springer-Verlag, Berlin, 1985), vol. 17h.
4. G. A. Medvedkin, Yu. V. Rud', and M. A. Tairov, *Semiconductor Crystals for Linearly Polarized Radiation Photodetectors* (FAN, Tashkent, 1992).
5. *Abstracts 12th International Conference on Ternary and Multinary Compounds, ICTMC-12, Taiwan, 2000*, Special Issue; Jpn. J. Appl. Phys. (2000) (in press).
6. K. Sato and H. Karayama-Yoshida, Jpn. J. Appl. Phys. **39**, L555 (2000).
7. G. A. Medvedkin, T. Ishibashi, T. Nishi, *et al.*, Jpn. J. Appl. Phys. **39**, L949 (2000).
8. K. Sato, G. A. Medvedkin, and T. Ishibashi, in *Proceedings of the International Conference on Physics and Applications of Spin-Related Phenomena in Semiconductors, PASP 2000, Sendai, Japan, 2000*.

Translated by N. Korovin

**ELECTRONIC AND OPTICAL PROPERTIES
OF SEMICONDUCTORS**

Temperature Dependence of a Magnetoresistance Effect in the Films of Ferromagnetic Semiconductors Based on Oxides of Rare-Earth Elements

V. F. Kabanov, S. A. Karasev, and Ya. G. Fedorenko*

Saratov State University, Universitetskaya ul. 42, Saratov, 410026 Russia

* e-mail: fedorenkoyg@info.sgu.ru

Submitted June 8, 2000; accepted for publication July 26, 2000

Abstract—A temperature dependence of a positive magnetoresistance effect for films of certain oxides of rare-earth elements (Gd, Eu, and a Eu–Sm solid solution) close to the Curie temperature was considered and analyzed. It was demonstrated that the temperature dependence of the effect and the effect sign and magnitude are determined by the dependence of a magnetic moment for a magnetic cluster on both an external magnetic field strength and film parameters. These are the spin of the magnetic ion, exchange energy, defect density, etc. © 2001 MAIK “Nauka/Interperiodica”.

The effect of positive magnetoresistance, which was found for films of certain rare-earth (RE) oxides, which is not characteristic of this type of material, was considered elsewhere [1]. The purpose of this study was to investigate and analyze the temperature dependence of the effect close to the range of the magnetic phase transition (Curie temperature).

We investigated the oxides of RE elements Eu, Gd, and a Eu–Sm solid solution, which were obtained on a single-crystal *n*-Si substrate by vacuum thermal evaporation of the corresponding alloy followed by further oxidation. The films were 0.1 μm thick, and Al contacts were used as electrodes. The transverse current across the structure was measured in the enhancement mode for the (RE oxide)–Si boundary. The magnitude of magnetoresistance was determined from a current variation in the ranges of variation of the magnetic field strength $H = 3.0\text{--}7.5$ kOe, temperature $T = 77\text{--}300$ K, and electric field strength $E = 10^3\text{--}10^6$ V/cm. The direction of the vector of the magnetic field strength \mathbf{B} was selected parallel to the vector of the electric current density \mathbf{j} .

Typical temperature dependences of the specific relative magnetoresistance ($\Delta\rho/\rho_0$) for the films mentioned are shown in Fig. 1. For almost all samples under investigation, the $\Delta\rho/\rho_0$ quantity for the Curie temperature range [1] exhibited a jumplike decay. The T_c for various samples ranged from 90 to 110 K. For the $T < T_c$ range (near-ferromagnetic range), the specific magnetoresistance was practically independent of temperature. For a near-paramagnetic range ($T > T_c$), the $\Delta\rho/\rho_0$ quantity, which had a value larger than 1% even at $T > 200$ K for certain samples, fell off rather gradually. For

a near-ferromagnetic range, the dependences of specific magnetoresistance for samples of various composition on the external magnetic field strength were investigated at $T = 77$ K. The dependences obtained, which were almost linear for a magnetic field strength range under consideration, are shown in Fig. 2.

Based on known theoretical notions [2, 3], it was concluded that magnetization fluctuations (magnetic clusters) exist in the films under investigation. These fluctuations are related to the clustering of magnetic RE element ions close to defects that usually incorporate oxygen vacancies [4]. Clustering is caused by a stronger exchange interaction and correspondingly ferromagnetic coupling in this region. The magnetic moment \mathbf{K} for the cluster considerably exceeds that for a single RE ion. This makes a substantial contribution to the scattering of free charge carriers by magnetization fluctuations in the magnetic phase-transition range. Not only can the external magnetic field suppress these fluctuations, which is characteristic of the bulk samples of the materials under consideration (the negative magnetic resistance effect), but it can enhance them as well. For example, if the clusters are arranged randomly in the absence of the field and the average magnetization over the sample is small, then the field can induce an additional magnetization, which fluctuates along with the electron density. The consequence of the process considered above is the appearance of positive magnetoresistance, whose magnitude is a complex function dependent on the external magnetic field strength, temperature, electron density close to the defect, and on certain parameters of the material itself. It seems important that the overall moment of the magnetic ions

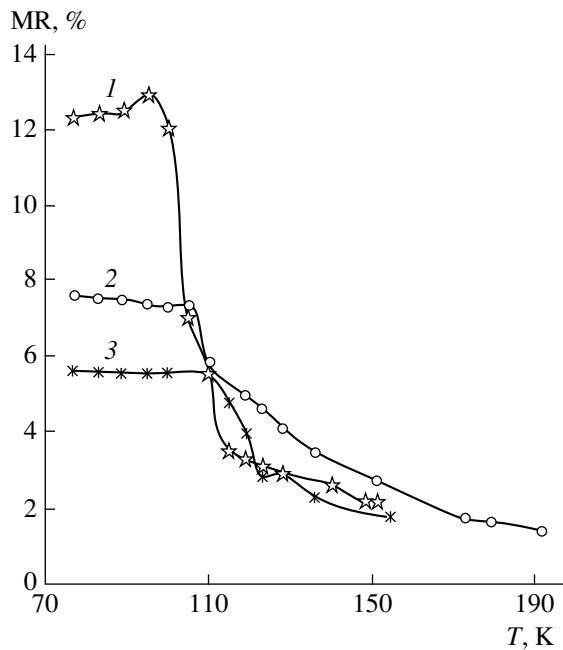


Fig. 1. Temperature dependence of the relative magnetoresistance. Curves (1) and (3) are for different samples of the solid solution of Eu and Sm oxides, and (2) is for Gd oxide. $H = 7.6$ kOe.

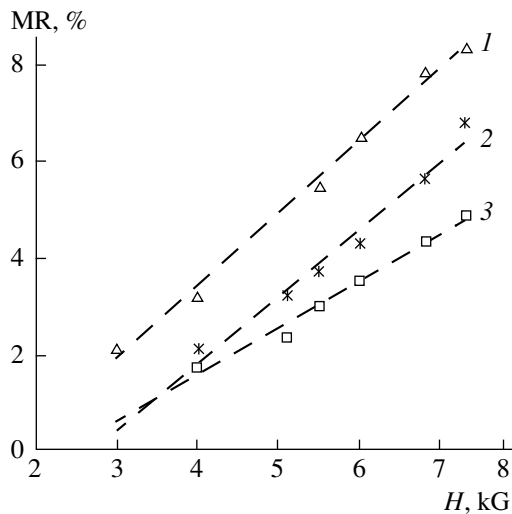


Fig. 2. Dependence of the specific magnetoresistance on the magnetic field strength H . Curve (1) is for Gd oxide; (2) for Sm oxide; and (3) for solid solution of Sm and Eu oxides. $T = 77$ K.

close to the defect (\mathbf{K}) can be rather large for the paramagnetic temperature range as well.

In [2], the temperature dependence of the magnetoresistance was analyzed using the positive feedback function (Γ_0), through which the effective field influencing the electron was expressed. This field involves the electric field in the crystal and electron exchange with magnetic ions.

For weak magnetic fields in the near-ferromagnetic temperature range, we take into account the dominant indirect exchange to obtain

$$\frac{\Delta\rho}{\rho} = -\frac{2HS}{T_c} \frac{\Gamma_0}{1-\Gamma_0}, \quad (1)$$

where

$$\Gamma_0 = QT; \quad (2)$$

$$Q = \frac{3N}{2n} \frac{1}{E_i}; \quad (3)$$

N is the concentration of magnetic ions; n is the concentration of charge carriers localized in the vicinity of the defect, which is determined by the density of states for the energy level of the defect; E_i is the donor-level energy depth, and S is the spin of the magnetic ion.

The curves shown in Fig. 3 were calculated for the temperature range under consideration using the following parameters: $H = 7$ kOe, $S = 7/2$, $N/n = 2 \times 10^2$, E_i from 0.1 to 0.3 eV, and $T_c = 100$ K. Satisfactory qualitative agreement with the experimental results was observed for the effect sign, effect magnitude, and behavior of the temperature and field dependences. The qualitative agreement even transformed into a quantitative one if the parameters varied were properly chosen (Figs. 1, 2).

For a paramagnetic temperature range, the $\Delta\rho/\rho_0(T)$ curves obtained from corresponding formulas [2] were in total disagreement with the experimental data as concerns both the effect magnitude and the temperature dependence shape. Therefore, we used the following approach. It is known that the relaxation time of the carriers scattered by magnetic clusters for the near-paramagnetic range is related to the cluster moment as follows: $\tau \sim K^{-2}$ [2, 5]. When specifying the dependence of the magnetic moment of the cluster on the material parameters and external effects, it is possible to evaluate the variation in the relaxation time and corresponding magnitudes of the specific magnetoresistance.

We assumed that the magnetic moment of the cluster could be expressed as

$$K = K_0 + \Delta K, \quad (4)$$

where $K_0 = zS$ is the magnetic moment of the cluster, which is determined by the amount of magnetic ions (z) introduced into the cluster; and

$$\Delta K = \frac{S(S+1)}{3(T-T_c)} \left(H + \frac{An}{2N} \right) \quad (5)$$

is the additional local magnetization, which is determined by both the external effects (H , T) and the parameters of the material (A is the exchange energy).

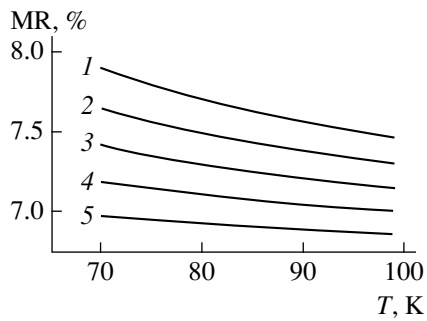


Fig. 3. Temperature dependence of the specific magnetoresistance for the near-ferromagnetic temperature range. $E_i =$ (1) 0.1, (2) 0.15, (3) 0.2, (4) 0.25, and (5) 0.3 eV. $H = 7$ kOe, $n = 5 \times 10^{18} \text{ cm}^{-3}$, and $z = 12$.

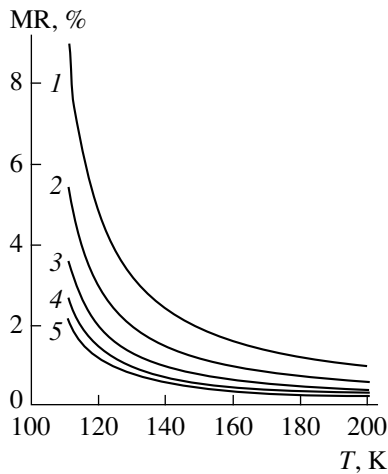


Fig. 4. Temperature dependence of the specific magnetoresistance for the near-paramagnetic temperature range. $z =$ (1) 12, (2) 20, (3) 30, (4) 40, and (5) 50. $H = 7$ kOe and $n = 5 \times 10^{18} \text{ cm}^{-3}$.

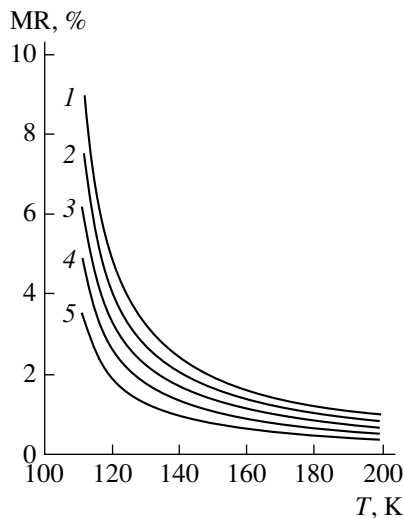


Fig. 5. Temperature dependence of the specific magnetoresistance for the near-paramagnetic temperature range, $n =$ (1) 1, (2) 2, (3) 3, (4) 4, and (5) $5 \times 10^{18} \text{ cm}^{-3}$. $H = 7$ kOe and $z = 12$.

Upon simple rearrangements, we derive the following dependence of specific magnetoresistance in the presence of the external magnetic field:

$$\frac{\Delta\rho}{\rho_0} \cong \left(1 + \frac{S+1}{3z(T-T_c)} \left(H + \frac{A}{2} \frac{n}{N}\right)\right)^2 - 1. \quad (6)$$

If the field is absent, the magnetoresistance is equal to zero.

We considered the temperature dependence of Eq. (6) derived for various parameters of the films under investigation, which lie in the ranges characteristic of these materials. Namely, n varied from 10^{18} to $5 \times 10^{18} \text{ cm}^{-3}$, z varied from 12 to 50, $A = 0.12$ eV, $H = 7$ kOe, and $T_c = 100$ K. Corresponding results are shown in Figs. 4 and 5. The curves calculated are in close agreement with the experimental data (Fig. 1) both by the behavior of the temperature dependences of the magnetoresistance and by the effect magnitude and sign.

Thus, we analyzed the temperature dependence of the positive magnetoresistance in RE oxide films for near-ferromagnetic and near-paramagnetic ranges in terms of the scattering of the charge carriers by magnetization fluctuations. It was demonstrated that the temperature dependence of the effect and effect sign and magnitude are determined by the dependence of the cluster magnetic moment on both the external magnetic field strength and the parameters of the samples under investigation. These are the spin of the magnetic ion, exchange energy, defect density, etc.

REFERENCES

1. V. F. Kabanov and A. M. Sverdlova, *Fiz. Tekh. Poluprovodn.* (St. Petersburg) **31**, 626 (1997) [*Semiconductors* **31**, 531 (1997)].
2. É. L. Nagaev, *Physics of Magnetic Semiconductors* (Nauka, Moscow, 1979).
3. V. A. Kapustin, in *Rare-Earth Semiconductors* (Nauka, Leningrad, 1977), p. 82.
4. V. G. Bamburov, A. S. Borukhovich, and A. A. Samokhvalov, *Introduction to the Physical Chemistry of Ferromagnetic Semiconductors* (Metallurgiya, Moscow, 1988).
5. V. F. Kabanov, *Fiz. Tekh. Poluprovodn.* (St. Petersburg) **26**, 1837 (1992) [*Sov. Phys. Semicond.* **26**, 1032 (1992)].

Translated by N. Korovin

ELECTRONIC AND OPTICAL PROPERTIES OF SEMICONDUCTORS

Specific Features of the Nonequilibrium Distribution Function for Electron Scattering by Polar Optical Phonons in III–V Semiconductors

S. I. Borisenko

Kuznetsov Siberian Physicotechnical Institute, Tomsk, 634050 Russia

Submitted July 12, 2000; accepted for publication July 26, 2000

Abstract—Numerical analysis of a nonequilibrium distribution function for electron scattering by polar optical phonons in a GaAs semiconductor is carried out. The Boltzmann equation for the nonequilibrium function was solved by the iteration method, with allowance made for electron distribution over the states. It is shown that the nonequilibrium addition to the distribution function has a complex form at low temperatures. The mobility values calculated using this function are compared with the value obtained within a conventional approximation. © 2001 MAIK “Nauka/Interperiodica”.

1. INTRODUCTION

As is known, one of the main scattering mechanisms in diamond-like III–V semiconductors is the scattering by longitudinal polar optical (LO) phonons. The consideration of this scattering in the inelasticity region presents certain difficulties associated with the necessity of numerically solving the Boltzmann equation beyond the framework of the relaxation time approximation. In many papers [1–4] related to the analysis of experimental data on the temperature dependence of mobility in III–V semiconductors in the region of dominant LO-phonon scattering, the formula obtained in [5, 6] with the help of the variational method is used; i.e.,

$$\mu_{\text{LO}} = \frac{8\sqrt{T}\hbar^2\varepsilon^*[\exp(\Theta/T) - 1]}{3\sqrt{2\pi k_0(m^*)^3}e^\Theta}\chi(\Theta/T) \quad (1)$$

$$= \mu_0(T)\chi(\Theta/T),$$

where m^* is the charge-carrier effective mass, $\varepsilon^* = \varepsilon_s\varepsilon_\infty/(\varepsilon_s - \varepsilon_\infty)$, ε_s and ε_∞ are the low-frequency and high-frequency dielectric constants, T is temperature, and $\Theta = \hbar\omega/k_0$ is the effective temperature of the long-wavelength LO-phonon. This formula, along with the parameters of the electronic and phonon spectra, contains a function χ assigned numerically, the argument of which is the ratio of the phonon energy $\hbar\omega$ to the value of k_0T . In the range of high ($\hbar\omega \ll k_0T$) and low ($\hbar\omega \gg k_0T$) temperatures, the value of this function results in the formulas obtained within the relaxation time approximation [7]. The shortcoming of these formulas consists in the following: they disregard the screening of the LO-phonon potential, as well as the

electron distribution over the states in the vicinity of the conduction band bottom. The aforementioned factors can turn out to be important in the case of samples with partially or completely degenerate electron gas.

In this paper, we derive a functional equation; with it, the Boltzmann equation for the electron scattering by LO-phonons is solved numerically by the iteration method. The approximations of a weak field and effective mass are used in deriving this equation, with the screening of scattering by LO-phonons and electron distribution over the states taken into consideration. By the example of GaAs, the numerical calculation was carried out, as well as the analysis of a nonequilibrium addition to the distribution function and to the temperature dependence of mobility. We compared our results with those obtained using different methods.

2. METHOD OF NUMERICAL SOLUTION OF THE BOLTZMANN EQUATION

As is known, in the approximation of a weak electric field with the intensity \mathbf{E} , the Boltzmann equation for a nonequilibrium addition to the distribution function $g(\mathbf{k})$ can be written as

$$g(\mathbf{k}) = \tau_0(\mathbf{k}) \times \left\{ \sum_{\mathbf{k}'} g(\mathbf{k}') [w_{\mathbf{k}\mathbf{k}'} + f_0(\mathcal{E})(w_{\mathbf{k}\mathbf{k}'} - w_{\mathbf{k}'\mathbf{k}})] + e \frac{\partial f_0}{\partial \mathcal{E}} \mathbf{E} \mathbf{v}_{\mathbf{k}} \right\}, \quad (2)$$

where

$$\tau_0(\mathbf{k}) = 1 / \sum_{\mathbf{k}'} \{ w_{\mathbf{k}\mathbf{k}'} + f_0(\mathcal{E})(w_{\mathbf{k}\mathbf{k}'} - w_{\mathbf{k}'\mathbf{k}}) \}; \quad (3)$$

$f_0(\mathcal{E}) = 1/[\exp(\mathcal{E} - \xi) + 1]$ is an equilibrium Fermi–Dirac distribution function; $\mathcal{E} = \mathcal{E}(\mathbf{k})$, $\mathcal{E}' = \mathcal{E}(\mathbf{k}')$ is the electron energy dependent on the wave vector; $w_{\mathbf{k}\mathbf{k}'}$ is the probability for transition per unit time from the state with the wave vector \mathbf{k} to a state with the wave vector \mathbf{k}' ; and $\mathbf{v}_{\mathbf{k}} = \nabla_{\mathbf{k}}\mathcal{E}/\hbar$ is the electron velocity. As is known, for the electron scattering by LO-phonons in III–V semiconductors with allowance made for their emission (+) and absorption (–), we have

$$w_{\mathbf{k}\mathbf{k}'} = w_{\mathbf{k}\mathbf{k}'}^+ + w_{\mathbf{k}\mathbf{k}'}^-, \quad (4)$$

where

$$w_{\mathbf{k}\mathbf{k}'}^+ + w(\mathbf{q}) \left(N_\omega + \frac{1}{2} \pm \frac{1}{2} \right) \delta(\mathcal{E}' - \mathcal{E} \pm \hbar\omega) \delta_{\mathbf{k}, \mathbf{k}' \pm \mathbf{q}}, \quad (5)$$

$$w(\mathbf{q}) = C \frac{\mathbf{q}^2}{(\mathbf{q}^2 + \alpha^2)^2}, \quad C = \frac{\pi e^2 \omega}{\epsilon_0 \epsilon^*}, \quad (6)$$

$$N_\omega = \frac{1}{\exp(\hbar\omega/k_0T) - 1}$$

is the Bose–Einstein distribution function, α is the Debye screening coefficient, and \mathbf{q} is the phonon wave vector.

Choosing a nonequilibrium addition in the form relevant to the relaxation time approximation $g(\mathbf{k}) = e(\partial f_0/\partial \mathcal{E})\tau(\mathcal{E})\mathbf{E}\mathbf{v}_{\mathbf{k}}$ and taking into account Eq. (2), we obtain the following functional equation for the unknown function $\tau(\mathcal{E})$:

$$\begin{aligned} & \tau(\mathcal{E}) \\ &= \tau_0(\mathcal{E}) \{ S^+(\mathcal{E})\tau(\mathcal{E} + \hbar\omega) + S^-(\mathcal{E})\tau(\mathcal{E} - \hbar\omega) + 1 \}. \end{aligned} \quad (7)$$

Here,

$$1/\tau_0(\mathcal{E}) = S_0^+(\mathcal{E}) + S_0^-(\mathcal{E}). \quad (8)$$

In the effective mass approximation for the electron energy spectrum, expressions for the functions appearing in Eq. (7) in view of (4)–(6) have analytical forms

$$\begin{aligned} S^\pm(\mathcal{E}) &= A \left[N_\omega + \frac{1}{2} \pm \frac{1}{2} \mp f_0(\mathcal{E}) \right] \frac{f_0'(\mathcal{E}')}{f_0'(\mathcal{E})} \\ &\times \frac{(\mathcal{E}' + \mathcal{E} + 2\eta^2)}{\mathcal{E}\sqrt{\mathcal{E}}} S(\mathcal{E}, \mathcal{E}')|_{\mathcal{E}' = \mathcal{E} \pm \hbar\omega}, \\ & S_0^\pm(\mathcal{E}) \\ &= A \left[N_\omega + \frac{1}{2} \pm \frac{1}{2} \mp f_0(\mathcal{E}) \right] \frac{2}{\mathcal{E}\sqrt{\mathcal{E}}} S_0(\mathcal{E}, \mathcal{E}')|_{\mathcal{E}' = \mathcal{E} \mp \hbar\omega}, \\ & S(\mathcal{E}, \mathcal{E}')| = \ln \left[\frac{(\sqrt{\mathcal{E}'} + \sqrt{\mathcal{E}})^2 + \eta^2}{(\sqrt{\mathcal{E}'} - \sqrt{\mathcal{E}})^2 + \eta^2} \right] \end{aligned} \quad (9)$$

$$-4 \frac{\sqrt{\mathcal{E}\mathcal{E}'} [(\mathcal{E}' - \mathcal{E})^2 + 3\eta^2(\mathcal{E}' + \mathcal{E}) + 2\eta^4]}{(\mathcal{E}' + \mathcal{E} + 2\eta^2)[(\mathcal{E}' - \mathcal{E})^2 + 2\eta^2(\mathcal{E}' + \mathcal{E}) + \eta^4]},$$

$$S_0(\mathcal{E}, \mathcal{E}') = \ln \left[\frac{(\sqrt{\mathcal{E}'} + \sqrt{\mathcal{E}})^2 + \eta^2}{(\sqrt{\mathcal{E}'} - \sqrt{\mathcal{E}})^2 + \eta^2} \right]$$

$$-4 \frac{\sqrt{\mathcal{E}\mathcal{E}'}\eta^2}{(\mathcal{E}' - \mathcal{E})^2 + 2\eta^2(\mathcal{E}' + \mathcal{E}) + \eta^4},$$

where $f_0'(\mathcal{E}) = \partial f_0(\mathcal{E})/\partial \mathcal{E}$, $\eta^2 = \hbar^2\alpha^2/2m^*$, $A = (\sqrt{2m^*}/32\pi^2\hbar)C$, and m^* is the effective electron mass at the conduction band bottom.

Equation (7) for function $\tau(\mathcal{E})$, the relaxation time, is solved numerically by the iteration method. As the zero approximation, we can use the function $\tau_0(\mathcal{E})$. In this case, we obtain the following iteration equation for the $(n + 1)$ th approximation:

$$\begin{aligned} & \tau_{n+1}(\mathcal{E}) \\ &= \tau_0(\mathcal{E}) \{ S^+(\mathcal{E})\tau_n(\mathcal{E} + \hbar\omega) + S^-(\mathcal{E})\tau_n(\mathcal{E} - \hbar\omega) + 1 \}. \end{aligned} \quad (10)$$

For $\mathcal{E} \gg \hbar\omega$, we use Eq. (7) to derive a formula for the high-temperature relaxation time with allowance made for screening of the LO-phonon long-range potential

$$\tau(\mathcal{E}) = \frac{\sqrt{\mathcal{E}}}{2A(2N_\omega + 1)\Phi(\mathcal{E})}, \quad (11)$$

where

$$\Phi(\mathcal{E}) = \frac{\eta^2}{\mathcal{E}} \ln \left(\frac{\eta^2}{4\mathcal{E} + \eta^2} \right) + 4 \frac{2\mathcal{E} + \eta^2}{4\mathcal{E} + \eta^2}. \quad (12)$$

For $\eta \rightarrow 0$, the function $\Phi(\mathcal{E}) \rightarrow 2$ and formula (11) takes a conventional form for the high-temperature relaxation time by LO-phonons disregarding the screening.

As is known, at low temperatures, the relaxation time for scattering by LO-phonons cannot be strictly introduced. The approximate approach to the solution of this problem results in the formula obtained by Callan [8], which due to its relative complexity is not in practice used for the analysis of the charge carrier mobility. Taking into account the screening, this formula can be written in the effective mass approximation as

$$\begin{aligned} & \frac{1}{\tau(\mathcal{E})} = 2A\mathcal{E}^{-3/2} \\ & \times \{ N_\omega \Phi^-(\mathcal{E}) + (N_\omega + 1)\Phi^+(\mathcal{E})\vartheta(\mathcal{E} - \hbar\omega) \}, \end{aligned} \quad (13)$$

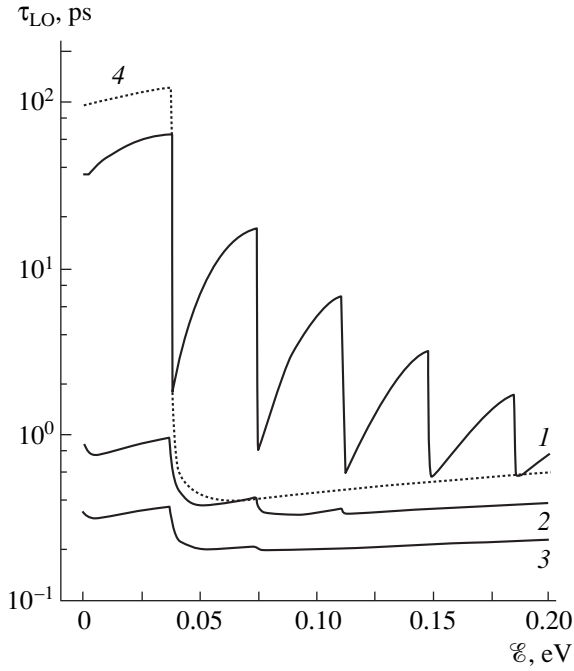


Fig. 1. Shape of $\tau_{LO}(\mathcal{E})$ function for a nondegenerate electron gas ($\xi = -k_0T$) at $T = (1)$ 77, (2) 300, and (3) 600 K; curve 4 represents the result of calculation according to the Callan formula at $T = 77$ K.

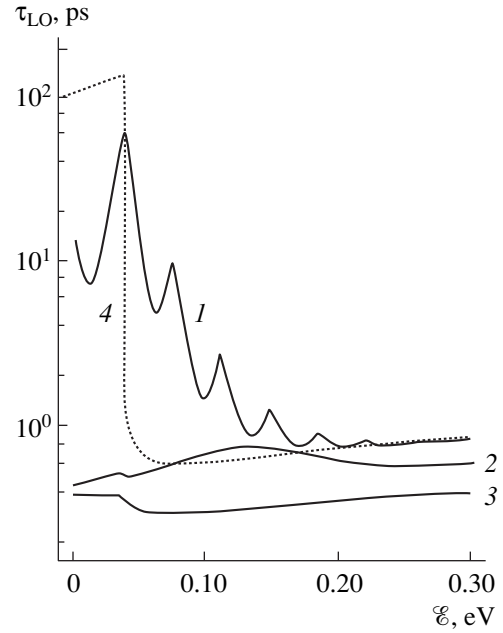


Fig. 2. Shape of $\tau_{LO}(\mathcal{E})$ function for a degenerate electron gas ($\xi = 5k_0T$) at $T = (1)$ 77, (2) 300, and (3) 600 K; curve 4 represents the result of calculation according to the Callan formula at $T = 77$ K.

where $\vartheta(x)$ is the Heaviside function,

$$\begin{aligned} \Phi^\pm(\mathcal{E}) &= 2\sqrt{\mathcal{E}(\mathcal{E} \mp \hbar\omega)} \\ &- \frac{(2\eta^2 \mp \hbar\omega)}{2} \ln \left[\frac{\eta^2 + (\sqrt{\mathcal{E} \mp \hbar\omega} + \sqrt{\mathcal{E}})^2}{\eta^2 + (\sqrt{\mathcal{E} \mp \hbar\omega} - \sqrt{\mathcal{E}})^2} \right] \\ &+ \frac{2\eta^2(\eta^2 \mp \hbar\omega)\sqrt{\mathcal{E}(\mathcal{E} \mp \hbar\omega)}}{[\eta^2 + (\sqrt{\mathcal{E} \mp \hbar\omega} + \sqrt{\mathcal{E}})^2][\eta^2 + (\sqrt{\mathcal{E} \mp \hbar\omega} - \sqrt{\mathcal{E}})^2]}. \end{aligned} \quad (14)$$

In the approximation of elastic scattering for $\mathcal{E} \gg \hbar\omega$, formula (13) transforms into formula (11) as one should expect.

3. NUMERICAL ANALYSIS OF THE RELAXATION TIME AND MOBILITY

The results of the numerical solution of Eq. (7) are presented in Fig. 1 for function $\tau_{LO}(\mathcal{E}) = \tau(\mathcal{E})$ for several temperatures (see curves 1–3) with parameters corresponding to the nondegenerate *n*-GaAs: $m^*/m_0 = 0.067$, $\epsilon_s = 13.7$, $\epsilon_\infty = 11.6$, $\hbar\omega = 37$ meV, and $\xi = -k_0T$. It follows from Fig. 1 that in the region of liquid-nitrogen temperatures the function $\tau_{LO}(\mathcal{E})$ is oscillating. The oscillation period is equal to the LO-phonon energy. As the electron energy and temperature increase, the oscillation amplitude decreases. Function $\tau(\mathcal{E})$ calculated according to the Callan formula (13) (curve 4) has a

shape close to the envelope of $\tau_{LO}(\mathcal{E})$ from below. With the Fermi level rising, the shape of oscillations changes, but their period remains unchanged. This follows from Fig. 2, where the results of $\tau_{LO}(\mathcal{E})$ calcula-

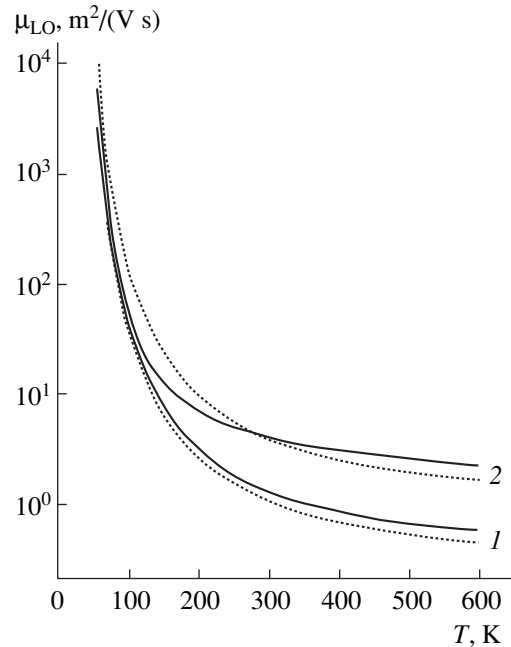


Fig. 3. Mobility temperature dependence for $\xi = (1)$ $-k_0T$ and (2) $5k_0T$. Explanations are in the text.

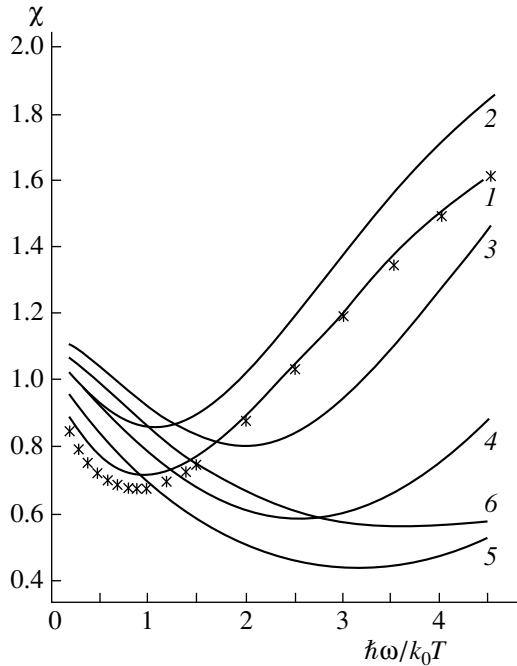


Fig. 4. Values of χ function for an electron gas with a various degrees of degeneracy: $\xi = (1) -10k_0T, (2) -k_0T, (3) 2k_0T, (4) 3k_0T, (5) 4k_0T, (6) 6k_0T$. Explanations are in the text.

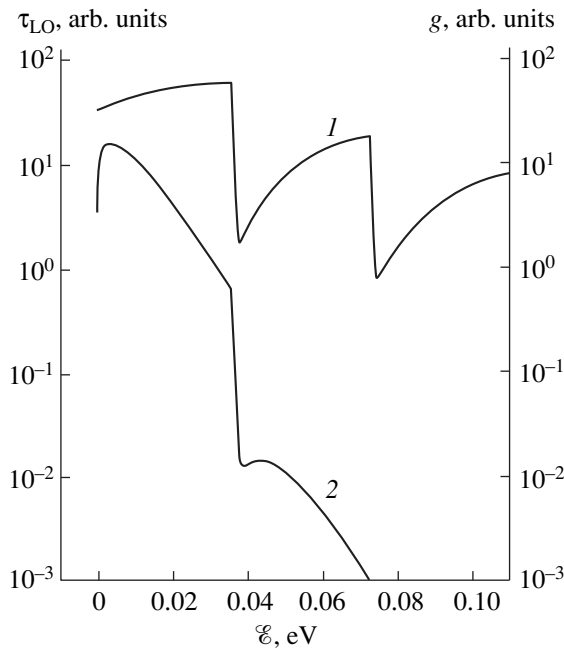


Fig. 5. Dependence of (1) τ_{LO} and (2) g in arbitrary units on the energy for n -GaAs at $T = 77$ K and $\xi = -k_0T$.

tions are presented; they are performed for a degenerate n -GaAs ($\xi = 5k_0T$).

The results of the drift mobility calculations in the temperature range from 50 up to 600 K are shown in Fig. 3. A solid line corresponds to the calculation of μ_{LO} with the function $\mu_{LO}(\xi)$ obtained from the numerical

solution of Eq. (7), and a dotted one corresponds to the calculation according to formula (1). It follows from Fig. 3 that the largest difference between the curves calculated by the two methods is observed, as should be expected, for a degenerate electron gas. Figure 4 shows the function χ calculated according to the formula

$$\chi(\Theta/T) = \mu_{LO}(T)/\mu_0(T), \quad (15)$$

where $\mu_{LO}(T)$ is the mobility calculated on the basis of the numerical solution of Eq. (7), and $\mu_0(T)$ is the mobility in the relaxation-time approximation for the nondegenerate electron gas [see (1)]. The solid curves 1–6 correspond to the values of this function for various degrees of degeneracy of the electron gas. The dots correspond to the values of this function obtained in deriving formula (1) [2]. According to Fig. 4, the values of function χ calculated with and without consideration of the filling of the states in the conduction band by electrons differ markedly for the samples with a degenerate electron gas in the region of liquid-nitrogen temperatures. This can lead to a severalfold increase in mobility, which is calculated according to formula (1), compared to the exact calculation.

4. CONCLUSION

According to the results of numerical solution of the Boltzmann equation for GaAs, it is shown that, in III–V semiconductors at low temperatures, the energy dependence of the nonequilibrium addition to the distribution function has a complicated form if scattering by LO-phonons is taken into account (Fig. 5). This can manifest itself in strong magnetic fields for intrinsic or lightly doped semiconductors of this type and in the structures based on them, e.g., in superlattices and other low-dimensional structures, specific features of which manifest themselves at low temperatures.

REFERENCES

1. V. M. Ardyshv, M. V. Ardyshv, and S. S. Khludkov, *Fiz. Tekh. Poluprovodn.* (St. Petersburg) **34**, 28 (2000) [*Semiconductors* **34**, 27 (2000)].
2. M. B. Kokhanyuk, *Indium Phosphide in Semiconductor Electronics* (Kishinev, 1988).
3. Ya. É. Kirson, É. É. Klotyn'sh, and R. K. Kruminya, *Izv. Akad. Nauk Latv. SSR, Ser. Fiz. Tekh. Nauk*, No. 3, 47 (1982).
4. B. Podor and N. Nador, *Acta Phys. Acad. Sci. Hung.* **37**, 317 (1974).
5. A. Fortini, B. Diguët, and J. Lugand, *J. Appl. Phys.* **32**, 2155 (1961).
6. H. Ehrenreich, *Phys. Rev.* **120**, 1951 (1960).
7. A. I. Anselm, in *Introduction to Semiconductor Theory* (Nauka, Moscow, 1978; Prentice-Hall, Englewood Cliffs, 1981), Chap. 8.
8. B. Ridley, in *Quantum Processes in Semiconductors* (Clarendon, Oxford, 1982; Mir, Moscow, 1986), Chap. 3.

Translated by T. Galkina

ELECTRONIC AND OPTICAL PROPERTIES OF SEMICONDUCTORS

On the Stabilization of Electrical Properties of Compensated Silicon as a Result of Irradiation with ^{60}Co Gamma-Ray Quanta

M. S. Yunusov*, M. Karimov, and M. A. Dzhalolev

Institute of Nuclear Physics, Academy of Sciences of Uzbekistan, Ulugbek, Tashkent, 702132 Uzbekistan

* e-mail: yunusov@suninp.tashkent.su

Submitted May 27, 1999; accepted for publication August 2, 2000

Abstract—A change in the charge-carrier concentration in compensated silicon (obtained by preliminary irradiation) as a result of gamma-ray irradiation was studied. It was found that the removal rate of charge carriers in compensated silicon is lower than in the reference sample. A new mechanism responsible for the immunity of electrical properties of compensated silicon to radiation is discussed. © 2001 MAIK “Nauka/Interperiodica”.

In silicon, the formation of defects introducing deep energy levels in the band gap is one of the methods for attaining the required electrical and photoelectric properties of material exposed to radiation. It has been shown that impurities significantly affect the radiation stability of defect parameters introducing deep levels in the silicon band gap. In the majority of publications [1–6], this fact has been explained by competition of the following two mechanisms operative under irradiation: (i) the conversion of a fraction of electrically inactive impurity atoms to an electrically active state (channel 1) and (ii) an enhancement of the escape of primary radiation defects [vacancies (V) and self-interstitials (I)] to additional sinks (channel 2) in the doped material; the interfaces between the impurity microinclusions and the matrix may function in the capacity of the sinks mentioned above.

It is worth noting that a decrease in the concentration of radiation-produced compensating centers (as a result of the realization of channels 1 and 2) and a simultaneous increase in the concentration of compensating impurity centers (as a result of the realization of channel 1) in the course of irradiation are not the primary factors behind the decrease in the carrier removal rate in the doped silicon with deep-level centers. The use of this idea for solving the problem of radiation stability (with respect to electrical conductivity) of the doped material should be justified, because the mechanism of increasing the radiation resistance of material with deep-level centers has not been completely clarified so far. This is due to inadequate insight into the behavior of impurities in silicon with deep-level centers after thermal diffusion in relation to the cooling rate, repeated thermal treatment, and the effect of penetrating radiation. It is noteworthy that each of the aforementioned factors affects the mobility and concentration of charge carriers (the compensation factor) and also the conditions of their recombination. This gives

rise to significant changes in the volume-gradient phenomena caused by nonuniform distribution of the main and technology-induced impurities in compensated silicon [7, 8]. Each microregion has a positive or negative potential with respect to the adjacent region, depending on the compensation factor; i.e., a random electric potential, which significantly affects the charge-carrier transport, emerges in the bulk of the crystal. However, in spite of this, there have been no purposeful investigations into the role of the charge-carrier concentration gradient and the electrical-conductivity nonuniformity in the radiation stability of electrical properties of compensated material with deep-level centers.

The objective of this study was to identify the processes responsible for the radiation stability of electrical properties of compensated silicon.

Compensated silicon with deep-level centers was obtained by exposing the samples to two kinds of radiation, differing by the properties of the defects they generated in the material. More specifically, we used nuclear-reactor neutrons (samples of type 1) and ^{60}Co gamma-ray quanta (samples of type 2); i.e., compensated silicon was obtained by compensation with radiation defects. Thereby, both channels of the impact of irradiation were eliminated in the samples of type 2 (the agglomerations of impurity atoms giving rise to deep-level centers necessary for realization of channels 1 and 2 were absent in the samples). In the samples of type 1, channel 1 was eliminated, and channel 2 was operative (there were the disordered regions required for the realization of channel 2 in the samples).

As an initial material, we used Czochralski-grown $n\text{-Si:P}$ crystals with $\rho \approx 3 \Omega \text{ cm}$ and a dislocation density of $\sim 10^4 \text{ cm}^{-2}$. Various degrees of micrononuniformity in electrical conductivity were accomplished by varying (i) the degree of impurity compensation and (ii) the electrical conductivity of silicon using irradiation.

tion with fast neutrons (samples of type 1) or with gamma-ray quanta (samples of type 2). In this situation, the compensation factor $K = N_{RD}/n$ (where N_{RD} is the concentration of compensating radiation defects and n is the average concentration of the majority charge carriers) was equal to 0.2–0.9 for the samples of types 1 and 2. Parameters of the samples are listed in the table. We calculated the spatial sizes (r) and amplitudes (Δ_0) of fluctuation in relation to the radiation-defect concentration in silicon using the following known formulas [9]:

$$r = (N_{RD})^{1/3}/n^{2/3}, \quad \Delta_0 = (e^2\chi)(N_{RD})^{2/3}/n^{1/3}.$$

Here, e is the elementary charge, and χ is the dielectric constant. The difference in the charge-carrier concentration between the high-resistivity (n^{\max}) and low-resistivity (n^{\min}) regions was also calculated using the known formulas [10]

$$\delta = 2(n^{\max} - n^{\min})/(n^{\max} + n^{\min}).$$

As can be seen from the table, partially compensated samples (of types 1 and 2) with various degrees of micrononuniformity in electrical conductivity were obtained by irradiation with neutrons and gamma-ray quanta. As the concentration of radiation defects increases, the spread in the concentration of charge carriers δ and the amplitude Δ_0 and spatial size r of fluctuations increase, whereas the charge-carrier mobility μ decreases.

For the sake of comparison, we also studied reference silicon samples that were not first irradiated and had an electrical conductivity similar to the n -Si:P crystals (the samples of type 3).

The initial (10%) charge-carrier removal rate ($\Delta n/\Phi$) under irradiation with gamma-ray quanta with a dose rate of ~ 2000 R/s was studied using the Hall-effect and resistivity measurements.

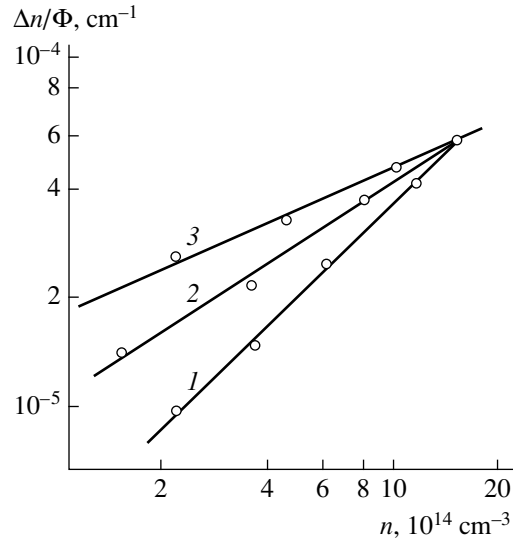


Fig. 1. Dependences of initial rate of the charge-carrier removal as a result of irradiation with ^{60}Co gamma-ray quanta on the initial charge-carrier concentration in the compensated Si samples obtained by irradiation with (1) fast neutrons and (2) gamma-ray quanta, and (3) in the reference sample.

Figure 1 shows the dependences of the initial carrier-removal rate in the gamma-irradiated silicon upon the initial charge-carrier concentration (before the gamma-ray irradiation). The experimental results obtained are satisfactorily described by the following dependences:

$$\Delta n/\Phi = 3 \times 10^{-20} n \text{ for the samples of type 1, (1)}$$

$$\Delta n/\Phi = 5 \times 10^{-15} n^{0.66} \text{ for the samples of type 2, (2)}$$

$$\Delta n/\Phi = 4.2 \times 10^{-11} n^{0.4} \text{ for the samples of type 3, (3)}$$

Parameters of the samples of types 1 and 2 at $T = 300$ K

The sample type	Resistivity, ρ , Ω cm	The charge-carrier mobility, μ , $\text{cm}^2/(\text{V s})$	The charge-carrier concentration, n , cm^{-3}	The compensation factor, K	The relative spread in the charge-carrier concentration, δ , %	The fluctuation amplitude, Δ_0 , eV	The spatial size of fluctuation, r , 10^{-5} cm
Unirradiated sample	2.8	1500	1.5×10^{15}		13		
The sample of type 1 (irradiated with neutrons)*	4.6	1500	8.5×10^{14}	0.43	23	0.0053	0.97
	12	1390	3.7×10^{14}	0.75	54	0.022	2.00
	32	1150	1.7×10^{14}	0.87	117	0.031	3.54
The sample of type 2 (irradiated with gamma-ray quanta)	3.7	1400	1.2×10^{15}	0.2	16	0.0060	0.59
	8.5	1270	5.8×10^{14}	0.61	35	0.016	1.40
	16	1000	3.9×10^{14}	0.74	51	0.021	1.94
	33	900	2.1×10^{14}	0.85	95	0.029	3.08

* The influence of disordered regions was not taken into account when calculating the amplitude and spatial size of fluctuations and also the spread of concentration in the samples of type 1.

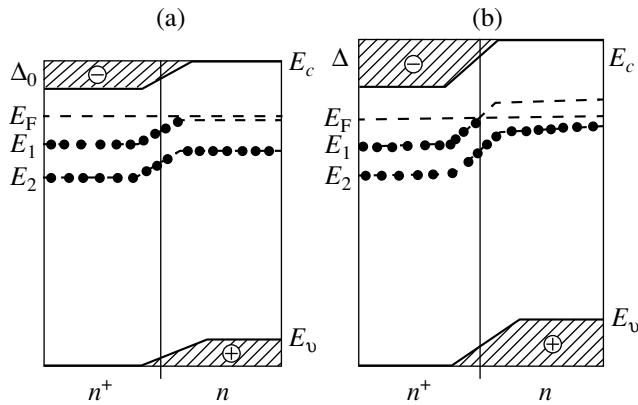


Fig. 2. Models of inhomogeneous n^+ - and n -regions formed in n -Si:P compensated by radiation defects (a) before and (b) after repeated gamma-ray irradiation. $E_1 = E_c - 0.34$ eV and $E_2 = E_c - 0.44$ eV.

where n is the initial electron concentration (at $T = 300$ K).

When expressions (1)–(3) are used, it is necessary to take into account that they are valid in the concentration range of 10^{14} – 2×10^{15} cm^{-3} . It is noteworthy that the results obtained for the samples of type 3 are virtually identical to those reported previously [11].

As can be seen from Fig. 1, the initial carrier-removal rate $\Delta n/\Phi$ for the samples of type 1 is significantly lower than for the samples of type 2 with an identical charge-carrier concentration; this may be attributed to an enhanced escape of the primary radiation defects to sinks (disordered regions) [12–14]. It is also evident that the value of $\Delta n/\Phi$ is much smaller in compensated samples (straight lines 1 and 2) than in the reference Si sample (straight line 3); furthermore, $\Delta n/\Phi$ decreases with the increasing compensation factor in the samples of types 1 and 2. In order to explain this fact, we suggest a barrier model (Fig. 2). The essence of this model is in the following.

With modern methods of growing silicon crystals, low-resistivity (n^+) and high-resistivity (n) regions are formed in the crystals' bulk as a result of the nonuniform distribution of main dopants (phosphorus or boron). A nonuniform compensation of electrically active impurities occurs in the irradiated samples owing to an initial nonuniform distribution of impurities (in the case under consideration, phosphorus) even if the compensating radiation defects are distributed uniformly. Furthermore, as the compensation factor increases (see table), the magnitude of differences between the charge-carrier concentrations in the above regions increases. The presence of contacts between the n^+ - and n -regions leads to the emergence of a potential barrier (Δ_0). We assume, first, that the centers with levels at $E_c - 0.18$ eV (the A centers), $E_c - 0.23$ eV (divacancies), $E_c - 0.34$ eV, and $E_c - 0.44$ eV (the E centers) are formed as a result of impurity compensation in the sil-

icon samples of types 1 and 2 [15]. Second, we assume that the Fermi level in the n^+ region is located between the energy levels at $E_c - 0.34$ eV and $E_c - 0.44$ eV; i.e., the energy levels of the A center and divacancy are located above the Fermi level, so that these levels are completely ionized. As for the centers with levels at $E_c - 0.34$ eV and $E_c - 0.44$ eV, they are filled with electrons because of their location in reference to the Fermi level. In the n region, the $E_c - 0.34$ eV level is partially ionized, whereas the center with the level at $E_c - 0.44$ eV is occupied with electrons (Fig. 2a).

As a result of gamma-ray irradiation (at the initial stages), the n regions of the crystals (of types 1 and 2) acquire higher resistivity, whereas the n^+ regions virtually do not respond to compensation and remain as highly resistive as they were before irradiation; i.e., the height of the potential barrier between the n^+ and n regions increases $\Delta_0 \rightarrow \Delta$, owing to a significant difference between the compensation factors in the n^+ and n regions. In the case under consideration, the A centers and divacancies are not involved in the charge-carrier removal, because the Fermi level E_F is located at $E_F > E_c - 0.23$ eV (Fig. 2). An increase in the barrier height $\Delta_0 \rightarrow \Delta$ leads to an increase in the concentration of ionized centers with $E_c - 0.34$ eV in the n region and, correspondingly, to a decrease in the occupancy. Electrons released as result of the ionization of the centers with $E_c - 0.34$ eV in the n regions are captured by deep-level radiation defects with the level at $E_c - 0.44$ eV. The charge-carrier concentration in the conduction band of nonuniform (compensated) material remains almost unchanged as the irradiation dose increases, until the concentration of electrons released as a result of ionization of the level at $E_c - 0.34$ eV in the n regions becomes equal to the concentration of radiation defects formed. In the case under consideration, this occurs in the course of gamma-ray irradiation; i.e., as long as the Fermi level position in the low-resistivity n^+ region does not change significantly, because it is the n^+ region which mainly conducts current in such a nonuniform material [16].

Thus, a decrease in the charge-carrier removal rate under the effect of gamma-ray irradiation can be largely explained by the radiation-induced enhancement of fluctuation barriers between the low- and high-resistivity regions and by an enhanced escape of a fraction of the vacancy V and interstitial I radiation defects to sinks in compensated silicon with deep-level centers.

REFERENCES

1. E. F. Uvarov and M. V. Chukichev, in *Radiation Physics of Non-Metallic Crystals* (Nauka i Tekhnika, Minsk, 1970), p. 81.
2. M. K. Bakhadyrkhanov, S. Z. Zaïnabiddinov, and A. T. Teshabaev, *Fiz. Tekh. Poluprovodn. (Leningrad)* **11**, 285 (1977) [*Sov. Phys. Semicond.* **11**, 165 (1977)].

3. M. K. Bakhadyrkhanov and F. M. Talipov, *Fiz. Tekh. Poluprovodn. (Leningrad)* **16**, 574 (1982) [*Sov. Phys. Semicond.* **16**, 371 (1982)].
4. S. Z. Zaïnabiddinov and É. É. Rubinov, *Neutron Transmutation Doping of Silicon* (Fan, Tashkent, 1983).
5. K. P. Abdurakhmanov, R. F. Vitman, Kh. S. Daliev, *et al.*, *Fiz. Tekh. Poluprovodn. (Leningrad)* **19**, 1617 (1985) [*Sov. Phys. Semicond.* **19**, 995 (1985)].
6. S. Z. Zaïnabiddinov and Kh. S. Daliev, *Defect Formation in Silicon* (Tashkentsk. Gos. Univ., Tashkent, 1993).
7. I. D. Konozenko, A. K. Semenyuk, and V. I. Khivrich, in *Radiation Effects in Silicon* (Naukova Dumka, Kiev, 1974), p. 199.
8. V. L. Vinetskiĭ and G. A. Kholodar', in *Radiation Physics of Semiconductors* (Naukova Dumka, Kiev, 1979), p. 336.
9. B. I. Shklovskiĭ and A. L. Éfros, *Electronic Properties of Doped Semiconductors* (Nauka, Moscow, 1979; Springer-Verlag, New York, 1984).
10. J. M. Meese and P. J. Glairon, in *Neutron Transmutation Doping Semiconductors*, Ed. by J. M. Meese (Plenum, New York, 1979; Mir, Moscow, 1982).
11. E. Sonder and L. C. Templeon, *J. Appl. Phys.* **36**, 1811 (1965).
12. V. V. Bolotov, A. V. Vasil'ev, V. P. Kozhevnikov, *et al.*, *Fiz. Tekh. Poluprovodn. (Leningrad)* **12**, 1104 (1978) [*Sov. Phys. Semicond.* **12**, 656 (1978)].
13. *Semiconductor Doping by Nuclear Reaction Method*, Ed. by L. S. Smirnov (Nauka, Novosibirsk, 1981), p. 181.
14. A. V. Vasil'ev, S. A. Smagulova, and S. S. Shaĭmeev, *Fiz. Tekh. Poluprovodn. (Leningrad)* **16**, 140 (1982) [*Sov. Phys. Semicond.* **16**, 84 (1982)].
15. A. V. Vasil'ev, S. A. Smagulova, and S. S. Shaĭmeev, *Fiz. Tekh. Poluprovodn. (Leningrad)* **16**, 1183 (1982) [*Sov. Phys. Semicond.* **16**, 1279 (1982)].
16. M. K. Sheĭnkman and A. Ya. Shik, *Fiz. Tekh. Poluprovodn. (Leningrad)* **10**, 209 (1976) [*Sov. Phys. Semicond.* **10**, 128 (1976)].

Translated by A. Spitsyn

ELECTRONIC AND OPTICAL PROPERTIES OF SEMICONDUCTORS

Generation–Recombination Processes in Semiconductors

I. N. Volovichev^{1,2} and Yu. G. Gurevich²

¹ Institute of Radioelectronics, National Academy of Sciences of Ukraine, Kharkov, 310085 Ukraine

² Departamento de Fisica, CINVESTAV-IPN, 07000 Mexico, D.F., Mexico

Submitted June 22, 2000; accepted for publication August 16, 2000

Abstract—A unified methodical approach to investigate the transport phenomena in semiconductors is formulated. Various recombination models used in studying the transport phenomena and the establishment of equilibrium in semiconductor structures are analyzed. New expressions describing the recombination processes under the steady-state conditions in arbitrary temperature fields are derived. The recombination process in the hot-carrier theory used when the temperatures of the charge carriers and phonons do not coincide was analyzed. Manifestations of the quasi-neutrality condition in thermodynamic equilibrium and transport phenomena are studied. © 2001 MAIK “Nauka/Interperiodica”.

1. INTRODUCTION

In connection with a broad interest in transport phenomena in semiconductors and semiconductor structures, researchers often have to deal with nonequilibrium charge carriers. These may appear owing to various factors, more specifically, to the injection of majority or minority charge carriers, illumination with photons with energies higher than the band gap (photoeffect), etc. It has been shown recently that the emergence of nonequilibrium charge carriers affecting the charge transport is possible even in the approximation linear in the temperature and electric fields and is related to the redistribution of charge carriers in these fields [1]. The nonequilibrium-carrier recombination in the sample plays an important role in the above problems. The concentration of these carriers is defined by the following well-known continuity equations:

$$\begin{aligned}\frac{\partial n}{\partial t} &= g_n + \frac{1}{e} \operatorname{div} \mathbf{j}_n - R_n, \\ \frac{\partial p}{\partial t} &= g_p - \frac{1}{e} \operatorname{div} \mathbf{j}_p - R_p.\end{aligned}\quad (1)$$

Here, $n = n_0 + \delta n$ and $p = p_0 + \delta p$ are the electron and hole concentrations, where δn and δp are the concentrations of nonequilibrium charge carriers; \mathbf{j}_n and \mathbf{j}_p are the partial current densities of electrons and holes; g_n and g_p are the external-generation rates; and R_n and R_p are the carrier-recombination rates. In turn, the recombination rate $R_{n,p} = r_{n,p} - g_{T_n,T_p}$ is defined by the difference between the rates of two competing processes: the capture of charge carriers $r_{n,p}$ and their thermal generation g_{T_n,T_p} .

It is clear that the system of Eqs. (1) is generally incomplete and should be supplemented with the Poisson equation

$$\operatorname{div} \mathbf{E} = \frac{4\pi}{\epsilon} \rho, \quad (2)$$

where \mathbf{E} is the electric-field strength in a semiconductor, ρ is the space-charge density, and ϵ is the semiconductor permittivity.

In order to be able to use the system of Eqs. (1) and (2), we should specify the dependences of partial currents, the space-charge density, and the recombination rates on the nonequilibrium-carrier concentration. Unfortunately, in a great many publications devoted to these problems, there are the cases of incorrectness and, frequently, obvious errors; these fallacies are caused by the recombination itself [the terms R_n and R_p in Eqs. (1)] often described by the incorrect expressions

$$R_n = \delta n / \tau_n, \quad R_p = \delta p / \tau_p,$$

where τ_n and τ_p are the lifetimes of nonequilibrium charge carriers and are parameters of the semiconductor under consideration [2–7]. However, since the condition for the total-current continuity $\operatorname{div} \mathbf{j} = 0$ should be satisfied under the static conditions, an additional condition $\delta n / \tau_n = \delta p / \tau_p$ arises; the latter condition does not follow from any physical concepts and is difficult to interpret. In certain cases (see, for example, monograph [2]), this condition is used to reduce the number of variables, which is completely wrong. Sometimes, this condition is also considered as an expression relating to the lifetimes of charge carriers [3]. The latter approach is not physically meaningful and, in addition, is hardly constructive, because the carrier lifetimes no longer constitute the semiconductor parameters; rather, the

lifetimes are functions of the nonequilibrium-carrier concentrations that, in turn, should be determined, which leads to considerable mathematical difficulties.

Another approach based on the assumption that $R_n = R_p = \delta p / \tau_p$, where δp and τ_p are the concentration and lifetime, respectively, of the nonequilibrium minority carriers, is widely accepted [8]. In this case, the condition for the total-current continuity is identically satisfied; however, another basic contradiction takes place. This contradiction becomes especially evident if we consider a majority-carrier injection. Physically, it is obvious that the injected nonequilibrium majority carriers recombine. At the same time, formally, the recombination rate is equal to zero because there are no nonequilibrium charge carriers ($\delta p = 0$).

The problem is appreciably complicated if the temperature distribution in the sample is nonuniform (i.e., the temperature is coordinate-dependent). As a result, it becomes unclear from which value the nonequilibrium-carrier concentration is measured (i.e., what is meant by the quantities n_0 and p_0). A method for overcoming this difficulty has been suggested recently [9]; however, this method is rather artificial and is applicable only in the case of the known (fixed) temperature field.

Another problem is related to Poisson equation (2). Even when calculating the built-in electric fields that appear in inhomogeneous materials and semiconductor structures under the equilibrium conditions, the space charge is often described by expressions that are applicable to the analysis of only certain particular cases, without specifying the general applicability domain of the approximation used. In general, this issue remains poorly studied. Such a situation is even more widespread when one deals with nonequilibrium conditions.

We believe that all the above errors and inaccuracies are caused by this scope of phenomena not having been described from the standpoint of general concepts in either of the available monographs (or reviews). Sometimes, the correct starting expressions are written out, and then unjustified and uncontrolled approximations are used. An example of this type is provided by the wide-spread statement that the nonequilibrium concentrations of electrons and holes are equal to each other at each point of the sample in the case of band-to-band recombination [2].

We believe that it is expedient to consistently describe the procedure for determining the nonuniform equilibrium and nonequilibrium concentrations of the charge carriers in terms of the simplest models. We emphasize first of all that the majority of inferences (however, not all of them) presented below may be found in monographs, reviews, and papers published in journals. However, a correct consideration of one of the factors in the aforementioned publications is accompanied by the neglect of other factors that affect the studied effect to the same extent.

2. THERMODYNAMIC EQUILIBRIUM

It is convenient to start the construction of a completely self-consistent general procedure for solving the charge-transport problems by considering the simplest situation; i.e., the state of thermodynamic equilibrium. Henceforth, we restrict ourselves to linear analysis in order to avoid mathematical difficulties.

Thus, let us assume that we consider an arbitrary homogeneous semiconductor, in which the electron and hole concentrations are equal to n_0 and p_0 , respectively. Since we usually have $n_0 \neq p_0$, there is also a charge of electrons that have the concentration n_i^0 and are bound by ionized impurity centers. The total impurity-center concentration is equal to N_i . The sample is neutral at each point ($n_0 + n_i^0 - p_0 = 0$); consequently, there is no built-in field. The temperature distribution in the sample is also uniform ($T_0 = \text{const}$). The chemical-potential levels for electrons μ_n^0 and holes μ_p^0 are constant in space ($\mu_{n,p}^0 = \text{const}$) and coincide with each other ($\mu_n^0 = -\epsilon_g - \mu_p^0$, where ϵ_g is the semiconductor band gap); i.e., as should follow from the condition for thermodynamic equilibrium, the electrochemical-potential level remains unchanged in space and is common to all charge-carrier subsystems.

The situation in an inhomogeneous semiconductor may be described on the basis of above-outlined initial state of a homogeneous semiconductor. For the sake of definiteness, we assume that the inhomogeneity is caused by nonuniform doping; i.e.,

$$N_i(x) = N_i^0 + \delta N_i(x).$$

We now conceptually partition the sample into thin layers isolated from each other (so that drain of the charge carriers is impossible). After the introduced impurities have been ionized, the "equilibrium" charge-carrier concentrations are established in each such layer; these concentrations are identical to those in a massive homogeneous sample with the same impurity concentration in the entire volume of the sample. We denote these "equilibrium" concentrations as

$$n^0(x) = n_0 + \delta n(x), \quad p^0(x) = p_0 + \delta p(x),$$

correspondingly, the chemical potentials are defined by

$$\mu_{n,p}^0(x) = \mu_{n,p}^0 + \delta \mu_{n,p}(x).$$

Since electrons and holes are in equilibrium with one another in each layer, their chemical-potential levels coincide; i.e.,

$$\mu_n^0(x) = -\epsilon_g - \mu_p^0(x).$$

However, the chemical potentials are now spatially nonuniform; i.e., $\nabla \mu_{n,p} \neq 0$, so that there is no thermodynamic equilibrium between the layers. Nevertheless,

since the charge carriers have not yet been drained off, there is no space charge in the semiconductor.

If we now "join" the layers under consideration, the charge carriers flow from one layer to another, this being accompanied by the emergence of a built-in electric field and with the leveling-off of the electron and hole electrochemical potential. The state of thermodynamic equilibrium of an inhomogeneous system under consideration is characterized by a new charge-carrier distribution

$$n(x) = n^0(x) + \delta n_1(x), \quad p(x) = p^0(x) + \delta p_1(x)$$

as a result, a built-in electric field with the potential $\phi(x)$ comes into existence in the semiconductor. The chemical-potential level of electrons and holes changes and becomes

$$\mu_n = \mu_n^0(x) + \delta\mu_n'(x), \quad \mu_p = \mu_p^0(x) + \delta\mu_p'(x),$$

however, this level still satisfies the relation

$$\mu_n(x) = -\varepsilon_g - \mu_p(x)$$

and is not spatially constant, whereas the electrochemical-potential gradient is equal to zero $\nabla \tilde{\mu}_{n,p} = 0$ [$\tilde{\mu}_{n,p} = \mu_{n,p} \mp e\phi(x)$].

We note that, in fact, the transient process of the equilibrium establishment differs generally from the above-outlined scheme, because the duration of the establishment of equilibrium in each layer (this duration is on the order of the lifetime of nonequilibrium charge carriers in the semiconductor under consideration) much exceeds the Maxwell time during which the carriers flow from one layer to another. Thus, the flow of the charge carriers from one layer to another responds adiabatically to their generation, which is the source of nonequilibrium charge carriers in the case under consideration; i.e., these processes occur simultaneously, and it is impossible to physically separate the two stages of the transient process. In contrast, when the inhomogeneity is formed by bringing a fairly thin semiconductor into contact with another material, the transfer of the charge carriers under the effect of the difference between the thermodynamic work functions of the two contacting materials becomes the primary process. Formation of the common chemical-potential level sets in only at the next stage. Nevertheless, the above-outlined procedure (albeit artificial and conceptual) for partitioning the transient process into several stages, which imply the existence of equilibrium with respect to one of the factors at each of the stages, is rather productive. This procedure makes it possible to solve certain problems of analyzing the transport processes [9, 10] and to gain better insight into the special features of formation of the equilibrium state (for example, the variation of the total number of charge carriers in a heterojunction structure [11]).

Physically, the commonness (but in general not the constancy) of the charge-carrier chemical potential

($\mu_n = -\varepsilon_g - \mu_p$) implies that the rate of charge-carrier capture by impurity centers (or the rate of band-to-band recombination) is equal to the rate of the carriers' thermal generation. Thus, it is assumed that the recombination rate in the sample is equal to zero; this rate depends on the concentrations of all types of particles involved in a recombination event.

Thus, for the state of equilibrium, we have

$$R_n(n, p, n_t) = 0, \quad (3)$$

$$R_p(n, p, n_t) = 0. \quad (4)$$

The third equation is, in fact, the condition for the balance of particles at the impurity levels. Under static conditions, this condition is given by

$$R_n(n, p, n_t) = R_p(n, p, n_t). \quad (5)$$

We call attention to the fact that Eq. (5), formulated on the basis of considering the balance of particles at an impurity level, also ensures the identical fulfillment of the requirement imposed on any static charge transport $\text{div} \mathbf{j} = 0$; this requirement follows from the Maxwell equations.

It can be easily seen that Eqs. (3)–(5) are not linearly independent if there is thermodynamic equilibrium; however, we have the condition for the vanishing of the charge-carrier partial currents $\mathbf{j}_n = \mathbf{j}_p = 0$ instead of one of those equations. We note that this condition is simply the condition (reformulated in terms of partial currents) for the constancy of the electrochemical potential.

The fourth equation, closing the system of equations with the four unknowns under consideration, is Poisson Eq. (2). It is this system of equations that represents the most general formulation of the problem of thermodynamic equilibrium in an inhomogeneous semiconductor.

This problem allows an evident transition to a uniform semiconductor. In fact, if the sample is homogeneous, there is neither an electric field nor space charge ($\mathbf{E} = 0$ and $\rho = 0$), the Poisson equation is fulfilled identically, and the system consists of only three equations with the three unknowns n , p , and n_t ; i.e., this passage to the limit leads, as before, to the correct mathematical formulation of the problem.

If the concentration of charges at the impurity levels n_t is also known (specified), the number of variables and equations are further reduced to two. Self-consistency of such a passage is caused by the condition $R_n(n, p, n_t) = R_p(n, p, n_t)$ being satisfied identically for a correctly specified concentration of charges at the impurity levels, at least for the equilibrium (sought-for) charge-carrier concentrations, and there is no overtermination in the system of equations.

Finally, we study the outlined passage in the frequently used approximation of quasi-neutrality [12]. We assume that the characteristic parameters of the problem (in this case, these are the dimensions of the sample) are much larger than the Debye screening

radius r_D of the majority charge carriers. In this case, we may assume that $\delta p = 0$; thus, the Poisson equation becomes redundant. If, as was mentioned above, we employ the widely used assumption that the charge concentration at the impurity levels is unchanged (we present the corresponding criteria in Section 4), the quasi-neutrality condition is reduced to the equality $\delta n = \delta p$. On the other hand, the commonness of the chemical-potential level (i.e., the absence of recombination) requires that $\delta \mu_n = -\delta \mu_p$ or, for a nondegenerate semiconductor, $\delta p = -(p_0/n_0)\delta n$. The latter means that, in a monopolar semiconductor (for example, in an n -type one where $n_0 \gg p_0$), the space charge of the minority charge carriers may be disregarded. However, in view of the quasi-linearity condition, this means that the majority charge carriers do not form the space charge as well ($\delta n = 0$). Similarly, for an intrinsic semiconductor, the consistency of the conditions for quasi-neutrality and for the commonness of the chemical-potential level is possible only if $\delta n = \delta p = 0$. In other words, for any semiconductor, quasi-neutrality in equilibrium means that the charge-carrier concentration is invariant under any external effect (for example, if a polarizing field is applied or a solid-state structure is formed). This inference can be easily understood physically. Actually, any such effect which leaves the system in the state of equilibrium (i.e., does not give rise to a current) and does not affect the charged-impurity concentration is bound to be screened at a distance on the order of the Debye radius; i.e., in the approximation under consideration ($L \gg r_D$), the screening is due to the surface charges.

3. HOT CHARGE CARRIERS IN A HOMOGENEOUS SAMPLE

As an example of a more complex situation, we consider a homogeneous bipolar semiconductor, in which uniform heating of one of the subsystems (for the sake of definiteness, the electron subsystem) occurs. Such a situation may occur under exposure of a semiconductor to low-absorption light with photons that have energies lower than the band gap, in which case the free-carrier absorption is dominant.

In this example, as in the case of thermodynamic equilibrium, there is neither a total current (the circuit is open) nor are there partial currents of charge carriers. However, there is an energy nonequilibrium: due to the heating of electrons, their temperature (T_e) differs from the temperature of holes (T_h) and phonons (we assume that the hole and phonon temperatures are equal); thus, $T_e \neq T_h = T_0$.

We consider the process of establishing the steady state consequently (in two stages).

At the first stage, the concentration of the electron gas remains unchanged under heating; however, the chemical-potential level changes (as a result of its explicit dependence on temperature) but remains uni-

form owing to the uniformity of heating. In the linear approximation, this change is equal to

$$\delta \mu_n = \mu_n^0(T_e - T_0)/T_0, \quad (\mu_n'(T_e) = \mu_n^0 + \delta \mu_n).$$

The chemical-potential level of the holes remains unchanged in this situation; i.e., the chemical-potential levels of electrons and holes split as

$$\mu_n'(T_e) \neq -\epsilon_g - \mu_p^0(T_0).$$

However, splitting the chemical-potential levels means, in turn, that there is recombination, which ultimately forms the chemical-potential level common to both electrons and holes $\mu_n(T_e) = -\epsilon_g - \mu_p(T_0)$. In fact, if we have a spatially uniform and static situation with the absence of external generation, Eqs. (1) are reduced to the equalities $R_n = 0$ and $R_p = 0$, which occurs only if the chemical-potential levels coincide for two types of charge carriers. We note that, generally, both chemical potentials change; i.e.,

$$\mu_n(T_e) \neq \mu_n'(T_e), \quad \mu_p(T_0) \neq \mu_p^0(T_0).$$

In other words, an energy nonequilibrium gives rise to nonequilibrium in the concentration as a result of recombination.

Mathematical analysis of the situation under consideration is similar to the consideration of thermodynamic equilibrium in a homogeneous sample, except for the fact that, in the model of a specific recombination mechanism, the relevant expression should be derived for the recombination rate. This rate is a function not only of the charge-carrier concentration but also of the temperatures of the holes (of the lattice) and electrons. The latter is caused by an explicit temperature dependence of the cross sections for the charge-carrier capture by impurities or by each other.

As a result, in order to describe the case of uniform heating under consideration, we use a system of four equations; these include the equations

$$R_n(n, p, n_i; T_e, T_0) = 0, \quad R_p(n, p, n_i; T_e, T_0) = 0,$$

an equation for the concentration of occupied impurity levels n_i ; and a condition for electroneutrality (i.e., the Poisson equation for a homogeneous material). One of these equations results from the other three, which ensures the solvability of this system of equations (we emphasize that we have just three independent variables: n , p , and n_i).

We draw attention to the fact that, as in the previously considered situation, the expressions for the recombination rates $R_n(n, p, n_i; T_e, T_0)$ and $R_p(n, p, n_i; T_e, T_0)$ generally differ; i.e., the above representation does not include the identity $R_n \equiv R_p$. However, if we eliminate n_i using the electroneutrality condition or an equation for the impurity level (this equation is reduced

exactly to the condition $R_n = R_p$ under static conditions), we return to the identity

$$\begin{aligned} & R_n(n, p, n_t; T_e, T_0) \\ & \equiv R_p(n, p, n_t; T_e, T_0) \equiv R(n, p; T_e, T_0) \end{aligned}$$

which is in complete conformity with the condition for continuity of the total current $\text{div} \mathbf{j} = 0$.

It should be remembered that we consider the charge-carrier temperatures as given. Otherwise, it is necessary to add the thermal-balance equation.

Further simple calculations show that, as was mentioned above, energy nonequilibrium results (if there is a temperature dependence of the capture cross sections) in a shift of the state of dynamic equilibrium between the processes of capture and inverse thermal generation, thus changing the charge-carrier concentration. This effect has been considered in detail recently [13]; therein, the conditions under which the effect is most pronounced or is negligible have been analyzed.

4. THE PHENOMENA OF TRANSPORT OF NONEQUILIBRIUM CHARGE CARRIERS

We come now to a consideration of the situation when the current flows, with the nonequilibrium charge carriers being present in the semiconductor. We assume that the charge transport is not accompanied by the heating of the sample; i.e., we assume that the temperature is constant throughout the semiconductor and is equal to its equilibrium value T_0 . We first analyze the situation when the nonequilibrium state is not related to generation (i.e., when there is no external bulk generation of nonequilibrium charge carriers, e.g., with light). However, a surface generation or injection of charge carriers may exist, which should be taken into account by introducing the relevant terms into the boundary conditions. We note that the correct formulation of the boundary conditions with allowance made for the current is very important in order to adequately describe the kinetic phenomena in bounded semiconductors. This problem is discussed in the last section of this paper.

In what follows, we restrict ourselves to the analysis of the static charge transport (when the nonequilibrium-carrier concentration is time-independent), because it is under these conditions that the contradictions in the conventional description of kinetic effects manifest themselves most clearly. In order to avoid mathematical difficulties, we perform the consideration in the linear approximation, although the approach outlined below is applicable also to a general nonlinear case. It can be used to construct a correct model of nonlinear charge transport for numerical simulation.

Henceforth, we use the symbol “ $\delta \dots$ ” to denote the deviations of the corresponding quantities from their equilibrium values (indicated by the subscript “0”).

The system of equations describing the situation under consideration is written as

$$\text{div} \mathbf{j}_n = eR_n(n, p, n_t), \quad \text{div} \mathbf{j}_p = -eR_p(n, p, n_t), \quad (6)$$

$$R_n(n, p, n_t) = R_p(n, p, n_t), \quad (7)$$

$$\text{div} \mathbf{E} = 4\pi\rho(n, p, n_t). \quad (8)$$

This system of equations is complete because we have four independent equations for four unknowns n, p, n_t , and ϕ .

We emphasize two circumstances. First, in Eq. (8), the space charge ρ is generally a function of not only the charge-carrier concentrations n and p but also of the impurity-charge concentration n_t , which may vary when the current flows. Second, we once again draw attention to the fact that equality (7) is an equation for the concentration of electrons at the impurity level n_t . After elimination of the latter, equality (7) transforms into an identity in complete conformity with the equation for the charge continuity $\text{div} \mathbf{j} = 0$.

We now assess the role of the nonequilibrium charge of trapped charge carriers in the formation of nonequilibrium space charge and the criteria for disregarding the quantity n_t . To this end, we eliminate n_t from Eqs. (6)–(8) choosing the Shockley–Read model for recombination [14]. According to this model, the rate of electron capture by an impurity level and the rate of the inverse process (thermal generation) are given, respectively, by

$$r_n = \alpha_n n (N_t - n_t), \quad g_{nT} = \alpha_n n_1 n_t, \quad (9)$$

and the electron-recombination rate is equal to $R_n = r_n - g_{nT}$, where N_t is the total concentration of the impurity states (in order to avoid confusion, we remind the reader that, in the model under consideration, n_t is the concentration of occupied impurity states), α_n is the capture coefficient for electrons, and n_1 is the parameter characterizing the impurity level and, physically, represents the electron concentration which would take place should the Fermi level in the semiconductor coincide with the impurity level.

Similarly, for holes we have

$$r_p = \alpha_p n_t p, \quad g_{pT} = \alpha_p p_1 (N_t - n_t). \quad (10)$$

Substituting expressions (9) and (10) into Eq. (7) and using the linear approximation, we obtain the following expression for the concentration of occupied impurity states:

$$\delta n_t = a \delta n + b \delta p.$$

Here,

$$a = \frac{\alpha_n n_1 N_t}{(n_0 + n_1)[\alpha_n(n_0 + n_1) + \alpha_p(p_0 + p_1)]}, \quad (11)$$

$$b = \frac{\alpha_p n_0 N_t}{(n_0 + n_1)[\alpha_n(n_0 + n_1) + \alpha_p(p_0 + p_1)]}. \quad (12)$$

As a result, we have $R_n = R_p = \delta n/\tau_n + \delta p/\tau_p$, with $\tau_n/\tau_p = n_0/p_0$. We emphasize once again that the quantities τ_n and τ_p are not strictly speaking the lifetimes of charge carriers even in the linear approximation, although these quantities have the dimension of time.

It can be easily recognized that $\tau_n \gg \tau_p$ in an n -type semiconductor and $\tau_p \gg \tau_n$ in a p -type semiconductor. Thus, in a monopolar semiconductor and in situations close to quasi-linearity ($\delta n \approx \delta p$), the recombination rate is actually defined by the characteristic ("lifetime") of minority charge carriers. In an intrinsic semiconductor, the parameters τ_n and τ_p are equal to each other. However, these parameters physically represent the doubled lifetime of electron-hole pairs only in the case of quasi-neutrality. If there is no quasi-neutrality, we cannot use the term lifetime even for an intrinsic semiconductor if $\delta n \neq \delta p$. As can be easily verified by analyzing expressions (11) and (12), in the case of an n -type semiconductor ($n_0 \gg p_0$) and high temperatures (when the quasi-Fermi levels of electrons and holes are distant from the impurity level, which means that the donor level is completely ionized), we have

$$1 \gg a \gg b, \text{ i.e. } \delta n_t \ll \delta n. \quad (13)$$

Similarly, for a p -type semiconductor ($p_0 \gg n_0$) and at high temperatures, we have the inequality

$$1 \gg b \gg a, \quad (14)$$

so that the concentration of nonequilibrium trapped charge carriers δn_t may be again neglected.

The situation changes if temperatures are low or if there is a fairly high concentration of deep impurity levels located in the vicinity of the midgap, i.e., in the vicinity of the Fermi level in an intrinsic semiconductor at equilibrium. In this case, the concentration δn_t is comparable (to an order of magnitude) to the concentration of nonequilibrium charge carriers and should be taken into account in the Poisson equation. In other words, if the quasi-Fermi levels of electrons and holes are located far away from the impurity level when the current flows, the system of Eqs. (6)–(8) can be simplified by ignoring the variation in the bound-charge concentration; thus, we have

$$\text{div} \mathbf{j}_n = eR(n, p), \quad \text{div} \mathbf{j}_p = -eR(n, p), \quad (15)$$

$$\text{div} \mathbf{E} = 4\pi\rho(n, p). \quad (16)$$

Both the space charge and the recombination rate depend now only on the concentrations of nonequilibrium mobile charge carriers δn and δp . The equation for the impurity level (7) is in this case an identity and, naturally, is eliminated from the system of equations.

We also note that, if in a specific problem we have, in addition, $\delta p \ll \delta n_t$, we should drop δp in the Poisson equation (16), in the expression for the charge density

$\rho(n, p)$, in order to avoid exceeding the accuracy; i.e., we should assume that $\rho = \rho(n)$.

This system of equations can be further simplified if the conditions for quasi-neutrality are satisfied; i.e., if the characteristic parameters of the problem much exceed the Debye radius. In general, especially in the nonlinear case, we have to verify the obtained solutions because the characteristic parameters of the problem may depend on, e.g., an applied field and, consequently, on the nonequilibrium concentrations and may become comparable to the Debye radius in strong fields.

In the quasi-neutrality approximation, we have $\delta p = 0$. In view of conditions (13) and (14), the concentrations of the nonequilibrium electrons and holes coincide: $\delta n = \delta p$; thus, the Poisson equation becomes redundant and may be subsequently used to validate the solution obtained:

$$\text{div} \delta \mathbf{E} \ll 4\pi(\delta p - \delta n)/\epsilon;$$

finally, the charge transport is described by two equations for $\delta n = \delta p$ and ϕ :

$$\text{div} \mathbf{j}_n = eR(n, p), \quad \text{div} \mathbf{j}_p = -eR(n, p). \quad (17)$$

5. KINETIC PHENOMENA UNDER CONDITIONS OF CHARGE-CARRIER GENERATION

As was already mentioned, the consideration suggested above is applicable if there is no external charge-carrier generation (photogeneration). In order to take into account this generation, we have to repeat all the above-outlined reasoning [starting with Eqs. (1)], retaining, however, the terms g_n and g_p .

It is worth noting that, in general, the generation rates for electrons and holes may differ even under static conditions (for example, if we deal with the impurity absorption of light, as a result of which only one type of charge carriers are generated). In turn, in the static situation, the recombination rates may also differ, because the equality $R_n - R_p + G = 0$, where $G \equiv g_n + g_p$, must be satisfied in order to meet the condition for the current continuity $\text{div} \mathbf{j} = 0$. As before, the latter equality represents a kinetic equation for impurity levels in the static situation. After the concentration of bound charges n_t has been eliminated, the system of equations describing the static flow of current under conditions of constant external generation of charge carriers has the following form:

$$\frac{1}{e} \text{div} \mathbf{j}_n = \beta_n g_n + \beta_p g_p + R(n, p), \quad (18)$$

$$-\frac{1}{e} \text{div} \mathbf{j}_p = \beta_n g_n + \beta_p g_p + R(n, p), \quad (19)$$

$$\text{div} \mathbf{E} = 4\pi\rho(n, p, g_n - g_p). \quad (20)$$

We emphasize that, in contrast to Eqs. (1), the “effective” generation rates

$$g_{\text{eff}} \equiv \beta_n g_p + \beta_p g_n,$$

which appear in Eqs. (18) and (19), coincide irrespective of the values of true generation rates g_n and g_p . This circumstance ensures that the conditions for the continuity of the total current are satisfied identically for any concentrations of nonequilibrium charge carriers and for the arbitrary rates of their generation.

The coefficients β_n and β_p in Eqs. (18) and (19) are specified by the recombination mechanism. For example, $\beta_n = \beta_p = 1/2$ for the band-to-band recombination, whereas, for the Shockley–Read model of recombination, we have

$$\beta_n = \frac{\alpha_p(p_0 + p_1)}{\alpha_n(n_0 + n_1) + \alpha_p(p_0 + p_1)}, \quad (21)$$

$$\beta_p = \frac{\alpha_n(n_0 + n_1)}{\alpha_n(n_0 + n_1) + \alpha_p(p_0 + p_1)}.$$

In all the cases, the relationship $\beta_n + \beta_p = 1$ is valid.

We draw attention to the fact that, in the static situation, the generation-related terms also appear in the Poisson equation but only in the form of the difference between the generation rates of electrons and holes. Physically, this is clearly evident; in fact, a variation in the concentration of occupied impurity states (i.e., the emergence of space charge caused directly by photogeneration) may occur only if the generation rates of electrons and holes differ.

For the band-to-band generation, we have $g_n \equiv g_p = g$ and $\beta_n = \beta_p$, so that the charge-transport equations have the following well-known form:

$$\frac{1}{e} \text{div} \mathbf{j}_n = g + R(n, p), \quad -\frac{1}{e} \text{div} \mathbf{j}_p = g + R(n, p), \quad (22)$$

$$\text{div} \mathbf{E} = 4\pi\rho(n, p). \quad (23)$$

We would like to attract attention to the following circumstance. It is often assumed in various publications (see, for example [2]) that the concentrations of nonequilibrium charge carriers are always equal to each other ($\delta n = \delta p$) in the cases of band-to-band recombination and generation. However, this assumption by no means follows from Eqs. (22) and (23). In fact, if the generation rates for electrons and holes (like the rates of their recombination) coincide, their concentrations are not necessarily equal (as the equality of the derivatives of two functions does not ensure that the functions themselves are equal). Generated charge carriers may be immediately separated, for example, by an external field. For the equality $\delta n = \delta p$ to be satisfied, the fulfillment of the quasi-neutrality conditions (rather than the presence of only the band-to-band transitions) is required (generally speaking, the latter represents a necessary but not sufficient condition for the equality of

concentrations of the nonequilibrium electrons and holes).

For a monopolar semiconductor (for the sake of definiteness, an n -type semiconductor), we have $\beta_n \ll \beta_p$, and, if $g_n \approx g_p$, the system of Eqs. (18)–(20) has the following form:

$$\frac{1}{e} \text{div} \mathbf{j}_n = g_p + R_n(n, p), \quad (24)$$

$$-\frac{1}{e} \text{div} \mathbf{j}_p = g_p + R_p(n, p),$$

$$\text{div} \mathbf{E} = 4\pi\rho(n, p, g_n - g_p). \quad (25)$$

We emphasize that in this case the static charge transport is directly affected only by the minority-carrier generation (whereas the majority-carrier generation with a rate different from that of the minority-carrier generation manifests itself indirectly via the Poisson equation).

As an illustration of using the above-outlined approach, we analyze a homogeneous monopolar semiconductor (for the sake of definiteness, let it be an n -type semiconductor) under conditions of uniform photogeneration of charge carriers.

Let us assume that only the generation of majority charge carriers (electrons) takes place, so that $g_p = 0$; i.e., only the transitions of electrons from the impurity level to the conduction band and back occur (the photon energy exceeds the impurity-ionization energy but is smaller than the band gap). The system of equations describing this situation may be then written as

$$g_n + R_n(n, n_t) = 0, \quad \text{div} \mathbf{E} = 4\pi\rho(n, n_t, g_n). \quad (26)$$

It is noteworthy, as is generally accepted in such a situation, that we ignore the presence of the minority charge carriers ($p = 0$ and $R_p = 0$).

In view of the homogeneity of the problem under consideration, the Poisson equation is reduced to the condition for electroneutrality of the sample $\delta n = -\delta n_t$ (with electroneutrality occurring for arbitrary dimensions of the semiconductor, in contrast to the quasi-neutrality approximation).

At a high temperature ($n_1 \gg N_t$), a solution to the system of Eqs. (26) is given by

$$\delta n = \frac{g_n}{\alpha_n n_1}, \quad \delta n_t = -\delta n, \quad \delta p = 0. \quad (27)$$

If we do not neglect the minority charge carriers, we naturally obtain the same result; i.e., the generation of majority charge carriers virtually does not affect the concentration of the minority charge carriers ($\delta p \ll \delta n$).

We now consider the opposite limiting case, i.e., the generation of only the minority charge carriers ($g_n = 0$). We note that, although such a situation is hardly feasible (since the photon energy required for the minority-carrier generation is more than sufficient for the majority-carrier generation), this case is quite interesting

methodically and provides an insight into the processes that occur when the charge carriers of both types are generated with different rates. As can be easily verified, a solution of the system of equations for this limiting case yields the following result:

$$\delta n = \frac{n_1 g_p}{\alpha_p n_0 N_t}, \quad \delta p = \delta n, \quad \delta n_i \ll \delta n. \quad (28)$$

We note that the first expression in (28) can be represented as

$$\delta n = \frac{n_1 n_1 \alpha_n}{N_t n_0 \alpha_p} \delta n_{(27)}, \quad (29)$$

where $\delta n_{(27)}$ is the concentration of nonequilibrium majority photocarriers in the above-considered situation of generation of only the majority charge carriers; i.e., we arrive at solution (27). Since $n_1 \gg N_t$ and $n_1 \gg n_0$ at high temperatures as follows from the definition of n_1 , it is obvious that the generation of minority charge carriers affects the majority-carrier concentration more profoundly than their direct generation does. We also draw attention to the fact that although $\delta n_i \ll \delta n$, we nevertheless have $\delta n_i \gg \delta n_{(27)}$.

Thus, if both the majority and minority charge carriers are simultaneously generated in a semiconductor, the minority-carrier generation more profoundly affects both the occupation of the impurity states and the majority-carrier concentration, and, as a result, the flow of current or the formation of photovoltage.

6. GENERATION AND RECOMBINATION IN NONUNIFORM TEMPERATURE FIELDS

We now analyze the establishment of a steady mode of charge transport in a nonuniform temperature field $T = T_0 + \delta T(x)$. In order to simplify the calculations, we assume that the temperature nonuniformity is small (i.e., $\delta T(x) \ll T_0$) and that the temperature gradient is constant ($\nabla T = \text{const}$). When describing this seemingly simple thermoelectric problem, a number of difficulties arise nevertheless; these difficulties are most evident in the case of a bipolar semiconductor. The main difficulty is related to the form of representation of the recombination-related term. To the linear approximation, this term may be represented as $R(\delta n, \delta p)$. However, the question arises as to value from which the nonequilibrium-carrier concentration should be reckoned in a nonuniform temperature field: from $n_0(T_0)$, $n_0[\overline{T(x)}]$, or $n_0[T(x)]$. The answer to this question was provided for the first time by Gurevich *et al.* [9] on the basis of considering the stage-by-stage establishment of a steady-state mode in a temperature field. By analogy with the previously considered example of the equilibrium establishment in a nonuniformly doped semiconductor, the equilibrium charge-carrier concentration is established at the first stage in each conceptually iso-

lated layer; this concentration corresponds to the specified local temperature and is given by $n = n_0(T_0) + \delta n'[\delta T(x)]$. This change in the concentration due to the temperature nonuniformity may be conceived as a manifestation of the chemical-potential inhomogeneity, however at a constant temperature. At the second stage, the drain of electrons and holes occurs under the effect of the chemical-potential gradient. The resulting distribution of charge carriers in the second stage is related to a built-in thermoelectric field and to the vanishing of the electrochemical-potential gradient $\nabla(\mu - e\phi) = 0$. Naturally, the resulting charge-carrier distribution at the second stage should ensure that the chemical-potential level is common to both electrons and holes ($\mu_p = -\epsilon_g - \mu_n$), which is exactly one of the conditions for determining the corrections to the concentrations. It is the carrier-concentration distribution obtained at the second stage that should be considered as the equilibrium one in the formulas for recombination. In the third stage, the temperature gradient plays the role of an external driving force; this circumstance is taken into account in determining the true carrier-concentration distribution in a semiconductor subjected to a nonuniform temperature field.

It is worth noting that the above-outlined procedure is found to be very convenient mathematically; in fact, in each stage (we emphasize that, in contrast to the method of successive approximations, all the corrections are of the same order in the case under consideration), linear differential equations with constant coefficients are obtained.

A drawback of the outlined method is (in addition to a certain awkwardness) that it cannot be used if the temperature field is not specified and should be determined from the self-consistent solution of the transport problem. This difficulty may be obviated by reconsidering the statistics of the transitions between the bands and impurity levels with allowance made for the temperature dependence of the recombination characteristics.

By performing simple calculations similar to those presented in Section 4, we easily verify that the recombination rate in the case of static charge transport in a nonuniform temperature field can be generally described in the linear approximation by the following expression valid for any recombination mechanism:

$$R_n = R_p = \frac{\delta n}{\tau_n} + \frac{\delta p}{\tau_p} + \gamma \delta T. \quad (30)$$

Here, the parameter γ is given by

$$\gamma = \frac{2 n_i \partial n_i}{\tau_n p_0 \partial T} = \frac{2 n_i \partial n_i}{\tau_p n_0 \partial T}, \quad (31)$$

where n_i is the charge-concentration in an intrinsic semiconductor at a temperature of T_0 .

It is instructive to note that the generation (recombination) rate in a semiconductor subjected to a nonuniform temperature field is, generally speaking, found to be nonzero even in the absence of current and photoexcitation. Thus, in the problems where this effect cannot be disregarded (for example, when dealing with the photoacoustic phenomenon; for more details, see [15]), we should consider not only the energy balance but also transport Eqs. (1). It can be easily seen from formula (31) that this is especially important for intrinsic semiconductors with a fairly narrow band gap and, consequently, with a high concentration of intrinsic charge carriers.

7. THE BOUNDARY CONDITIONS

We would like to draw the reader's attention to another issue which very often acts as a source of inaccuracies and errors in describing transport phenomena and, in our opinion, has not been adequately considered in the publications available. The above equations are differential and, as such, require the boundary conditions to be specified.

In general, additional specific mechanisms of the charge-carrier recombination are operative at the semiconductor surface; it is in the boundary conditions that these mechanisms should be correctly taken into account. Since the surface recombination is statistically similar to the volume recombination, all the above reasoning should be used in formulating the boundary conditions.

In addition, it is necessary to pay attention to the fact that the charge carriers of each type can exist and move in any of the contacting media. As an example, we can mention a metal–(hole semiconductor)–metal structure. Assuming that neither the volume nor surface types of recombination occur and taking into account that the hole current is zero in a metal, we can easily see that only the minority carriers (electrons) would be involved in charge transport through the semiconductor. It is clear that, in this case, the resistance of the sample will be found to be much higher than it might be expected [9].

Unfortunately, the boundary conditions often used even in the widely known publications are incorrect. We give just a single example that confirms the aforesaid. In considering the transport problems in semiconductor structures, the following boundary conditions (for example, for electrons, irrespective of whether they are the majority or minority charge carriers) are widely used [2]:

$$j_n|_I = s\delta n|_I.$$

Here, s is the surface-recombination rate at the interface between two conducting media I. However, this condition physically means that the charge carriers are not transported through the contact; rather, they are

generated or recombine at this contact. Thus, the entire current in the circuit is formed solely by the surface-recombination mechanisms. As a rule, this is not the case in actual structures.

Another example is related to the disregard to surface recombination in transport problems without properly assessing the correctness of such an approximation. Such an approach may yield erroneous results because the effect of surface recombination on transport processes is evident even in the approximation linear in the field [1]. The method outlined in [10] and aimed at formulating the correct boundary conditions by introducing phenomenological constants that characterize carrier transport through the interface between two media appears to be very effective in solving the above problems. If required, these constants should be calculated using the microscopic theory of a specific contact.

8. CONCLUSION

The above analysis shows that, in the context of unified physical concepts, it is possible to describe the transport phenomena in semiconductors and semiconductor structures without detailing the specific mechanisms of the generation–recombination processes. We demonstrated that the presence of temperature fields and a difference between the temperatures of charge carriers and phonons may appreciably affect the recombination processes in studying the transport phenomena even in an approximation that is linear in its external factors.

We clarified the physical significance of the widely used quasi-neutrality approximation and studied the possible consequences of using this approximation.

ACKNOWLEDGMENTS

We thank CONACyT (Mexico) for partial support of this study.

REFERENCES

1. Yu. G. Gurevich, G. N. Logvinov, G. Espejo, *et al.*, *Fiz. Tekh. Poluprovodn.* (St. Petersburg) **34**, 783 (2000) [*Semiconductors* **34**, 755 (2000)].
2. V. L. Bonch-Bruевич and S. G. Kalashnikov, *Physics of Semiconductors* (Nauka, Moscow, 1990).
3. R. A. Smith, *Semiconductors* (Cambridge Univ. Press, Cambridge, 1961).
4. P. I. Baranskiĭ, V. P. Klochkov, and I. V. Potykevich, *Semiconductor Electronics: A Handbook* (Naukova Dumka, Kiev, 1975).
5. I. Auth, D. Genzow, and K. Herrmann, *Photoelektrische Erscheinungen* (Akademie-Verlag, Berlin, 1977; Mir, Moscow, 1980).
6. S. M. Ryvkin, *Photoelectric Effects in Semiconductors* (Fizmatgiz, Leningrad, 1961; Consultants Bureau, New York, 1964).

7. D. A. Neamen, *Semiconductor Physics and Devices: Basic Principles* (Irwin, Homewood, 1992).
8. S. Sze, *Physics of Semiconductor Devices* (Wiley, New York, 1981; Mir, Moscow, 1984).
9. Yu. G. Gurevich, G. N. Logvinov, O. I. Lubimov, and O. Yu. Titov, *Phys. Rev. B* **51**, 6999 (1995).
10. Yu. G. Gurevich, *J. Thermoelectr.*, No. 2, 5 (1997).
11. I. M. Rarenko, S. L. Korolyuk, V. M. Koshkin, and S. S. Moskalyuk, *Nauk. Visn. Chernivets. Univ., Fiz.*, No. 29, 45 (1998).
12. V. P. Silin and A. A. Rukhadze, *Electromagnetic Properties of Plasma and Plasmalike Media* (Gosatomizdat, Moscow, 1961).
13. Yu. G. Gurevich and I. N. Volovichev, *Phys. Rev. B* **60**, 7715 (1999).
14. W. Shockley and W. T. Read, *Phys. Rev.* **87**, 835 (1952).
15. I. N. Volovichev, L. Villegas, G. González de la Cruz, and Yu. G. Gurevich, *J. Appl. Phys.* (in press).

Translated by A. Spitsyn

**ELECTRONIC AND OPTICAL PROPERTIES
OF SEMICONDUCTORS**

Capacitance–Voltage Characteristics of p – n Structures Based on (111)Si Doped with Erbium and Oxygen

A. M. Emel'yanov*, N. A. Sobolev*, and A. N. Yakimenko**

* *Ioffe Physicotechnical Institute, Russian Academy of Sciences, St. Petersburg, 194021 Russia*

** *St. Petersburg State Technical University, St. Petersburg, 195251 Russia*

Submitted August 24, 2000; accepted for publication September 5, 2000

Abstract—Capacitance–voltage characteristics of tunneling diodes fabricated by co-implantation of erbium and oxygen in single-crystal (111)Si wafers have been studied. Anomalous enhancement of the p – n -junction capacitance with increasing reverse bias has been observed at certain temperatures depending on the implantation dose. The rise in capacitance (decrease in the space charge region width) is associated with the formation of deep levels of high density in the band gap of n -layer of the p – n junction and electron emission from these levels in the space charge region with increasing voltage. The obtained results show that the parameters of the defects responsible for the levels depend on the erbium and oxygen implantation doses. © 2001 MAIK “Nauka/Interperiodica”.

1. INTRODUCTION

Implantation of erbium and oxygen ions in single-crystal silicon is used to fabricate Si(Er,O) light emitting diodes [1–7]. These diodes emit at a wavelength $\lambda \approx 1.54 \mu\text{m}$ corresponding to electron transitions of Er^{3+} ions from the first excited state $^4I_{13/2}$ to the ground state $^4I_{15/2}$. The room temperature electroluminescence (EL) from erbium ions has been observed under direct [1] and reverse [1–7] bias in Si(Er,O) diodes in tunnel [1–3] and avalanche [3–7] breakdown regimes, with (100) [1, 4, 6] and (111) [2, 3, 5–7] Si orientations. In earlier studies of electroluminescent and electrical properties of Si(Er,O) diodes in the avalanche regime, we found a substantial difference between (100) and (111)Si diodes [2–7]. In particular, the temperature dependences of the EL intensity differ widely. A steady decrease in the EL intensity from 80 K to room temperature is typical of (100)Si diodes at fixed reverse current [4, 6]; for (111)Si(Er,O) diodes, “anomalous” temperature dependences are observed in the breakdown regime, including a portion of rising EL intensity (temperature enhancement) with increasing sample temperature [3, 5, 6]. This effect was explained for the first time in [5] on the assumption that a high density of levels filled by the flowing current are present in the silicon band gap (at low temperature, hole traps) in the erbium- and oxygen-doped (111)Si region. In terms of this model, the EL temperature enhancement is accounted for by thermal depletion of traps, modifying the breakdown characteristics.

In the present work, another unusual property of (111)Si(Er,O) diodes was discovered and studied. Namely, in the pre-avalanche range of bias, intervals of

a rise in capacitance with increasing applied voltage are observed in the capacitance–voltage (C – V) characteristics of reverse-biased p – n junctions at certain temperatures, depending on the erbium and oxygen implantation dose.

2. EXPERIMENTAL

Erbium ions with energies of 2.0 and 1.6 MeV and doses $3 \times 10^{14} \text{ cm}^{-2}$ (sample 3.2) and $9 \times 10^{14} \text{ cm}^{-2}$ (samples 3.3 and 3.5) and oxygen ions with energies of 0.28 and 0.22 MeV and doses $3 \times 10^{15} \text{ cm}^{-2}$ (sample 3.2) and $9 \times 10^{15} \text{ cm}^{-2}$ (samples 3.3 and 3.5) were implanted in polished Czochralski-grown n -Si wafers. Samples 3.2 and 3.3 were fabricated on (111)Si with $5\text{-}\Omega \text{ cm}$ resistivity, and sample 3.5, on $15\text{-}\Omega \text{ cm}$ (100)Si. The implantation was accompanied by amorphization of the surface layer. To produce heavily doped p^+ - and n^+ -layers, boron (40 keV, $5 \times 10^{15} \text{ cm}^{-2}$) and phosphorus ions (80 keV, 10^{15} cm^{-2}) were implanted in the front and back sides of the wafers, respectively. Annealing at 620°C for 1 h and 900°C for 0.5 h recrystallized the amorphous layer and gave rise to optically and electrically active (donor) centers. According to secondary ion mass-spectrometry (SIMS), the implantation and annealing formed an erbium-doped silicon layer with practically constant concentration of Er atoms at a depth of 0.5–0.8 μm from the sample surface: 10^{19} cm^{-3} in sample 3.2 and $\sim 4 \times 10^{19} \text{ cm}^{-3}$ in sample 3.3 [3]. The maximal boron concentration determined for these samples from SIMS data was $\sim 3 \times 10^{20} \text{ cm}^{-3}$ [3]. Mesa-diodes with working area $s = 0.12 \text{ mm}^2$ were fabricated by the standard pro-

cedure [4]. The reverse-bias current-voltage (I - V) characteristics were recorded at 32 Hz with 0.5-ms pulse duration. The room-temperature breakdown voltage V_{th} (found by extrapolating a nearly linear portion of I - V characteristic at high currents) was ~ 4.2 , ~ 5.2 , and ~ 3.2 V for samples 3.2, 3.3, and 3.5, respectively. For all the diodes studied, V_{th} increased upon cooling, which is typical of the tunneling breakdown. The capacitance and active conductance of the diodes in the pre-breakdown regime under reverse bias V were measured at $f = 1$ MHz with a 25-mV test signal, using a E7-12 capacitance and active conductance meter. The E7-12 meter is designed for the parallel equivalent circuit of an object under study, containing a capacitance and a resistance. For our diodes, the equivalent circuit included, along with the in-parallel connected capacitance C and resistance R of the p - n -junction, the series resistance r of the silicon substrate (base). As known in radio engineering, C and R can be determined from the capacitance C_m and resistance R_m measured in the parallel circuit, using the following system of equations:

$$C_m = \frac{C}{(1 + r/R)^2 + \omega^2 C^2 r^2}, \quad (1)$$

$$\frac{1}{R_m} = \frac{(r + R) + \omega^2 C^2 R^2 r}{(r + R)^2 + \omega^2 C^2 R^2 r^2}, \quad (2)$$

where $\omega = 2\pi f$. This system cannot be solved in the usual way, the equations being nonlinear. Therefore, the C values were determined in the present study from nomographs constructed as described below.

The measured capacitance C_m was plotted against the measured conductance G_m at different C and r values as a result of a study of the equivalent circuit composed of resistance boxes R and r and a capacitance box C . G_m was varied by changing R . Figure 1 shows an example of these dependences for $r = 50 \Omega$ at varied C . As seen, a set of experimental dependences of the type presented in Fig. 1 constitutes a system of nomographs suitable for determining the p - n -junction capacitance from the measured C_m , G_m , and r . The r value was assumed equal to the differential resistance of a diode in the developed-breakdown regime, when the resistance of the p - n -junction is well below that of the substrate. At 300 K, the r values were 50Ω for samples 3.2 and 3.3 and 150Ω for sample 3.5. With decreasing temperature, r became lower. According to our estimations, applying the described procedure to the C_m and G_m data recorded with E7-12 provides an error less than 10% in determining the capacitance C .

3. EXPERIMENTAL RESULTS AND DISCUSSION

Studies of EL and reverse-bias I - V characteristics of diodes fabricated by the same technology as samples 3.2 and 3.3 were reported in [2, 3]. Figure 2 shows the p - n -junction capacitance versus the reverse-bias volt-

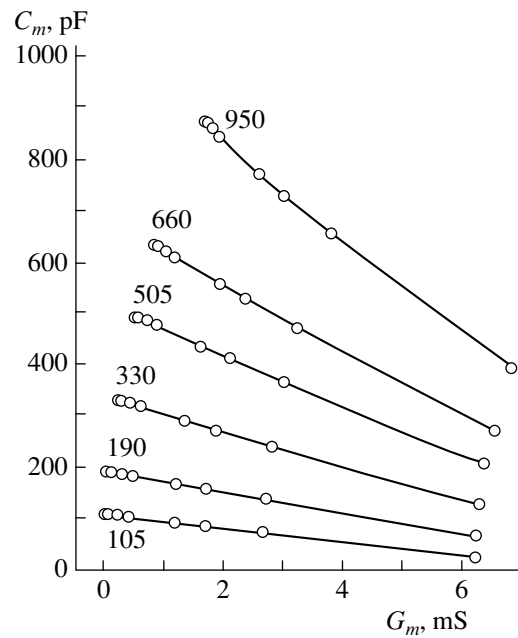


Fig. 1. Measured capacitance C_m vs. measured conductance G_m for an equivalent circuit comprising in-parallel connected resistance box R and capacitance box C and a series resistance $r = 50 \Omega$. G_m was varied by changing R . Figures at the curves give the capacitance C , pF.

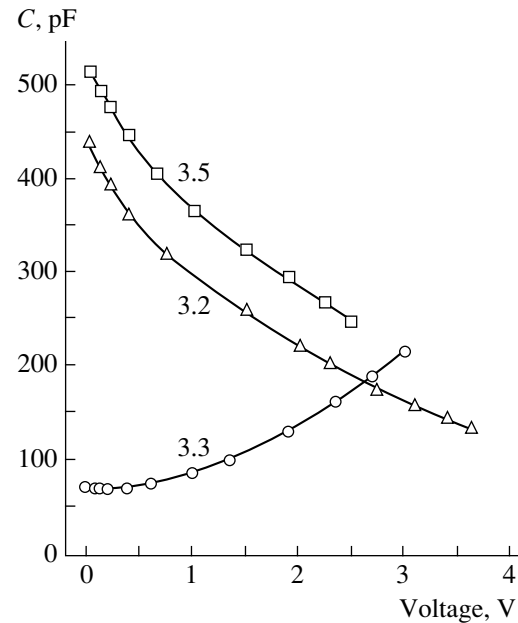


Fig. 2. p - n -junction capacitance vs. reverse bias for diodes 3.2, 3.3, and 3.5. $T = 300$ K. Sample nos. are indicated at the curves.

age at room temperature. The C - V characteristics of samples 3.2 and 3.5 are common (the p - n -junction capacitance decreases with increasing voltage because of the growing width of the depletion layer). At the same time, for sample 3.3 the p - n -junction capacitance

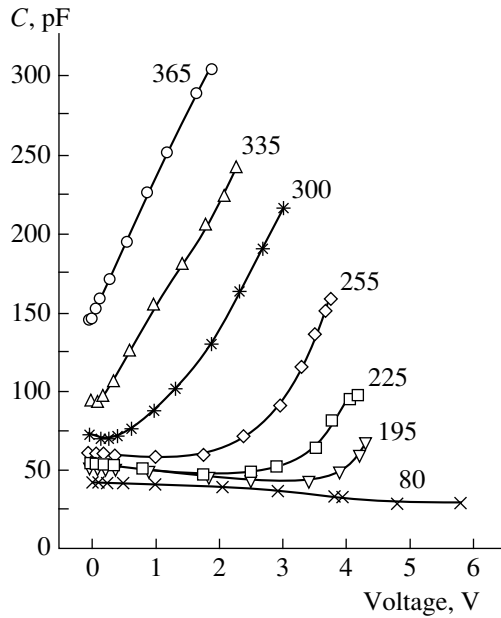


Fig. 3. *p-n*-junction capacitance vs reverse bias for diode 3.3 at different temperatures. Figures at the curves show the measurement temperatures T , K.

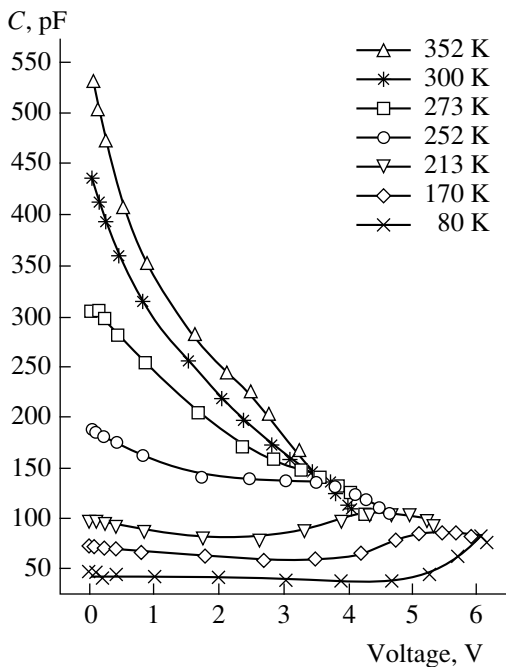


Fig. 4. *p-n*-junction capacitance vs reverse bias for diode 3.2 at different temperatures.

grows with increasing bias at $V > 0.5$ V. The range of biases in the prebreakdown region at which the capacitance increases corresponds to average electric field strengths F^*

$$\sim 3 \times 10^4 \text{ V/cm} < F^* < \sim 5 \times 10^5 \text{ V/cm.}$$

F^* was determined from the relation

$$F^* = \frac{VC}{\epsilon\epsilon_0 s}, \quad (3)$$

where ϵ is the relative permittivity of Si, and ϵ_0 is the permittivity of vacuum. Another unusual property of sample 3.3 is that the *p-n*-junction capacitance at $V \approx 0$ is several times less than the capacitance of samples 3.2 and 3.5 having the same area and characterized by doses of implanted erbium and oxygen not exceeding those in sample 3.3. It should also be noted that the dependences $G_m(V)$ for samples 3.3 and 3.5 at 300 K are similar; at $0.8 \leq V \leq 3$ V they differ by no more than 40%, with G_m for sample 3.5 higher than that for 3.3 at $0 \leq V \leq 1.8$ V, and, conversely, lower at $2.2 < V \leq 3$ V.

Figure 3 presents *C-V* characteristics taken for sample 3.3 in the pre-breakdown range of biases at different temperatures. In the 195–385 K temperature range, portions of capacitance increasing with bias are observed in all the *C-V* curves. With decreasing temperature, the bias corresponding to the onset of the capacitance rise increases, and at temperatures of about 80 K no capacitance rise is observed.

Figure 4 shows *C-V* characteristics taken for sample 3.2 at different temperatures. Portions of capacitance rise with increasing V are also observed in this sample, but in the temperature range below room temperature, including 80 K. The onset voltage of the capacitance rise in sample 3.2 also increases as the sample temperature is lowered, but the capacitance increment with increasing bias is much smaller than that for sample 3.3.

For (100)Si sample 3.5 subjected to the same technological operations as sample 3.3, the *C-V* characteristics contain no sections of capacitance rise with increasing bias in the pre-breakdown range of voltages at 80–350 K.

Figure 5 presents temperature dependences of the *p-n*-junction capacitance plotted on the basis of *C-V* measurements for diodes 3.5 (at $V = 0.5$ V) and 3.3 (at $V = 0.5$ – 2.5 V). For (100)Si sample 3.5, the *p-n*-junction capacitance slightly decreases as the temperature is lowered from 350 K to 80 K. For (111)Si sample 3.3, the *p-n*-junction capacitance at 80 K is an order of magnitude smaller than that for sample 3.5, and portions of steep (and substantial) rise in capacitance with increasing temperature are observed. At higher voltage, the onset of the steep rise in capacitance is shifted to lower temperatures. For sample 3.2 with implanted erbium and oxygen doses smaller than those in sample 3.3, a sharp increase in capacitance occurs at lower temperatures compared with sample 3.3 (see Fig. 6).

The presented experimental data indicate a high concentration of deep levels (DL) in the forbidden band in the *n*-region of the *p-n*-junction for (111)Si samples; the filling of these levels with electrons increases with decreasing temperature. The centers are depleted in the

space charge region (SCR) through the joint effect of lattice thermal vibrations and the electric field. The current flow can also affect the concentration of filled DLs, due to the possible recombination of electrons on DLs with holes and to electron capture by DLs. Raising the bias can enhance the probability of electron release from DLs to the conduction band [8], for example, through the Frenkel-Poole effect, and can also make the current density higher. It is worth noting that the diodes under study are characterized by considerable reverse currents. For example, at $V \approx 2$ V the currents in samples 3.2 and 3.3 practically coincided, being ~ 0.5 mA. Such a considerable current may also be due to a high density of defect levels in the forbidden band of Si, these becoming efficient centers of carrier generation under certain conditions. Measurements of I - V characteristics demonstrated that at 300 K, in the $0 \leq V \leq 3$ V range, currents in samples 3.2 and 3.3 differed at the same V by no more than 40% and increased steadily with growing V , the current in sample 3.2 being smaller than that in 3.3 at $0 \leq V \leq 1.8$ V, and, conversely, higher at $2.2 \leq V \leq 3$ V. Therefore, the observed difference between the C - V and C - T characteristics of samples 3.2 and 3.3 cannot be accounted for solely by the difference in their reverse currents.

It is the decreasing electron density on DLs in the SCR of the n -region that is responsible for the unusual rise in the capacitance of the p - n -junction with increasing bias. Within this approach, the shift of the temperature interval in which the capacitance grows with voltage and the shift to lower temperatures in the region of the steep rise in capacitance for sample 3.2, compared with sample 3.3, can both be ascribed to the lower activation energy of DLs in the former. The presented experimental data indicate that the parameters of the defects responsible for the appearance of DLs in samples 3.2 and 3.3 are different. It seems the most likely that in the course of the implantation and the subsequent annealings, extended defects are formed in (111)Si, with parameters varying, e.g., due to a change in their size, depending on the implantation dose. Even when neutral before capturing an electron, such defects, because of their large dimensions, can have a potential that is effective at long range, with the energy barrier for the electron emission in an electric field being substantially lowered. Indeed, the reduction of the energy barrier (ΔE) for electron emission in an electric field F from a potential well of radius δ to the conduction band can be evaluated by the relation [8]:

$$\Delta E = eF\delta. \quad (4)$$

According to [8], at $F = 10^5$ V/cm and $\delta = 0.1$ nm, $\Delta E = 10^{-3}$ eV (i.e., negligible), whereas at the same field value and $\delta = 10$ nm the barrier lowering $\Delta E = 0.1$ eV, which is essential.

As mentioned above, the concept of the presence of high-density DLs in the forbidden band in (111)Si(Er,O) diodes has already been used to explain

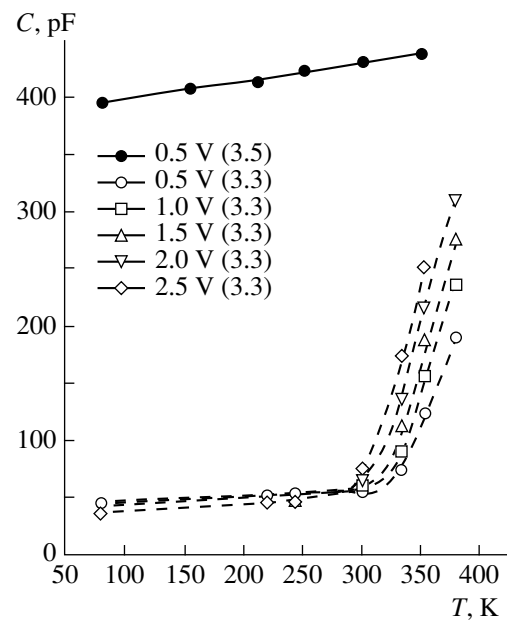


Fig. 5. p - n -junction capacitance vs temperature for diodes 3.3 and 3.5 at different biases.

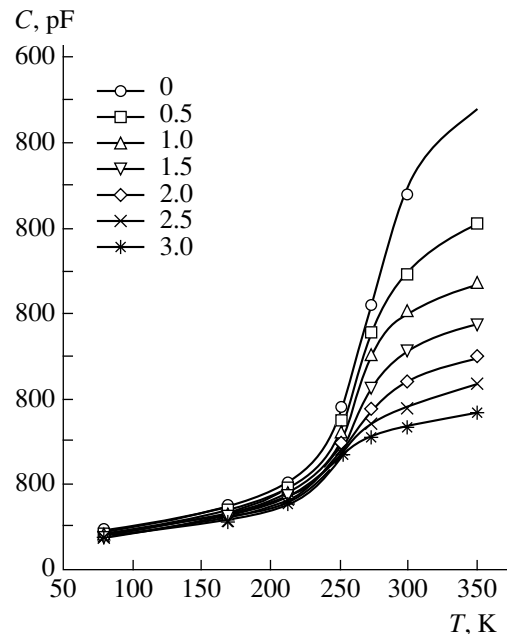


Fig. 6. p - n -junction capacitance vs. temperature for diode 3.2 at different biases. Figures at curve designations show the reverse bias V , V.

the temperature enhancement of the erbium EL intensity in the breakdown regime. Our results lend further support to the appearance of a high density of DLs in such structures. The formation of various structural defects in (111)Si(Er,O) and (100)Si(Er,O) diodes was established in [6], the defects evidently determining the

difference in the electroluminescent and capacitive properties of the diodes.

4. CONCLUSION

Sections of rise in the p - n -junction capacitance with increasing reverse bias have been observed in (111)Si(Er,O) diodes in certain temperature intervals, depending on the erbium and oxygen implantation dose. The rise in capacitance is attributed to the high density of deep levels in the forbidden band of the n -Si layer of the p - n junction, the electrons being released from these levels in the SCR with increasing bias. The experimental data show that the parameters of the defects responsible for the levels depend on the erbium and oxygen implantation dose.

ACKNOWLEDGMENTS

The authors are grateful to T.M. Mel'nikova, E.O. Parshin, and A.V. Shestakov for assistance in sample preparation.

This study was supported in part by the Russian Foundation for Basic Research (project no. 99-02-17750) and INTAS (grant no. 99-01872).

REFERENCES

1. G. Franzo, S. Coffa, F. Priolo, and C. Spinella, *J. Appl. Phys.* **81**, 2784 (1997).
2. A. M. Emel'yanov, N. A. Sobolev, P. E. Khakuashev, and M. A. Trishenkov, *Fiz. Tekh. Poluprovodn. (St. Petersburg)* **34**, 965 (2000) [*Semiconductors* **34**, 927 (2000)].
3. N. A. Sobolev, A. M. Emel'yanov, and Yu. A. Nikolaev, *Fiz. Tekh. Poluprovodn. (St. Petersburg)* **34**, 1069 (2000) [*Semiconductors* **34**, 1027 (2000)].
4. N. A. Sobolev, A. M. Emel'yanov, and K. F. Shtel'makh, *Appl. Phys. Lett.* **71**, 1930 (1997).
5. A. M. Emel'yanov, N. A. Sobolev, and A. N. Yakimenko, *Appl. Phys. Lett.* **72**, 1223 (1998).
6. N. A. Sobolev, A. M. Emel'yanov, Yu. A. Nikolaev, and V. I. Vdovin, *Fiz. Tekh. Poluprovodn. (St. Petersburg)* **33**, 660 (1999) [*Semiconductors* **33**, 613 (1999)].
7. N. A. Sobolev, Yu. A. Nikolaev, A. M. Emel'yanov, *et al.*, *J. Lumin.* **80**, 315 (1998).
8. J. Bourgoin and M. Lanoo, *Point Defects in Semiconductors* (Springer-Verlag, New York, 1983; Mir, Moscow, 1985).

Translated by D. Mashovets

SEMICONDUCTOR STRUCTURES, INTERFACES, AND SURFACES

Negative Luminescence in *p*-InAsSbP/*n*-InAs Diodes

M. Aïdaraliev, N. V. Zotova, S. A. Karandashev, B. A. Matveev*, M. A. Remennyi,
N. M. Stus', and G. N. Talalakin

Ioffe Physicotechnical Institute, Russian Academy of Sciences, Politekhnikeskaya ul. 26, St. Petersburg, 194021 Russia

**e-mail: bmat@iropt3.ioffe.rssi.ru*

Submitted July 25, 2000; accepted for publication July 26, 2000

Abstract—Negative luminescence (NL) at $\lambda_{\max} = 3.8 \mu\text{m}$ from reverse-biased *p*-InAsSbP/*n*-InAs diode heterostructures has been studied at temperatures of 70–180°C. The NL power increases with temperature and exceeds the power of direct-bias electroluminescence at temperatures over 110°C. An NL power of 5 mW/cm², efficiency of 60%, and a conversion efficiency of 25 mW/(A cm²) have been obtained at 160°C. © 2001 MAIK “Nauka/Interperiodica”.

1. INTRODUCTION

Mid-IR (3–5 μm) light emitting diodes (LEDs) are used in gas analyzers to detect carbon dioxide CO₂ (4.3 μm), methane CH₄ (3.3 μm), and other hydrocarbons. LPE-grown InGaAs ($\lambda = 3.3 \mu\text{m}$) and InAsSbP ($\lambda = 4.3 \mu\text{m}$) LEDs have a service life over 30000 h [1] and can operate at temperatures of up to $t = 180^\circ\text{C}$ [2]. The operation of LEDs in the temperature interval $t = 20\text{--}180^\circ\text{C}$ is well described by classical models of the injection radiation sources and the carrier recombination processes. Temperature dependences of the reverse current in the saturation regime conform to the Shockley theory, indicating an increasing intrinsic carrier concentration. Emission spectra are described on the assumption of direct band-to-band transitions, spherical symmetry of bands, and thermalized carriers. The emission power decreases exponentially with increasing temperature, which is typical of Auger processes.

On the other hand, carrier extraction from the regions adjacent to the *p*–*n* junction would be expected for a reverse-biased *p*–*n* junction, with carrier concentration decreasing to below the equilibrium value, so that $(n \times p) < (n_0 \times p_0) = n_i^2$, where n_0 , p_0 and n , p are the equilibrium and nonequilibrium concentrations of electrons and holes, respectively, and n_i is the intrinsic carrier concentration. The extraction of carriers leads to a decrease in the radiative recombination intensity P , it becoming lower than the thermal background P_0 :

$$\Delta P = P - P_0 = P_0 \left(\frac{np}{n_i^2} - 1 \right) \leq 0;$$

i.e., the luminescence becomes “negative.” The effect of negative luminescence (NL) has been known since 1965, when V.I. Ivanov-Omskii *et al.* studied the NL in InSb in crossed electric and magnetic fields [3]. Negative luminescence has been studied in bulk InAs crystals [4], InSb- and CdHgTe-based diodes [5, 6], and,

more recently, in superlattice structures [7, 8]. The NL power, or “thermal contrast,” depends on the intensity of the ambient radiation and is limited by the black-body (BB) radiation power at a given temperature. Thus, the room-temperature NL power of 0.4 ($\lambda = 4.3 \mu\text{m}$) [7], 0.53 ($\lambda = 6 \mu\text{m}$), 4 ($\lambda = 8 \mu\text{m}$) [6], and 0.2 mW/cm² ($\lambda = 5.3 \mu\text{m}$) [8] is substantially lower than that for the direct-bias LEDs: 46 mW/cm², $I = 0.4 \text{ A}$ ($\lambda = 3.3 \mu\text{m}$) [9]; 36 mW/cm², $I = 2 \text{ A}$ ($\lambda = 4.2 \mu\text{m}$) [10]; and 25 mW/cm², $I = 1 \text{ A}$ ($\lambda = 5.5 \mu\text{m}$) [11]. However, NL power grows with increasing temperature and wavelength [4], thus reflecting the BB properties, in contrast to EL power, which decreases with increasing temperature and wavelength owing to the Auger recombination. Consequently, there exists a temperature at which the efficiency of NL exceeds that of EL. For InAs/InAsSb superlattices ($\lambda = 4.3 \mu\text{m}$), this temperature was determined to be 310 K [7], but, as far as we know, no attempts have been made to study the NL in *p*–*n* junctions at $T > 310 \text{ K}$. The present study is concerned with the NL in *p*-InAsSbP/*n*-InAs diode heterostructures ($\lambda = 3.8 \mu\text{m}$, 80°C) in the temperature range 70–180°C.

2. OBJECTS UNDER STUDY AND EXPERIMENTAL TECHNIQUE

Lattice-matched *p*-InAsSb_{0.09}P_{0.18}/*n*-InAs diode heterostructures were grown by LPE on (111)*n*-InAs substrate at 630–680°C. The substrate was 350 μm thick, with electron concentration of $2 \times 10^{16} \text{ cm}^{-3}$; a 2–4- μm -thick wide-gap *p*-InAsSbP layer ($E_g = 390 \text{ meV}$, 300 K) was doped with Zn to a hole concentration of $5\text{--}7 \times 10^{16} \text{ cm}^{-3}$. Round mesa-structures 430 μm in diameter, with upper Au(Zn) *p*-contact 160 μm in diameter, were fabricated by means of photolithography. The radiation was emitted through a wide-gap InAsSbP layer.

EL and NL were recorded in pulse regime $\tau = 30 \mu\text{s}$, $f = 500 \text{ Hz}$, using a cooled (77 K) InSb photodiode for

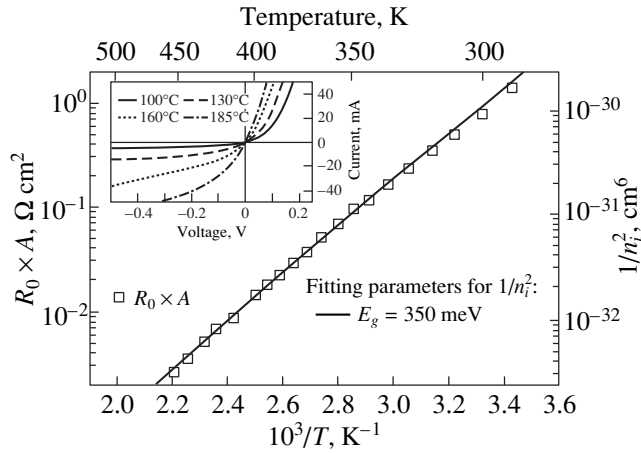


Fig. 1. Product of the zero-bias differential resistance by the p - n -junction area, $R_0 \times A$, and the inverse square of the intrinsic concentration, $1/n_i^2$, vs. inverse temperature. Inset: I - V characteristics at $t = 100, 130, 160,$ and 185°C .

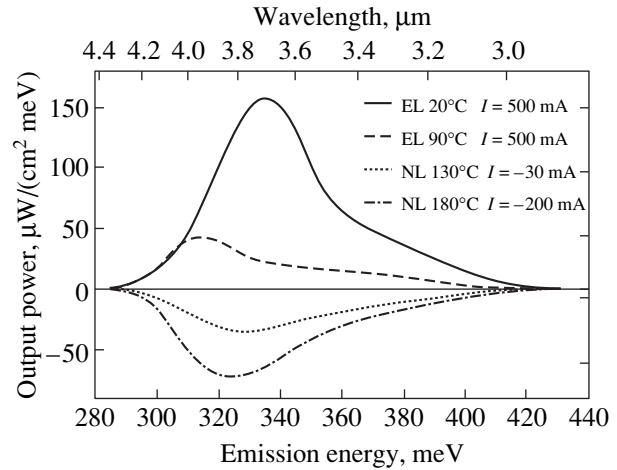


Fig. 2. EL ($I = 500$ mA, $t = 20, 90^\circ\text{C}$) and NL spectra ($I = -30, -200$ mA, $t = 130, 180^\circ\text{C}$).

spectral measurements. The absolute power values were measured with a cooled (77 K) HgCdTe photodiode, taking into account the directional pattern of the LED and the spectral sensitivity of a photodetector.

3. EXPERIMENTAL RESULTS AND DISCUSSION

As shown in [12, 13], the “diffusion” mechanism of current flow dominates at temperatures over 200 K in p - n junctions in InAs and solid solutions of close composition; i.e., the current-voltage (I - V) characteristics are governed by the recombination in the “ n ” and “ p ” regions of the p - n junction, in accordance with the Shockley theory. Figure 1 presents I - V characteristics at $t = 100, 130, 160,$ and 185°C (see the inset), the product of the zero-bias differential resistance by the p - n -junction area $R_0 \times A$, and the inverse square of the intrinsic concentration, $1/n_i^2$, as functions of inverse temperature. The absence of any pronounced saturation of the reverse current indicates that the current contains not only the diffusion component. On the other hand, the coincidence of slopes for $R_0 \times A$ and $1/n_i^2$ (Fig. 1) indicates that the diffusion mechanism of current flow dominates at small currents. This suggests carrier extraction from the p - n -junction under reverse bias in this temperature range. The experimental curve coincides with the $1/n_i^2$ curve for $E_g = 350$ meV, which means that the p - n -junction is shifted away from the InAs/InAsSbP heterointerface and lies inside the n -InAs substrate.

Figure 2 shows EL ($I = 500$ mA, $t = 20, 90^\circ\text{C}$) and NL spectra ($I = -30, -200$ mA, $t = 130, 180^\circ\text{C}$). With increasing temperature, emission peaks shift to longer

wavelengths, in accordance with the temperature narrowing of the band gap; however, the NL peak is shifted relative to the EL spectrum to shorter wavelengths.

Figure 3 presents the NL emission power vs. current for temperatures $t = 80$ – 190°C . The linear rise in power with increasing current is followed by a leveling-off, which indicates that the active region of the structure is depleted and there is no diode heating-up. Under these conditions, the NL power approaches the power of the equilibrium recombination radiation P_0 at a given temperature. A clearly pronounced leveling-off of the NL power is observed up to $t = 135^\circ\text{C}$. The absence of definite leveling-off and the nonlinear increase in power at small currents at higher temperatures can be attributed to leakages or to some additional source of carriers, e.g., a nonohmic contact supplying carriers into the active region, thus preventing total carrier extraction. The NL power saturation currents correlate with the saturation currents of reverse I - V characteristics, which is clearly visible in the inset of Fig. 3 and in Fig. 4 showing the differential resistance dU/dI vs. current at temperatures in the range 40 – 190°C . Similar dependences have been observed for InAs/InAsSb superlattices [7].

Upon total depletion of the active region, the NL power approaches the power of the equilibrium recombination emission P_0 calculated in [14] for direct interband transitions in a nondegenerate semiconductor with energy gap E_g :

$$P_0 = \frac{E_g^2 h^3 F(q) n_i^2}{4\pi^2 c^2 (m_n m_p)^{3/2} (kT)^2}, \quad (1)$$

where h is the Planck constant, $F(q) \approx 0.1$ is a function of the refractive index of a semiconductor, c is the speed of light, and m_n and m_p are the electron and heavy-hole effective masses. Figure 5 presents temper-

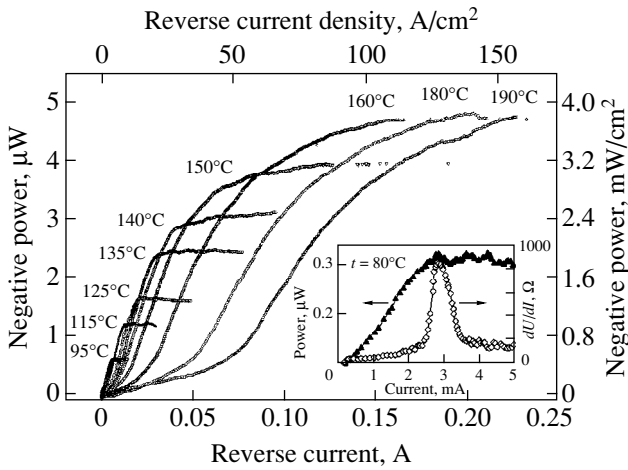


Fig. 3. NL emission power vs. current at $t = 95\text{--}190^\circ\text{C}$. Insert: NL power and differential resistance dU/dI vs. current, $t = 80^\circ\text{C}$.

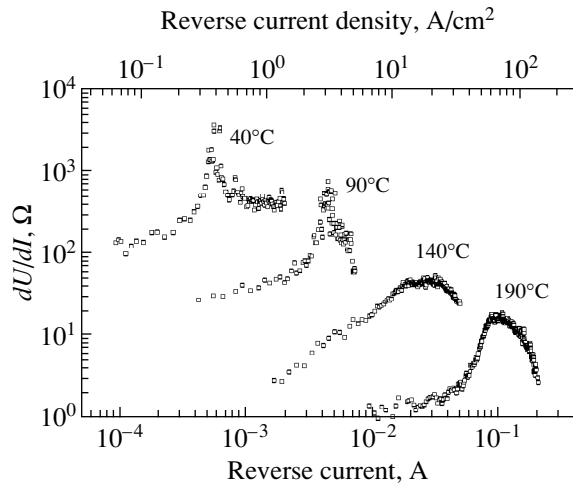


Fig. 4. Differential resistance dU/dI vs. current for $t = 40\text{--}190^\circ\text{C}$.

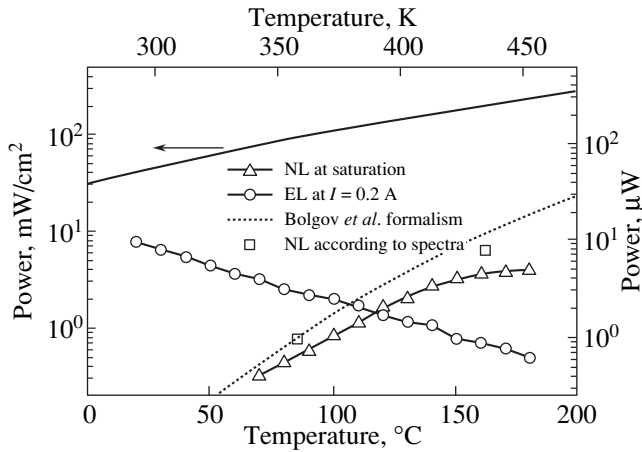


Fig. 5. Temperature dependences of the BB radiation power (solid line), calculated power P_0 of the equilibrium recombination emission for InAs, power of the equilibrium recombination emission calculated with account of the experimental NL spectra, EL power at $I = 0.2\text{ A}$, and NL power at $I = I_{\text{SAT}}$.

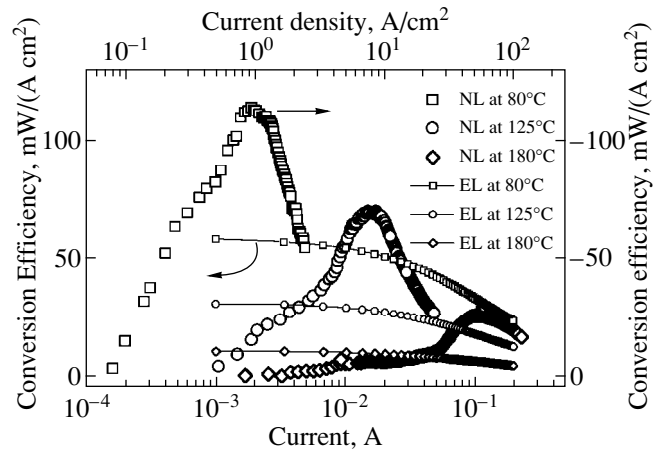


Fig. 6. Conversion efficiency vs. current for direct and reverse bias at $t = 80, 125, \text{ and } 180^\circ\text{C}$.

ature dependences of the BB radiation power; calculated power of the equilibrium recombination emission P_0 for InAs; and power of the equilibrium recombination emission, calculated with account of experimental NL spectra, EL power at a current $I = 0.2\text{ A}$, and NL power at the saturation current $I = I_{\text{SAT}}$. As seen, the $P_0(t)$ dependence calculated from (1) coincides well with the power of the equilibrium recombination emission, calculated with account of the experimental NL spectra. The NL power steeply increases with temperature, and exceeds the EL power at 110°C . The temperature dependence of the NL power reflects the temperature dependence of the BB radiation, with the peak in the NL spectral characteristics, corresponding to the InAs band gap, shifted toward the BB radiation peak. The NL efficiency η is defined as the ratio of the NL

power to the BB power that falls within the limits of the NL spectrum (i.e., P_0). The obtained value $\eta = 0.63$ (160°C) is close to the best values known in the literature: $\eta = 0.5$ (CdHgTe, $\lambda = 9.5\ \mu\text{m}$, 300 K) [6].

Figure 6 shows the conversion efficiency (the ratio of the luminescence power per unit area to the working current) vs. current for direct and reverse bias in the temperature range $80\text{--}180^\circ\text{C}$. The EL conversion efficiency is seen to decrease with increasing current and temperature, which has also been observed for InAs [15] and InAsSbP [16] diodes. The room-temperature EL conversion efficiency decreases from $210\text{ mW}/(\text{A cm}^2)$ at 5 mA to $75\text{ mW}/(\text{A cm}^2)$ at 200 mA , owing to the Joule heating, Auger recombination, and absorption by free carriers. The ratio of the NL to EL conversion efficiencies grows with increasing temperature, demon-

strating the advantage of reverse-biased p - n -junctions at higher temperatures.

4. CONCLUSION

High-intensity negative luminescence at $\lambda = 3.8 \mu\text{m}$ was observed in reverse-biased p -InAsSbP/ n -InAs diode heterostructures, with its power growing with increasing current and temperature. The spectral and power characteristics of the NL in the temperature range 70–180°C can be accounted for by the carrier depletion of the active region, resulting in the rate of radiative recombination decreasing below the equilibrium level.

The NL power (5 μW) and the conversion efficiency (25 $\text{mW}/(\text{A cm}^2)$) at 160°C exceed the respective values for the electroluminescence, thus showing promise for application of reverse-biased p - n junctions in optoelectronic devices operating at elevated temperatures.

ACKNOWLEDGMENTS

This study was performed with the administrative support of the US Civilian Research and Development Foundation for CIS countries (CRDF).

REFERENCES

1. B. Matveev, M. AĬdaraliev, G. Gavrilov, *et al.*, *Sens. Actuators* **51** (1–3), 233 (1998).
2. M. AĬdaraliev, N. V. Zotova, S. A. Karandashev, *et al.*, *Fiz. Tekh. Poluprovodn. (St. Petersburg)* **34** (1), 102 (2000) [*Semiconductors* **34**, 104 (2000)].
3. V. I. Ivanov-Omskiĭ, B. T. Kolomiets, and V. A. Smirnov, *Dokl. Akad. Nauk SSSR* **161** (6), 1308 (1965) [*Sov. Phys. Dokl.* **10**, 345 (1965)].
4. S. S. Bolgov, V. K. Malyutenko, and A. P. Savchenko, *Fiz. Tekh. Poluprovodn. (St. Petersburg)* **31** (5), 526 (1997) [*Semiconductors* **31**, 444 (1997)].
5. T. Ashley, C. T. Elliot, N. T. Gordon, *et al.*, *J. Cryst. Growth* **159**, 1100 (1996).
6. T. Ashley, C. T. Elliot, N. T. Gordon, *et al.*, *Infrared Phys. Technol.* **36**, 1037 (1995).
7. M. J. Pullin, H. R. Hardaway, J. D. Heber, and C. C. Phillips, *Appl. Phys. Lett.* **75** (22), 3437 (1999).
8. L. J. Olafsen, I. Vurgaftman, W. W. Bewley, *et al.*, *Appl. Phys. Lett.* **74** (18), 2681 (1999).
9. M. K. Parry and A. Krier, *Electron. Lett.* **30** (23), 1968 (1994).
10. M. J. Pullin, H. R. Hardaway, J. D. Heber, *et al.*, *Appl. Phys. Lett.* **74** (16), 2384 (1999).
11. B. Matveev, N. Zotova, S. Karandashov, *et al.*, *IEE Proc.: Optoelectron.* **145** (5), 254 (1998).
12. N. P. Esina, N. V. Zotova, and D. N. Nasledov, *Fiz. Tekh. Poluprovodn. (Leningrad)* **3** (9), 1370 (1969) [*Sov. Phys. Semicond.* **3**, 1140 (1969)].
13. A. Krier and Y. Mao, *Infrared Phys. Technol.* **38**, 397 (1997).
14. S. S. Bolgov, V. K. Malyutenko, and V. I. Pipa, *Pis'ma Zh. Tekh. Fiz.* **5** (23), 1444 (1979) [*Sov. Tech. Phys. Lett.* **5**, 610 (1979)].
15. M. J. Kane, G. Braithwaite, M. T. Ereny, *et al.*, *Appl. Phys. Lett.* **76** (8), 943 (2000).
16. M. K. Parry and A. Krier, *Semicond. Sci. Technol.* **8**, 1764 (1993).

Translated by D. Mashovets

**SEMICONDUCTOR STRUCTURES, INTERFACES,
AND SURFACES**

Characterization of Electroluminescent Structures Based on Gallium Arsenide Ion-Implanted with Ytterbium and Oxygen

D. W. Palmer*, V. A. Dravin, V. M. Konnov**, E. A. Bobrova**, N. N. Loiko**,
S. G. Chernook**, and A. A. Gippius****

* *University of Sussex, Falmer, Brighton, Sussex, BN1 9QJ, UK*

** *Lebedev Institute of Physics, Russian Academy of Sciences, Leninskii pr. 53, Moscow, 117924 Russia*

Submitted July 5, 2000; accepted for publication July 26, 2000

Abstract—Light-emitting diodes based on GaAs crystals ion-implanted with ytterbium and oxygen were fabricated. The current–voltage and capacitance–voltage characteristics of these diodes were analyzed. The deep-level centers were studied by the deep-level transient spectroscopy. The electroluminescence spectra of the structures include the emission lines related to optical transitions within the $4f$ shell of Yb^{3+} ions. © 2001 MAIK “Nauka/Interperiodica”.

1. INTRODUCTION

Semiconductors doped with rare-earth (RE) elements have been intensively studied in recent years in connection with the prospects for developing optoelectronic devices that combine the characteristics of the f – f transitions in RE ions (narrow and temperature-independent lines) with the compactness of semiconductor devices. The narrow-line sources of light are indispensable, in particular, for extending the capabilities of optical-fiber communication links.

We have shown previously that efficient photoluminescent centers based on Yb^{3+} ions in the bulk implantation-doped GaAs crystals and in the layers doped with Yb in the course of molecular-beam epitaxy are three-component complexes that include atoms of Yb, O, and other chemical elements; the latter act as coactivators of the RE luminescence. We have observed a systematic variation in the energy characteristics of complex RE centers in relation to the properties of the coactivator atoms. We have suggested that the coactivators are not only responsible for the fine structure of the Yb-ion emission but are also necessary for obtaining the required charge state of the Yb ion (i.e., Yb^{3+}). Oxygen atoms do not affect the energy-spectrum fine structure of RE centers; however, they apparently play a decisive role in the energy transfer from electron–hole pairs to the RE luminescent centers [1–3].

Two mechanisms for the excitation of an RE ion embedded in a semiconductor matrix have so far been ascertained. These are the impact and injection-based mechanisms. Apparently, the impact excitation is more characteristic of the II–VI compounds, whereas the injection-based mechanism is typical of the III–V compounds [4, 5]. The main objective of this study was to

realize the conditions for exciting the electroluminescence (EL) of GaAs crystals implantation-doped with both ytterbium and oxygen and to compare the photoluminescence (PL) and EL spectra of these crystals.

2. EXPERIMENTAL

Wafers of n -GaAs grown by liquid-phase epitaxy and having electron concentrations of 10^{16} , 10^{17} , or 10^{18} cm^{-3} were used as starting samples. The samples were implanted at room temperature, first with ytterbium ions and then with oxygen ions. The implantation parameters are listed in Table 1.

We take the term “calculated impurity concentration” to mean the impurity concentration at the peak of its distribution in the depth of the crystal. The energy and doses of Yb and O ions were chosen such that the distribution peaks for different implants were at the same depth and their peak concentrations coincided.

Figure 1 shows the calculated Yb and O concentration profiles for the chosen implantation conditions. According to theoretical estimates, more than 100 primary radiation defects are produced for every Yb ion implanted into GaAs. It is noteworthy that radiation defects penetrate much deeper into the crystal than the implanted impurity does [6].

In order to reduce the radiation-defect concentration and activate the implanted impurities, we performed a postimplantation photostimulated annealing of the samples for 5 min at a temperature of 650°C . The GaAs wafers were then cut into samples with the surface area of $4 \times 8 \text{ mm}^2$. A Sn contact was deposited electrochemically onto the rear (unimplanted) surface of each sample. A semitransparent contact site 1 mm in diameter was formed at the front (implanted) surface using cath-

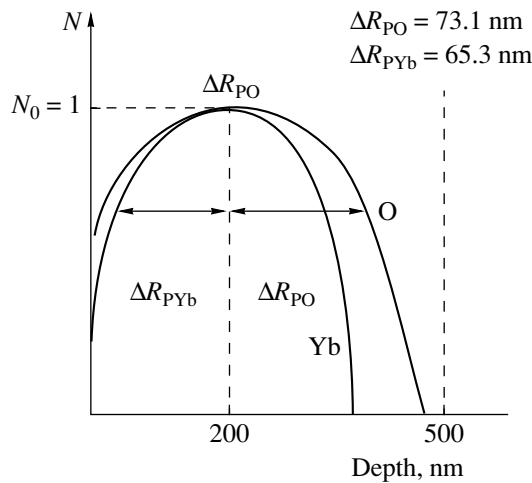


Fig. 1. Calculated concentration profiles for ion-implanted Yb and O impurities in a GaAs crystal.

ode sputtering; an Au wire $\sim 20 \mu\text{m}$ in diameter was then bonded to this contact with the use of a conducting cement. Each sample had a common rear contact and two front (measurement) contacts. The fabricated semiconductor structures were mounted in a conventional transistor-case chip holder; this arrangement ensured that the samples were well protected and that it was convenient to deal with them.

In order to control the various stages of sample preparation, we fabricated similar structures from starting crystals subjected only to part of the technological treatment. To this end, we used, for example, the GaAs crystals implanted only with ytterbium (without oxygen-ion implantation). In order to gain better insight into the formation of defects and complexes character-

istic of the crystals used, we irradiated several starting wafers with ~ 1 MeV protons and then cut these wafers into conventional samples. A fraction of these samples were annealed at temperatures in the range of 400–650°C. The reference structures were then fabricated from these crystals.

3. RESULTS AND DISCUSSION

3.1. Electrical Measurements

Measurements of the current–voltage (I – V) characteristics showed that the structures fabricated from GaAs crystals implantation-doped with Yb and O to concentrations on the order of 10^{17} and 10^{18} cm^{-3} were rectifying (the rectification was much more pronounced at 77 K than at 300 K). Thus, for a forward bias of 2–4 V (a positive voltage was applied to the top Au electrode), the currents ranged from 50 to 200 mA. Under a reverse bias of up to -10 V, the current did not exceed $10 \mu\text{A}$. The structures based on GaAs crystals implanted with Yb and O ions to a concentration of 10^{19} cm^{-3} feature more intricate I – V characteristics, which indicates that there is either a layer with fairly high resistivity or a system of several p – n junctions in the structure. Thus, in order to attain the forward current of ~ 100 mA in these structures, we had to apply a bias of ~ 6 – 12 V, rather than 2–4 V as in the case of the lower level of implantation doping. Measurements of the electrical parameters of the structures made of undoped GaAs crystals irradiated with protons and then annealed at 400–600°C showed that the majority of radiation defects were annealed out at a temperature of ~ 450 – 500°C .

Studies performed by the method of deep-level transient spectroscopy (DLTS) made it possible to identify a number of trap states both in the starting and the ion-implanted samples. Positive and negative peaks are observed in the DLTS spectra, which is indicative of injection and trapping of both electrons and holes. In the starting samples, we detected no less than four types of hole traps ($H2$, $H4$, $H5$, and $H6$) and four types of electron traps ($E3$, $E4$, $E5$, and $E7$). Additional electron traps $E1$ and $E2$ and hole traps $H1$ and $H3$ were observed in the ion-implanted sample (the numbering of the peaks in increasing order corresponds to an increase in temperature, from 80 to 380 K, at which these peaks were detected). The peaks related to traps $E2$ and $H3$ have the largest magnitude. It is difficult to resolve the peaks because they are closely spaced. By selecting the conditions of measurements (the bias voltage applied to the structure and the injecting-pulse voltage), we managed to make one of the close traps dominant in the DLTS spectra and to determine its activation energy E and the trapping cross section σ (Table 2).

The traps in the ion-implanted region are observed using an injecting pulse at a current of up to 20 mA, in which case the EL of RE ions is already detected. The

Table 1

Ion	Ion energy, keV	Dose, cm^{-2}	Calculated concentration, cm^{-3}
Yb	1000	3×10^{12}	10^{17}
		3×10^{13}	10^{18}
		3×10^{14}	10^{19}
O	120	3×10^{12}	10^{17}
		3×10^{13}	10^{18}
		3×10^{14}	10^{19}

Table 2

	$E1$	$E2$	$E4$	$H2$	$H3$
E , eV	0.16	0.54	0.58	0.5	0.57
σ , cm^2	3×10^{-16}		1.7×10^{-13}	6×10^{-14}	

trap $E4$ in unimplanted samples has parameters close to those of the known center $EL3$ which is usually related to an oxygen-containing complex [7, 8]; the trap $E7$ is close to the $EL2$ center in temperature position. Henceforth, we use the trap classification suggested previously [9, 10].

The poorly resolved peaks $H5$ and $H6$ observed at high temperatures may correspond to the $HL2$ and $HL16$ centers with activation energies of 0.73 and 0.79 eV, respectively. After implantation, the concentration of the centers increases significantly and becomes comparable to the doping level of the semiconductor. The $H1$, $H2$, and $H3$ traps are close in their temperature positions to the $HL11$, $HL5$, and $HL4$ centers, whose activation energies range from 0.35 to 0.42 eV. The $E4$ ($EL3$) trap is not observed in the DLTS spectra of ion-implanted samples, which may be caused by a transfer of oxygen atoms to the ion-implanted region as a result of gettering and by a variation in the position of the Fermi level in the surface layers.

Thus, the results of electrical measurements indicate that ion implantation and subsequent annealing bring about the formation of a layer either with conduction close to intrinsic (an i -layer) or with hole conduction (a p -layer); in addition, deep-level centers of several types that can be involved in recombination and energy transfer to the RE centers are formed. Electrical measurements show that the photostimulated-annealing temperature of 650°C may be considered adequate only for the ion-implanted samples with implant concentrations of 10^{17} and 10^{18} cm $^{-3}$, whereas this temperature is clearly too low for samples with implant concentrations on the order of 10^{19} cm $^{-3}$.

3.2. Photoelectric Measurements

The short-circuit current I_{sc} and the contact-potential difference U_c were measured at 77 K under irradiation with photons in the wavelength range of 0.4–1.0 μ m; the illumination intensity was as high as 3 W at a spot 3 mm in diameter. The dependence of I_{sc} on the illumination intensity was found to be linear for both unimplanted (reference) and implanted (and annealed) structures. The dependence of the contact-potential difference on illumination intensity was sublinear and leveled off ($U_c = 1.02$ V) at the illumination intensity of 200 mW for an implanted structure. For the reference structures, U_c did not exceed 0.6 V. We mention that, according to the published data [11], the barrier height is ~ 0.9 V in an Au- n -GaAs system and ~ 0.5 V in an Au- p -GaAs system.

Apparently, a Schottky barrier is formed in a system composed of a metallic (Au, in the case under consideration) contact and starting GaAs crystal. In the course of annealing, recrystallization of the implantation-damaged layer starts from the undamaged deep layers and proceeds toward the outer boundary of the structure. It

follows from photoelectric measurements that the layer incorporating the RE impurity has a conductivity at least close to intrinsic. Thus, an extended junction of the n - n^+ or i - n type is formed in the bulk of the structure at a depth of 200 to 500 nm. In this region of the structure, the Fermi level is located in the vicinity of the midgap. When the electron-hole pairs are generated, electrons freely leave the surface layers and move into the bulk of the structure, whereas there is a barrier for holes. Thus, it should be expected that positive voltage has to be applied to the top electrode during measurements of U_c and I_{sc} , which is exactly what is observed experimentally.

3.3. Studies of Electroluminescence

The EL spectra were measured upon the application of a forward bias to the semiconductor structures at 77 K. It is noteworthy that the RE emission related to the intracenter transitions involving the Yb^{3+} ions was detected only for the samples ion-implanted with both Yb and O. In the structures fabricated from the crystals doped with the Yb impurity alone, RE emission in the EL spectra was not observed.

Figure 2 shows the EL spectra of a reference sample ($H2A$) and two implanted and annealed samples ($H13A$ and $H14A$). We now describe the groups of the most typical bands distinguishable in the spectra shown in Figs. 2 and 3.

1. The edge-emission band D peaked at 822–826 nm is related both to the band-to-band ($E_c - E_v$) transitions and to the shallow-level donors, most likely, to Se_{As} and Si_{Ga} . The edge-emission band A peaked at 837–839 nm is related to shallow-level acceptors (in the case under consideration, to Si_{As}).

2. There is also a complex C band that extends from 870 to 980 nm. Another band E which peaked at 912–920 nm is distinguishable against the background of the C band. The E band is presumably related to impurity-defect associations that are based on Cu atoms and can be represented as $Cu_{Ga}-V_{As}$ -(a background impurity), where V_{As} stands for the arsenic vacancy.

3. Finally, we have a complex F band that extends from 989 to 1200 nm and whose main peak is at 1000–1060 nm. In addition to the main peak, additional peaks (for example, the one located at ~ 1080 nm) are fairly often observed. The origin of the F band in GaAs crystals has not been clarified. It is believed that the impurity-defect complexes based on a number of background impurities are responsible for emission in this spectral region. Thus, the long-wavelength portion of this band is most probably related to emission from the complexes that incorporate oxygen atoms.

As can be seen from Fig. 2, the RE emission is present in the spectra of implanted and annealed structures, in addition to the luminescence that is characteristic of the reference structure. The short-wavelength edge of emission of the complex centers based on Yb^{3+}

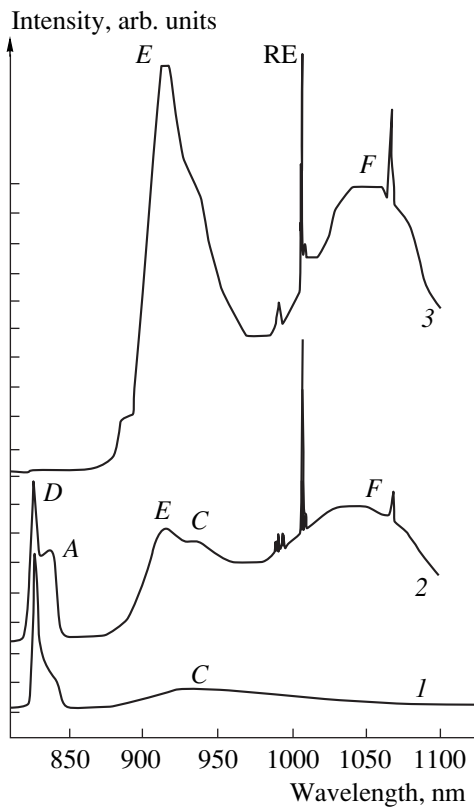


Fig. 2. Electroluminescence spectra of the samples for the injection current of 100 mA. Spectrum 1 corresponds to the reference sample; spectra 2 and 3 correspond to the ion-implanted and annealed samples *H13A* and *H14A*. The bias voltage applied to the samples was (1) 2.9, (2) 3.8, and (3) 3.2 V. The spectra were measured at 77 K.

ions is located at 980 nm. The range of 980–1250 nm is related to “purely electronic” transitions within the $4f$ shell of an Yb^{3+} ion, whereas the spectral region with wavelengths longer than 1250 nm is related to vibronic transitions [12].

A systematic comparison of the PL and EL spectra of the same GaAs:(Yb,O) crystals showed that these spectra are qualitatively quite similar to each other, especially so for wavelengths longer than 850 nm (i.e., those corresponding to the RE-emission range). Quantitative differences between the intensities of the *D* and *A* edge-emission bands in the PL and EL spectra were very significant. The edge emission could be observed with confidence in the PL spectra only for samples with an implant concentration of $\sim 10^{17} \text{ cm}^{-3}$. For samples with an implant concentration of $\sim 10^{18} \text{ cm}^{-3}$, the edge emission (the *D* or *A* bands) in the PL spectra was observed only occasionally, whereas this emission was virtually absent for the samples ion-implanted with Yb and O to concentrations of $\sim 10^{19} \text{ cm}^{-3}$. Quenching of edge emission in the PL spectra with increasing Yb and O concentrations is caused by the accumulation of postimplantation defects in the surface layers of the structure and by inefficient annealing. The intensities of

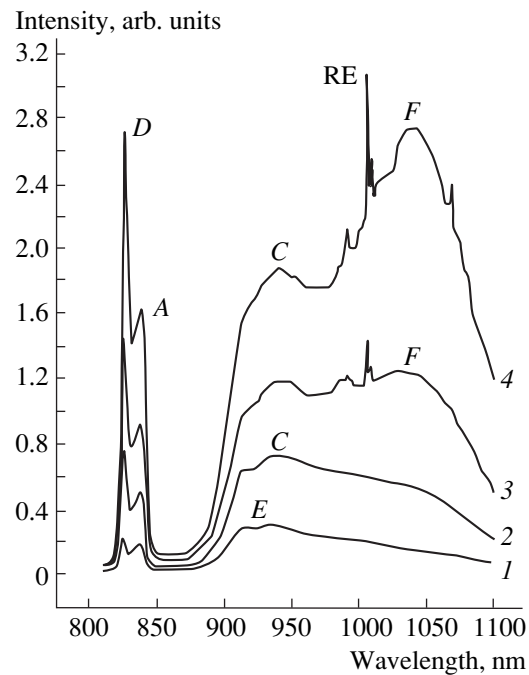


Fig. 3. Electroluminescence spectra of sample *H13A* for the injection currents and bias voltages equal to (1) 10 mA and 2.85 V; (2) 15 mA and 3.1 V; (3) 20 mA and 3.25 V; and (4) 30 mA and 3.4 V. The spectra were measured at 77 K.

the edge-emission bands *D* and *A* in the EL spectra also decrease with an increasing concentration of ion-implanted impurities; however, this decrease is not as drastic as in the case of the PL spectra.

Figure 4 shows a portion of the EL spectrum in the RE-emission range in an implanted and annealed structure for an injection current of ~ 200 mA. The line peaked at 1006 nm and its phonon replica at 1067.2 nm were the most intense in the spectrum. The line peaked at 1008 nm and a group of lines in the region of 990–991 nm are clearly distinguishable. As has been established previously, the lines peaked at 1006 and 1008 nm are related to the complexes of the $\text{Yb}^{3+}\text{-Se-O}$ type, whereas emission in the range of 990–991 nm is related to associations of the $\text{Yb}^{3+}\text{-Si-O}$ type [5, 12].

Figure 3 shows the EL spectra of an implanted and annealed structure for various injection currents. The *C* band appeared for currents of 1–3 mA, whereas the *D* and *A* lines became most intense in the EL spectrum measured for an injection current of ~ 5 mA. The RE emission is observed against the background of the *F* band for injection currents no lower than 18–20 mA. The intensities of the lines peaked at 1006 and 1067.2 nm and also of the main lines in the EL spectra of an implanted and annealed structure depend sublinearly on the injection current. The RE emission of Yb^{3+} ions is distinctly distinguished by its line features (the full width at the half-height for the line peaked at 1006 nm is smaller than 0.1 nm at 77 K).

As can be seen from Fig. 3, the intensities of the donor (D) and acceptor (A) bands in the EL spectrum of the studied structure were almost the same for low injection currents (5–8 mA). For large injection currents, the intensity of the donor band was higher by a factor of 1.5–2 than that of the acceptor band. Almost the same ratio of intensities of the edge-emission bands was also observed in the EL spectra of the reference structure. However, the “normal” ratio between the intensities of the donor and acceptor bands was not recovered by increasing the injection current even for the highest injection level (Fig. 2, curve 3) in the majority of structures with the Yb and O concentrations of $\sim 10^{18} \text{ cm}^{-3}$, in contrast to the structure whose spectra are shown in Fig. 3. For the GaAs structures with Yb and O concentrations of $\sim 10^{19} \text{ cm}^{-3}$, the D band was absent in the EL spectra for all injection levels, and only the A band peaked at 837–839 nm was distinguishable.

3.4. Interaction of Impurities and Defects in the Ion-Implanted GaAs Layers

Recently [13], we determined the conditions necessary for the emergence of the RE emission bands in the PL spectra of GaAs:Yb crystals. These conditions imply that atoms of chemical elements whose interaction with Yb atoms results in the formation of Yb^{3+} ions should be present in the crystal in addition to the Yb and O atoms. Presumably, the same conditions should be satisfied in order to obtain the RE emission in the EL spectra. The starting GaAs crystals were doped with selenium; therefore, it is this impurity that largely controls the fine structure of RE features in the EL spectra (Fig. 4). In addition, the spectra are indicative of the presence of silicon as the dominant background impurity in the starting GaAs samples (the bands peaked at 988–994 nm). An increase in the concentration of ion-implanted Yb and O impurities resulted in a significant decrease in the intensities of the edge-emission bands. However, the acceptor-band intensity was found to be less sensitive to an increase in the Yb concentration compared to the donor-band intensity. This is indicative of specific features of interaction of RE ions with shallow-level donors in GaAs crystals.

As it has been found previously, diffusion of silicon, carbon, sulfur, and selenium atoms is observed in GaAs crystals annealed at a temperature of $\sim 640^\circ\text{C}$ [5, 12]. Therefore, we may assume that variation in the intensity of the donor band in the EL spectra of the GaAs:(Yb,O) crystals is related both to an increase in the concentration of ion-implanted impurities and to a high concentration of radiation defects, as well as to the gettering properties of RE atoms. The Se atoms can diffuse through the crystal at a temperature of $\sim 650^\circ\text{C}$ and can interact with Yb atoms; as a result, Yb–Se complexes are formed. On the one hand, this represents a necessary prerequisite for the origination of RE emission in the GaAs crystal; on the other hand, formation

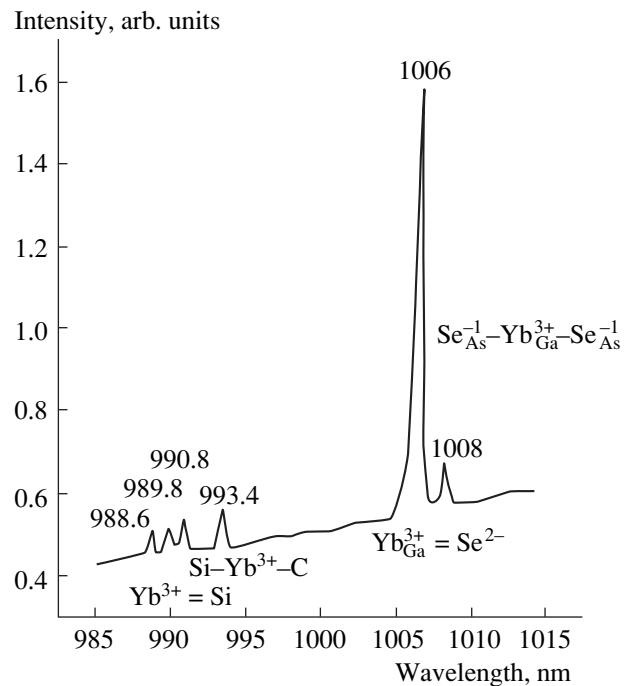


Fig. 4. Fine structure of electroluminescence spectrum in the region of the RE emission. Sample is H13A, the injection current is 200 mA, and the bias voltage is equal to 4.4 V.

of such a complex results in an Se impurity bound to a Yb ion ceasing to be a shallow-level donor. Thus, the gettering effect of Yb atoms manifests itself both in an increase in the RE-emission intensity and in a decrease in the donor-band intensity in the EL spectra.

For the Yb concentrations of $\sim 10^{18} \text{ cm}^{-3}$, it is quite possible that the shallow-donor concentration decreases significantly in a GaAs layer $\sim 200 \text{ nm}$ thick as a result of annealing. The GaAs region that was initially of n -type conductivity may acquire either a conductivity close to intrinsic (i) or even the hole (p) conductivity after ion implantation and annealing. If the concentration of implanted Yb exceeds $\sim 10^{18} \text{ cm}^{-3}$, a drain of Se atoms is possible from the region adjoining the layer containing the RE element to this layer. This may bring about the formation of a p - n junction as a result of the diffusion of Se atoms from the implantation-damaged layer to the layer doped with Yb. It is important that the Yb implantation and subsequent annealing are conducive to the formation of either p - n or n - n^+ junctions; it is the latter that were used for obtaining the EL.

4. CONCLUSION

In this study, we accomplished for the first time an excitation of f - f optical transitions in Yb^{3+} -based complexes in GaAs in the electroluminescence mode in a structure that included an injecting junction. We showed that interaction of implanted Yb atoms with

background impurities (Se) brought about the formation of both Yb-containing complexes and the *i*- or *p*-layers that ensure injection in the structures under consideration.

The data we obtained indicate that it is possible to develop the GaAs:Yb-based optoelectronic devices.

ACKNOWLEDGMENTS

We thank M.V. Yakimov for his help with conducting this study. This study was supported by the Russian Foundation for Basic Research (RFBR) (project no. 00-02-17521), the Interdisciplinary Science and Technology Program (project no. 97-1046), and the INTAS-RFBR (grant no. 95053).

REFERENCES

1. V. M. Konnov, T. V. Larikova, N. N. Loyko, *et al.*, *Mater. Res. Soc. Symp. Proc.* **422**, 58 (1996).
2. V. A. Dravin, V. M. Konnov, T. V. Larikova, and N. N. Loïko, *Kratk. Soobshch. Fiz.* **5-6**, 18 (1995).
3. V. M. Konnov, T. V. Larikova, N. N. Loïko, and V. V. Ushakov, *Kratk. Soobshch. Fiz.* **5-6**, 50 (1995).
4. R. Boyn, *Phys. Status Solidi B* **148** (1), 11 (1988).
5. V. F. Masterov and L. F. Zakharenkov, *Fiz. Tekh. Poluprovodn. (Leningrad)* **24** (4), 610 (1990) [*Sov. Phys. Semicond.* **24**, 383 (1990)].
6. O. M. Borodina, V. A. Dravin, I. P. Kazakov, *et al.*, *Kratk. Soobshch. Fiz.* **9-10**, 41 (1996).
7. U. Kaufmann, E. Klausman, J. Schneider, and H. Ch. Alt, *Phys. Rev. B* **43** (14), 12106 (1991).
8. H. Ch. Alt, *Appl. Phys. Lett.* **54**, 1445 (1989).
9. G. M. Martin, M. Mittoneau, and A. Mircea, *Electron. Lett.* **13**, 191 (1977).
10. A. Mittoneau, G. M. Martin, and A. Mircea, *Electron. Lett.* **13**, 667 (1997).
11. S. M. Sze, in *Physics of Semiconductor Devices* (Wiley, New York, 1969; Énergiya, Moscow, 1973), Chap. 5.
12. V. M. Konnov, N. N. Loïko, and A. A. Gippius, *Kratk. Soobshch. Fiz.* **9-10**, 18 (1995).
13. V. M. Konnov, N. N. Loïko, A. M. Gilinskiï, *et al.*, *Kratk. Soobshch. Fiz.* **8**, 17 (1999).

Translated by A. Spitsyn

**SEMICONDUCTOR STRUCTURES, INTERFACES,
AND SURFACES**

Type II Heterojunctions in an InGaAsSb/GaSb System: Magnetotransport Properties

**T. I. Voronina, B. E. Zhurtanov, T. S. Lagunova, M. P. Mikhailova,
K. D. Moiseev, A. E. Rozov, and Yu. P. Yakovlev**

*Ioffe Physicotechnical Institute, Russian Academy of Sciences, Politekhnicheskaya ul. 26,
St. Petersburg, 194021 Russia*

Submitted July 26, 2000; accepted for publication August 2, 2000

Abstract—Magnetotransport properties of the narrow-gap $\text{In}_x\text{Ga}_{1-x}\text{As}_y\text{Sb}_{1-y}/\text{GaSb}$ heterojunctions grown by liquid-phase epitaxy with various In content in the solid solution ($x = 0.85\text{--}0.95$ and $E_g \leq 0.4$ eV) were studied. It is shown that, depending on the In content in these heterostructures, type II staggered-lineup ($x = 0.85$) or broken-gap heterojunctions ($x = 0.95$) with high mobility in the electron channel at the interface ($\mu \approx 20\,000$ cm²/(V s)) can be realized. For $x = 0.92$, depending on temperature, both types of heterojunctions were observed. Obtained results are in good agreement with the band energy diagram of the type II InGaAsSb/GaSb heterostructures under study. © 2001 MAIK “Nauka/Interperiodica”.

INTRODUCTION

In recent years, type II broken-gap alignment InAs/GaSb heterojunctions (HJs) have attracted much attention. In such a HJ, the valence band of the wide-gap semiconductor lies higher in energy than the conduction band edge of the narrow-gap semiconductor in such a way that there is an energy gap $\Delta \approx 150$ meV at the interface [1]. Due to the flow of electrons through the interface, an electron channel whose characteristics can be modulated by light and also by electric or magnetic fields is formed [1].

The InAs/GaSb heterosystems are similar to the type II HJs based on the quaternary $\text{In}_x\text{Ga}_{1-x}\text{As}_y\text{Sb}_{1-y}$ solid solutions grown by liquid-phase epitaxy (LPE), lattice-matched to both InAs and GaSb substrates. Magnetotransport, photoelectric, and luminescent properties of the GaInAsSb/InAs HJs were studied in detail in [2–6]. It was found that at the isotype $p\text{-Ga}_{1-x}\text{In}_x\text{As}_y\text{Sb}_{1-y}/p\text{-InAs}$ interface with a wide-gap quaternary layer ($x < 0.22$) there exists an electron channel which has high carrier mobility and is located on the InAs side. Characteristics of the channel depend on the composition and level of doping of the solid solution. The band energy diagram of the HJ and the energy spectrum of two-dimensional carriers at the interface were obtained from combined investigation of magnetotransport and electroluminescence in this system at liquid-helium temperature [6]. At the same time, properties of the type II narrow-gap HJs grown on the GaSb substrate [7] are insufficiently studied.

This paper continues a series of studies of type II heterostructures based on quaternary solid solutions, and it is devoted to the magnetotransport study of HJs

in structures with the narrow-gap InGaAsSb/GaSb solid solution. We studied electrical conductivity, the Hall effect, and mobility at $T = 77\text{--}300$ K in the $\text{In}_x\text{Ga}_{1-x}\text{SbAs}/\text{GaSb}$ heterostructures with varied composition of the solid solution ($x = 0.85, 0.92, \text{ and } 0.95$). In this case, the solid solution was either undoped or doped with acceptor impurities. We used $n\text{-GaSb}$ or $p\text{-GaSb}$ as the material for the substrate.

The aim of this study was to identify the type of such HJs and to determine the existence domain of the broken-gap HJ and the conditions for forming a semi-metallic channel at the interface at room temperature.

2. ENERGY BAND DIAGRAM OF AN InGaAsSb/GaSb HETEROJUNCTION

It is interesting to analyze the energy band diagram to identify the HJ type. According to the electron affinity rule [8], an offset in the conduction band at the interface is equal to the difference of the electron affinity values of two semiconductors $\Delta E_c = \chi_1 - \chi_2$. For hetero-combination InAs/GaSb ($\chi_{\text{InAs}} = 4.9$ eV and $\chi_{\text{GaSb}} = 4.06$ eV [9]), the electron affinity rule yields the conduction-band offset $\Delta E_c = 0.84$ eV. The GaSb band gap ($E_{g2} = 0.727$ eV at $T = 300$ K [10]) is smaller than the band offset ΔE_c . Due to this fact, the broken-gap HJ with the energy gap between the GaSb valence band and the InAs conduction band occurs at $T = 300$ K in InAs/GaSb heterostructures:

$$\Delta = \chi_{\text{GaSb}} - \chi_{\text{InAs}} - E_{g\text{GaSb}} \approx -0.150 \text{ eV.} \quad (1)$$

Using, instead of InAs, quaternary $\text{In}_x\text{Ga}_{1-x}\text{As}_y\text{Sb}_{1-y}$ solid solutions with about the same composition as

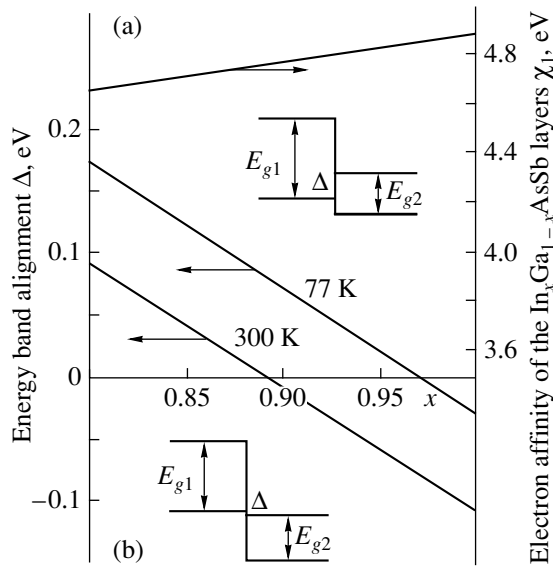


Fig. 1. (a) Electron affinity χ_1 for the $\text{In}_x\text{Ga}_{1-x}\text{As}_y\text{Sb}_{1-y}$ solid solution and (b) energy band offset Δ in the $\text{In}_x\text{Ga}_{1-x}\text{As}_y\text{Sb}_{1-y}/\text{GaSb}$ heterostructures as a function of the solid solution composition.

InAs, we can vary the composition to change the band overlap at the interface and to obtain both staggered-lineup and broken-gap HJs [11]. The conduction band offset will be defined in this case by the difference between the electron affinities χ_1 for the InGaSbAs solid solution and χ_2 for the GaSb substrate. If this band offset is smaller than the GaSb band gap, a type II staggered-lineup HJ forms. If it is larger than the band gap, a broken-gap HJ forms. In the multicomponent $\text{In}_x\text{Ga}_{1-x}\text{As}_y\text{Sb}_{1-y}$ solid solutions, we can determine electron affinity χ_1 as a function of x , taking into account the electron affinity of each binary compound according to the empirical formula [12]

$$\chi_{\text{InGaSbAs}}(x, y) = \chi_{\text{InSb}}x(1-y) + \chi_{\text{InAs}}xy + \chi_{\text{GaSb}}(1-x)(1-y) + \chi_{\text{GaAs}}(1-x)y. \quad (2)$$

The electron affinities χ_1 for the $\text{In}_x\text{Ga}_{1-x}\text{AsSb}$ ($x \geq 0.80$) solid solutions calculated by formula (2) as a function of x are shown in Fig. 1 (we took the electron affinity values for binary compounds from [9]). It should be noted that calculation for $x = 1$ yields the electron affinity value $\chi_1 = 4.87$ eV, which is in good agreement with the experimental data for the $n\text{-InAs}_{0.91}\text{Sb}_{0.08}$ ternary solid solutions reported in [13].

Based on these data (the GaSb band gap $E_{g2} = 0.727$ eV at $T = 300$ K and $E_{g2} = 0.805$ eV at $T = 77$ K [10]), it is possible to define by Eq. (1) the energy gap Δ between the GaSb valence band and the conduction band of the solid solution. Composition dependence for the solid solution is shown in Fig. 1. It follows that in

the $\text{In}_x\text{Ga}_{1-x}\text{AsSb}/\text{GaSb}$ heterostructures a staggered-lineup HJ should be realized in the composition region $x \approx 0.85$ and in the entire temperature range from 77 to 300 K. A broken-gap HJ can exist for $x \geq 0.95$. It is interesting to note that, for $x = 0.92$, the type of the $\text{In}_x\text{Ga}_{1-x}\text{As}_y\text{Sb}_{1-y}/\text{GaSb}$ HJ varies with temperature, due to the temperature dependence of E_g in GaSb: the transition from staggered-lineup to broken-gap HJ occurs as the temperature increases.

3. EXPERIMENT AND DISCUSSION

3.1. Preparation and Characteristics of the Samples

$\text{In}_x\text{Ga}_{1-x}\text{As}_y\text{Sb}_{1-y}/\text{GaSb}$ heterostructures with different In content ($x = 0.85, 0.92, \text{ and } 0.95$) were grown by LPE on GaSb(100) substrates at $T = 600^\circ\text{C}$. According to X-ray studies, the lattice mismatch of layer and substrate amounted to $\Delta a/a \leq 1.2 \times 10^{-3}$. Both binary $n\text{-GaSb:Te}$ single crystals grown by the Czochralski method ($n \approx 5 \times 10^{17} \text{ cm}^{-3}$) and an undoped high-resistivity $p\text{-GaSb}$ epilayer ($p \approx 5 \times 10^{15} \text{ cm}^{-3}$) grown by LPE from a solution-melt with the addition of Pb as a neutral solvent [14] were used as substrates. In the first case, a high potential barrier exists at the InGaAsSb-substrate interface. In the second case, the $p\text{-GaSb}$ epilayer may be considered as a semi-insulator.

The conductivity of undoped InGaAsSb epilayers is of the n -type. Acceptor impurities Mn and Zn were used for growing the p -type layers. The thicknesses of the epilayers were 3–5 μm . Ohmic contacts to rectangular samples were formed on the epilayer for measurements of electrical conductivity σ , the Hall coefficient R_H , and the mobility μ in the temperature range of 77–300 K in magnetic fields of 1–20 kOe. Parameters of investigated samples are listed in the table (conductivity σ and the Hall coefficient R_H were calculated with allowance made for the epilayer thickness of the solid solution). Because the solid solution and substrate were both of n -type and p -type, we could study both isotype ($n\text{-N}$ and $p\text{-P}$) and anisotype ($p\text{-N}$ and $n\text{-P}$) HJs (henceforth, capital letters refer to GaSb, and lowercase letters refer to the narrow-gap material).

3.2. InGaAsSb/GaSb Heterostructures with Undoped Layers of Solid Solution ($n\text{-N}$, $n\text{-P}$, Samples 1–6 in Table)

All $\text{In}_x\text{Ga}_{1-x}\text{As}_y\text{Sb}_{1-y}/\text{GaSb}$ heterostructures with undoped InGaAsSb layers are usually of n -type in the composition range of $0.85 < x < 0.95$ at $T = 77$ and 300 K (see table). However, the Hall mobility values differ: mobility increases as In content in solid solution increases; thus, we have $3 \times 10^3 \text{ cm}^2/(\text{V s})$ and $1.4 \times 10^4 \text{ cm}^2/(\text{V s})$ in the samples with $x = 0.85$ and 0.95, respectively.

In addition, an increase in the In content in solid solution leads to an abrupt change in the temperature dependences of the Hall coefficient and the Hall mobility in heterostructures. In the $\text{In}_{0.85}\text{Ga}_{0.15}\text{SbAs}/\text{GaSb}$ heterostructures (samples 1 and 4) R_H versus $1/T$ dependences have an activation character which is characterized by three slopes, corresponding to the activation energies of $E_A = 0.002, 0.02, \text{ and } 0.09 \text{ eV}$ (Fig. 2). Such values of the activation energy were previously observed in the solid solution epilayers enriched with InAs, and they were ascribed to shallow-level uncontrolled impurities and structural defects [15]. The value and the temperature dependence of Hall mobility of the samples 1 and 4 (Fig. 3) are also typical of InGaSbAs solid solutions, and they are controlled by the carrier scattering from defects and lattice vibrations.

Temperature dependences of the Hall coefficient and the Hall mobility are quite different in heterostructures with a high In content in solid solution (samples 2 and 3, 5 and 6). In these compounds, the Hall coefficient varies only slightly in the temperature range of 77–250 K (Fig. 2). However, in curves corresponding to samples 2 and 3 grown on the $n\text{-GaSb:Te}$ substrate, the slope characterized by the activation energy of $E_A = 0.09 \text{ eV}$ appears at $T > 250 \text{ K}$. This energy, as well as those in samples 1 and 4, may be related to structural defects in the solid solution. The Hall mobility in the $\text{In}_x\text{Ga}_{1-x}\text{AsSb}/\text{GaSb}$ heterostructures with In content in the solid solution $x = 0.95$ (samples 3 and 6) equals $14000 \text{ cm}^2/(\text{V s})$ at $T = 77 \text{ K}$. It decreases insignificantly as temperature increases, but its values are still large, even at room temperature ($\mu_H = 10\,000 \text{ cm}^2/(\text{V s})$). This value is several times larger than that in heterostructures with $x = 0.85$. In the $\text{In}_x\text{Ga}_{1-x}\text{AsSb}/\text{GaSb}$

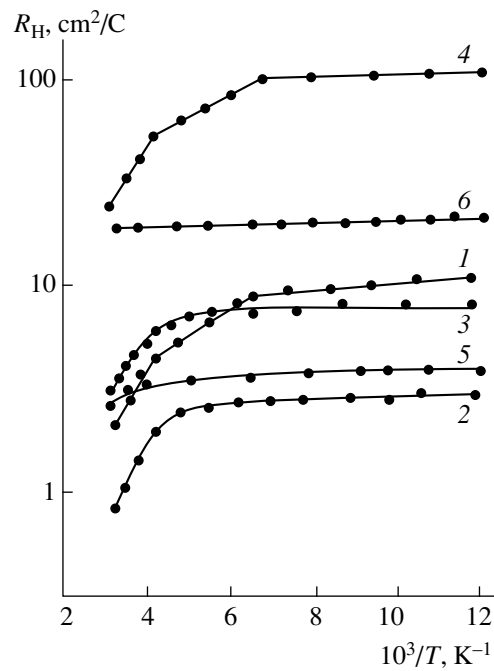


Fig. 2. Dependences of the Hall coefficient on reciprocal temperature for samples 1–6 (curves 1–6) with undoped layers of solid solution. Numbers of the curves correspond to the sample numbers in the table.

heterostructures with $x = 0.92$ (samples 2 and 5), mobility slightly increases with temperature.

These results show that, in the $n\text{-In}_{0.85}\text{Ga}_{0.15}\text{AsSb}/\text{GaSb}$ heterostructures, magnetotransport properties are defined only by the solid solution. This is consistent with the energy diagram of HJ (Fig. 1), from which it

Parameters of the $\text{In}_x\text{Ga}_{1-x}\text{AsSb}/\text{GaAs}$ heterostructures

Sample no.	In content, x	Type of structure	$T = 77 \text{ K}$			$T = 300 \text{ K}$				
			Sign of the Hall voltage	$\sigma, \Omega^{-1} \text{ cm}^{-1}$	$n, 10^{17} \text{ cm}^{-3}$	$\mu_H, \text{cm}^2/(\text{V s})$	Sign of the Hall voltage	$\sigma, \Omega^{-1} \text{ cm}^{-1}$	$n, 10^{17} \text{ cm}^{-3}$	$\mu_H, \text{cm}^2/(\text{V s})$
Undoped InGaAsSb solid solution										
1	0.85	$n\text{-N}$	n	330	11	3700	n	1200	1.6	1900
2	0.92	$n\text{-N}$	n	1300	3.5	4500	n	5300	0.95	5000
3	0.95	$n\text{-N}$	n	1600	8.7	14000	n	2600	3.8	10000
4	0.85	$n\text{-P}$	n	54	115	6300	n	130	30	4000
5	0.92	$n\text{-P}$	n	1900	4.2	8000	n	4700	2.1	10000
6	0.95	$n\text{-P}$	n	550	25.5	14000	n	5200	22	11500
InGaAsSb solid solution doped with acceptors (Mn or Zn)										
7	0.85	$p\text{-N}$	p	12	4.9	59	p	17	2.1	36
8	0.92	$p\text{-P}$	p	26	8.3	220	n	47	21.5	1000
9	0.95	$p\text{-P}$	n	135	22	3000	n	200	14	2800

Note: Thickness of the InGaAsSb epilayer was used in calculations of conductivity σ and the Hall coefficient R_H in heterostructures.

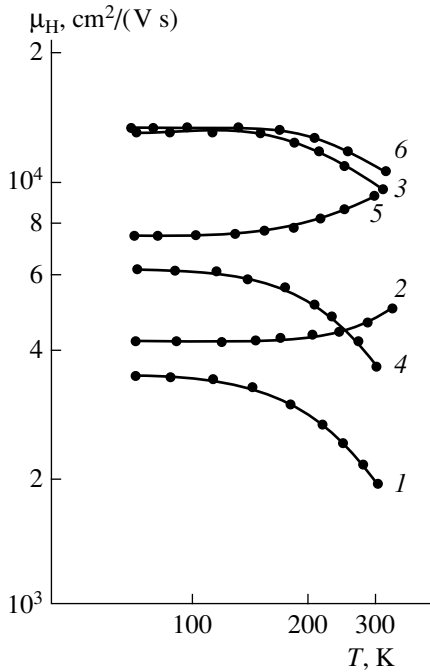


Fig. 3. The Hall mobility as a function of temperature for samples 1–6 (curves 1–6) with undoped layers of solid solution. Numbers of the curves correspond to the sample numbers in the table.

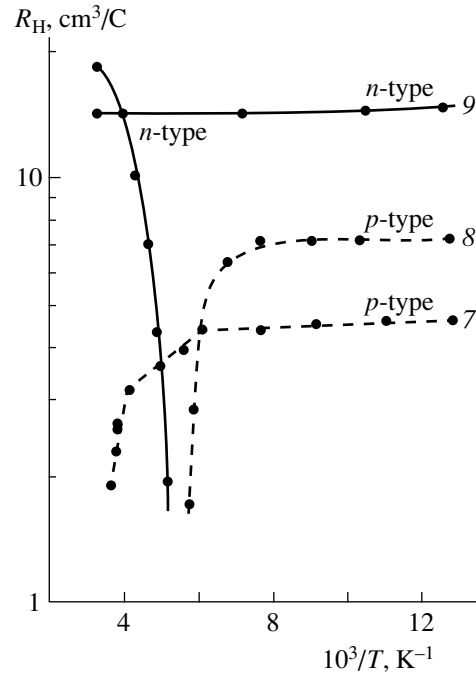


Fig. 4. Dependences of the Hall coefficient on reciprocal temperature for samples 7–9 (curves 7–9) with doped layers of solid solution. Numbers of the curves correspond to the sample numbers in the table.

follows that, for such a composition of solid solution, a staggered-lineup HJ should be observed in the entire temperature range from 77 to 300 K.

In the $\text{In}_{0.95}\text{Ga}_{0.05}\text{SbAs}/\text{GaSb}$ heterostructures, high electron mobility can be explained according to the energy diagram (Fig. 1) by the existence of the electron channel at the interface of the broken-gap HJ. In the $\text{In}_{0.92}\text{Ga}_{0.08}\text{SbAs}/\text{GaSb}$ heterostructures, an increase in the Hall mobility with temperature can be attributed to variation in the HJ type, due to variation in the GaSb band gap (Fig. 1): from a staggered-lineup type at $T = 77$ K to a broken-gap type at $T = 300$ K.

It is necessary to note that a significant difference in the magnetotransport properties of the $\text{In}_x\text{Ga}_{1-x}\text{AsSb}/\text{GaSb}$ heterostructures with $x = 0.85$ and $x \geq 0.92$ manifests itself in the Hall coefficient dependences on the magnetic field strength also. In the samples with $x = 0.85$, the Hall coefficient does not change as the magnetic field strength increases, which is typical of conduction with one kind of charge carrier (electrons in solid solution), whereas in the samples with $x \geq 0.92$ we observe a small decrease in the Hall coefficient as the magnetic field strength increases. This result shows that two kinds of charge carriers are involved in magnetotransport (electrons in solid solution and in the electron channel at the interface).

Therefore, σ , R_H , and μ_H measured in the $\text{In}_x\text{Ga}_{1-x}\text{AsSb}/\text{GaSb}$ heterostructures for $x = 0.85$ are

governed by the solid solution properties, but, for $x \geq 0.92$, properties of both solid solution and electron channel affect these quantities.

We can estimate mobility in the electron channel using well-known formulas for a double-layer model [16]:

$$\mu_1 = \mu_H(1 - \sigma_2/\sigma) - \mu_2/(1 - \sigma/\sigma_2), \quad (3)$$

where subscript 1 refers to the electron channel, subscript 2 refers to the solid solution epilayer, and σ and μ_H are measured values for the whole heterostructure.

If we accept data for sample 1 as electron mobility in solid solution, then mobility in the electron channel in sample 3, calculated according to formula (3), equals $\mu_1 = 16600 \text{ cm}^2/(\text{V s})$ at $T = 77$ K and $\mu_1 = 16700 \text{ cm}^2/(\text{V s})$ at $T = 300$ K.

3.3. Heterostructures with Doped Solid-Solution Layers (Junctions p–N and p–P, Samples 7–9)

Manganese and zinc were used as acceptor dopants for overcompensation of the $\text{In}_x\text{Ga}_{1-x}\text{As}_y\text{Sb}_{1-y}$ solid solutions and producing material with conduction of p-type. Both impurities in InAs and solid solutions enriched with InAs introduce the acceptor levels with the activation energy $E_A = 0.02\text{--}0.03$ eV [17]. Conductivity, the Hall coefficient, and mobility in the p- $\text{In}_x\text{Ga}_{1-x}\text{SbAs}/\text{GaSb}$ heterostructures, with varied

composition of solid solution but with the same level of doping with the acceptor impurities equal to 9×10^{-4} at. % (samples 7–9), are listed in the table. Dependences of the Hall coefficient and mobility on temperature and the magnetic field strength are shown for these samples in Figs. 4–6.

It was determined that $\text{In}_x\text{Ga}_{1-x}\text{AsSb}/\text{GaSb}$ heterostructures with $x = 0.85$ are of p -type in the entire temperature range from 77 to 300 K (see table, sample 7). Two slopes are distinguishable in the curve R_H versus $1/T$ (Fig. 4, sample 7): one of them corresponds to the activation energy of 0.02 eV, which is typical of acceptor levels in doped InGaSbAs solid solution, and the other corresponds to the activation energy of 0.09 eV, which is probably related to the structural defects. The Hall mobility μ_H is very low due to high compensation, and it decreases slightly as temperature increases (Fig. 5, sample 7). Therefore, we come to the conclusion that the magnetotransport properties of the $p\text{-In}_{0.85}\text{Ga}_{0.15}\text{SbAs}/\text{GaSb}$ heterostructures, as well as those of the samples with undoped epilayer of the same composition, are controlled by the solid solution properties, which may indicate that a staggered-lineup HJ exists (Fig. 1).

At the same time, conductivity of the n -type is observed in the entire temperature range from 77 to 300 K (see table, sample 9) in the $p\text{-InGaAsSb}/\text{GaSb}$ heterostructures with a high In content in the solid solution ($x = 0.95$) and with a similar level of zinc doping. The Hall coefficient is independent of temperature (Fig. 4, sample 9) and of the magnetic field strength. The Hall mobility in these samples retains the value of $3000 \text{ cm}^2/(\text{V s})$ up to room temperature (Fig. 5, sample 9). These magnetotransport properties suggest the predominance of only one type of carrier (electrons in the electron channel at the interface) and the existence of a broken-gap HJ (Fig. 1).

Transition from a staggered-lineup HJ at $T = 77 \text{ K}$ to a broken-gap HJ at $T = 300 \text{ K}$ is observed in both $p\text{-In}_x\text{Ga}_{1-x}\text{SbAs}/\text{GaSb}$ heterostructures with $x = 0.92$ and in heterostructures with undoped layers of solid solution of the same composition. However, in isotype $p\text{-}P$ heterostructures, such a modification of HJ is more pronounced in the experiment. At $T = 77 \text{ K}$, the heterostructure is of the p -type, with a mobility of $\mu_H = 220 \text{ cm}^2/(\text{V s})$, typical of the $p\text{-InGaSbAs}$ solid solution. Conductivity in heterostructures changes sign from hole- to electron-type as the temperature increases (see table, sample 8). This change in sign and the simultaneous increase of the electron mobility with temperature (Figs. 5 and 6, sample 8) are possibly related to the electron channel at the interface on the solid-solution side.

Strong Hall coefficient dependence on the magnetic field strength (Fig. 6) is characteristic of the

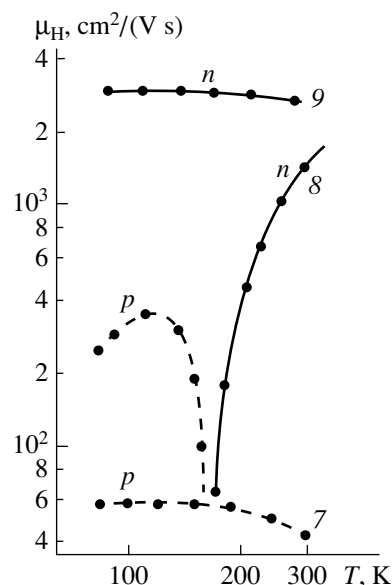


Fig. 5. Temperature dependence of the Hall mobility for samples 7–9 (curves 7–9) with doped layers of solid solution. Numbers the curves correspond to the sample numbers in the table.

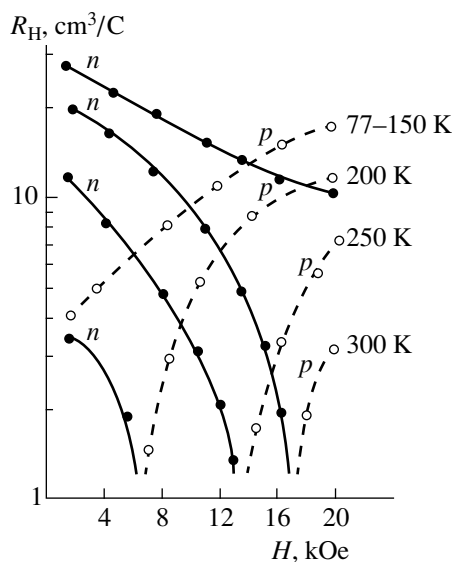


Fig. 6. The Hall coefficient as a function of the magnetic field strength for sample 8. Temperature of measurements is indicated at the curves.

$p\text{-InGaSbAs}/p\text{-GaSb}$ heterostructures with $x = 0.92$. It can be seen that at $T = 77\text{--}150 \text{ K}$ conductivity is of the p -type; i.e., holes are dominant in the solid solution. The electron channel (the combined conduction of electrons in the channel and holes in the solid solution) manifests itself in the decrease of the Hall coefficient as the magnetic field strength decreases. At temperatures above 150 K and in low fields, only the electron channel is important; its contribution increases with temper-

ature. These results are in agreement with the energy diagram (Fig. 1), and they show that the energy gap Δ increases with temperature, and, as a result, the transition from a staggered-lineup HJ to a broken-gap HJ occurs. At the same time, the depth of the potential wells at the interface increases, and the contribution of carriers localized at the interface becomes dominant.

Comparing our experimental data obtained for the $\text{In}_x\text{Ga}_{1-x}\text{As}_y\text{Sb}_{1-y}/\text{GaSb}$ ($x > 0.92$, $E_g < 0.4$ eV) heterostructures with previously studied $p\text{-Ga}_{1-x}\text{In}_x\text{As}_y\text{Sb}_{1-y}/p\text{-InAs}$ heterostructures ($x < 0.22$ and $E_g > 0.56$ eV [2]), we see that mobility in the electron channel in the $\text{InGaAsSb}/\text{GaSb}$ heterostructures is an order of magnitude lower than in the $p\text{-GaInAsSb}/p\text{-InAs}$ heterostructures. Such a distinction in magnitude between the carrier mobility in the electron channel in structures based on the narrow-gap InGaAsSb solid solutions grown on the GaSb substrates and the carrier mobility in structures based on the wide-gap GaInAsSb solid solutions grown on InAs can be attributed to changes in the interface smoothness with an accompanying increase in scattering by the interface roughness, and also to differences in the character of bonds formed at the interface. If a narrow-gap solid solution is grown on a wide-gap substrate, bonds of the Ga-As type are formed at the interface. In the case of a wide-gap solid solution grown on a narrow-gap substrate, bonds of the In-Sb type are formed. In the latter case, an abrupt planar interface with a transition layer of ~ 12 Å thickness is produced, and high electron mobilities are attained in the electron channel [18, 19].

4. CONCLUSION

Magnetotransport properties in the type II $\text{In}_x\text{Ga}_{1-x}\text{As}_y\text{Sb}_{1-y}/\text{GaSb}$ narrow-gap HJs grown by liquid-phase epitaxy with a varied composition of solid solution ($x = 0.85, 0.92, \text{ and } 0.95$) were studied. It is shown that, in accordance with the energy diagram (Fig. 1), at $T = 77\text{--}300$ K, a type II staggered HJ is formed in the $\text{In}_x\text{Ga}_{1-x}\text{AsSb}/\text{GaSb}$ heterostructures with $x = 0.85$ and that a type II broken-gap HJ is formed for $x = 0.95$. At the $\text{InGaAsSb}/\text{GaSb}$ interface with $x = 0.92$, either staggered-lineup or broken-gap type II HJs may be formed, depending on the temperature.

The highest electron mobility in the electron channel (about $20000 \text{ cm}^2/(\text{V s})$) is observed in heterostructures with undoped layers of the $\text{In}_x\text{Ga}_{1-x}\text{AsSb}$ ($x = 0.95$) solid solution. We believe that lower values of the electron mobility in the $\text{InGaAsSb}/\text{GaSb}$ channel in comparison with heterostructures based on the wide-gap $\text{GaInAsSb}/\text{InAs}$ solid solutions, in which mobilities higher than $50000 \text{ cm}^2/(\text{V s})$ were obtained, are related to variation of the type of bonds at the interface (from In-Sb to Ga-As) and to special features of the epitaxial-growth conditions of solid solutions on the wide-gap and narrow-gap substrates.

Doping of solid solution with the acceptor impurities results in a decrease in the highest carrier mobility in the electron channel to $3000 \text{ cm}^2/(\text{V s})$. Low mobility in the electron channel is explained in this case by the high compensation of solid solution and, as a result, by an increase in the potential fluctuation amplitude at the interface.

We showed that in the $\text{InGaAsSb}/\text{GaSb}$ heterostructures with type II broken-gap HJ the electron channel controlled magnetotransport properties of the heterostructure up to room temperature, because the wide-gap GaSb substrate in this case completely eliminated the electron-channel shunting.

ACKNOWLEDGMENTS

This study was supported in part by the Ministry of Science Grant "Physics of the Solid-State Nanostructures", project no. 97-1035; by the Russian Foundation for Basic Research, project no. 99-02-18330; and by the Czech Academy of Sciences Grant, grant no. A1010807/1988.

REFERENCES

1. G. A. Sai-Halasz, L. Esaki, and W. A. Harrison, *Phys. Rev. B* **18** (6), 2812 (1978).
2. T. I. Voronina, T. S. Lagunova, M. P. Mikhaïlova, *et al.*, *Fiz. Tekh. Poluprovodn. (St. Petersburg)* **30**, 985 (1996) [*Semiconductors* **30**, 523 (1996)].
3. T. I. Voronina, T. S. Lagunova, M. P. Mikhaïlova, *et al.*, *Fiz. Tekh. Poluprovodn. (St. Petersburg)* **31**, 897 (1997) [*Semiconductors* **31**, 763 (1997)].
4. T. I. Voronina, T. S. Lagunova, M. P. Mikhaïlova, *et al.*, *Fiz. Tekh. Poluprovodn. (St. Petersburg)* **32**, 215 (1998) [*Semiconductors* **32**, 195 (1998)].
5. T. I. Voronina, T. S. Lagunova, M. P. Mikhaïlova, *et al.*, *Fiz. Tekh. Poluprovodn. (St. Petersburg)* **34**, 194 (2000) [*Semiconductors* **34**, 189 (2000)].
6. M. P. Mikhailova, N. L. Bazhenov, V. A. Berezovets, *et al.*, in *Proceedings of International Symposium on Nanostructures: Physics and Technology, St. Petersburg, 1997*, p. 152.
7. M. A. Afraimov, A. N. Baranov, A. P. Dmitriev, *et al.*, *Fiz. Tekh. Poluprovodn. (Leningrad)* **24**, 1397 (1990) [*Sov. Phys. Semicond.* **24**, 876 (1990)].
8. A. G. Milnes and D. L. Feucht, *HJs and Metal-Semiconductor Junctions* (Academic, New York, 1972; Mir, Moscow, 1975).
9. M. Nako, S. Yoshida, and S. Ganda, *Solid State Commun.* **49**, 663 (1984).
10. M. P. Mikhailova and A. N. Titkov, *Semicond. Sci. Technol.* **9**, 1279 (1994).
11. O. Madelung, *Physics of III-V Compounds* (Wiley, New York, 1964; Mir, Moscow, 1967).
12. J. C. Dewinter, M. A. Pollack, A. K. Srivastava, and J. L. Zyskind, *J. Electron. Mater.* **4**, 727 (1985).

13. M. Mebarki and A. Kadri, *Solid State Commun.* **72**, 795 (1989).
14. A. N. Baranov, T. I. Voronina, T. S. Lagunova, *et al.*, *Pis'ma Zh. Tekh. Fiz.* **13**, 1103 (1987) [*Sov. Tech. Phys. Lett.* **13**, 460 (1987)].
15. T. I. Voronina, T. S. Lagunova, K. D. Moiseev, *et al.*, *Fiz. Tekh. Poluprovodn. (St. Petersburg)* **33**, 781 (1999) [*Semiconductors* **33**, 719 (1999)].
16. K. Subashiev and S. A. Plotnikov, *Fiz. Tverd. Tela (Leningrad)* **2**, 1169 (1960) [*Sov. Phys. Solid State* **2**, 1059 (1960)].
17. T. I. Voronina, T. S. Lagunova, M. P. Mikhaïlova, *et al.*, *Fiz. Tekh. Poluprovodn. (Leningrad)* **25**, 276 (1991) [*Sov. Phys. Semicond.* **25**, 167 (1991)].
18. M. S. Daly, D. M. Simons, M. Lakrimi, *et al.*, *Semicond. Sci. Technol.* **11**, 823 (1996).
19. Yu. B. Vasil'ev, S. D. Suchalkin, S. V. Ivanov, *et al.*, *Fiz. Tekh. Poluprovodn. (St. Petersburg)* **31**, 1246 (1997) [*Semiconductors* **31**, 1071 (1997)].

Translated by I. Kucherenko

SEMICONDUCTOR STRUCTURES, INTERFACES,
AND SURFACES

Extension of the Frequency Range of the Noise Spectral Density in Silicon $p-n$ Structures Irradiated with Gamma-Ray Quanta

O. K. Baranovskii*, P. V. Kuchinskii**, V. M. Lutkovskii*,
A. P. Petrunin**, and E. D. Savenok**

* *Belarussian State University, ul. Leningradskaya 14, Minsk, 220050 Belarus*
e-mail: alehb@rfe.bsu.unibel.by

** *Sevchenko Research Institute of Applied Problems in Physics, Minsk, 220064 Belarus*

Submitted July 12, 2000; accepted for publication September 5, 2000

Abstract—The possibility of intentionally shifting the high-frequency edge of plateau in the noise spectral density of silicon $p-n$ structures to higher frequencies under irradiation with gamma-ray quanta was studied. The largest increase in the extent of the operating-frequency range was observed to amount to 2–2.5 times. As the irradiation dose increased further, the plateau width did not increase, and its boundary became less abrupt. Correlation between the variation in the effective lifetime of minority charge carriers and the width of low-frequency plateau in the noise spectral density was found. A qualitative model describing the variation in the noise spectral density with increasing irradiation dose for silicon $p-n$ structures with microplasma channels governed by the $p-n$ junction dimensions is suggested. © 2001 MAIK “Nauka/Interperiodica”.

INTRODUCTION

Silicon diodes with reverse-biased $p-n$ junctions are used in electronic engineering as the sources of broadband signals for checking the sensitivity of receivers and amplifiers, for determining the interference immunity of automatic- and remote-control systems, and as reference-noise sources in the measurements of noise.

Localized regions of a higher field strength (compared to the remaining portion of the space-charge region (SCR)) are observed during avalanche breakdown of reverse-biased $p-n$ junctions [1]. It is generally agreed that these regions are formed owing to minor inhomogeneities in the $p-n$ junction. The presence of such inhomogeneities, which are regions of reduced breakdown voltage, gives rise to microplasma channels, i.e., to a short-term flow of a current of 10–200 μA through these inhomogeneities. In this paper, we report the results of studying the effect of ionizing radiation on the ratio between the probabilities of initiating and suppressing the microplasma channels; we were interested in the value of this ratio where the current fluctuations were at a maximum.

Random behavior of the microplasma-channel initiation-suppression is caused by fluctuations of the number of charge carriers in the regions of the $p-n$ junction and the base; these fluctuations accompany both the impact ionization in the multiplication region and the transport of electrons and holes through the transit areas of the $p-n$ junction. The fluctuations are related to the processes of thermal generation and recombination of charge carriers in the bulk of the crystal. The ava-

lanche-charge retention time is controlled to a large extent by the lifetime τ of the minority charge carriers, which depends on the electron-capture cross section, the concentration of centers, and the depth of the corresponding energy levels [2]. We may assume that the value of τ will decrease if additional radiation defects are introduced; this should result in an increase in the noise spectral density (NSD) in the regions of medium or high frequencies. In connection with this, the objective of this study was to gain insight into the possibility of intentionally varying the frequency characteristics of diodes.

EXPERIMENTAL

The studied samples were silicon structures with an abrupt $p-n$ junction that has an area of 10^{-4} or 1 mm^2 . The doping level of the base region of the $p-n$ junction amounted to $\sim 10^{17} \text{ cm}^{-3}$, which corresponded to a breakdown voltage of $\sim 8\text{--}10 \text{ V}$.

The measurements were performed at a temperature of $(20 \pm 1)^\circ\text{C}$, with the average current through the samples being equal to $50 \mu\text{A}$ and controlled by the load-resistor value ($20 \text{ k}\Omega$). Instability of the output current was observed in the bias range of $7.7\text{--}10.7 \text{ V}$. In the case under consideration, the behavior of the current-pulse shapes was similar to that reported previously [3]. The largest NSD width was observed when a voltage of 8.7 V was applied, which corresponded to the largest amplitude and frequency of the current fluctuations. Correlation between the pulsed current flow and the microplasma breakdown is verified by the lin-

earity of the current–voltage characteristic in the instability region [3].

The samples were irradiated with ^{60}Co gamma-ray quanta at a temperature of 50°C . The NSD was calculated using a conventional algorithm of fast Fourier transform [4] on the basis of measurements of the noise current in the structures studied. The error in calculations was no larger than 8%. Distortions introduced by the measurement circuits were no larger than 5%. The lifetime of the minority charge carriers was determined from measurements of the transient-process characteristics in the course of switching the current [5].

RESULTS AND DISCUSSION

The output current of the p – n structures studied is represented by a sequence of pulses which include two portions: a steep leading edge and a gently sloping trailing edge (the oscillograms of current in p – n structures before irradiation are shown in Fig. 1). The leading edge corresponds to the initiation of microplasma and to the multiplication of charge carriers in the avalanche due to impact ionization, whereas the trailing edge corresponds to the suppression of the avalanche and a decrease in the avalanche current. Suppression of the avalanche may be caused by a decrease in the mean free path of the charge carriers in the multiplication region as a result of heating of microplasma [6] or as a result of a decrease in the field strength due to the effect of the charge-carrier space charge in the transit regions [3]. The dependences of the microplasma pulses on temperature and applied voltage were studied. It was found that an increase in voltage and temperature results in an increase in the probability of the microplasma initiation and does not affect the delay in the microplasma suppression. After the microplasma has been suppressed, the rate of the avalanche-charge decay may be controlled by the drift rate of charge carriers in the SCR and in the region of the neutral base, by the characteristic times of capture by and emission from the traps, and by recombination of charge carriers. A repeat initiation of an avalanche is probabilistic and depends on the recovery of the field strength sufficient for breakdown and on the presence of charge carriers that initiate the avalanche.

Figures 2 and 3 show the spectra of noise pulses generated in the p – n structures with small and large areas. In the spectra, a portion of the NSD independence of frequency (a low-frequency plateau) and a region of falloff in the high-frequency region are observed.

A change in NSD of p – n structures with a large area as the irradiation integrated flux increases (Fig. 3) is accompanied by an increase in the width of the low-frequency plateau and a decrease in the absolute value of the noise density in the entire frequency range; simultaneously, the slope angle of the high-frequency fall-off decreases. For p – n structures with a small area (Fig. 2),

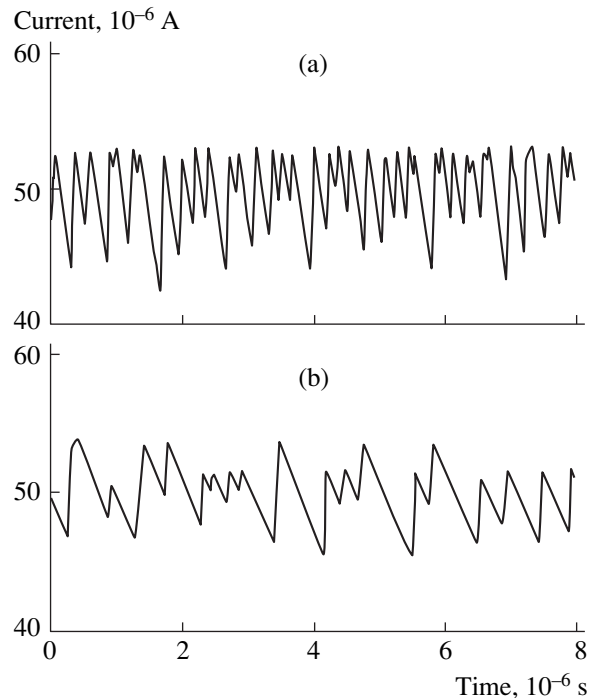


Fig. 1. Oscillograms of output current of unirradiated p – n structures having (a) small area and (b) large area.

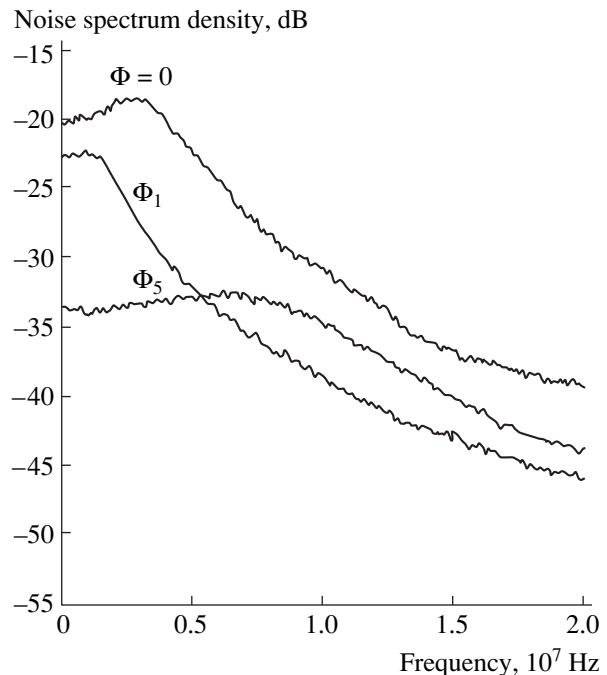


Fig. 2. The noise spectral density of p – n structures with small area. Φ , Φ_1 , and Φ_5 stand for the integrated fluxes of gamma-ray quanta irradiating the structures ($\Phi_5 > \Phi_1$).

the opposite phenomenon is observed; i.e., the width of the low-frequency plateau decreases drastically for the integrated radiation fluxes of up to $\Phi_1 = 2 \times 10^{16} \text{ cm}^{-2}$. However, a further increase in the integrated irradiation

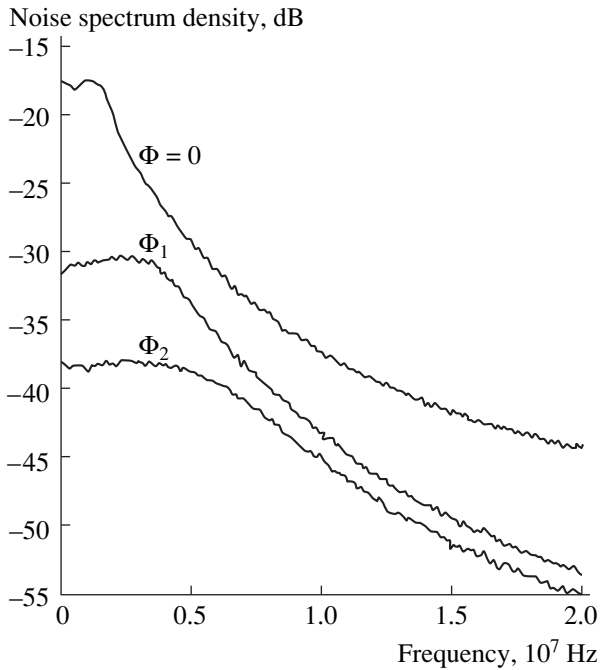


Fig. 3. The noise spectral density of p - n structures with large area. Φ , Φ_1 , and Φ_2 stand for integrated fluxes of the gamma-ray quanta irradiating the structures ($\Phi_2 > \Phi_1$).

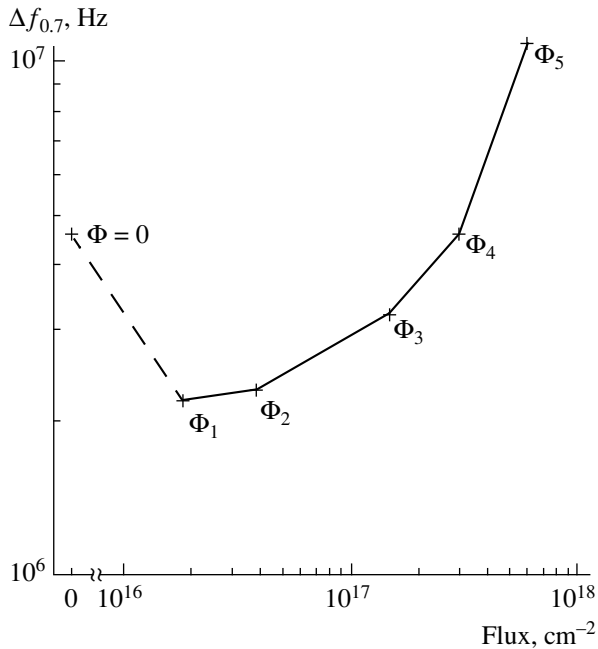


Fig. 4. The width of the low-frequency plateau in the frequency dependence of the noise spectral density in the small-area p - n structures as a function of integrated flux of gamma-ray quanta that irradiated the structures.

flux leads to a gradual extension of the width of the low-frequency plateau; for integrated fluxes on the order of $\Phi_5 = 6 \times 10^{17} \text{ cm}^{-2}$, this width becomes 2–2.5 times larger than the initial width.

We observed the existence of a certain critical value of the integrated radiation flux, such that, if exceeded, the width of the plateau in the spectral characteristic ceases to increase, and the plateau boundaries become less abrupt. In addition, the average amplitude of the noise-current fluctuations decreases drastically.

Figure 4 illustrates the variation in the NSD plateau width in the diodes studied (at the level of 0.7 with respect to the maximum) with the integrated flux of radiation. It can be seen that the rate of variation in the NSD width is not constant. Up to the radiation integrated fluxes of $\Phi_3 = 1.5 \times 10^{17} \text{ cm}^{-2}$, the plateau width increases slowly. For integrated fluxes higher than $1.5 \times 10^{17} \text{ cm}^{-2}$, we observe an increased rate of shift of the high-frequency plateau edge to higher frequencies.

A change in the lifetime of minority charge carriers in the base region of the structures under irradiation is illustrated in Fig. 5 and can be described by the following formula:

$$\Delta(1/\tau) = 1/\tau_1 - 1/\tau_0. \quad (1)$$

Here, τ_0 is the initial lifetime, and τ_1 is the lifetime after irradiation. We can distinguish two portions in the $\Delta(1/\tau)$ variation with the integrated irradiation flux: there is a slight linear increase in the charge-carrier lifetime as the integrated irradiation flux increases up to $1.5 \times 10^{17} \text{ cm}^{-2}$, and there is a much steeper linear increase for the integrated irradiation fluxes higher than $1.5 \times 10^{17} \text{ cm}^{-2}$.

The behavior of NSD in the output current of diodes may be explained in terms of the following qualitative model. The latter is based on the linear dimensions of p - n junctions in the p - n structures under consideration. The p - n junction area is $1 \times 1 \text{ mm}^2$ in the large-area structures and is $10^{-2} \times 10^{-2} \text{ mm}^2$ in the small-area structures. We may assume that in the small-area p - n structures the contribution of surface states to variation in electrical properties is comparable to the bulk effects. In this case, anomalous behavior of NSD in the small-area p - n structures under low irradiation doses of up to $2 \times 10^{16} \text{ cm}^{-2}$ may be attributed to the surface recombination of the minority charge carriers. The surface traps are involved in the avalanche-charge decay, because they act as recombination centers for the charge carriers. After irradiation of the samples, the surface channel of recombination becomes ineffective. As a result, the trailing edge of the current pulses becomes more extended in time, and, correspondingly, the high-frequency edge of the NSD plateau shifts to lower frequencies.

Irradiation gives rise to new recombination centers in the bulk of the diodes. The number of the events of the charge-carrier capture and release from the traps during the avalanche development increases. These processes lead to a decrease in the number of electrons involved in the impact ionization and, correspondingly, to an increase in the probability of the microplasma suppression. Such an assumption is strengthened by an

insignificant increase in the variance of the largest pulse amplitudes. On the other hand, irradiation also affects the probability of microplasma initiation. The traps that captured the charge carriers during the preceding stage of the avalanche development become the centers of emission of electrons initiating the avalanche. These processes entail an increase in the pulse-repetition rate and, consequently, an increase in the width of the low-frequency NSD plateau.

Variation in the lifetime of minority charge carriers is typically related to the integrated irradiation flux by the following formula [7]:

$$\Delta(1/\tau) = k\Phi. \quad (2)$$

Here, k is the damage-rate factor, and Φ is the radiation integrated flux. The nonlinear dependence $\Delta(1/\tau)$ observed experimentally is inconsistent with formula (2).

Such behavior of the quantity $\Delta(1/\tau)$ may be explained in terms of the suggested qualitative model. We analyze this behavior taking into account the dependence of the diffusion length L of the minority charge carriers on their lifetime τ_n and the diffusion coefficient D , as given by

$$L = \sqrt{D\tau_n}. \quad (3)$$

Up to certain integrated fluxes on the order of $1.5 \times 10^{17} \text{ cm}^{-2}$, the value of $\Delta(1/\tau)$ is governed by linear dimensions of the p - n junction; in this case, the diffusion length L of the minority charge carriers is larger than the junction linear dimension l . Thus, we have

$$L \gg l.$$

For integrated radiation fluxes exceeding $1.5 \times 10^{17} \text{ cm}^{-2}$, the concentration of the formed charge traps begins to play a significant role; i.e., the effect of generation-recombination processes increases in magnitude. The diffusion length becomes comparable to or smaller than the junction linear dimensions ($l \geq L$).

It is important that the rate of variations in the lifetime of the minority charge carriers correlates with the rate of variations in the width of the NSD low-frequency plateau in the studied diodes. It follows from an analysis of the data presented in Figs. 4 and 5 that the rate of variation in the width of the low-frequency plateau in the model we suggested is controlled by the ratio between the diffusion length L of the minority charge carriers and the linear dimensions of p - n junction. In this case, the value of L is specified by the integrated irradiation flux.

Comparing the NSD of output currents in the small- and large-area p - n structures (Figs. 2, 3), we can easily perceive that even for much higher integrated radiation fluxes the value of the low-frequency NSD is larger in the small-area p - n junctions than in the large-area ones. Consequently, the noise-pulse amplitude is larger. This fact is also explained in terms of the suggested model. The diameter of microplasma channels emerging for the actual diode-bias voltages is approximately

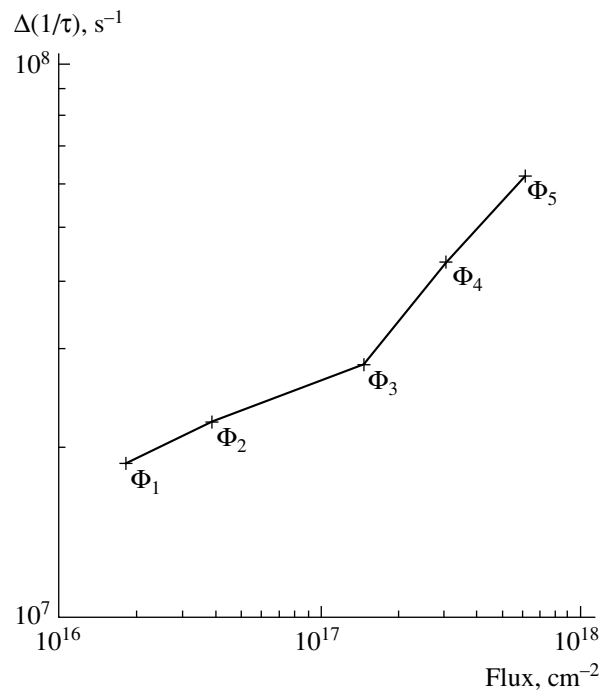


Fig. 5. The lifetime of the minority charge carriers in the small-area p - n structures as a function of integrated flux of gamma-ray quanta that irradiated the structures.

equal to the SCR width and amounts to ~ 0.3 – $0.5 \mu\text{m}$. For the structures with linear p - n junction dimensions of $1 \text{ mm} \times 1 \text{ mm}$, there can exist several microplasma channels with almost the same breakdown voltages; these microplasma channels may operate either alternatively or superimposing on each other (and thus increasing the rate of output noise pulses). Such an assumption is corroborated by the spread of the microplasma pulses in the maximum amplitude (Fig. 1b); intermediate plateaus can be easily recognized in the current oscillograms as the bias voltage increases. The probability of initiation of the avalanche current through such p - n junctions is a sum of the probabilities of formation of individual microplasma channels. Under the same conditions for p - n structures with an area of $10^{-2} \times 10^{-2} \text{ mm}^2$, the probability of formation of several microplasma channels in the region of the p - n junction is lower. Therefore, the time interval between the instants of initiation of avalanches through a p - n junction is larger than for p - n structures with a large area.

Thus, for the small-area p - n structures, a shift of the high-frequency edge of the NSD plateau to lower frequencies after low-dose irradiation may be attributed to suppression of the surface-recombination channel. The shift of the high-frequency edge to higher frequencies after irradiation with integrated fluxes larger than $1.5 \times 10^{17} \text{ cm}^{-2}$ is caused by a decrease in the lifetime of the minority charge carriers in the bulk of semiconductor.

CONCLUSION

We suggested a qualitative model for describing the variations in the noise spectral density (NSD) in $p-n$ structures subjected to gamma-ray irradiation, with the development of individual microplasma channels controlled by dimensions of the $p-n$ junction. Our experimental data show that the irradiation of silicon $p-n$ structures with gamma-ray quanta makes it possible to shift the high-frequency edge of the NSD plateau to higher frequencies. As a result, the width of the operating-frequency band may extend by a factor of 2–2.5. As the integrated flux of radiation is increased further, the plateau width does not increase any more, whereas the edges of this plateau become less abrupt. Amplitude characteristics of structures under conditions of the development of no more than a single microplasma channel are less affected by irradiation. We observed a correlation between the effective lifetime of the minority charge carriers and the width of the NSD low-frequency plateau.

REFERENCES

1. A. S. Tager and V. M. Val'd-Perlov, *Avalanche Transit-Time Diodes and Their Application in Microwave Technology* (Sov. Radio, Moscow, 1968).
2. N. B. Luk'yanchikova, *Fluctuation Phenomena in Semiconductors and Semiconductor Devices* (Radio i Svyaz', Moscow, 1990).
3. I. V. Grekhov and Yu. N. Serezhkin, *Avalanche Breakdown of $p-n$ Junction in Semiconductors* (Énergiya, Leningrad, 1980).
4. J. Bendat and A. Piersol, *Random Data. Analysis and Measurement Procedures* (Wiley, New York, 1986; Mir, Moscow, 1989).
5. S. M. Krakauer, Proc. IEEE **50** (7), 1665 (1962).
6. B. I. Datsko, Fiz. Tekh. Poluprovodn. (St. Petersburg) **31**, 186 (1997) [Semiconductors **31**, 146 (1997)].
7. V. S. Vavilov and N. A. Ukhin, *Radiation Effects on Semiconductors and Semiconductor Devices* (Atomizdat, Moscow, 1969).

Translated by A. Spitsyn

LOW-DIMENSIONAL
SYSTEMS

Carrier Photoexcitation from Levels in Quantum Dots to States of the Continuum in Lasing

L. V. Asryan^{1,2} and R. A. Suris²

¹ Department of Electrical and Computer Engineering, State University of New York at Stony Brook,
Stony Brook, NY 11794-2350, USA

e-mail: asryan@ece.sunysb.edu

² Ioffe Physicotechnical Institute, Russian Academy of Sciences, Politekhnicheskaya ul. 26,
St Petersburg, 194021 Russia

e-mail: suris@theory.ioffe.rssi.ru

Submitted August 7, 2000; accepted for publication August 16, 2000

Abstract—Carrier photoexcitation from levels in quantum dots to continuous-spectrum states during lasing is analyzed theoretically. The simplest approach is used to provide upper estimates of the absorption coefficient and the photoexcitation cross section. Light absorption in carrier photoexcitation is shown to be essential for quantum dot laser operation only at very low total losses, e.g., in the case of long cavities. © 2001 MAIK “Nauka/Interperiodica”.

In this paper, the absorption coefficient and cross sections of carrier photoexcitation from levels in quantum dots (QDs) to continuous-spectrum states in lasing are estimated. The simplest approach is used, neglecting the complex structure of the valence band and the interaction between *c*- and *v*-bands. The values thus obtained give the upper estimates of the absorption coefficient and cross section. These rough estimates are necessary to understand the role played by carrier photoexcitation in QD laser operation.

Carrier photoexcitation from levels in the QDs to continuous-spectrum states is analogous to free-carrier absorption in a bulk material. However, in contrast to the latter process, no third particle need be involved [other than an electron (hole) and a photon] in the absorption event in a QD to satisfy the momentum conservation law. The boundaries of a three-dimensional (3D) QD fulfill the role of the “third particle,” imparting the required momentum to a carrier.

For electron photoexcitation from a QD level to continuous-spectrum states in the conduction band, the absorption coefficient reduced to one QD is given by

$$\beta_{\text{ex}, n} = 4\pi^2 \frac{\alpha}{\sqrt{\epsilon}} \frac{\hbar}{m_c^2 \omega} \langle |M|^2 \rangle_{\Omega_{\mathbf{k}}} \rho_c(\epsilon_n + \hbar\omega) \times [f_n(\epsilon_n) - f_n(\epsilon_n + \hbar\omega)], \quad (1)$$

where $\alpha = e^2/\hbar c$ is the fine structure constant; ϵ is the dielectric constant; m_c is the electron effective mass; $\hbar\omega = E_g + \epsilon_n + \epsilon_p$ is the energy of an absorbed photon, equal to the energy of a photon emitted in a transition from the quantized energy level of an electron to that of a hole in a QD (Fig. 1); E_g is the band gap of the QD material; ϵ_n and ϵ_p are the quantized energy levels of an

electron and a hole in a QD, measured from the band edges (Fig. 1); $\epsilon_n + \hbar\omega = \hbar^2 k^2 / (2m_c)$ is the electron energy in a continuous-spectrum state of the conduction band; $\langle |M|^2 \rangle_{\Omega_{\mathbf{k}}}$ is the squared momentum matrix element, averaged over all directions of the wave vector \mathbf{k} of final states for a given electron energy;

$$\rho_c(\epsilon_n + \hbar\omega) = (\sqrt{2}m_c^{3/2}/\pi^2\hbar^3) \sqrt{\epsilon_n + \hbar\omega}$$

is the density of continuous-spectrum states in the conduction band; and the occupation probability f_n is given by the Fermi–Dirac distribution function.

We can write $\langle |M|^2 \rangle_{\Omega_{\mathbf{k}}}$ as

$$\langle |M|^2 \rangle_{\Omega_{\mathbf{k}}} = \frac{\hbar^2}{4\pi a^3} \quad (2)$$

$$\times \iiint \Psi_0(\mathbf{r}_1) \Psi_0^*(\mathbf{r}_2) k_x^2 \exp[i\mathbf{k}(\mathbf{r}_1 - \mathbf{r}_2)] d\mathbf{r}_1 d\mathbf{r}_2 d\Omega_{\mathbf{k}},$$

where $d\Omega_{\mathbf{k}} = (\sin\theta)d\theta d\varphi$ is a solid angle element. Since the Bloch functions of the initial and final states have already been accounted for in (1) [$1/m_c$ appears in (1) instead of $1/m_0$], the corresponding envelope functions, i.e., the ground-state wave function in a 3D square well, $\Psi_0(\mathbf{r})$, and the plane-wave $(1/a^{3/2})\exp(i\mathbf{k}\mathbf{r})$ enter into (2). Since the transition energy is far in excess of the threshold energy for the transition to the continuum ($\hbar\omega \gg \Delta E_c - \epsilon_n$, where ΔE_c is the conduction band offset at the QD–barrier heteroboundary), the difference between the envelope function for the continuous-spectrum state wave function near a QD and a plane-wave is neglected. Here, cubic QDs are considered, and a is the QD size.

Using Eq. (10), averaging (1) over the QDs, and taking account of both the electron and hole photoexcitation from QD levels to conduction- and valence-band continuous-spectrum states, we obtain β_{ex} and the photoexcitation cross section σ_{ex} to be

$$\beta_{\text{ex}} = \frac{1}{\bar{a}^3} \sigma_{\text{ex}} = C_n \langle f_n \rangle + C_p \langle f_p \rangle, \quad (11)$$

with $C_{n,p}$ given by

$$C_{n,p} = 128 \sqrt{2} \pi \frac{\alpha \hbar^3 \epsilon_{n,p}^{(x)} \Delta E_{c,v}}{\sqrt{\epsilon} m_{c,v}^{3/2} \bar{E}_0^{7/2}} \times \frac{1}{1 + 2/(\bar{a} \kappa_{n,p})} \frac{1}{\bar{a}^4} \left\langle \sin^2 \frac{ka}{2} \right\rangle, \quad (12)$$

where the brackets $\langle \dots \rangle$ signify averaging over the inhomogeneously broadened ensemble of QDs, \bar{a} is the mean size of the QDs, and \bar{E}_0 is the transition energy in a mean-sized QD. Since our interest here is in the maximum losses caused by the photoexcitation process, the factor $\langle \sin^2 ka/2 \rangle$ in expression (12) will be taken to be equal to its maximum value of unity.

Equation (12) is similar to that for the absorption coefficient in the photoexcitation of a neutral hydrogen-like donor [3]. Let us consider a sheet of QDs formed in the optical confinement layer of a laser structure and acting as an active region [4–7]. Then we can write the following equation for the effective absorption coefficient of the optical confinement layer for the process of electron (or hole) photoexcitation [4]:

$$\bar{\Gamma}_y N_S \bar{a}^2 \beta_{\text{ex},n,p} = 128 \sqrt{2} \frac{1}{\mathcal{L}} \frac{\alpha \Delta E_{c,v} \epsilon_{n,p}^{(x)}}{\sqrt{\epsilon} \bar{E}_0} \times \left(\frac{\hbar^2}{m_{c,v} \bar{a}^2 \bar{E}_0} \right)^{3/2} \frac{1}{1 + 2/(\bar{a} \kappa_{n,p})} \langle f_{n,p} \rangle N_S \bar{a}^2, \quad (13)$$

where N_S is the QD surface density in the QD sheet, $\bar{\Gamma}_y = \bar{a}/\mathcal{L}$ is the optical confinement factor in the QD sheet (along the direction perpendicular to the sheet), and \mathcal{L} is the characteristic length of wave localization in the transverse direction of the waveguide.

Figure 2a shows a universal dependence of the dimensionless cross sections for electron and hole photoexcitation

$$\sigma_{\text{ex},n,p} \left[128 \pi \frac{\alpha}{\sqrt{\epsilon} m_{c,v} \bar{E}_0^{7/2}} (\Delta E_{c,v})^{5/2} \langle f_{n,p} \rangle \right]^{-1} \quad (13a)$$

on the dimensionless mean size of QDs

$$\bar{a} \left(\frac{\hbar^2}{m_{c,v} \Delta E_{c,v}} \right)^{-1/2}. \quad (13b)$$

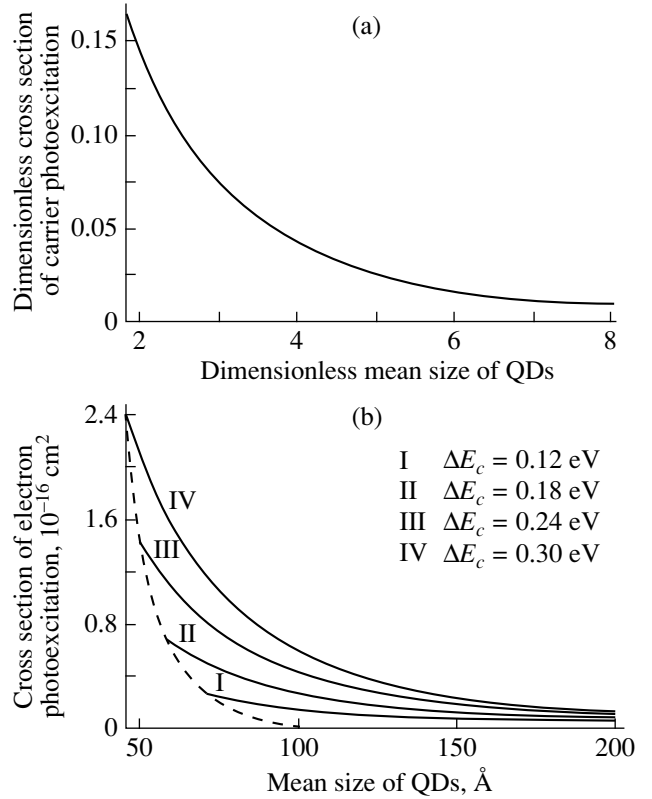


Fig. 2. (a) Universal dependence of the dimensionless cross sections of carrier photoexcitation from QDs [see (13a)] on the dimensionless mean QD size [see (13b)]. (b) Dependence of the cross section of electron photoexcitation from a QD, $\sigma_{\text{ex},n}$ on the mean QD size \bar{a} at different well depths ΔE_c . The abscissas of the intersection points of each of the solid lines with the dashed curve determine the minimum QD size below which there are no bound electron states in the 3D QD potential well.

Figure 2b exemplifies the dependence of the electron photoexcitation cross section on the mean size of QDs for various well depths ΔE_c , obtained from the above universal dependence. InGaAs QDs in an InGaAsP matrix are considered (see [4–7]). The abscissas of the intersection points of each of the solid lines with the dashed curve determine the minimum QD size, below which there are no bound electron states in the 3D QD potential well. The condition for the existence of a bound state in a 3D potential well of typical size \bar{a} and depth ΔE_c can be written as

$$\left(\frac{m_c \Delta E_c \bar{a}^2}{\hbar^2} \right)^{1/2} \geq \zeta, \quad (14)$$

where ζ is a numerical constant. The exact value of ζ depends on the shape of a 3D well. To estimate ζ in the case of a cubic QD, the 3D rectangular well potential was replaced by an effective spherical well potential obtained by averaging the QD well potential over the solid angle. Further, the Schrödinger equation was

solved numerically with this effective spherical potential. Using this method, we obtained a value $\zeta \approx 1.83$ for a cubic QD. In the case of a spherical QD fitted inside the cubic one, the well-known result is as follows: $\zeta = \sqrt{\pi^2/2} \approx 2.22$ [8].

At $\hbar\omega \gg \epsilon_n$, the absorption coefficient β_{ex} , carrier photoexcitation cross section σ_{ex} , and the high-frequency conductivity ($\sqrt{\epsilon}/4\pi$) $c\beta_{\text{ex}}$ occurring due to the photoexcitation process, decrease as $\omega^{-7/2}$ with increasing ω .

The quantity

$$\bar{\Gamma}_y N_S \bar{a}^2 \beta_{\text{ex}} = (1/\mathcal{L}) N_S \sigma_{\text{ex}}$$

is much less than the cavity losses in the laser. For the representative N_S values on the order of 10^{11} cm^{-2} and $\bar{\Gamma}_y$ of several percent, the quantity $\bar{\Gamma}_y N_S \bar{a}^2 \beta_{\text{ex}}$ is less than, or on the order of, 0.1 cm^{-1} , whereas the typical cavity losses are on the order of 10 cm^{-1} . Thus, it is necessary to take into account the light absorption in carrier photoexcitation from QD levels to continuous-spectrum states only at very low total losses ($\beta < 1 \text{ cm}^{-1}$), e.g., in the case of long cavities.

In calculating β_{ex} and σ_{ex} , no account was taken of the complex structure of the valence band and of the interaction between the c - and v -bands. However, it can be readily seen from (12) that $\sigma_{\text{ex}, n, p} \propto m_{c, v}^{-5/2}$; i.e., the hole contribution to absorption is negligible compared with that from electrons. Taking into account the interaction between the bands within the framework of Kane's model (the necessity of doing this stems from the fact that the electron transition energy in the process under study is comparable to the band gap) would lead to an effective increase in m_c . Thus, the obtained

expressions furnish somewhat too large values of $\beta_{\text{ex}, n}$ and $\sigma_{\text{ex}, n}$.

In conclusion, a theoretical analysis of carrier photoexcitation from levels in quantum dots to continuous-spectrum states during the laser operation has been made. It has been shown that the light absorption in carrier photoexcitation is essential for quantum dot laser operation only at very low total losses, e.g., in the case of long cavities.

ACKNOWLEDGMENTS

The study was supported by the Russian Foundation for Basic Research (project no. 99-02-16796) and the Program "Physics of Solid State Nanostructures" of the Ministry of Science and Technical Policy of Russia (grant nos. 99-1106 and 97-1035).

REFERENCES

1. M. V. Fedoryuk, *Asymptotic: Integrals and Series* (Nauka, Moscow, 1987).
2. L. D. Landau and E. M. Lifshitz, *Course of Theoretical Physics, Vol. 3: Quantum Mechanics: Non-Relativistic Theory* (Nauka, Moscow, 1989, 4th ed.; Pergamon, New York, 1977, 3rd ed.).
3. B. K. Ridley, *Quantum Processes in Semiconductors* (Clarendon Press, Oxford, 1982).
4. L. V. Asryan and R. A. Suris, *Semicond. Sci. Technol.* **11**, 554 (1996).
5. L. V. Asryan and R. A. Suris, *IEEE J. Sel. Top. Quantum Electron.* **3**, 148 (1997).
6. L. V. Asryan and R. A. Suris, *Electron. Lett.* **33**, 1871 (1997).
7. L. V. Asryan and R. A. Suris, *IEEE J. Quantum Electron.* **34**, 841 (1998).
8. K. J. Vahala, *IEEE J. Quantum Electron.* **24**, 523 (1988).

Translated by M. Tagirdzhanov

LOW-DIMENSIONAL
SYSTEMS

Composition Analysis of Coherent Nanoinsertions of Solid Solutions on the Basis of High-Resolution Electron Micrographs

I. P. Soshnikov*, O. M. Gorbenko*, A. O. Golubok**, and N. N. Ledentsov*

* *Ioffe Physicotechnical Institute, Russian Academy of Sciences, Politekhnicheskaya ul. 26,
St. Petersburg, 194021 Russia*

e-mail: ipsosh@beam.ioffe.rssi.ru

** *Institute of Analytical Instrument Making, Russian Academy of Sciences, Rizhskii pr. 26,
St. Petersburg, 198103 Russia*

Submitted August 30, 2000; accepted for publication September 5, 2000

Abstract—A program package is presented, ensuring fast direct and inverse Fourier transformations of images, various methods of noise filtration and use of spectral windows, and determination of local interplanar spacings (LIS) from cross-sectional high-resolution electron micrographs. The algorithm for determining the LIS consists in obtaining, by double fast Fourier transformation, a high-resolution image filtered by selecting an appropriate combination of reflections and using this image to find the characteristic LIS. A specific feature of this algorithm is that it employs weighting with correction of the integration domain. The resulting maps of LIS can be used to determine the chemical composition, e.g., in substitutional solid solutions, such as A_xB_{1-x} , $A_xB_{1-x}C$. The method is applied to process a high-resolution electron micrograph of a heterostructure with a submonolayer InGaAs/GaAs lattice. © 2001 MAIK “Nauka/Interperiodica”.

1. INTRODUCTION

Progress in modern microelectronics and semiconductor physics is associated with the appearance of a new class of objects—heterostructures with coherent nanodomains. Heterostructures of this kind have been named heterostructures with quantum dots (QDs) [1, 2]. The properties of QD heterostructures are determined by specific features of their structure: composition, geometric characteristics, and QD dimension. The conventional methods, such as X-ray diffraction analysis (XDA), X-ray photoelectron spectroscopy (XPS), and electron-probe X-ray microanalysis (XMA) fail to characterize an object with the necessary precision because of the insufficient spatial resolution [3, 4]. High-resolution transmission electron microscopy (HREM) furnishes all the necessary structural information [5–7]. It should be noted that methods for obtaining high-quality electron micrographs have been extensively discussed and are now well mastered [5–9]. However, determining the composition from images furnished by transmission electron microscopy (TEM) requires their quantitative processing, and this problem has not been solved completely [7, 8]. Therefore, the aim of the present study was to develop methods to analyze the local composition of QDs on the basis of cross-sectional HREM micrographs of a structure and to create a program package for this purpose.

The proposed method for composition analysis is based on the postulate that the lattice distances are composition-dependent [9, 10]; i.e., it is stated that in the case of a solid solution of the A_xB_{1-x} or $A_xB_{1-x}C$ type the lattice parameters depend on the composition. Cross-sectional HREM micrographs of insertions of such solid solutions will have a pattern spacing different from that of the matrix [6–8]. This allows the local composition to be determined quantitatively by applying the proposed processing algorithm.

2. DESCRIPTION OF THE PROCEDURE

In this part of the paper, we outline the technique for processing cross-sectional HREM images to obtain information about the composition distribution. The results obtained by applying various numerical methods are demonstrated using, as an example, the processing of electron micrographs of a superlattice heterostructure with submonolayer InAs insertions in the GaAs matrix.

2.1. Noise Filtration

A digitized HREM micrograph contains noises arising from the TEM sample preparation, from taking micrographs in the microscope, and from the optical

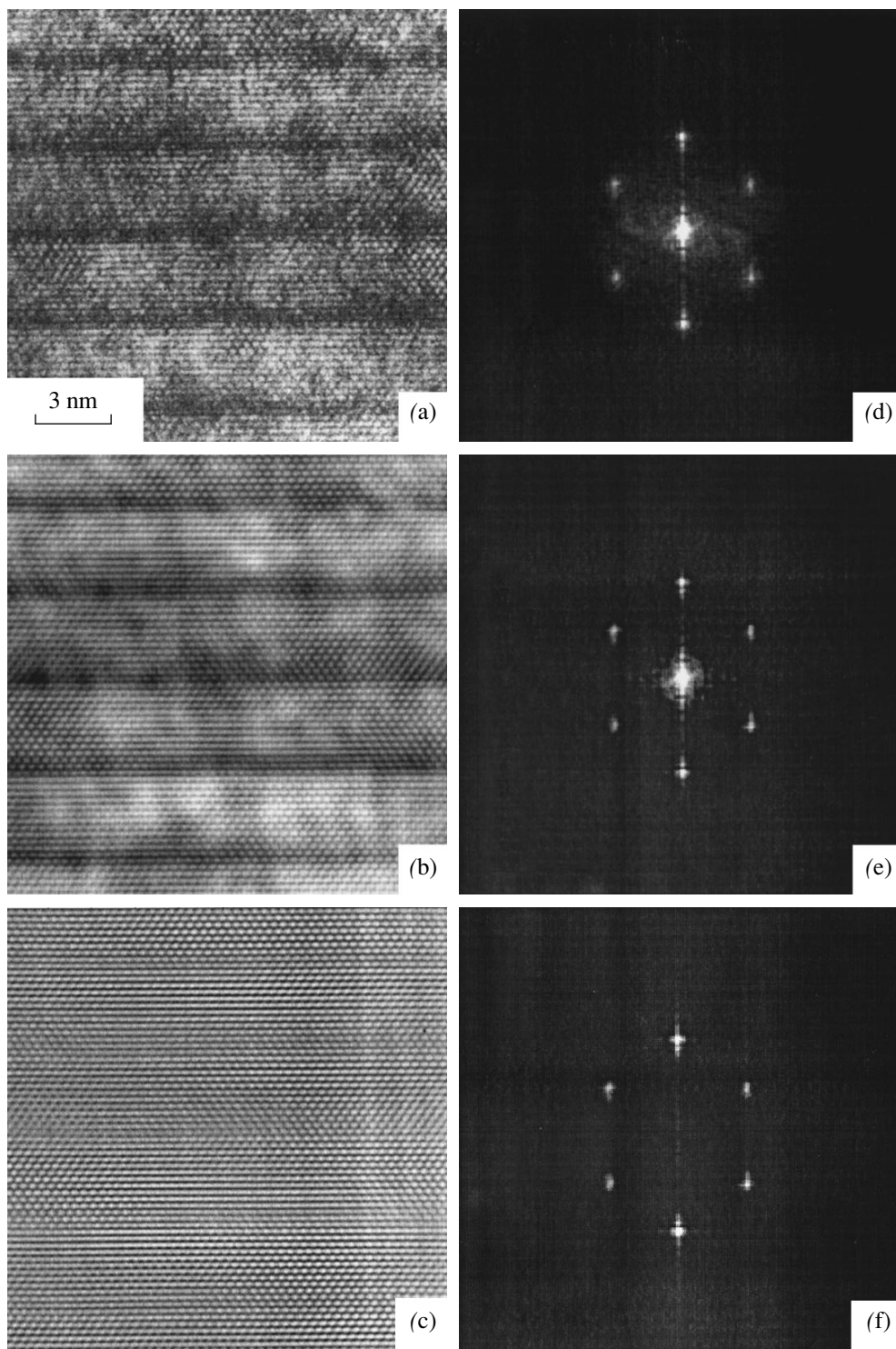


Fig. 1. (a–c) High-resolution bright-field (110) cross-sectional electron micrograph of a superlattice heterostructure with submonolayer InAs insertions (~0.5 ML) in a GaAs matrix, taken on a CM20FEG electron microscope: (a) before filtration, (b) after noise filtration by the Wiener method, and (c) after noise filtration and long-wave subtraction. (d–f) Fourier images of the micrographs: (d) a, (e) b, and (f) c.

processing of the micrographs into a digitized form [5, 6, 11]. Therefore, long-wave subtraction and noise filtration by the Wiener method were performed as a first step.

The long-wave length subtraction can be represented as [11]:

$$I'(x, y) = I(x, y) - I(x, y) \otimes A(x, y),$$

where $I(x, y)$ and $I'(x, y)$ are the initial signal and that processed by the long-wave length subtraction method; \otimes is the convolution operation; and $A(x, y)$ is a matrix of unit elements, whose dimension corresponds to that of the elements of the informative part of the micrograph. The Fourier image obtained by executing this operation contains no zero reflection.

The filtration of additive noises in the micrograph was done by the spectral subtraction method [11]:

$$\hat{I}'(k_x, k_y) = \hat{I}(k_x, k_y) - V(k_x, k_y),$$

where $\hat{I}(k_x, k_y)$ and $\hat{I}'(k_x, k_y)$ are, respectively, the initial and Fourier-transformed signals; $V(k_x, k_y) = \hat{I}(k_x, k_y)$ at $\hat{I} < \hat{I}_0$ and $V = 0$ at $\hat{I} > \hat{I}_0$ is the instrumental function of the filter with an adaptively determined threshold \hat{I}_0 .

The algorithm can also employ \hat{I}_0 in the form of a Gaussian curve whose height and width along the OX and OY axes are determined adaptively.

The results obtained by applying the operations of long-wave subtraction and noise filtration by the Wiener method to a cross-sectional HREM micrograph of a superlattice heterostructure with submonolayer InAs insertions in a GaAs matrix and their Fourier images are given in Fig. 1. It is noteworthy that the Fourier image contains no zero reflection after noise filtration and long-wave subtraction, which may facilitate further processing of the micrograph.

2.2. Filtration of Selected Frequencies

The program allows filtration of reflections in the frequency domain. This operation is represented as

$$\hat{I}'(k_x, k_y) = \hat{I}(k_x, k_y)P,$$

where $\hat{I}(k_x, k_y)$ and $\hat{I}'(k_x, k_y)$ are, respectively, the initial and Fourier-transformed signals and P is the frequency filter. The program allows the use of various filters of the window type. The window function is expressed as

$$P = 1 \text{ for } k_x, k_y \in W, \quad P = 0 \text{ for } k_x, k_y \notin W,$$

where W is the domain of definition of the window. The program can use window functions of the annular, rectangular, and selective types [12].

Since different reflections carry different kinds of structural information, it is important to isolate spectral components related to the material composition. There have been numerous reports [5–10] that the (002) reflections are the most informative in this regard. Therefore, one of the possible calculation algorithms consists in the selective filtration of these reflections. Figure 2 exemplifies the application of selective filtration to the micrograph in Fig. 1.

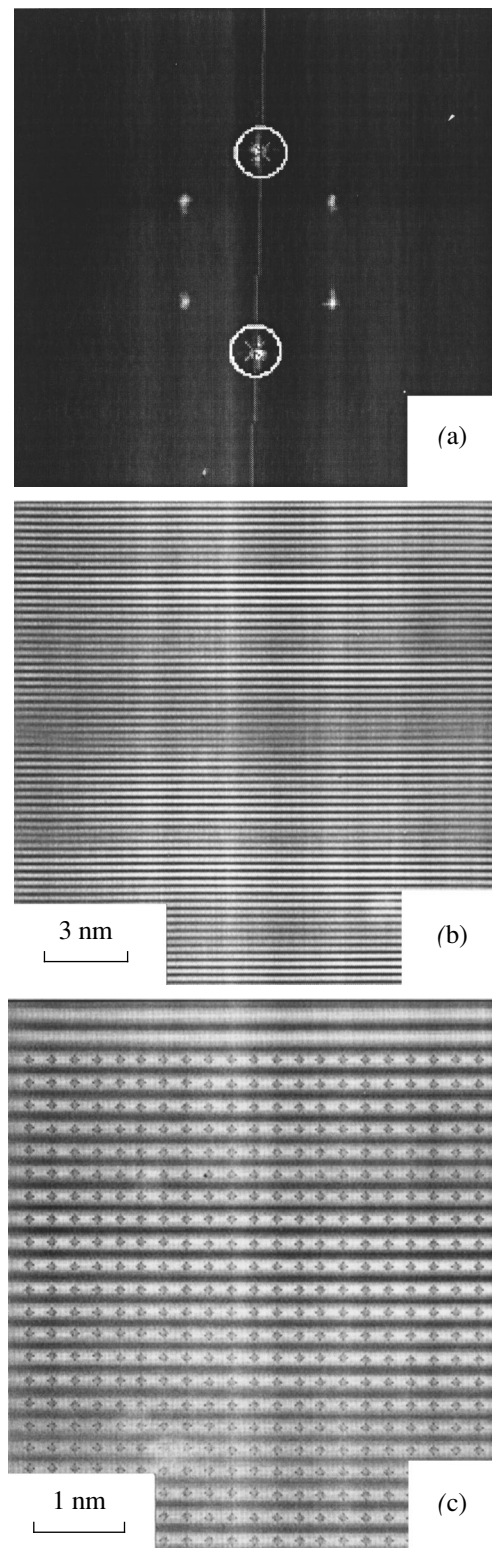


Fig. 2. (a) Fourier image of the micrograph in Fig. 1 after noise filtration and long-wave subtraction with marked regions chosen for selective filtration of (002) reflections, (b) micrograph obtained upon filtration keeping the region of (200) reflections, and (c) the same after fragmentation.

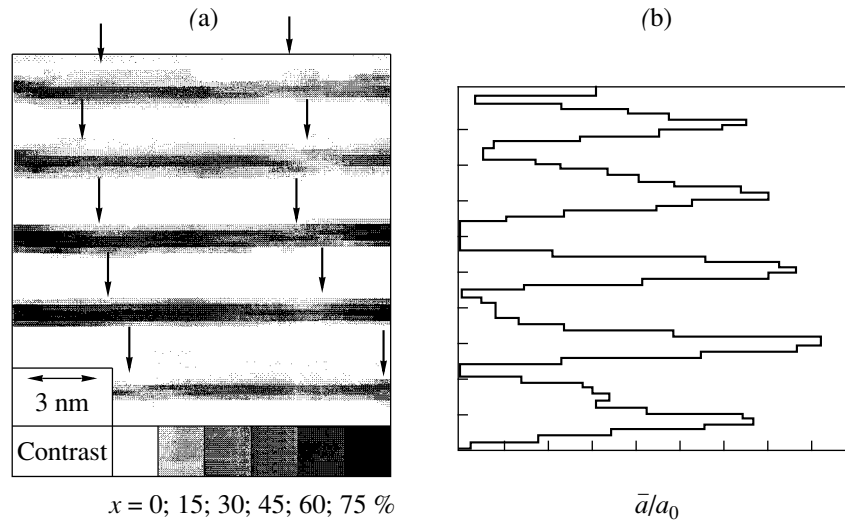


Fig. 3. (a) Half-tone map reflecting LIS and (b) average LIS.

2.3. Procedure for Determining LIS

This procedure requires a micrograph oriented in such a way that the normal to the layers is close to the vertical axis.

The micrograph obtained upon filtration is fragmented in directions parallel and perpendicular to the surface vector coinciding with the crystallographic direction (002). Thus, the area boundaries in the direction perpendicular to the surface are chosen in such a way that y_n is a local minimum. It should be noted that the minimum was determined to within 0.05 of a pixel. In the direction parallel to the surface, the fragment boundaries were chosen adaptively and found to be close to the pattern period in the micrograph. Then the signal was integrated numerically within each fragment and weight centers of the fragments (x_{mb} , y_{ml}) were found. The weight center positions were determined to within no less than 0.01 of a pixel, which, at common fragment dimensions of ~10 pixels, amounts to about 0.1%. The positions obtained are used to determine the local relative interplanar spacings

$$a_{m,l} = y_{m,l+1} - y_{m,l}$$

The determined relative LIS can be represented as a half-tone map or plots of average LIS in the direction perpendicular to the surface. Figure 3 presents examples of such a map plotted for LIS, obtained by processing the micrograph in Fig. 2.

2.4. Determining the Local Composition from Interplanar Spacings

The problem of determining the composition from the lattice constant has been extensively discussed in the literature [5–10]. The basic formula relating the lattice constant a and the composition of substitutional

solid solutions of the A_xB_{1-x} or $A_xB_{1-x}C$ type can be represented as [9]:

$$x = f^{-1} \frac{a - a_A}{a_A} \frac{a_B - a_A}{a_A},$$

where a_A , a_B , and a are the lattice spacings of the matrix, insertion, and solid solution, respectively and f is the tetragonal distortion factor. It was shown in [13] that in cubic crystals the tetragonal distortion factor may vary between $f \approx (1 + \nu)/(1 - \nu)$ for thick samples and $f \approx 1 + \nu$ for thin samples. Here $\nu = C_{12}/(C_{11} + C_{12})$ is Poisson's ratio. The basic formulas for evaluating the distortion factor are given in the Appendix. The following elastic constants were used as calculation parameters:

$$C_{11} = 8.34, \quad C_{12} = 4.54, \quad C_{44} = 3.95$$

for InAs and

$$C_{11} = 11.9, \quad C_{12} = 5.34, \quad C_{44} = 5.96$$

for GaAs [14–16]. The tetragonal distortion factor f can be determined using data on sample thickness and the results of calculation by the technique proposed by Treacy and Gibson. The thickness of the sample whose HREM micrograph was analyzed above was ~30 nm, which gives an estimate $f \approx 2$ for the tetragonal distortion factor. The results obtained allow compositional calibration of the LIS maps, as is done in Fig. 3 where composition modulations are observed within each layer. The arrows in Fig. 3 denote the positions of InAs content minima. The characteristic size of these modulations is within 12–16 nm. In addition, it should be noted that the modulations are, as a rule, correlated at a spacer thickness of 3 nm. This result is in good agreement with the theory of QD superlattice formation [17, 18], which predicts that, depending on the spacer thickness, the QD arrangement may be correlated, anti-

correlated, or random. According to the theory [17, 18], the correlated arrangement of QDs is possible when the spacer thicknesses do not exceed values of the order of the QD size. Anticorrelated and random arrangements of QDs become possible at spacer thicknesses exceeding the QD size.

Plan view TEM studies demonstrated that the sample under study contains nanodomains of nearly square shape, with sides oriented in the (100) directions. The characteristic size of nanodomains in the direction (100) is 6–8 nm and their density is $3 \times 10^{10} \text{ cm}^{-2}$. Comparison shows that the results of quantitative processing and plan view TEM data are in good agreement.

3. CONCLUSION

Thus, an unconventional algorithm is proposed for the quantitative analysis of cross-sectional HREM micrographs of samples with coherent insertions of substitutional solid solutions in order to determine the local composition. The working of the algorithm is demonstrated for the example of the processing of a cross-sectional micrograph taken from a superlattice heterostructure with submonolayer InAs insertions in a GaAs matrix.

APPENDIX

Procedure for Calculating the Distortion Factor

Treacy and Gibson [9, 19] analyzed the elastic relaxation for a superlattice with a lattice constant following the sinusoidal law $a = a_0 + \varepsilon_0 \cos(2\pi z/L)$, where a_0 is the mean lattice constant; ε_0 is the modulation amplitude of an unrelaxed lattice constant related to the target composition by $x = 2\varepsilon_0/(a_B - a_A)$; a_B and a_A are the lattice constants of materials B and A; and L is the spacing of a model superlattice. Analysis of elastic strains gives the following formula for the modulation amplitude of the lattice constant in the modulation direction after relaxation of elastic strains ε_{xx} :

$$\frac{\varepsilon_{xx}}{\varepsilon_0 \cos\left(\frac{\pi z}{L}\right)} = \frac{1 + \nu}{1 - \nu} \left[1 - \beta \frac{AE - CD}{R} + \gamma(1 - 2\nu) \frac{AD + CE}{R} \right],$$

where

$$A = \cosh(\beta t/2) \sin(\gamma t/2), \quad E = \cosh(\beta x) \cos(\gamma x),$$

$$C = \sinh(\beta t/2) \cos(\gamma t/2), \quad D = \sinh(\beta x) \sin(\gamma x),$$

$$R = \beta \sin(\gamma t) + \gamma \sinh(\beta t),$$

$$\beta = \frac{2\pi\sqrt{2+B}}{L}, \quad \gamma = \frac{2\pi\sqrt{2-B}}{L},$$

$$B = \frac{(C_{11} - C_{12})(C_{11} + 2C_{12}) - 2C_{12}C_{44}}{C_{44}(C_{11} + C_{12})},$$

C_{11} , C_{12} , and C_{44} are the coefficients of elasticity and t is the sample thickness.

If the lattice constant is now represented as a Fourier series

$$a = a_0 + \sum g_k \varepsilon_0 \cos(2\pi k z/L),$$

then the distortion factor can be estimated as

$$f = \sum g_k f_k,$$

where $f_k = \varepsilon_{zz}^{\max}/\varepsilon_0$ is the distortion factor for a superlattice with sinusoidal modulation of the lattice constant with a period $L/2\pi k$.

ACKNOWLEDGMENTS

We thank Prof. V.M. Ustinov for providing the sample and Prof. D.Gerthsen for the opportunity to use an electron microscope.

The study was supported in part by the Russian Foundation for Basic Research (projects nos. 98-02-18229, 00-02-17006, and 00-02-17007), INTAS (projects nos. 96-0467, 97-751, and 99-00928), and the NanOp program.

REFERENCES

1. D. Bimberg, M. Grundmann, and N. N. Ledentsov, *Quantum Dot Heterostructures* (Wiley, New York, 1999).
2. N. N. Ledentsov, in *Springer Tracts in Modern Physics*, Vol. 156: *Growth Processes and Surface Phase Equilibria in Molecular Beam Epitaxy* (Springer-Verlag, Berlin, 1999).
3. D. P. Woodruff and T. A. Delchar, *Modern Techniques of Surface Science* (Cambridge Univ. Press, Cambridge, 1986).
4. D. Brandon and W. D. Kaplan, *Microstructural Characterization of Materials* (Wiley, New York, 1999).
5. P. Hirsch, A. Howie, R. Nicolson, D. Pashley, and M. Whelan, *Electron Microscopy of Thin Crystals* (Butterworths, Washington, 1965; Mir, Moscow, 1968).
6. J. C. H. Spencer, *Experimental High-Resolution Electron Microscopy* (Clarendon Press, Oxford, 1980; Nauka, Moscow, 1986).
7. R. Bierwolf, M. Hohenstein, F. Phillipp, *et al.*, *Ultramicroscopy* **49**, 273 (1993).
8. A. Rosenauer, S. Kaiser, T. Reisinger, *et al.*, *Optik* **102** (2), 63 (1996).
9. M. M. J. Treacy and J. M. Gibson, *J. Vac. Sci. Technol. B* **4**, 1458 (1986).
10. *Modern Crystallography*, Vol. 2: *Structure of Crystals*, Ed. by B. K. Vainshtein, A. A. Chernov, and L. A. Shuvalov (Nauka, Moscow, 1979; Springer-Verlag, Berlin, 1982).

11. L. P. Yaroslavskii, *Introduction to Digital Image Processing* (Sov. Radio, Moscow, 1979).
12. O. M. Gorbenko, D. V. Kurochkin, and A. O. Golubok, in *Proceedings of the I International Conference on Digital Signal Processing and Its Application, Moscow, 1998*, Vol. III, Part E, p. 130.
13. J. W. Cahn, *Acta Metall.* **9**, 795 (1961).
14. Yu. A. Burenkov, Yu. M. Burdukov, S. Yu. Davydov, and S. P. Nikanorov, *Fiz. Tverd. Tela (Leningrad)* **15** (6), 1757 (1973) [*Sov. Phys. Solid State* **15**, 1175 (1973)].
15. Yu. A. Burenkov, S. Yu. Davydov, and S. P. Nikanorov, *Fiz. Tverd. Tela (Leningrad)* **17**, 2183 (1975) [*Sov. Phys. Solid State* **17**, 1446 (1975)].
16. Landolt-Börnstein, *Numerical Data and Functional Relationships in Science and Technology* (Springer-Verlag, Berlin, 1982), Vol. 17e.
17. V. A. Shchukin, N. N. Ledentsov, P. S. Kop'ev, and D. Bimberg, *Phys. Rev. Lett.* **75**, 2968 (1995).
18. V. A. Shchukin and D. Bimberg, *Rev. Mod. Phys.* **71**, 1125 (1999).
19. M. M. J. Treacy and J. M. Gibson, *Ultramicroscopy* **14**, 345 (1984).

Translated by M. Tagirdzhanov

AMORPHOUS, VITREOUS, AND POROUS SEMICONDUCTORS

Electrical and Photoelectric Properties of *a*-Si:H Layered Films: The Influence of Thermal Annealing

I. A. Kurova*, N. N. Ormont*, E. I. Terukov**, I. N. Trapeznikova**,
V. P. Afanas'ev***, and A. S. Gudovskikh***

* Moscow State University, Vorob'evy gory, Moscow, 119899 Russia

** Ioffe Physicotechnical Institute, Russian Academy of Sciences, Politekhnicheskaya ul. 26, St. Petersburg, 194021 Russia

*** St. Petersburg Electrotechnical University, St. Petersburg, 197376 Russia

Submitted July 26, 2000; accepted for publication August 2, 2000

Abstract—The electrical and photoelectric properties of layered *a*-Si:H films obtained by cyclic plasmochemical deposition and the effect of thermal annealing on these properties have been studied. Unannealed films demonstrate high photosensitivity, with a photoconductivity to dark conductivity ratio of $K = 3.4 \times 10^6$. Increasing the annealing temperature causes the film photosensitivity to fall because of a considerable decrease in the photoconductivity and increase in the dark conductivity. For films annealed at temperatures above 500°C, the conductivity is the sum of the band conductivity and the hopping conductivity via states at the Fermi level.
© 2001 MAIK "Nauka/Interperiodica".

It is well known that the electrical and photoelectric properties of *a*-Si:H films are determined by the methods and technology of their fabrication, and also depend on subsequent external treatments. For example, high-temperature annealing substantially changes the properties of *a*-Si:H films, in particular, owing to the increased efficiency of doping, hydrogen effusion, and crystallite formation [1–3].

Currently, high-quality films are obtained by layer-by-layer growth, each layer undergoing hydrogen plasma treatment. Wide-gap (up to 2.1 eV) *a*-Si:H films and films containing microcrystallites, μc -Si:H, have been obtained by this technique [4, 5]. The effect of thermal annealing and illumination on the photoelectric and structural characteristics of μc -Si:H films have been studied too [6, 7].

The present study is concerned with the electrical and photoelectric properties of layered *a*-Si:H films and the effect of thermal annealing on these properties. The *a*-Si:H films were deposited onto substrates by cyclic plasmochemical deposition in an rf diode system. During deposition, the gas mixture composition was modified by means of leak valves controlled by timers determining the duration of deposition and thermal treatment in the hydrogen plasma, with a varied ratio between the deposition and thermal treatment times. The thickness of a layer deposited in a single cycle was varied by changing the deposition time [8]. Cross-sectional transmission electron microscopy (TEM) of *a*-Si:H films revealed a well-defined layered structure: periodic 12–25 nm thick *a*-Si:H layers, separated by thin interlayers with higher concentrations of the nanocrystalline silicon phase (the average nanocrystal

size being 4 nm), appeared during thermal treatment in hydrogen plasma.

The temperature dependences of the dark conductivity σ_d and photoconductivity σ_{ph} of layered *a*-Si:H films, unannealed and annealed at various temperatures, were recorded at $T = 100$ –470 K during slow heating, after a preliminary 30-min annealing at 190°C under a residual pressure of 10^{-5} Torr. The photoconductivity was measured under brief illumination by a halogen lamp with an IR filter.

Sputtered aluminum contacts were deposited in a planar configuration. The measured current increased linearly with an applied electric field of up to 500 V/cm, and was independent of the field direction. All further measurements were performed at an electric field of 100 V/cm.

Figures 1 and 2 present temperature dependences of σ_d and σ_{ph} for, respectively, unannealed film and films annealed at different temperatures T_a (see table). The dark conductivity of films 1, 2, and 3 (the first group in the table) depends on the temperature exponentially over the entire temperature range:

$$\sigma_d(T) = \sigma_0 \exp(-E/kT). \quad (1)$$

The σ_0 and E values determined for these films using relation (1) are typical of the band conduction in *a*-Si:H. They are given in the table along with other parameters of the films studied. The E value is the highest for the unannealed film, $E = 0.89$ eV. It follows from the data for films 2 and 3 that E decreases upon increasing the annealing temperature, being equal to 0.81 and 0.71 eV, respectively. The table also presents room-temperature dark conductivities and photoconductivi-

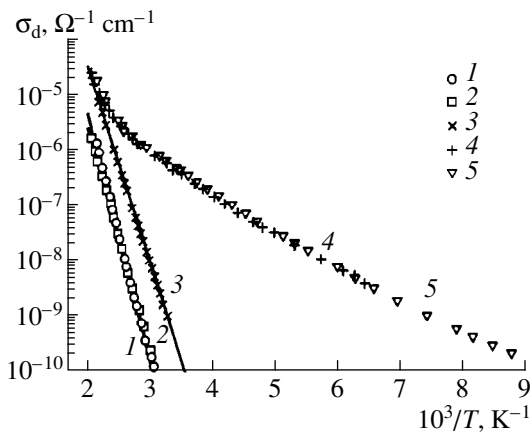


Fig. 1. Temperature dependences of the dark conductivity of films. Curve numbers correspond to sample numbers in the table.

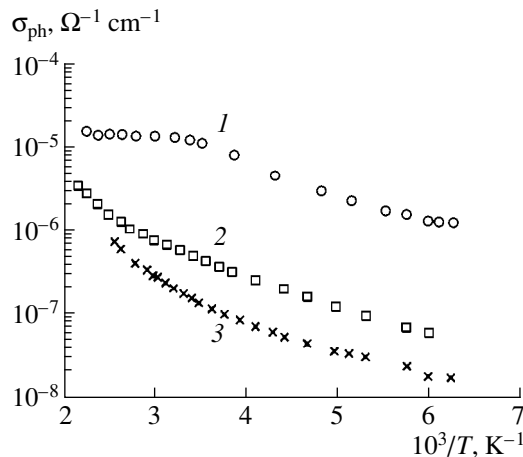


Fig. 2. Temperature dependences of the photoconductivity of films. Illumination intensity $W = 100 \text{ mW/cm}^2$. Curve numbers correspond to sample numbers in the table.

ties and their ratio $K = \sigma_{ph}/\sigma_d$ characterizing the film photosensitivity.

As follows from the figures and the table, the dark conductivity of the films grows with increasing annealing temperature, while the photoconductivity and the

photosensitivity decrease. It is noteworthy that the photosensitivity of the unannealed film is high, reaching a value of $K = 3.4 \times 10^6$ at an incident light power of 100 mW/cm^2 . The high photosensitivity indicates a perfect structural quality of the obtained films. This quality is presumably determined by the structural relaxation during annealing in hydrogen, following the deposition of each layer. In addition, according to IR spectroscopic data, the hydrogen concentration in unannealed films is high, up to $C_H = 15 \text{ at. \%}$. Consequently, the band gap and the activation energy of dark conductivity E increase, and σ_d decreases, thus also possibly improving the photosensitivity of unannealed films.

The IR absorption spectra show that the hydrogen concentration C_H in annealed films decreases with increasing annealing temperature (see table, films 2 and 3). This results in a higher concentration of silicon dangling bonds (DB), thus raising the concentration of recombination centers and depressing the photoconductivity. Moreover, the decrease in C_H causes narrowing of the band gap E_g and leads to a decrease in the activation energy E , making the dark conductivity higher. However, the observed variation of σ_d and E for film 3 (an increase of two orders of magnitude in the ambient temperature σ_d and a decrease in E by 0.18 eV , compared with that in film 1) presumably cannot be accounted for by only a decrease in E_g , equal to $\sim 0.4 \text{ eV}$ upon total dehydrogenation of the film [9]. Therefore, we suppose that the decrease in E and increase in σ_d in the course of annealing may also be due to a higher efficiency of film doping with uncontrolled impurities, e.g., oxygen. Oxygen is often observed in films grown in silane plasma strongly diluted with hydrogen [6]. In our case, the oxygen content in initial $a\text{-Si:H}$ films was 0.3 at. \% , and it almost doubled upon annealing at 450°C . Thus, the substantial reduction in the film photosensitivity upon annealing results from a considerable decrease in the photoconductivity and increase in the dark conductivity.

It is noteworthy that the above analysis does not take into account the influence of nanocrystalline inclusions in the amorphous silicon matrix on the electrical and photoelectric parameters of films 1, 2, and 3 because of the small volume fraction of the nanocrystalline phase

Parameters of films

Sample no.	$T_a, ^\circ\text{C}$	$C_H, \text{ at. \%}$	$\chi, \%$	$E, \text{ eV}$	$\log(\sigma_0, \Omega^{-1} \text{ cm}^{-1})$	$\sigma_d, \Omega^{-1} \text{ cm}^{-1}$ ($T = 294 \text{ K}$)	$\sigma_{ph}, \Omega^{-1} \text{ cm}^{-1}$	$k = \sigma_{ph}/\sigma_d$	$T_0, \text{ K}$	$A, \Omega^{-1} \text{ cm}^{-1}$
1	190	15	<1	0.89	3.45	3.5×10^{-12}	1.2×10^{-5}	3.4×10^6	—	—
2	350	12	<1	0.81	2.64	6.3×10^{-12}	5×10^{-7}	8×10^4	—	—
3	450	6.5	<1.5	0.71	2.57	3.3×10^{-10}	1.4×10^{-7}	4.2×10^2	—	—
4	500	<1	<2	0.75	2.5	2.5×10^{-7}	—	—	2.6×10^6	71
5	550	<1	<2	0.76	2.9	3×10^{-7}	—	—	2.8×10^6	80

relative to the total film volume ($\chi < 1.5\%$). The effect of this structural feature on the conductivity invites further study. TEM data for annealed films show only an insignificant increase in the crystal phase fraction for films 2–5 (see table); it nearly doubles at the highest annealing temperature 550°C . This gives no way of relating the observed strong variations of σ_d and σ_{ph} to film crystallization.

The second group of films under study includes films 4 and 5, annealed at $T_a = 500$ and 550°C . They are not photosensitive, and their dark conductivity at low temperatures is large and shows no activation. Thus, the properties of films 4 and 5 differ sharply from those of the first group of $a\text{-Si:H}$ films. As stated above, this difference cannot be accounted for by an increase in the crystallinity of these films, this parameter being low ($< 2\%$).

IR spectroscopic data for films 4 and 5 indicate that $C_H < 1$ at. %. Such a small concentration of hydrogen and the absence of photoconductivity indicate a high concentration of silicon dangling bonds. This suggests the appearance of hopping conduction via dangling bonds at the Fermi level, observed in annealed standard $a\text{-Si:H}$ films [3]. For bulk films, this hopping conductivity is described by the relation

$$\sigma_2(T) = A \exp[-(T_0/T)^n], \quad (2)$$

where $0.25 \leq n \leq 0.5$ [10].

Figure 3 presents experimental data on the dark conductivity of film 5 (the temperature dependence of σ_d for film 4 is similar). As can be seen, this temperature dependence becomes stronger at $T > 380$ K. This may be due to band conduction at high temperatures or to activated hopping conduction via the localized states of the conduction band tail. Describing this portion of the $\sigma_d(T)$ curve by relation (1), we find the parameters $\sigma_0 = 2.9 \Omega^{-1} \text{cm}^{-1}$ and $E = 0.51$ eV. Extrapolation of the Arrhenius dependence $\sigma_d(T)$ with the obtained σ_0 and E values to lower temperatures (curve θ) shows that at $T < 250$ K this conductivity is less than the conductivity of the measured film. Therefore, it may be assumed that at $T < 250$ K, conductivity σ_d is entirely accounted for by hopping and is described by relation (2).

A fitting procedure to obtain the parameters A , T_0 and n best describing the experimental points in the temperature range $100 \text{ K} < T < 200 \text{ K}$ yields: $A = 80 \Omega^{-1} \text{cm}^{-1}$, $T_0 = 2.8 \times 10^6 \text{ K}$, $n = 0.325$. By extrapolating dependence (2) with these parameters to $T > 200 \text{ K}$ (Figs. 3, 4, curves I), we obtain good coincidence with the experimental points up to $T > 380 \text{ K}$. Also, the extrapolated value of the hopping conductivity is comparable with the experimentally determined film conductivity at $T > 380 \text{ K}$. Therefore, the parameters of the activated conductivity cannot correspond to curve θ . Assuming that the experimentally observed conductivity of film 5 is the sum of the activated conductivity σ_1 and the conductivity via localized states at

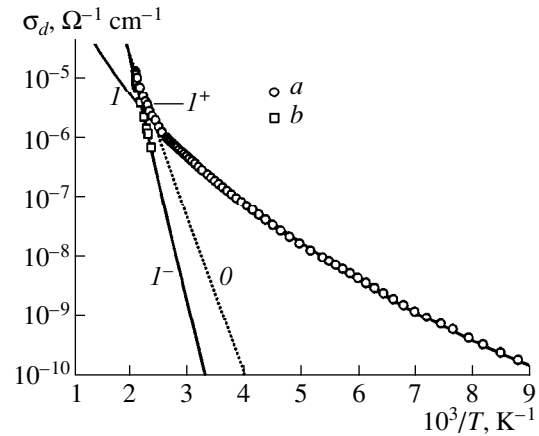


Fig. 3. Temperature dependences of the dark conductivity of annealed film 5: experimental (points a) and calculated (lines and points b). (θ) $\sigma_d(T) = \sigma_0 \exp(-E/kT)$, (I) $\sigma_2(T) = A \exp[-(T_0/T)^{0.325}]$, (I^-) $\sigma_1(T) = \sigma_0 \exp(-E/kT)$, and (I^+) $\sigma_d(T) = \sigma_1(T) + \sigma_2(T)$; calculation parameters: $\sigma_0 = 768 \Omega^{-1} \text{cm}^{-1}$, $E = 0.76$ eV, $A = 80 \Omega^{-1} \text{cm}^{-1}$, $T_0 = 2.8 \times 10^6 \text{ K}$, $n = 0.325$.

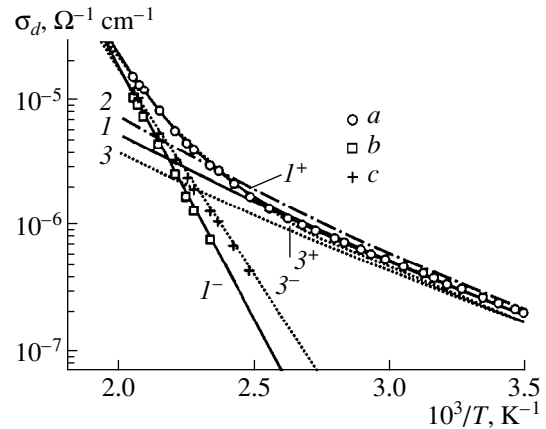


Fig. 4. Temperature dependences of the dark conductivity of annealed film 5: experimental (points a) and calculated (lines and points b , c). ($1-3$) $\sigma_2(T) = A \exp[-(T_0/T)^n]$: (1) $A = 80 \Omega^{-1} \text{cm}^{-1}$, $T_0 = 2.8 \times 10^6 \text{ K}$, $n = 0.325$; (2) $A = 1 \times 10^8 \Omega^{-1} \text{cm}^{-1}$, $T_0 = 1.5 \times 10^8 \text{ K}$, $n = 0.25$; (3) $A = 1.9 \Omega^{-1} \text{cm}^{-1}$, $T_0 = 4.34 \times 10^5 \text{ K}$, $n = 0.38$. (I^- , 3^-) $\sigma_1(T) = \sigma_0 \exp(-E/kT)$: (I^-) $\sigma_0 = 768 \Omega^{-1} \text{cm}^{-1}$, $E = 0.76$ eV; (3^-) $\sigma_0 = 44 \Omega^{-1} \text{cm}^{-1}$, $E = 0.64$ eV; (I^+ , 3^+) sums of the corresponding band and hopping conductivities.

the Fermi level σ_2 , we find $\sigma_1(T)$ by subtracting $\sigma_2(T)$ (curve I) from the experimental curve $\sigma_d(T)$. The obtained values $\sigma_1(T)$ (curve I^-) are described by the Arrhenius equation (1) with $\sigma_0 = 768 \Omega^{-1} \text{cm}^{-1}$, $E = 0.76$ eV. The resulting values of σ_0 and E are typical of the band conduction, rather than corresponding to the

conduction via localized states in the band tail. Assuming that the dark conductivity of the film is determined by the band and hopping conductivities, we calculated their sum, represented by curve 1⁺. A good agreement with the experiment was obtained over the entire temperature range under study.

It was established that at $100 < T < 200$ K the measured temperature dependence $\sigma_d(T)$ can be described by relation (2) with different parameters A , T_0 , and n . However, extrapolation of the calculated dependences $\sigma_2(T)$ with these different parameters to the high-temperature range and representation of $\sigma_d(T)$ as the sum of the band and hopping conductivities makes it possible to choose the A , T_0 and n values at which the simulated $\sigma_d(T) = \sigma_1(T) + \sigma_2(T)$ curve fits the experimental data over the entire temperature interval under study.

Figure 4 presents curves 1, 2, and 3 calculated using relation (2) with the respective values of n : $n_1 = 0.325$, $n_2 = 0.25$, and $n_3 = 0.38$. Curve 2 runs above the experimental points at $T > 350$ K. This clearly shows that the hopping conductivity of film 5 cannot be described by relation (2) with $n = 0.25$. Curve 3 runs below the experimental points, and, consequently, the activated component of the conductivity, $\sigma_1(T)$, in the high-temperature range can be determined (curve 3⁻). Curve 3⁺ is calculated as the sum of the conductivities represented by curves 3 and 3⁻. This curve runs below the experimental points in a certain temperature range, and the difference between the conductivities cannot be accounted for by the occurrence of a third type of conduction in the film (e.g., hopping conduction via localized states in the conduction band tail) with reasonable parameters.

Thus, the conductivity of annealed films 4 and 5 in the temperature range under study is determined by the sum of the band conductivity and hopping conductivity via states at the Fermi level. The exponent n in the relation (2) for the hopping conductivity is 0.325, differing from the theoretical value of 0.25. This difference may be due, e.g., to the temperature dependence of the pre-exponential factor A [11]. In addition, an increase in the exponent n to $n = 0.33$ has been observed experimentally upon decrease in the thicknesses of amorphous silicon and germanium films [12]. In the case in question, a nonuniform distribution of dangling bonds across the film thickness is possible, with their density being high-

est at the layer interfaces. Then, the hopping conductivity of the film can be described by relation (2) with $n = 0.325$.

ACKNOWLEDGMENTS

We are grateful to I.P. Zvyagin and A.G. Kazanskiĭ for helpful discussions.

This study was supported by INTAS (grant no. 97-1910) and COPERNICUS (grant no. IC15-CT98-0819, TIMOC).

REFERENCES

1. Jung-Chuan Chou, Shen-Kan Hsiung, and Chih-Yuan Lu, *J. Non-Cryst. Solids* **99**, 23 (1988).
2. T. Sakka, K. Toyoda, and M. Iwasaki, *Appl. Phys. Lett.* **55**, 1068 (1989).
3. I. A. Kurova, A. N. Lupacheva, N. V. Meleshko, and É. V. Larina, *Fiz. Tekh. Poluprovodn. (St. Petersburg)* **28**, 1092 (1994) [*Semiconductors* **28**, 628 (1994)].
4. K. Fukutani and M. Kanbe, *J. Non-Cryst. Solids* **227–230**, 63 (1998).
5. J. P. Hong, C. O. Kim, T. U. Nahm, and C. M. Kim, *J. Appl. Phys.* **87**, 1676 (2000).
6. K. Lips, T. Kanschat, D. Will, *et al.*, *J. Non-Cryst. Solids* **227–230**, 1021 (1998).
7. M. Kondo, T. Nishimiya, K. Saito, and K. Matsuda, *J. Non-Cryst. Solids* **227–230**, 1031 (1998).
8. V. P. Afanas'ev, A. S. Gudovskikh, O. I. Kon'kov, *et al.*, *Fiz. Tekh. Poluprovodn. (St. Petersburg)* **34**, 495 (2000) [*Semiconductors* **34**, 477 (2000)].
9. *The Physics of Hydrogenated Amorphous Silicon*, Vol. 2: *Electronic and Vibrational Properties*, Ed. by J. D. Joannopoulos and G. Lucovsky (Springer-Verlag, New York, 1984; Mir, Moscow, 1987).
10. B. I. Shklovskiĭ and A. L. Éfros, *Electronic Properties of Doped Semiconductors* (Nauka, Moscow, 1979; Springer-Verlag, New York, 1984).
11. V. L. Bonch-Bruевич, I. P. Zvyagin, R. Kaĭper, A. G. Mironov, R. Enderlein, and B. Esser, *The Electronic Theory of Disordered Semiconductors* (Nauka, Moscow, 1981).
12. M. L. Knotek, *Solid State Commun.* **17**, 1431 (1975).

Translated by D. Mashovets

PHYSICS OF SEMICONDUCTOR DEVICES

Optically Pumped Mid-Infrared InGaAs(Sb) LEDs

N. V. Zotova, S. A. Karandashev, B. A. Matveev*, M. A. Remennyĭ,
N. M. Stus', G. N. Talalakin, and V. V. Shustov

Ioffe Physicotechnical Institute, Russian Academy of Sciences, St. Petersburg, 194021 Russia

* e-mail: bmat@iropt3.ioffe.rssi.ru

Submitted August 2, 2000; accepted for publication August 2, 2000

Abstract—Spectral and power characteristics of optically pumped light-emitting diodes (LEDs) for the 3.1–3.6 μm range are presented. The LED structure contains narrow-gap InGaAs or InGaAsSb layers on an n^+ -InAs substrate; the pumping is done with a GaAs LED. A conversion efficiency of 90 mW/(A cm^2), comparable with that for injection LEDs, is achieved. © 2001 MAIK “Nauka/Interperiodica”.

1. INTRODUCTION

In p - n structures based on compounds close in composition to indium arsenide, carriers mainly recombine in the p -region owing to the high electron mobility. This is one of the reasons for the relatively low efficiency of mid-IR emitters, since nonradiative Auger recombination is enhanced in p -type materials by the energy resonance between the forbidden and the spin-orbit-split bands [1].

Hence, it follows that the quantum efficiency of a radiation source can be raised by ensuring preferential carrier injection into the n -type active region. This can be done, for example, by optical pumping (OP), i.e., without participation of the p - n junction. Optical pumping is widely used in designing double-heterostructure lasers and LEDs for the near-IR range [2, 3]; also, several studies are known to be devoted to the room-temperature photoluminescence (PL) of narrow-band III–V materials [4, 5]. However, we are not aware of any works describing optically pumped III–V LEDs for the mid-IR range. At the same time, inexpensive and efficient $\lambda = 3$ –5 μm emitters can find their application in gas analysis, communications, etc.

In this work, we report characteristics of optically pumped LEDs operating in the 3.1–3.6 μm range, based on InGaAs and InGaAsSb solid solutions enriched in InAs.

2. SAMPLES AND EXPERIMENT

Undoped n -type $\text{In}_{0.94}\text{Ga}_{0.06}\text{As}_{0.94}\text{Sb}_{0.06}$ and $\text{In}_{0.96}\text{Ga}_{0.04}\text{As}$ layers, 3- to 8- μm thick, were grown by LPE at 650–720°C on heavily doped (111) or (100) n^+ -InAs(Sn) substrates with electron concentration $n = (2$ – $4) \times 10^{18} \text{ cm}^{-3}$. The growth was performed from a Gd-doped melt. According to [6, 7], this ensures defect gettering accompanied by a decrease in the residual donor concentration and an increase in the quantum efficiency of luminescence. The density of inclined dis-

locations in $\text{In}_{0.94}\text{Ga}_{0.06}\text{As}_{0.94}\text{Sb}_{0.06}$ substrate-matched layers was about 10^4 – 10^5 cm^{-2} , whereas for a strongly lattice-mismatched $\text{In}_{0.96}\text{Ga}_{0.04}\text{As}/\text{InAs}$ system ($\Delta a/a \approx 0.3\%$) the dislocation density increased to 10^7 cm^{-2} . In some cases, a 2- μm -thick wide-gap n - $\text{InAs}_{0.74}\text{Sb}_{0.09}\text{P}_{0.17}$ “buffer” layer was deposited onto the substrate prior to fabrication of the “working” n -InGaAsSb layer. For optical studies, the substrate was thinned to 50 μm .

Room temperature PL in the transmission mode was measured at room temperature under excitation by a GaAs LED (emission wavelength $\lambda \approx 0.87 \mu\text{m}$, external quantum efficiency $\eta_{\text{ext}} \approx 2\%$) $1 \times 0.9 \text{ mm}^2$ in size with a mesa diameter of 0.4 mm, mounted onto a silicon holder ($1.5 \times 1.7 \times 0.4 \text{ mm}$) having a U-shaped contact to the n -region and a round p -type contact lying in the same plane, as described in our earlier communications [8]. The absence of contacts on the external surface of the pumping GaAs diode allowed easy fixation of a narrow-gap structure on this surface. In this configuration, the narrow-gap layer and the pumping diode were optically coupled by a chalcogenide glass with refractive index $n = 2.6$. To perform a set of experiments with varying thickness of InGaAsSb layers, layer-by-layer chemical etching was used.

Photoluminescence in the reflection geometry, excited by an array of GaAs lasers, was measured at $T = 77 \text{ K}$.

In all spectral measurements, the pulsed signal from a cooled InSb photodiode was detected using a lock-in amplifier (pulse repetition rate 500 Hz frequency, pulse duration 5–30 μs). The LED power was measured with a cooled CdHgTe photodiode, with account taken of the directional pattern of the LED and the spectral sensitivity of the photodetector.

3. RESULTS AND DISCUSSION

Figure 1 presents spectra of the PL from epilayers, passed through an InAsSbP “window” and (100)

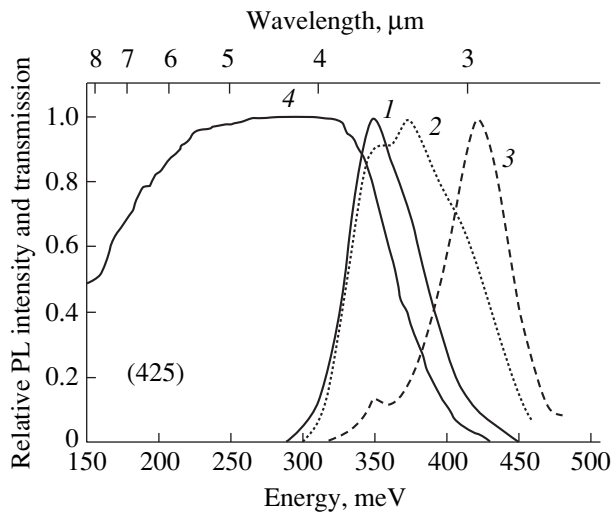


Fig. 1. PL intensity (1–3) and transmission (4) spectra for InGaAsSb/InAsSbP/ n^+ -InAs sample. InGaAsSb/InAsSbP layer thickness: (1, 4) 6/2, (2) 1.2/2, and (3) 0/0.8 μm .

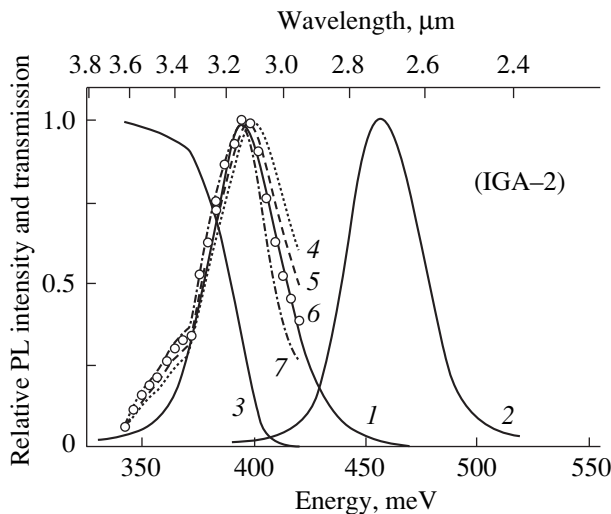


Fig. 2. Experimental PL intensity (1, 2) and transmission (3) spectra for InGaAs/ n^+ -InAs sample, and simulated PL spectra (4–7). Temperature (1, 3–7) 300 and (2) 77 K. Fitting parameter L_p : (4) $L_p \gg d$, (5) $L_p = 10$, (6) 5, and (7) 3 μm .

n^+ -InAs substrate, at varied thickness of InGaAsSb and InAsSbP epitaxial layers. Figure 1 also shows the transmission spectrum at $T = 300$ K, with the absorption edge at the peak of the PL band and long-wavelength absorption by free carriers in the substrate, beginning at $\lambda \approx 5 \mu\text{m}$.

We believe that the PL spectrum is not deformed by the presence of n^+ -InAs, because the expected substrate transmittance (t/t_0) is 0.83 at 3.14 μm and 0.5 at 3 μm , owing to the Moss–Burstein shift. The InGaAsSb PL spectrum taken in a reflection arrangement at $T = 77$ K (not shown in the picture) is a symmetric Gaussian curve peaked at $h\nu_{\text{max}} = 420$ meV, with full width at

half-maximum FWHM = 44 meV. The room-temperature InGaAsSb spectrum is asymmetric, having an extended short-wavelength edge that becomes more pronounced with decreasing layer thickness. When the InGaAsSb layer is etched off, a peak at $h\nu_{\text{max}} = 420$ meV appears, corresponding to emission from InAsSbP. In the case in question, the coincidence of InAsSbP (300 K) and InGaAsSb (77 K) spectral peaks is accidental. A minor shoulder at $h\nu_{\text{max}} = 350$ meV in the InAsSbP spectrum can be attributed to etching inhomogeneity and the presence of a small remainder of the InGaAsSb layer. The dependence of the integral PL intensity on the InGaAsSb layer thickness, similar to that of the EL intensity on the p - n junction depth [9, 10], has a maximum at a thickness $d \approx 4 \mu\text{m}$.

The obtained absorption and emission data can be correlated using the principle of detailed balancing proposed by Roosbroeck and Shockley. Taking into account the self-absorption of the emission and the exponential distribution of photoexcited carriers [11] allows simulation of the PL spectrum with the hole diffusion length (L_p) as a fitting parameter. For all reasonable L_p values, the simulated PL spectrum of InGaAsSb is shifted by 10 meV to shorter wavelengths, relative to the experimental spectrum. At the same time, its position corresponds to $h\nu_{\text{max}}(77 \text{ K}) = 60$ meV, which would be expected on the basis of the known temperature dependences of PL for similar materials [4, 12]. In this connection, it seems reasonable to assume that the observed PL band consists of two peaks associated with, e.g., “band-to-band” and “band-to-acceptor” recombination. This assumption is supported by the asymmetric shape of the spectrum (see Fig. 1) and also by the rather low absorption coefficient at the energy of the luminescence peak $\alpha(h\nu_{\text{max}}) = 417 \text{ cm}^{-1}$, which is much lower than $\alpha(h\nu_{\text{max}}) = 1400 \text{ cm}^{-1}$ obtained previously for lattice-mismatched InAs_{0.85}Sb_{0.15} gradient layers [13]. Thus, the reduced $\alpha(h\nu_{\text{max}})$ value for isoperiodic InGaAsSb does not reflect the general tendency for the absorption coefficient to increase with decreasing dislocation density, revealed in [13].

Figure 2 shows transmission and PL spectra for a (111) InGaAs/ n^+ -InAs sample. The PL spectra at $T = 77$ and 300 K have the same shape, well fitted by a Gaussian curve with FWHM = 30 meV and peaks at 400 and 462 meV, respectively. Simulated spectra are also presented for several diffusion lengths of extrinsic carriers. It can be seen that the simulated curve coincides well with the experimental curve at $L_p = 5 \mu\text{m}$ (points). The obtained L_p value is shorter than the diffusion length 10–20 μm for “pure” indium arsenide (with electron concentration $n = 10^{15} \text{ cm}^{-3}$) [14], but is in agreement with our evaluations based on the observed decrease in luminescence intensity in layer-by-layer etching of n -InAsSbP/ n -InAs [15]. It should be noted that, despite the substantial lattice mismatch and high dislocation density (10^7 cm^{-2}), InGaAs layers demon-

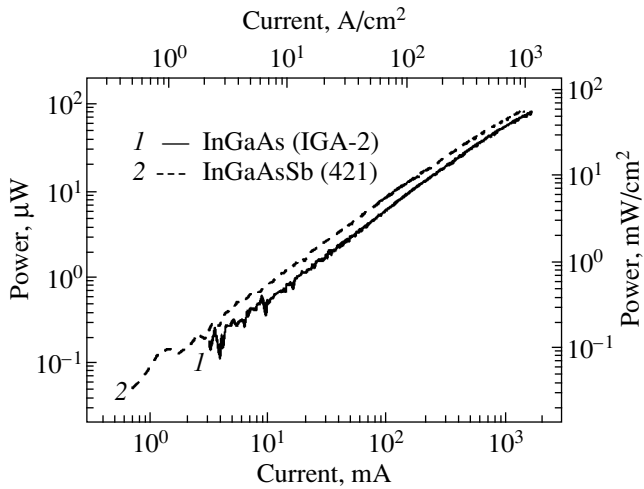


Fig. 3. Power of optically pumped LEDs vs. current pulse amplitude. Material of the narrow-gap active region: (1) InGaAs ($\lambda = 3.14 \mu\text{m}$) and (2) InGaAsSb ($\lambda = 3.6 \mu\text{m}$). $T = 300 \text{ K}$.

strate optical properties typical of perfect crystals: a sharp absorption edge $\alpha \propto \exp(h\nu/\epsilon)$ with $\epsilon = 10 \text{ meV}$, high absorption coefficient $\alpha(h\nu_{\text{max}}) = 1140 \text{ cm}^{-1}$, and a temperature coefficient of the PL peak position ($62 \text{ meV}/223 \text{ K}$) typical of InAs. This leads to a conclusion that the contribution of dislocations to carrier recombination in InGaAs is unimportant.

The above conclusion concerning the influence of dislocations is indirectly supported by comparison of the power levels of optically pumped InGaAs and InGaAsSb LEDs (Fig. 3). As seen, both diodes have close output powers with linear dependence on current. It is noteworthy that the InGaAs LED was not optimized, whereas the InGaAsSb LED had an optimal thickness of the narrow-gap active layer ($3 \mu\text{m}$).

The linearity of the power-current characteristics represents one more advantage of optically pumped LEDs, the standard mid-IR range LEDs being commonly saturated at high currents [10, 16]. It should also be noted that the conversion efficiency obtained for the InGaAsSb LED ($90 \text{ mW}/\text{A cm}^2$) is comparable with the best data for LEDs operating in the same spectral range ($115 \text{ mW}/(\text{A cm}^2)$, InGaAs [17]).

4. CONCLUSION

Thus, the first optically pumped LEDs for mid-IR range have been fabricated on the basis of III-V solid solutions, with the emission power close to the highest values achieved in standard LEDs. The high driving voltage and the resulting high power consumption of these LEDs are compensated for by the fabrication simplicity, since a narrow-gap active layer can be produced without photolithography and p - n -junction formation. It is also important that the operation of optically pumped LEDs is nearly insensitive to dislocations,

which allows fabrication of non-isoperiodic LED structures containing, e.g., InGaAs for the 2.5 – $3.5 \mu\text{m}$ range, important for gas analysis. Finally, it should be noted that the use of InAsSbP gradient structures [18] will extend the spectral range and the application areas of optically pumped LEDs.

ACKNOWLEDGMENTS

We thank O. N. Saraev for the presented GaAs LED chips, and the US Civilian Research and Development Foundation for CIS countries (CRDF) for the administrative support.

REFERENCES

1. M. Takeshima, *J. Appl. Phys.* **43** (10), 4114 (1972).
2. J. L. Malin, C. L. Felix, J. R. Meyer, *et al.*, *Electron. Lett.* **32** (17), 1593 (1996).
3. M. Boroditsky, T. F. Krauss, R. Coccioli, *et al.*, *Appl. Phys. Lett.* **75** (8), 1036 (1999).
4. Z. M. Fang, K. Y. Ma, D. H. Jaw, *et al.*, *J. Appl. Phys.* **67** (11), 7034 (1990).
5. X. Y. Gong, T. Yamaguchi, H. Kan, *et al.*, *Jpn. J. Appl. Phys.* **36**, 738 (1997).
6. N. V. Zotova, S. A. Karandashev, B. A. Matveev, *et al.*, *Fiz. Tekh. Poluprovodn. (St. Petersburg)* **33** (8), 1010 (1999) [*Semiconductors* **33**, 920 (1999)].
7. A. Krier, H. H. Gao, and V. V. Sherstnev, *J. Appl. Phys.* **85** (12), 8419 (1999).
8. B. Matveev, N. Zotova, S. Karandashev, *et al.*, *IEEE Proc.: Optoelectron.* **145** (5), 254 (1998).
9. A. A. Bergh and P. J. Dean, *Light-Emitting Diodes* (Clarendon, Oxford, 1976).
10. M. J. Kane, G. Braithwaite, M. T. Ereny, *et al.*, *Appl. Phys. Lett.* **76** (8), 943 (2000).
11. D. D. Sell and H. C. Casey, Jr., *J. Appl. Phys.* **45** (2), 800 (1974).
12. M. Aïdaraliev, N. V. Zotova, S. A. Karandashev, *et al.*, *Fiz. Tekh. Poluprovodn. (St. Petersburg)* **34** (1), 99 (2000) [*Semiconductors* **34**, 104 (2000)].
13. N. V. Zotova, A. V. Losev, B. A. Matveev, *et al.*, *Pis'ma Zh. Tekh. Fiz.* **16** (4), 76 (1990) [*Sov. Tech. Phys. Lett.* **16**, 155 (1990)].
14. <http://www.ioffe.rssi.ru/SVA/NSM/Nano/index.html>.
15. N. P. Esina, N. V. Zotova, B. A. Matveev, *et al.*, *Fiz. Tekh. Poluprovodn. (Leningrad)* **19** (11), 2031 (1985) [*Sov. Phys. Semicond.* **19**, 1250 (1985)].
16. M. K. Parry and A. Krier, *Semicond. Sci. Technol.* **8**, 1764 (1993).
17. M. K. Parry and A. Krier, *Electron. Lett.* **30** (23), 1968 (1994).
18. B. A. Matveev, N. V. Zotova, N. D. Il'inskaya, S. A. Karandashev, M. A. Remennyi, N. M. Stus', and G. N. Talalakin, RF Patent No. 2154324 with Application (April 27, 1999).

Translated by D. Mashovets

PHYSICS OF SEMICONDUCTOR
DEVICES

Current-Tunable Lasers with a Narrow Emission Line Operating at 3.3 μm

A. N. Imenkov*, N. M. Kolchanova*, P. Kubat**, K. D. Moiseev*,
C. Civiš**, and Yu. P. Yakovlev*

* *Ioffe Physicotechnical Institute, Russian Academy of Sciences, Politekhnicheskaya ul. 26,
St. Petersburg, 194021 Russia*

** *Heyrovsky Institute of Physical Chemistry, Academy of Sciences of the Czech Republic,
Dolejskova 3, 18223 Praha 8, Czech Republic*

Submitted July 17, 2000; accepted for publication August 22, 2000

Abstract—Current-tunable diode lasers with narrow emission lines for laser spectroscopy in the 3.2–3.4 μm wavelength range are developed. The lasers, based on an InAsSb/InAsSbP double heterostructure, have a wide-stripe cavity. The wave number increases from 3030 to 3034 cm^{-1} as the current is raised from 1.5 to 3 times the threshold value at 70 K, while the full width at half-maximum of the laser line decreases from 18 to 10 MHz. It is demonstrated that the linewidth is determined by fluctuations of the cavity resonance frequencies as a result of fluctuations in the concentration of nonequilibrium charge carriers. © 2001 MAIK “Nauka/Interperiodica”.

1. INTRODUCTION

Current-tunable diode lasers operating in the medium infrared spectral range represent a promising tool for high-resolution laser spectroscopy. To record accurately the absorption spectra of various natural and industrial gases and to detect the presence of these gases in the environment, it is important to use a laser with a narrow emission line. The example of the absorption spectra measured for CH_3Cl , OCS , N_2O , and H_2O gases at a pressure of 1 Torr demonstrated previously [1–3] that the power, speed of response, and noise characteristics of lasers based on InAsSbP/InAsSb/InAsSbP heterostructures make them suitable for the precise study of the rotation–vibration spectra of molecular gases.

In this paper, we report the results of measuring the linewidth of this kind of laser and the development of lasers with a narrow emission line; this study continues our earlier efforts to investigate the linewidth of lasers operating in the 2- μm [4] and 3- μm [5] regions.

It was shown [5] that, in diode lasers whose frequency can be current-tuned in a wide range [2], the emission linewidth is determined by the fluctuations of the cavity resonance frequencies, rather than by the spontaneous emission into the cavity mode considered by the theories [6–8]. These fluctuations originate from the fluctuations in the number of nonequilibrium charge carriers in the cavity (which lead to the corresponding variations in the refractive index) resulting from the restriction of the injection current by the substrate resistance. The restriction serves to increase the injection density near the side edges of the cavity relative to the central region, which ensures an increase in the tuning range. The relative fluctuation of the concen-

tration of nonequilibrium charge carriers $\langle\Delta N\rangle/N$ is inversely proportional to the square root of the active-region volume V . Consequently, as the active region volume increases, fluctuations of the refractive index and, thus, fluctuations of the cavity resonance frequencies should decrease, which results in a reduced linewidth of the laser emission.

An increase in the cavity length is undesirable due to the associated reduction in the cavity mode spacing, which makes multimode lasing more feasible. Increasing the active region thickness above the diffusion length (1 μm) should be avoided too, because of the resulting increase in the width of the gain spectrum, which also leads to multimode lasing.

Consequently, to develop a laser with a narrower emission line, the cavity width should be increased. This does not preclude the attainment of a wide tuning range if the structure layers are highly uniform. Thus, instead of a common 10- to 20- μm -wide cavity [1–3], we used a 100- μm -wide one.

2. EXPERIMENTAL

Laser structures were grown by liquid-phase epitaxy on (100)-oriented p -InAs substrates with the hole concentration equal to $5 \times 10^{18} \text{ cm}^{-3}$, as were those investigated in [2, 3]. The structures have a 0.8- μm -thick active InAsSb layer and 3- μm -thick wide-gap InAsSbP emitter layers. The equilibrium electron concentration in the active layer, which was not intentionally doped, equals $(2\text{--}4) \times 10^{16} \text{ cm}^{-3}$. The confining p -layer was doped with Zn up to the hole concentration of $(1\text{--}2) \times 10^{18} \text{ cm}^{-3}$, and the confining n -layer was doped with Te up to the electron concentration of

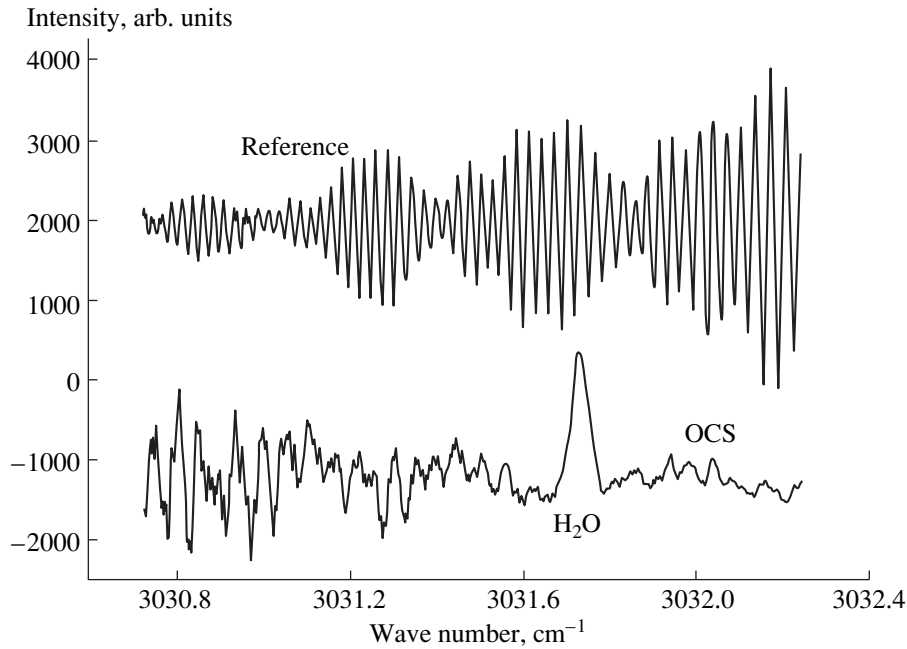


Fig. 1. Transmission spectrum of a cell containing OCS at a pressure of 1 Torr with an admixture of H₂O vapor.

$(5-8) \times 10^{18} \text{ cm}^{-3}$. After the growth of the epilayers, the substrate was ground to a thickness of 100 μm . Chips with a period of 500 μm and mesa width of 100 μm were prepared by photolithography. Cavities were obtained by cleaving; the cavity length was 250 μm . The laser structures were mounted on a copper heat-sink holder.

The laser to be studied was placed in a helium-flow closed-cycle thermostat (Laser Photonics L 573) operating in the temperature range of 12–100 K. The laser was pumped by a direct current modulated by a sawtooth function with varying modulation depth. Laser temperature and current were controlled by Laser Photonics units, Models L 5820 and L 5731. A laser mode emission was selected by a grating monochromator and was detected by a liquid-nitrogen-cooled InAs photodiode after passing through a cell containing the substance under investigation or through a reference cavity with 0.026 cm^{-1} resonance-mode spacing. The photodiode signal was first fed to a wideband amplifier and then to both a differentiating RC circuit and one of the inputs of a Le Croy 9361 digital oscilloscope. The filtered signal from the resistance of the RC circuit was fed to the second input of the oscilloscope. The RC circuit time constant was $\tau = 12 \mu\text{s}$, and the duration of the increasing portion of the sawtooth current was 5 ms.

The averaged value \bar{U} of the time derivative of the emission intensity in the region of the highest slope of the gas absorption band was measured in the second channel; rms deviation of the signal from its average value $\langle U \rangle$ was measured in this channel, too. The line

width at half-maximum Δf was calculated by the formula

$$\Delta f = 2\tau f' \frac{\langle U \rangle}{U}, \quad (1)$$

where f' is the time derivative of the laser emission frequency, determined by the time interval between the known absorption lines or reference cavity resonances in the first oscilloscope channel.

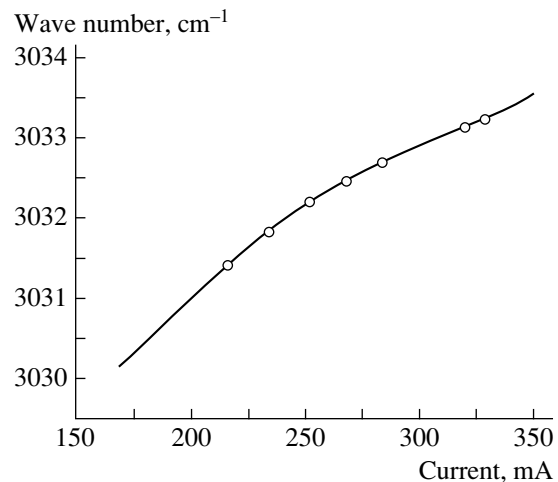


Fig. 2. Current dependence of emission wave number for an MK 694-1 laser at 70 K. The circles indicate the positions of the CH₃Cl absorption bands used to measure the laser linewidth.

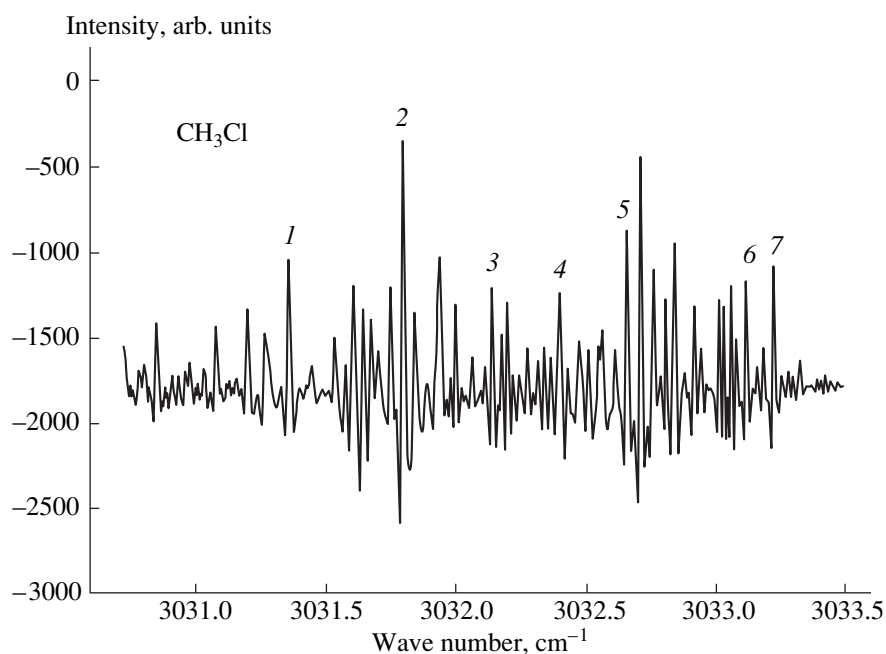


Fig. 3. Transmission spectrum of a cell containing CH_3Cl at a 1 Torr pressure.

To record the gas absorption spectra, additional sine modulation of the laser current was introduced. Its frequency was much higher and the amplitude was much smaller than those of the sawtooth modulation. The signal at the second harmonic of the sine modulation frequency is proportional to the second derivative of the intensity with respect to the wave number. This enabled us to carry out measurements at gas pressures much lower than 1 Torr.

3. RESULTS

At temperatures from 60 to 80 K, single-mode lasing occurs, and the tuning range is $2\text{--}4\text{ cm}^{-1}$. In a cell filled with OCS, the strongest absorption is related to the known H_2O band (Fig. 1) with the wave number equal to $3031.73463\text{ cm}^{-1}$ [9–11]. This band was used to calibrate the current dependence of the laser emission wave number (Fig. 2), obtained from the transmission spectrum of the Fabry–Perot etalon. The presence of OCS in the cell is evidenced by typical absorption oscillations with a period of 0.37 cm^{-1} (see Fig. 1). The laser emission linewidth was measured using the absorption bands of CH_3Cl gas marked by numbers in Fig. 3. It should be noted that this region of the CH_3Cl absorption spectrum is poorly known, but it contains a lot of narrow bands with $0.010\text{--}0.016\text{ cm}^{-1}$ half-widths at a 1 Torr pressure and has a number of other features.

The width of the emission line (see Fig. 4) is largest at lowest currents ($\sim 20\text{ MHz}$ at 216 mA) and gradually decreases with increasing current, approaching 10 MHz at 320 mA, the highest current for which the measure-

ments were performed. At higher currents, the linewidth was not measured due to the lack of suitable absorption bands. The laser linewidth is 15–20 times smaller than the gas absorption linewidth, which is sufficient for the precise measurement of the shape of the absorption bands by laser spectroscopy. Ten megahertz is the lowest value for the IR-laser linewidth ever obtained. However, the increase in the laser linewidth with decreasing current (Fig. 4) gives rise to problems with carrying out measurements at low currents. Thus, it is necessary to reduce the laser linewidth, which requires an investigation into the factors that govern its value.

4. ANALYSIS

According to the existing theories [6–8], the laser linewidth is controlled by the spontaneous emission of radiation into the laser mode and should decrease as a reciprocal of the current. In the current-tunable lasers, the linewidth decrease is observed only in the low-current region, and the line narrowing rate is lower than that specified by the hyperbolic law. For higher pump currents, the line ceases to narrow and even starts to broaden. The current dependence of the linewidth plotted in Fig. 4 contains only a decreasing portion; an increasing portion was not observed for this laser, since only a range of currents slightly above the threshold I_{th} is covered. The linewidth of the wide-cavity laser under study is six times larger than the value predicted by the theory taking into consideration the effect of the fluctuations in the nonequilibrium carrier concentration on

the spontaneous emission into the cavity mode [8] (see Fig. 4). Consideration of this effect yields a linewidth six times larger than that predicted by the theory [6, 7].

It has been previously assumed [6–8] that the nonequilibrium carrier concentration N is independent of the current I (and remains equal to the threshold value N_{th}) for $I > I_{th}$. However, in the current-tunable lasers, N continues to increase with the current above the threshold. This leads to a decrease in the refractive index n in the cavity and an increase in the cavity resonance frequencies f . In order to obtain a smooth-waveguiding distribution of n across the cavity width, the substrate should be made wider than the cavity, and its resistance should be made greater than the p – n junction differential resistance. Under these conditions, the only mechanism of relaxation of the fluctuations in the number of nonequilibrium charge carriers in the cavity is related to the laser emission, since the injection current is limited by the laser series resistance. The smoothed-out fluctuations result in deviations of the cavity resonance frequencies from their average values.

In the absence of lasing, the width of the probability function for the cavity resonance frequencies is

$$\Delta f_0 = 2 \frac{f}{\tau} \left| \frac{dn}{dN} \right| \sqrt{\frac{2}{V} (N_{th} + \delta N)}, \quad (2)$$

where δN is the excess concentration of the nonequilibrium charge carriers over the threshold value. The shift δf of the oscillation frequency from its value corresponding to the threshold current is related to δN by

$$\delta N = \frac{\delta f}{f} \frac{n}{(-dn/dN)}.$$

In the presence of lasing, the probability function narrows proportionally to the charge carrier lifetime, which decreases from τ_0 to τ_p . Thus, the laser linewidth is equal to

$$\Delta f = \Delta f_0 \frac{\tau_p}{\tau_0}. \quad (3)$$

From the rate equation for N at constant injection rate and gain, under the conditions of bimolecular recombination, which is typical of lasers, we obtain

$$\frac{\tau_0}{\tau_p} = 1 + \frac{(I/I_{th}) - (1 + \delta N/N_{th})^2}{2(1 - N_0/N_{th})(1 + \delta N/N_{th})}, \quad (4)$$

where N_0 is the nonequilibrium charge carrier concentration corresponding to the onset of the population inversion for a given mode; the ratio $N_0/N_{th} = 0.75$ – 0.80 .

The values of Δf (Fig. 4) calculated from formulas (2)–(4) with $n = 3.6$, $dn/dN = -0.25 \times 10^{-18} \text{ cm}^3$, and $N_{th} = 9.4 \times 10^{16} \text{ cm}^{-3}$ (which corresponds to the laser differential quantum efficiency $\eta = 75\%$) are close to the experimental data. The discrepancy does not exceed 10%, which is within the measurement error limits. In

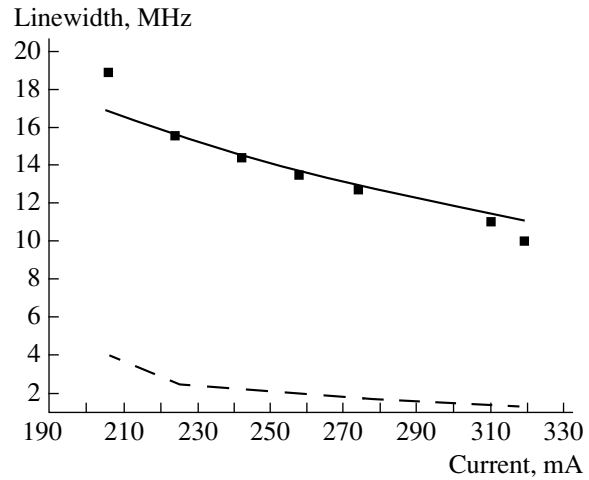


Fig. 4. Current dependence of emission linewidth for an MK 694-1 laser at 70 K. The squares represent experimental points, the dashed line corresponds to the theory developed in [8], and the solid line is calculated according to the model we suggested.

turn, theoretical formulas can be refined by taking into account the Auger recombination, the presence of donors in the active region, the deviation of the optical confinement factor from unity, etc.

5. CONCLUSION

The study of the spectral parameters of wide-cavity lasers based on InAsSb/InAsSbP demonstrates that it is possible to obtain single-mode lasing in a wide range of currents and temperatures. In the temperature range from 60 to 80 K, the laser emission wave number can be tuned with the current by 2–4 cm^{-1} . Increasing the cavity width makes it possible to obtain a small emission linewidth (as low as 10 MHz). The value of the linewidth, as well as its current dependence, is determined by the fluctuations of the cavity resonance frequencies, which are related to the fluctuations in the number of the charge carriers in the cavity. In this case, the width of the laser line is inversely proportional to the square root of the active region volume; thus, the linewidth can be reduced by increasing the cavity width. In the presence of lasing, the linewidth decreases with the current approximately in proportion to the nonequilibrium charge carrier lifetime.

The realization of single-mode lasing with narrow emission lines in the wide-cavity lasers indicates that crystal quality of the layers grown by liquid-phase epitaxy is high. The high power and small linewidth of such lasers makes them a promising tool for laser spectroscopy.

ACKNOWLEDGMENTS

This study was supported in part by the Ministry of Science of the Russian Federation, the Russian Foun-

dition for Basic Research (project nos. 99-02-18109 and 00-02-17047), and the Grant Agency of the Czech Republic (project no. 4040708).

REFERENCES

1. A. N. Baranov, T. N. Danilova, O. G. Ershov, *et al.*, *Pis'ma Zh. Tekh. Fiz.* **18** (22), 6 (1992) [*Sov. Tech. Phys. Lett.* **18**, 725 (1992)].
2. A. P. Danilova, A. N. Imenkov, N. M. Kolchanova, *et al.*, *Fiz. Tekh. Poluprovodn. (St. Petersburg)* **34** (2), 243 (2000) [*Semiconductors* **34**, 237 (2000)].
3. A. P. Danilova, A. N. Imenkov, N. M. Kolchanova, *et al.*, *Fiz. Tekh. Poluprovodn. (St. Petersburg)* **33**, 1469 (1999) [*Semiconductors* **33**, 1322 (1999)].
4. V. G. Avetisov, A. N. Baranov, A. N. Imenkov, *et al.*, *Pis'ma Zh. Tekh. Fiz.* **16** (14), 66 (1990) [*Sov. Tech. Phys. Lett.* **16**, 549 (1990)].
5. A. N. Imenkov, N. M. Kolchanova, P. Kubat, *et al.*, *Fiz. Tekh. Poluprovodn. (St. Petersburg)* **34** (12), 1468 (2000) [*Semiconductors* **34**, 1406 (2000)].
6. A. L. Shawlow and C. H. Townes, *Phys. Rev.* **112** (6), 1940 (1958).
7. C. H. Henry, *J. Lightwave Technol.* **LT-4**, 298 (1986).
8. M. Yamada, *IEEE J. Quantum Electron.* **QE-30**, 7 (1994).
9. *Water Vapor Line Parameters from Microwave to Medium Infrared*, Ed. by J.-M. Flaud, C. Camy-Peyret, and R. A. Toth (Pergamon, Oxford, 1981).
10. A. G. Maki and J. S. Wells, *Wavenumber Calibration Tables from Heterodyne Frequency Measurements* (US Dept. of Commerce, Technology Administration, National Inst. of Standards and Technology, Washington, 1991), NIST Special Publication 821.
11. G. Guelachvili and K. Nazahari Rao, *Handbook of Infrared Standards II: With Spectral Coverage of 1.4–4 μm and 6.2–7.7 μm* (Academic, Boston, 1993).

Translated by M. Skorikov

PHYSICS OF SEMICONDUCTOR DEVICES

Record Power Characteristics of InGaAs/AlGaAs/GaAs Heterostructure Lasers

D. A. Livshits, A. Yu. Egorov, I. V. Kochnev[†], V. A. Kapitonov, V. M. Lantratov,
N. N. Ledentsov, T. A. Nalyot, and I. S. Tarasov

*Ioffe Physicotechnical Institute, Russian Academy of Sciences, Politekhnicheskaya ul. 26,
St. Petersburg, 194021 Russia*

Submitted September 4, 2000; accepted for publication September 5, 2000

Abstract—Continuous-wave output powers of 9.2 W at a constant heatsink temperature of 10°C and 12.2 W at a stabilized temperature of the active region have been obtained on an InGaAs/AlGaAs laser with a 0.4- μm -thick waveguide, operating at 1.03 μm . Record-breaking output mirror power densities of, respectively, 29.9 and 40 MW/cm^2 have been achieved without catastrophic optical mirror damage in the two temperature-stabilization regimes. A maximum power conversion efficiency of 66% has been achieved in a laser with a cavity length of 2 mm. © 2001 MAIK “Nauka/Interperiodica”.

High-power stripe lasers with active regions intended for wavelengths in the interval $\lambda = 0.8\text{--}1.06 \mu\text{m}$ attract intense interest owing to their wide range of applications, such as optical pumping sources for solid-state fiber lasers, direct frequency doubling, laser welding, medicine, etc.

The work on developing high-power single- and multimode lasers has already been conducted for a long time [1, 2], and 1- and 2-W 100- μm stripe laser diodes operating in the continuous wave (CW) regime are already being produced commercially. Raising the working power of such diodes presents a complicated problem, which is commonly attributed to the following. The first reason is the catastrophic optical mirror damage (COMD) limiting the peak output power [3]. The second reason is the rise in the working temperature of the laser crystal, compared with the heatsink temperature, which occurs upon passing current through a laser, and which impairs its external differential efficiency and accelerates its degradation.

The quantity characterizing COMD is \bar{P} —the optical power density at the output mirror of a laser diode at which COMD begins [3]. In a review [4] the maximum achieved \bar{P} values of 11 MW/cm^2 were given for lasers containing Al in the active region. The peak output power density for any kind of lasers, 19 MW/cm^2 according to [4], has been obtained in an InGaAs/InGaAsP/GaAs structure [5].

In this communication, we demonstrate that the COMD threshold can be significantly raised by optimizing the technology of the deposition of high- and low-reflectivity coatings on the laser mirrors. The peak CW optical power density obtained at the output mirror

of the laser was 29.9 MW/cm^2 at a stabilized heatsink temperature (10°C), i.e., in the conventional laser cooling regime, and 40 MW/cm^2 with chip temperature maintained constant.

The decrease in efficiency and accelerated degradation of lasers at high powers can be precluded by lowering the laser crystal temperature at the working point. The amount of heat released in the laser diode can be reduced by improving the power conversion efficiency of the device. At the same time, overheating of the working region relative to the heatsink can be lowered by making the laser longer, thereby increasing the effective area from which heat is removed.

The power conversion efficiency of a laser is given by [6]

$$\eta_c = \eta_d(h\nu/q) \frac{I - I_{th}}{I(V_0 + I\sigma_s/LW)}, \quad (1)$$

$$\eta_d = \eta_i \left(\frac{1}{2L} \ln \frac{1}{R_f R_r} \right) \left(\alpha_i + \frac{1}{2L} \ln \frac{1}{R_f R_r} \right), \quad (2)$$

where R_f and R_r are the reflectivities of the front and back facets of the laser, I_{th} is the threshold current, L is the cavity length, and W is the stripe width. Hence, it follows that the power conversion efficiency depends on the internal quantum efficiency η_i , cutoff voltage V_0 , and σ_s —the resistivity of the structure.

Thus, the problem of designing a high-power laser diode reduces to raising the COMD threshold and optimizing the structure parameters to achieve simultaneously a 100% internal quantum efficiency, low optical loss, low series resistance, and a cutoff voltage exactly corresponding to the energy gap of the active region.

[†] Deceased.

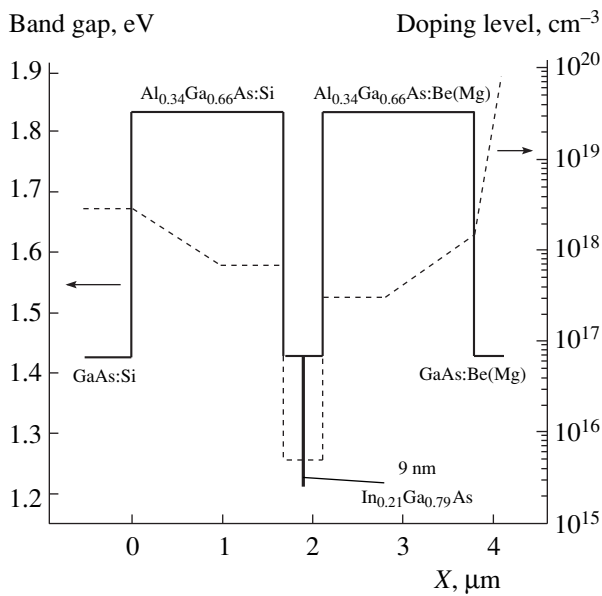


Fig. 1. Schematic band diagram (solid line) and doping profile of the epitaxial layers of the structures grown by MOCVD and MBE techniques.

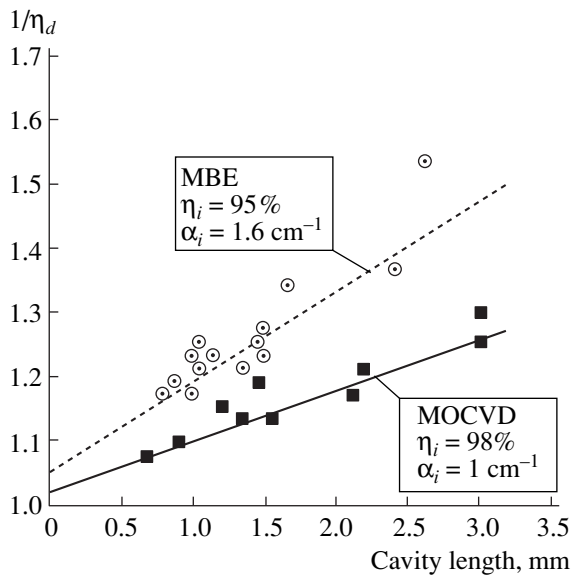


Fig. 2. Inverse differential quantum efficiency vs cavity length L of lasers based on InGaAs/AlGaAs/GaAs heterostructures.

To solve this problem, we fabricated more than ten heterostructures emitting at $\sim 1 \mu\text{m}$ by molecular-beam epitaxy (MBE) and metal-organic chemical vapor deposition (MOCVD). The structures grown had a simple design of a double-heterostructure with a separate confinement and optimized doping scheme. The heterostructure comprises a $0.4\text{-}\mu\text{m}$ -thick undoped GaAs waveguide with a $80\text{-}\text{\AA}$ -thick strained InGaAs quantum

well in its middle. The thicknesses, compositions, energy gaps, and doping levels of the epitaxial layers are shown schematically in Fig. 1. The emitter is doped with Mg in the case of MOCVD and Be in MBE. Correspondingly, the p -doping profile in MOCVD structures is smoother owing to the higher diffusion coefficient of magnesium.

Further, the structures were subjected to a conventional sequence of postgrowth operations to fabricate “shallow mesa” laser diodes with a stripe width of $100 \mu\text{m}$. In the design employed, the current spreading over heavily doped layers is diminished by etching as far as the middle of the top emitter. Ohmic contact systems to the p - and n -sides of the structure were deposited by vacuum evaporation of ZnAu/CrAu/Au and GeAu/Au, respectively.

The structures were cleaved along crystallographic directions into separate lasers with different cavity lengths L . Light-current (L - I) characteristics of the obtained devices were measured in a pulsed regime. The results of these measurements were used to calculate the basic parameters: transparency current density, internal quantum efficiency, and internal optical loss α_i . All the structures had very close parameters and, therefore, data are only presented here for one MOCVD-, and one MBE-grown, structure. Figure 2 shows the inverse differential quantum efficiency $1/\eta_d$ as a function of the cavity length for both the structures. A linear fit gave the internal quantum efficiency η_i and internal optical loss. For the MOCVD structure these parameters are 98% and 1 cm^{-1} , and are somewhat less optimal for the MBE structure—95% and 1.6 cm^{-1} . The transparency current density was 62 and 75 A/cm^2 , respectively.

To work in the CW regime, the p -side of each laser was soldered with indium to a copper heatsink. SiO_2/Si interference dielectric coatings were deposited onto the mirrors, ensuring 99% for the front and 5% for the back mirror reflectivities. In the conventional technology for the investigation and manufacture of semiconductor lasers, the process of mirror coating involves uncontrollable deposition of the dielectric onto a part of the p -contact near the laser mirrors, so that this area remains unsoldered in chip mounting, thereby impairing heat removal during laser operation. The technology employed for mirror deposition in the present study completely precludes undesirable deposition of the dielectric and ensures the best cooling of the output facet of the laser.

For CW measurements, a laser on a heatsink was mounted on a thermoelectric cooler that allowed the temperature to be maintained constant over a wide range. The measurements were done in two thermal stabilization regimes. The first, being conventional, used a feedback temperature sensor mounted on the heatsink. This method has a major drawback consisting in that the actual temperature of the laser chip strongly depends on the place where the thermal sensor is

mounted, because of the temperature gradient over the heatsink. This makes it difficult to compare laser characteristics measured on different setups. Therefore, we also used another measurement technique, with a second temperature sensor mounted directly onto the n -contact of the laser chip. This sensor served as a control element in the thermal stabilization feedback circuit. According to [7], in this regime the actual temperature of the laser's active region differs from that indicated by the temperature sensor by no more than 4°C . Thus, with this measurement technique it may be assumed that the laser's active region is maintained at a constant temperature.

Figure 3 shows the output power and the voltage across the structure as functions of the flowing current for a MOCVD laser. Using these data, the threshold current was found to be 165 mA; the differential and differential quantum efficiencies, 0.97W/A and 80%, respectively; the cut-off voltage, ~ 1.24 V; and the series differential resistance $R_s = 51$ m Ω , which gives $\sigma_s = 0.68 \times 10^{-4}$ Ω cm 2 per unit area. The combination of an internal quantum efficiency close to 100%, an internal optical loss of ~ 1 cm $^{-1}$, and the optimal electrical parameters compares well with the best published results [6]. The cutoff voltages exactly corresponding to the energy gap of the active region and the low series resistance of the laser structure indicate the absence of any additional electrical barriers and the optimal doping profile of the given structure.

Therefore, the power conversion efficiency is very high. Figure 4 presents experimental dependences of the power conversion efficiency on the driving current for lasers with cavity lengths of 1.34 and 2 mm at a heatsink temperature of 10°C . The maximum power conversion efficiencies are, respectively, 66 and 65%. Moreover, the laser with a cavity length of 2 mm retains a power conversion efficiency exceeding 60% up to an output power of 6 W. These results are also the best we are aware of for any kind of semiconductor lasers [7].

With the conventional measurement technique maintaining the heatsink temperature at 10°C , the maximum current was limited to 12 A to prevent degradation of the heterostructure (Fig. 3). An output power of 9.2 W was recorded at this current, with the temperature of the active region, measured by the second temperature sensor, equal to 56°C . The rise in the temperature of the active region leads to a higher threshold current, lower quantum efficiency, and lower photon energy. This results in a bending of the L - I characteristic at large currents and does not allow the achievement of the maximum possible output power or determination the COMD threshold. High peak CW output powers were obtained in a similar cooling regime on lasers with a $100\text{-}\mu\text{m}$ aperture. The highest power of 10.9 W has been achieved in the InGaAs/AlGaAs/GaAs system using a more efficient diamond heatsink [8], the maximum achieved output power for the InGaAs/InGaAsP/GaAs system being 11 W [5]. However, these results were

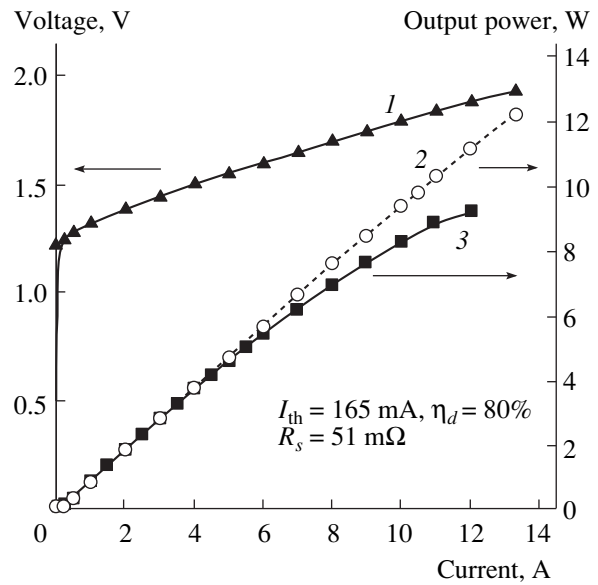


Fig. 3. Voltage across a laser diode with stripe width $W = 100$ μm and its output power vs driving current in the CW regime. Cavity length $L = 1.34$ μm , high- (99%) and low-reflectivity (5%) coatings on facets. (1) V - I and (2) L - I characteristics with the temperature of the active region stabilized at 10°C . (3) L - I characteristic with heatsink temperature stabilized at 10°C .

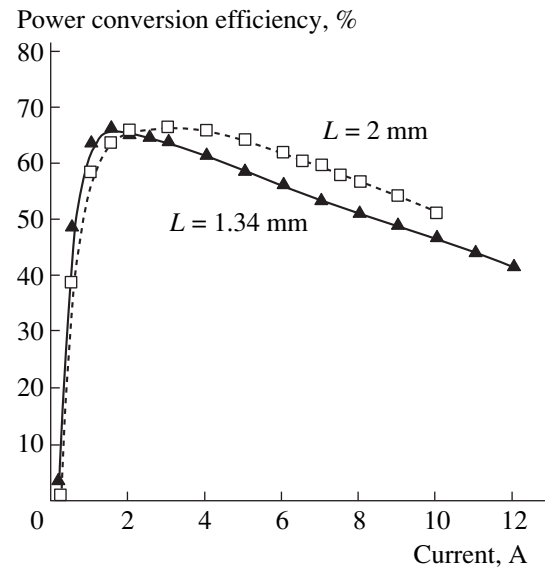


Fig. 4. Power conversion efficiency of InGaAs/AlGaAs/GaAs lasers vs. driving current.

obtained on structures with a broad waveguide (>1 μm), which reduces the power density at the output mirror.

The achieved peak power density \bar{P} is found from

$$\bar{P} = P_{\text{max,CW}} \frac{1}{W(d/\Gamma)} \left(\frac{1 + R_f}{1 - R_f} \right), \quad (3)$$

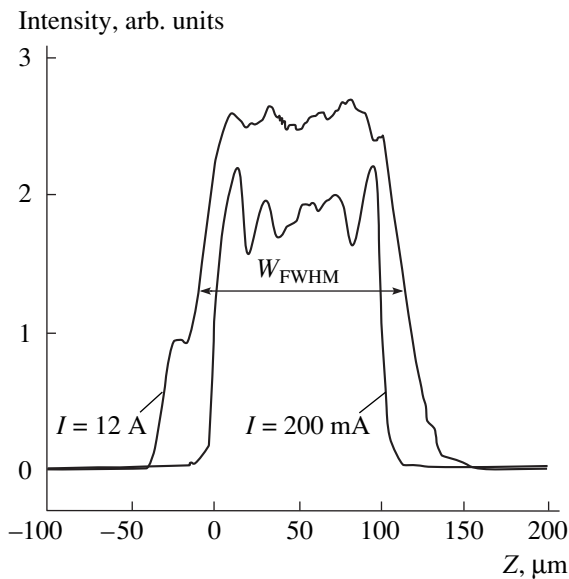


Fig. 5. Near-field patterns of the laser in the p - n junction plane (coordinate Z) at different driving currents.

where $P_{\max, CW}$ is the maximum achieved CW output power and d/Γ is the quantity characterizing the transverse spot size (d is the thickness of the active region and Γ is the optical confinement factor) [3]. With a broad waveguide ($\sim 1 \mu\text{m}$), the d/Γ value is 0.55 – $0.70 \mu\text{m}$, depending on the refractive indices of the waveguide and emitter materials. In the case in question, at a total waveguide thickness of $0.4 \mu\text{m}$, it is $0.34 \mu\text{m}$ (a lasing wavelength $\lambda = 1.03 \mu\text{m}$). Such a d/Γ value is in good agreement with the observed far-field pattern in the direction perpendicular to the p - n junction. The beam's full width at half-maximum was $\theta_{1/2} = 52^\circ$. Then the power density at the peak of the light wave at the front mirror is 29.9 MW/cm^2 at an output power of 9.2 W .

The measurement taken using the second method, with the laser crystal temperature stabilized at 10°C , precludes the heating of the active region, thus ensuring linear L - I and voltage-current (V - I) characteristics and making possible the achievement of the peak emission power of 12.2 W at a current of 13.3 A (Fig. 3). The heatsink temperature at the peak output power was -26°C . The peak optical power density at the output mirror of the laser, calculated by (3), was 40 MW/cm^2 . After the degradation of the laser at a power of 12.2 W , no changes were found on its output mirror, which meant that the degradation occurred in the heterostructure bulk, bearing no relation to mirror damage, and, therefore, the COMD threshold was even higher.

In our opinion, expression (3) fails to exactly describe the situation at high driving current densities, since the near-field of the laser expands beyond the "nominal" stripe width W with increasing current. The

increase in the near-field pattern relative to W depends on the laser diode design. For example, by using oxide stripe, the width of the near-field pattern may exceed W severalfold. Therefore, we propose to use in formula (3) the full near-field pattern width at half-maximum, W_{FWHM} , instead of the stripe width W . In the case in question, the near-field pattern of the laser also expands somewhat despite using the "shallow mesa" design. Pulsed measurements on the same laser (Fig. 5) demonstrated that the full width at half-maximum of the near-field pattern was $98 \mu\text{m}$ just above the threshold, increasing to $122 \mu\text{m}$ at a current of 12 A . With account taken of the near-field pattern expansion, the peak power density achieved in the present study is 24.5 MW/cm^2 . Even this value greatly exceeds the power densities of $\sim 19 \text{ MW/cm}^2$ previously obtained for a laser with a broad waveguide [3–5, 8, 9].

Laser diodes based on MBE-grown structures also exhibit good power and electrical characteristics. The maximum achieved CW power at a heatsink temperature stabilized at 20°C was 8.5 W .

Also, the degradation properties were studied. The tests were performed at a current of 4 A and output power of 3.3 W at a heatsink temperature of 30°C for 1000 h . In lasers based on MBE structures the output power changed during the test by no more than 3% . The lasers based on MOCVD structures showed a wide scatter of degradation parameters, which can be attributed to the quality of the substrates used for epitaxial growth. The MOCVD was done onto AGNK-3 GaAs substrates with a surface dislocation density exceeding 10^3 cm^{-2} , whereas the MBE technique used substrates manufactured by AXT, with a dislocation density of 10^2 cm^{-2} .

In conclusion, it should be emphasized that the peak CW output power of a laser diode with an aperture $W = 100 \mu\text{m}$ was 9.2 W at a heatsink temperature of 10°C and 12.2 W at a stabilized temperature of the active region. A 66% power conversion efficiency and a record optical power density at the output mirror (29.9 MW/cm^2), exceeding more than 1.5 -fold the previously published value, were achieved, and a value even higher than 40 mW/cm^2 was obtained for more intense laser cooling by keeping the temperature of the active region constant. It was demonstrated that the peak output power, power conversion efficiency, optical strength of mirrors, and service life of laser diodes depend on the quality of the substrate and epitaxial layers, the heterostructure doping scheme, and the way in which the coatings are deposited onto mirrors and the laser is mounted on a heatsink. The results obtained indicate that record power characteristics can be achieved without using complex heterostructures, as in [9], and intricate mirror protection technologies, as in [10].

ACKNOWLEDGMENTS

The authors wish to thank E.A. Tret'yakova and T.N. Drokina for help in performing the technological operations.

REFERENCES

1. D. Z. Garbuzov, N. Y. Antonishkis, A. D. Bondarev, *et al.*, IEEE J. Quantum Electron. **27**, 1531 (1991).
2. D. Z. Garbuzov, N. Ju. Antonishkis, S. N. Zhigulin, *et al.*, Appl. Phys. Lett. **62**, 1062 (1993).
3. D. Botez, Appl. Phys. Lett. **74**, 3102 (1999).
4. D. Botez, Compd. Semicond. **5** (6), 24 (1999).
5. A. Al-Muhanna, L. Mawst, D. Botez, *et al.*, Appl. Phys. Lett. **73**, 1182 (1998).
6. J. Wang, B. Smith, X. Xie, *et al.*, Appl. Phys. Lett. **74** (11), 1525 (1999).
7. D. Garbuzov, M. Maiorov, V. Khalfin, *et al.*, in *Proceedings of the SPIE Photonics West Conference'99, San Jose, 1999*, Paper 3625-93.
8. X. He, S. Srinivasan, S. Wilson, *et al.*, Electron. Lett. **34** (22), 2126 (1998).
9. D. A. Livshits, E. Yu. Kotelnikov, A. A. Katsnelson, *et al.*, in *Proceedings of the 8th International Symposium "Nanostructures: Physics and Technology," St. Petersburg, 2000*, p. 31.
10. J. K. Lee, K. H. Pack, D. H. Jang, *et al.*, IEEE Photonics Technol. Lett. **10** (9), 1226 (1998).

Translated by M. Tagirdzhanov